CHAPTER

7

HETERONUCLEAR NMR EXPERIMENTS

The 2D and 3D ^{1}H NMR methods discussed in Chapter 6 are ineffective for proteins with molecular masses greater than approximately 10–12 kDa. The number of hydrogen atoms present in proteins scales approximately linearly with molecular mass. The rotational correlation times of globular proteins, and thus the linewidths of the NMR resonances, also increase linearly with molecular mass. The increased number and linewidth of the resonances in homonuclear ^{1}H NMR spectra result in extensive chemical shift overlap and degeneracy. Conventional assignment procedures, based upon observation of sequential NOE correlations (Chapter 10), become difficult or impossible. In addition, larger linewidths (larger spin–spin relaxation rate constants) result in decreased sensitivity for ^{1}H correlation experiments that rely on small ($<$10Hz) homonuclear ^{3}J scalar couplings for coherence transfer (e.g., COSY, multiple-quantum, and TOCSY experiments).

Heteronuclear NMR spectroscopy (*1–3*) effectively circumvents these problems for proteins of at least up to molecular masses of 25–30 kDa, provided that the proteins can be uniformly labeled with the NMR active isotopes ^{13}C and ^{15}N (*4*); as discussed in Chapter 9, even larger proteins are accessible by combining ^{15}N and ^{13}C labeling with fractional or complete deuteration, in which nonexchangeable ^{1}H atoms

are replaced with ^{2}H atoms (*5*, *6*). Spectral resolution is improved by increasing the dimensionality of the NMR spectrum so that the highly overlapped ^{1}H resonances, present in ^{1}H 2D spectra, are separated in 3D and 4D spectra according to the more highly resolved heteronuclear resonances. At the same time, the efficiency of coherence transfer is increased by utilizing relatively large one-bond and two-bond (^1J and ^2J) scalar coupling interactions between pairs of heteronuclei and between heteronuclei and their directly attached hydrogen nuclei, rather than the relatively small ^{1}H homonuclear three-bond scalar coupling interactions.

The general principles of heteronuclear NMR spectroscopy are discussed in this Chapter. A selection of experiments is described, focusing on those that are necessary for resonance assignment and structure determination of isotopically labeled proteins. The selection of experiments presented in this chapter is made for pedagogical purposes and is by no means complete; indeed, a given resonance correlation may be obtained using several different methods, and development of new experimental techniques continues apace. Furthermore, except for certain illustrative cases, the pulse sequences presented do not include details concerning pulsed field gradient techniques for artifact suppression and coherence-selection or water-suppression techniques. Pulsed field gradients and water-suppression can be incorporated in multiple ways using the methods described in Chapters 3 and 4. A selection of pulse sequences containing such elaborations is presented in Chapter 9. A comprehensive survey of modern techniques has been published (*7*).

All multidimensional heteronuclear NMR experiments correlate heteronuclear resonances, typically ^{13}C or ^{15}N in proteins, with ^{1}H resonances by transfer of coherence (or polarization) between the heteronuclear (S) and ^{1}H (I) spins. Regardless of the specific protocol utilized to effect coherence transfer, the NMR experiment can start with excitation of either I or S spin polarization and must end with detection of either I or S spin magnetization. Ignoring the relative efficiency of different coherence or polarization transfer schemes, the overall sensitivity of heteronuclear correlation NMR experiments is proportional to (see [3.69] and [3.188])

$$\mathrm{S/N} \propto \gamma_{\mathrm{ex}}\gamma_{\mathrm{det}}^{3/2}[1 - \exp(-R_{1\mathrm{ex}}T)], \qquad [7.1]$$

in which γ_{ex} and γ_{det} are the magnetogyric ratios of each nucleus excited at the beginning of the sequence and detected at the end of the sequence, respectively, T is the recycle time of the experiment, and $R_{1\mathrm{ex}}$ is the spin–lattice relaxation rate constant of the excited nucleus (assuming

multiple transients are accumulated) (*8*). Therefore, *indirect*, or *proton*, *detection* is used whenever possible in order to maximize sensitivity. In these techniques, ^{1}H spin polarization initially is transferred to the heteronucleus, the desired heteronuclear spin manipulations are performed, and the heteronuclear coherence finally is transferred back to ^{1}H magnetization for detection. The gain in sensitivity compared to a correlation experiment in which ^{1}H magnetization is transferred to the S nucleus for detection is thus $n(\gamma_I/\gamma_S)^{3/2}$, in which γ_I and γ_S are the magnetogyric ratios of the I and S nuclei, respectively, and n is the number of hydrogen atoms attached to the S nucleus. For ^{1}H–^{13}C correlations, the gain in sensitivity is approximately 24 for methyl ^{1}H spins, 16 for methylene ^{1}H spins, and 8 for methine ^{1}H spins, while for ^{1}H–^{15}N correlations of backbone amides the gain is approximately 30. The sensitivity gain relative to an experiment that starts with S-nucleus polarization and detects ^{1}H magnetization is simply the ratio of the magnetogyric ratios, γ_I/γ_S; for ^{1}H–^{13}C correlations this ratio is about 4, and for ^{1}H–^{15}N correlations it is about 10. The larger spin–lattice relaxation rate constants of hydrogen nuclei compared to heteronuclei ($R_{1I} > R_{1S}$) give an additional sensitivity advantage to the experiments starting with ^{1}H magnetization (i.e., the schemes involving $I \rightarrow S$ and $I \rightarrow S \rightarrow I$ transfers) because of the $[1-\exp(-R_{1\mathrm{ex}}T)]$ factor in [7.1]. In practice, several factors can reduce the empirical gain in sensitivity, including splitting of the resonance signal into multiplets due to homonuclear scalar couplings, relaxation during coherence transfer steps, incomplete coherence transfer in multispin systems (e.g., I_2S and I_3S systems), and resonance offset effects arising from the increased heteronuclear, relative to ^{1}H, chemical shift range. Direct ^{13}C-detected experiments also have been introduced for application to biomacromolecules (*9*).

7.1 Heteronuclear Correlation NMR Spectroscopy

Two-dimensional proton-detected heteronuclear correlation experiments most commonly use HMQC, HSQC, or TROSY coherence transfer mechanisms. The techniques are distinguished by whether the transferred coherence evolves during an indirect evolution period as heteronuclear multiple-quantum coherence (HMQC), heteronuclear single-quantum coherence (HSQC), or heteronuclear coherence, usually but not always spin state selective, chosen for its favorable relaxation properties (TROSY) (*10–14*). As will be seen subsequently, the two-dimensional heteronuclear correlation experiments are integral

components of all heteronuclear three- and four-dimensional NMR experiments.

7.1.1 BASIC HMQC AND HSQC EXPERIMENTS

Pulse sequences for the HMQC and HSQC heteronuclear correlation experiments are illustrated in Fig. 7.1. A heteronuclear *IS* spin system ($I = {}^{1}\mathrm{H}$, $S = {}^{15}\mathrm{N}$ or ${}^{13}\mathrm{C}$), in which the I and S spins are directly covalently bonded and the ${}^{1}\mathrm{H}$ spin I is scalar coupled to a remote ${}^{1}\mathrm{H}$ spin, K, forms the basis for the following discussion. The homonuclear ${}^{1}\mathrm{H}$ scalar coupling constant (J_{IK}) is assumed to be much smaller than J_{IS}.

7.1.1.1 The HMQC Experiment Evolution during the HMQC scheme of Fig. 7.1a is described using the product operator formalism as follows:

$$\begin{aligned} I_z &\xrightarrow{\frac{\pi}{2}(I_x+K_x)-2\tau-\frac{\pi}{2}S_x} -2I_xS_y \\ &\xrightarrow{t_1/2-\pi(I_x+K_x)-t_1/2} -2I_xS_y\cos(\Omega_S t_1)\cos(\pi J_{IK}t_1) - 4I_yK_zS_y\cos(\Omega_S t_1) \\ &\qquad \times \sin(\pi J_{IK}t_1) \\ &\xrightarrow{\frac{\pi}{2}S_x-2\tau} -I_y\cos(\Omega_S t_1)\cos(\pi J_{IK}t_1) + 2I_xK_z\cos(\Omega_S t_1)\sin(\pi J_{IK}t_1), \end{aligned} \qquad [7.2]$$

in which the delay 2τ is set to $1/(2J_{IS})$ (approximately 5.4 ms for one-bond ${}^{1}\mathrm{H}$–${}^{15}\mathrm{N}$ $J_{\mathrm{NH}} = 92$ Hz, and 3.6 ms for one-bond ${}^{1}\mathrm{H}$–${}^{13}\mathrm{C}$ $J_{\mathrm{CH}} = 140$ Hz). If desired, all delays of nominal length $1/(2J_{IS})$ can be shortened slightly to account for relaxation (Section 5.1.1). Only operators leading to observable terms have been propagated through the pulse sequence. Evolution of scalar coupling interactions other than J_{IS} during the periods 2τ has been ignored. Chemical shift evolution of the I spin during the 2τ periods and during t_1 is refocused by the 180°(I) pulse. Heteronuclear multiple-quantum (MQ) coherence, represented by the $2I_xS_y$ operator, does not evolve under the influence of the active scalar coupling, J_{IS}, during the t_1 period (Section 2.7.5). Evolution under the homonuclear J_{IK} scalar coupling Hamiltonian is not refocused, because both ${}^{1}\mathrm{H}$ spins I and K experience the effect of the nonselective 180°(I) pulse. The resulting correlation spectrum exhibits homonuclear J coupling multiplet structure in the F_1 dimension. In addition, the F_2 lineshapes consist of the superposition of in-phase absorptive and

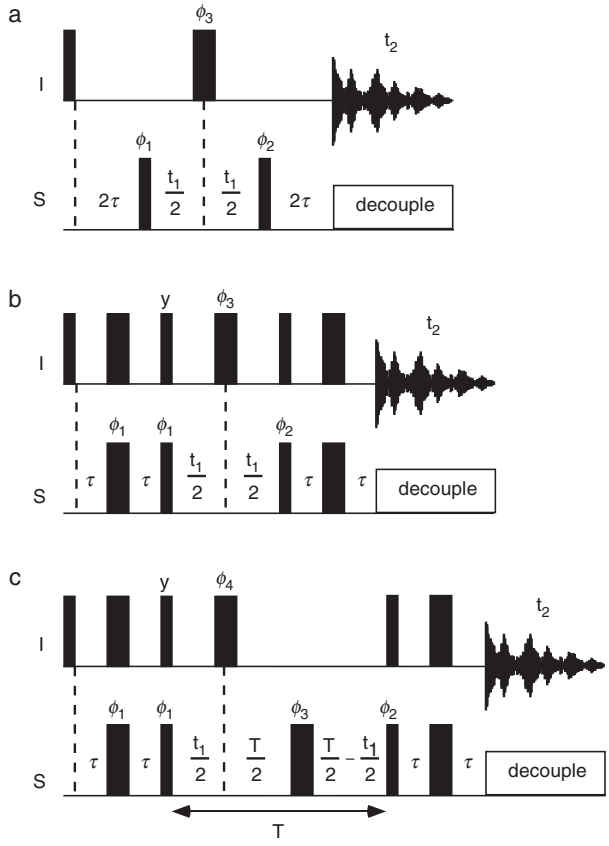

FIGURE 7.1 Pulse sequences for basic (a) HMQC, (b) HSQC, and (c) constant-time HSQC heteronuclear correlation experiments. Thin bars represent 90° pulses and thick bars represent 180° pulses. Pulses are applied with x-phase unless the phase is indicated above the bar. The nominal value for $2\tau = 1/(2J_{IS})$. Decoupling during t_2 is achieved by using GARP-1, WALTZ-16, or other decoupling sequences. (a) Phase cycling for the HMQC experiment is $\phi_1 = x, -x$; $\phi_2 = 8(x), 8(-x)$; $\phi_3 = 2(x), 2(y), 2(-x), 2(-y)$; and receiver $= 2(x, -x, -x, x), 2(-x, x, x, -x)$. (b) Phase cycling for the HSQC experiment is $\phi_1 = x, -x$; $\phi_2 = 2(x), 2(-x)$; $\phi_3 = 4(y), 4(-y)$; and receiver $= x, -x, -x, x$. (c) Phase cycling for the constant-time HSQC experiment is $\phi_1 = x, -x$; $\phi_2 = 8(x), 8(-x)$; $\phi_3 = 2(x), 2(y), 2(-x), 2(-y)$; $\phi_4 = 16(y), 16(-y)$; and receiver $= 2(x, -x, -x, x), 2(-x, x, x, -x)$. If desired, this 32-step phase cycle can be reduced to 8 steps by eliminating the cycling of ϕ_2 and using only the first 4 steps of the phase cycle of ϕ_3 (with appropriate changes to ϕ_4 and the receiver); an additional reduction by a factor of two can be obtained by eliminating cycling of ϕ_4. Frequency discrimination is obtained by TPPI, States, or TPPI–States phase cycling of ϕ_1.

antiphase dispersive components, represented by I_y and $2I_xK_z$ operators in the last line of [7.2], respectively.

The antiphase dispersive component of the signal can be purged by inserting a $90^\circ_y(I)$ pulse prior to the acquisition period. The purge pulse transforms the final operators in [7.2] to

$$\begin{aligned} &-I_y \cos(\Omega_S t_1) \cos(\pi J_{IK} t_1) + 2I_x K_z \cos(\Omega_S t_1) \sin(\pi J_{IK} t_1) \\ &\quad \xrightarrow{\frac{\pi}{2}(I_y + K_y)} -I_y \cos(\Omega_S t_1) \cos(\pi J_{IK} t_1) - 2I_z K_x \cos(\Omega_S t_1) \sin(\pi J_{IK} t_1). \end{aligned} \tag{7.3}$$

The antiphase I spin operator is transformed into an antiphase K spin operator. If the K spin resonance frequency occurs in an unimportant region of the spectrum (if it is not coupled to an S spin of interest), then the IS correlation spectrum has pure in-phase absorptive lineshapes in both frequency dimensions.

Inclusion of homonuclear scalar coupling evolution during the periods 2τ is facilitated by using [2.121] to simplify the propagator for the pulse sequence prior to product operator analysis. The propagator is

$$\begin{aligned} \mathbf{U} = &\exp[-i2\mathscr{H}\tau] \exp\left[-i\tfrac{\pi}{2}S_x\right] \exp[-i\mathscr{H}t_1/2] \exp[-i\pi(I_x + K_x)] \\ &\times \exp[-i\mathscr{H}t_1/2] \exp\left[-i\tfrac{\pi}{2}S_x\right] \exp[-i2\mathscr{H}\tau] \exp\left[-i\tfrac{\pi}{2}(I_x + K_x)\right], \end{aligned} \tag{7.4}$$

in which the free-precession Hamiltonian for weak scalar coupling is given by

$$H = \Omega_I I_z + \Omega_S S_z + 2\pi J_{IS} I_z S_z + 2\pi J_{IK} I_z K_z. \tag{7.5}$$

Inserting $\mathbf{E} = \exp[i\pi(I_x + K_x)] \exp[-i\pi(I_x + K_x)]$ and applying [2.121] yields

$$\begin{aligned} \mathbf{U} = &\exp[-i2\mathscr{H}\tau] \exp\left[-i\tfrac{\pi}{2}S_x\right] \exp[-i\mathscr{H}t_1/2] \exp[-i\pi(I_x + K_x)] \\ &\times \exp[-i\mathscr{H}t_1/2] \exp[i\pi(I_x + K_x)] \exp[-i\pi(I_x + K_x)] \\ &\times \exp\left[-i\tfrac{\pi}{2}S_x\right] \exp[-i2\mathscr{H}\tau] \exp\left[-i\tfrac{\pi}{2}(I_x + K_x)\right] \\ = &\exp[-i2\mathscr{H}\tau] \exp\left[-i\tfrac{\pi}{2}S_x\right] \exp[-i\mathscr{H}t_1/2] \\ &\times \exp[-i(-\Omega_I I_z + \Omega_S S_z - 2\pi J_{IS} I_z S_z + 2\pi J_{IK} I_z K_z)t_1/2] \exp\left[-i\tfrac{\pi}{2}S_x\right] \\ &\times \exp[-i(-\Omega_I I_z + \Omega_S S_z - 2\pi J_{IS} I_z S_z + 2\pi J_{IK} I_z K_z)2\tau] \exp\left[i\tfrac{\pi}{2}(I_x + K_x)\right] \\ = &\exp[-i2\pi J_{IK} I_z K_z(t_1 + 4\tau)] \exp[-i(\Omega_S S_z + 2\pi J_{IS} I_z S_z)2\tau] \exp\left[-i\tfrac{\pi}{2}S_x\right] \\ &\times \exp[-i\Omega_S S_z t_1] \exp\left[-i\tfrac{\pi}{2}S_x\right] \exp[-i(\Omega_S S_z - 2\pi J_{IS} I_z S_z)2\tau] \\ &\times \exp\left[i\tfrac{\pi}{2}(I_x + K_x)\right]. \end{aligned} \tag{7.6}$$

Evolution through the pulse sequence is represented as

$$
\begin{aligned}
I_z &\xrightarrow{-\frac{\pi}{2}(I_x+K_x)-(\Omega_S S_z-2\pi J_{IS} I_z S_z)2\tau-\frac{\pi}{2}S_x} -2I_xS_y \\
&\xrightarrow{\Omega_S S_z t_1} -2I_xS_y\cos(\Omega_S t_1) \xrightarrow{\frac{\pi}{2}S_x-(\Omega_S S_z+2\pi J_{IS} I_z S_z)2\tau} -I_y\cos(\Omega_S t_1) \\
&\xrightarrow{2\pi J_{IK} I_z K_z(t_1+4\tau)} -I_y\cos(\Omega_S t_1)\cos[\pi J_{IK}(t_1+4\tau)] \\
&\qquad + 2I_xK_z\cos(\Omega_S t_1)\sin[\pi J_{IK}(t_1+4\tau)]. \qquad [7.7]
\end{aligned}
$$

Evolution of the homonuclear scalar coupling during the 2τ periods introduces a phase error in the F_1 dimension of the 2D HMQC experiment. The magnitude of the phase error depends upon J_{IK} and thus will vary nonlinearly throughout the spectrum. For a 10 Hz scalar coupling constant and $2\tau = 1/(2J_{NH}) = 5.4$ ms, the phase error is 19.4°.

The linewidth in the F_1 dimension of an HMQC spectrum is determined by the relaxation rate constant of heteronuclear MQ coherence plus the contributions from inhomogeneous broadening (*10*, *13*). In this and the following discussions of other heteronuclear correlation experiments, inhomogeneous broadening is ignored and relaxation rate constants are calculated using the methods outlined in Chapter 5.

The model for relaxation assumes that (*i*) the S spins relax by dipole–dipole interactions with the directly attached I spins and by chemical shift anisotropy, (*ii*) the I spins relax by dipole–dipole interactions with the S spins, by dipole–dipole interactions with k additional remote ^{1}H spins and by chemical shift anisotropy, (*iii*) in the limit of slow overall tumbling, which typically applies for proteins, $\omega_I\tau_c \gg \omega_S\tau_c \gg 1$, and $J(0) \gg J(\omega_S) \gg J(\omega_I) \approx J(\omega_I \pm \omega_S)$, (*iv*) $\omega_I \approx \omega_K$, and (*v*) rotational diffusion is isotropic, with $J(\omega)$ given by [5.98]. Individual relaxation rate constants are obtained from Tables 5.5 and 5.8. in Chapter 5. In the resulting expressions, d_{IS} reflects the heteronuclear dipolar coupling between the scalar-coupled I and S spins; $d_{CSA(I)}$ and $d_{CSA(S)}$ arise from chemical shift anisotropy of the I and S spin, respectively, and the terms containing d_{Ik} reflect the homonuclear dipolar coupling between ^{1}H spins (Sections 5.4.1 and 5.4.4). In ^{13}C- or ^{13}C/^{15}N-labeled samples, the S spin (either ^{13}C or ^{15}N) has additional dipolar interactions with nearby, predominantly directly bonded, ^{13}C spins, designated as R spins. These interactions are smaller than the dipolar IS interaction by a factor of

$$d_{RS}/d_{IS} = \gamma_R^2 r_{IS}^6/\gamma_I^2 r_{RS}^6 \qquad [7.8]$$

and are neglected in the present discussion. The effects of relaxation interference are ignored until the TROSY experiment is discussed in Section 7.1.3.5.

The 180°(*I*) pulse during the HMQC scheme of Fig. 7.1a interconverts heteronuclear zero- and double-quantum coherences. Consequently, the relaxation rate constant for MQ coherence is the average of the relaxation rate constants for zero- and double-quantum coherences. Using the preceding model, the relaxation rate constant for MQ coherence is

$$\begin{aligned} R_{2\mathrm{MQ}} &= \tfrac{1}{2}\left[R_2^{IS}(\mathrm{ZQ}) + R_2^{IS}(\mathrm{DQ})\right] + R_2^{IK}(\mathrm{I}) + R_2^{\mathrm{CSA}}(\mathrm{I}) + R_2^{\mathrm{CSA}}(S) \\ &= \frac{d_{IS}}{8}\left\{J(\omega_I - \omega_S) + 3J(\omega_I) + 3J(\omega_S) + 6J(\omega_I + \omega_S)\right\} \\ &\quad + \frac{d_{\mathrm{CSA}(I)}}{6}\left\{4J(0) + 3J(\omega_I)\right\} + \frac{d_{\mathrm{CSA}(S)}}{6}\left\{4J(0) + 3J(\omega_S)\right\} \\ &\quad + \frac{1}{8}\sum_k d_{Ik}\left\{5J(0) + 9J(\omega_I) + 6J(2\omega_I)\right\}, \end{aligned} \qquad [7.9]$$

in which the summation, Σ, includes all the homonuclear $k \neq I$ spins. In the limit of slow overall tumbling, the relaxation rate constant is approximated by

$$R_{2\mathrm{MQ}} = \frac{\tau_c}{5}\left[\frac{4}{3}d_{\mathrm{CSA}(I)} + \frac{4}{3}d_{\mathrm{CSA}(S)} + \frac{5}{4}\sum_k d_{Ik}\right]. \qquad [7.10]$$

7.1.1.2 The HSQC Experiment In the HSQC experiment, illustrated in Fig. 7.1b, the INEPT sequence introduced in Section 2.7.7.2 is used to transfer I spin polarization (I_z) into antiphase heteronuclear single-quantum (SQ) coherence ($2I_zS_y$). The antiphase heteronuclear SQ coherence evolves during the subsequent t_1 evolution period. A second INEPT sequence is used to transfer the frequency-labeled heteronuclear SQ coherence back to ^{1}H magnetization for detection. For a heteronuclear IS spin system, evolution through the pulse sequence is described as follows:

$$\begin{aligned} I_z &\xrightarrow{\frac{\pi}{2}(I_x+K_x)-\tau-\pi(I_x+K_x),\,\pi S_x-\tau-\frac{\pi}{2}(I_y+K_y),\,\frac{\pi}{2}S_x} -2I_zS_y \\ &\xrightarrow{t_1/2-\pi(I_x+K_x)-t_1/2} 2I_zS_y\cos(\Omega_S t_1) - 2I_zS_x\sin(\Omega_S t_1) \\ &\xrightarrow{\frac{\pi}{2}(I_x+K_x),\,\frac{\pi}{2}S_x-\tau-\pi(I_x+K_x),\,\pi S_x-\tau} -I_x\cos(\Omega_S t_1) - 2I_yS_x\sin(\Omega_S t_1), \end{aligned} \qquad [7.11]$$

in which the delay $2\tau = 1/(2J_{IS})$ and evolution of the homonuclear ^{1}H scalar coupling interaction during the INEPT sequences has been ignored. The resultant term proportional to I_yS_x is unobservable multiple-quantum coherence. The $180^\circ(I)$ pulse in the middle of the evolution period refocuses evolution of the ^{1}H heteronuclear J_{IS} scalar coupling interaction. The $2I_zS_y$ operator present during t_1 commutes with the homonuclear ^{1}H scalar coupling Hamiltonian and the F_1 lineshape does not contain contributions from ^{1}H scalar coupling interactions.

Evolution of the homonuclear scalar coupling interaction during the INEPT sequences is analyzed most easily by using [2.121] to simplify the propagator for the pulse sequence:

$$\begin{aligned}
\mathbf{U} = {} & \exp[-i\mathscr{H}\tau]\ \exp[-i\pi(I_x + K_x)]\ \exp[-i\pi S_x]\ \exp[-i\mathscr{H}\tau] \\
& \times \exp\left[-i\tfrac{\pi}{2}(I_x + K_x)\right]\ \exp\left[-i\tfrac{\pi}{2}S_x\right]\ \exp[-i\mathscr{H}t_1/2]\ \exp[-i\pi(I_x + K_x)] \\
& \times \exp[-i\mathscr{H}t_1/2]\ \exp\left[-i\tfrac{\pi}{2}S_x\right]\ \exp\left[-i\tfrac{\pi}{2}(I_y + K_y)\right]\ \exp[-i\mathscr{H}\tau] \\
& \times \exp[i\pi(I_x + K_x)]\ \exp[-i\pi S_x]\ \exp[-i\mathscr{H}\tau]\ \exp\left[-i\tfrac{\pi}{2}(I_x + K_x)\right] \\
= {} & \exp[-i(2\pi J_{IS}I_zS_z + 2\pi J_{IK}I_zK_z)2\tau]\ \exp\left[i\tfrac{\pi}{2}(I_x + K_x)\right] \\
& \times \exp\left[-i\tfrac{\pi}{2}S_x\right]\ \exp[-i(\Omega_S S_z + 2\pi J_{IK}I_zK_z)t_1]\ \exp\left[-i\tfrac{\pi}{2}S_x\right] \\
& \times \exp\left[i\tfrac{\pi}{2}(I_y + K_y)\right]\ \exp[-i(2\pi J_{IS}I_zS_z + 2\pi J_{IK}I_zK_z)2\tau] \\
& \times \exp\left[-i\tfrac{\pi}{2}(I_x + K_x)\right]
\end{aligned} \qquad [7.12]$$

prior to evaluating evolution through the pulse sequence as

$$\begin{aligned}
I_z & \xrightarrow{\frac{\pi}{2}(I_x+K_x)-(2\pi J_{IS}I_zS_z+2\pi J_{IK}I_zK_z)2\tau-\left(-\frac{\pi}{2}\right)(I_y+K_y),\,\frac{\pi}{2}S_x} -2I_zS_y\cos(2\pi J_{IK}\tau) \\
& \xrightarrow{(-\Omega_S S_z+2\pi J_{IK}I_zK_z)t_1} -2I_zS_y\cos(\Omega_S t_1)\cos(2\pi J_{IK}\tau) \\
& \xrightarrow{\frac{\pi}{2}(I_x+K_x),\,\frac{\pi}{2}S_x-(2\pi J_{IS}I_zS_z+2\pi J_{IK}I_zK_z)2\tau} -I_x\cos(\Omega_S t_1)\cos^2(2\pi J_{IK}\tau) \\
& \qquad - I_yK_z\cos(\Omega_S t_1)\sin(4\pi J_{IK}\tau),
\end{aligned} \qquad [7.13]$$

in which only observable terms have been included. Evolution of the ^{1}H scalar coupling during the INEPT periods modulates the amplitude (but not the phase) of the in-phase absorptive resonance and introduces an antiphase dispersive contribution to the F_2 lineshape. As in the case of the HMQC experiment, the antiphase dispersive component can be purged by applying a $90^\circ_y(I)$ pulse prior to acquisition.

In Fig. 7.1b, the 90°(*I*) pulse following the t_1 period is phase shifted by 90° relative to the 90°(*I*) pulse preceding the t_1 period. If the two pulses have the same *y*-phase, then evolution through the pulse sequence becomes

$$
\begin{aligned}
I_z &\xrightarrow{\frac{\pi}{2}(I_x+K_x)-(2\pi J_{IS}I_zS_z+2\pi J_{IK}I_zK_z)2\tau-\left(-\frac{\pi}{2}\right)(I_y+K_y),\frac{\pi}{2}S_x} -2I_zS_y\cos(2\pi J_{IK}\tau) \\
&\quad + 4I_yS_yK_x\sin(2\pi J_{IK}\tau) \\
&\xrightarrow{(\Omega_S S_z+2\pi J_{IK}I_zK_z)t_1} -2I_zS_y\cos(\Omega_S t_1)\cos(2\pi J_{IK}\tau) \\
&\quad + 4I_yS_yK_x\cos(\Omega_S t_1)\sin(2\pi J_{IK}\tau) \\
&\xrightarrow{\frac{\pi}{2}S_x-\frac{\pi}{2}(I_y+K_y)-(2\pi J_{IS}I_zS_z+2\pi J_{IK}I_zK_z)2\tau} -I_y\cos(\Omega_S t_1)\cos(4\pi J_{IK}\tau)+2I_x \\
&\quad \times K_z\cos(\Omega_S t_1)\sin(4\pi J_{IK}\tau). \qquad [7.14]
\end{aligned}
$$

Comparison of [7.13] and [7.14] demonstrates that the phase shift of the final 90°(*I*) pulse reduces contributions from evolution of the homonuclear ^{1}H scalar coupling interaction during the initial INEPT period because $\cos^2(2\pi J_{IK}\tau) > \cos(4\pi J_{IK}\tau)$ and $\sin(4\pi J_{IK}\tau) < 2\sin(4\pi J_{IK}\tau)$.

The F_1 linewidth of the HSQC spectrum is determined by the relaxation rate of the heteronuclear SQ coherence under conditions of free precession during t_1. As discussed in Section 5.4.2, evolution under the scalar coupling Hamiltonian averages the relaxation rate constants for in-phase and antiphase SQ coherence to give

$$
\begin{aligned}
\bar{R}_{2S} &= \frac{1}{2}\left[R_2^{IS}(2I_zS^-) + R_2^{IS}(S) + R_1^{IK}(I) + R_1^{\mathrm{CSA}}(I)\right] + R_2^{\mathrm{CSA}}(S) \\
&= \frac{d_{IS}}{8}\left\{4J(0) + J(\omega_I-\omega_S) + 3J(\omega_S) + 3J(\omega_I) + 6J(\omega_I+\omega_S)\right\} \\
&\quad + \frac{d_{\mathrm{CSA}(I)}}{2}J(\omega_I) + \frac{d_{\mathrm{CSA}}}{6}\left\{4J(0)+3J(\omega_S)\right\} \\
&\quad + \frac{1}{8}\sum_k d_{Ik}\left\{J(0)+3J(\omega_I)+6J(2\omega_I)\right\}. \qquad [7.15]
\end{aligned}
$$

In the limit of slow overall tumbling, the relaxation rate constant is approximated by

$$
\overline{R}_{2S} = \frac{\tau_c}{5}\left[d_{IS} + \frac{4}{3}d_{CSA(S)} + \frac{1}{4}\sum_k d_{Ik}\right]. \qquad [7.16]
$$

7.1.1.3 The Constant-Time HSQC Experiment Constant-time evolution periods were originally used in ^{1}H NMR spectroscopy to produce F_1-decoupled homonuclear NMR spectra (*15–17*), but subsequently have been employed in a number of heteronuclear 3D and 4D experiments. The constant-time HSQC (CT-HSQC) experiment (*18*, *19*), illustrated in Fig. 7.1c, differs from the simple HSQC experiment (Fig. 7.1b) only in the way in which the heteronuclear SQ coherence evolves during the constant-time period, T, between the two INEPT sequences. The sequence fragment constituting the constant-time evolution period is

$$t_1/2 - 180^\circ(I,K) - T/2 - 180^\circ(S) - (T - t_1)/2 \qquad [7.17]$$

and has the propagator

$$\begin{aligned}\mathbf{U} = {} & \exp[-i\mathcal{H}(T - t_1)/2]\exp[-i\pi S_x]\exp[-i\mathcal{H}T/2]\exp[-i\pi(I_x + K_x)] \\ & \times \exp[-i\mathcal{H}t_1/2] \\ = {} & \exp[-i2\pi J_{IK} I_z K_z T]\exp[-i\Omega_I I_z(T - t_1)]\exp[i\Omega_S S_z t_1] \\ & \times \exp[-i\pi(I_x + K_x + S_x)]. \end{aligned} \qquad [7.18]$$

Evolution of the heteronuclear SQ coherence present following the initial INEPT sequence is given by

$$\begin{aligned} -\mathbf{U}2I_zS_y\mathbf{U}^{-1} &= -\exp(i\Omega_S t_1 S_z)2I_zS_y\exp(-i\Omega_S t_1 S_z) \\ &= -2I_zS_y\cos(\Omega_S t_1) + 2I_zS_x\sin(\Omega_S t_1). \end{aligned} \qquad [7.19]$$

As shown by [7.18], the heteronuclear scalar coupling interaction, J_{IS}, is active for a total time period $(T/2 - t_1/2) - T/2 + t_1/2 = 0$; consequently, the S spin coherence remains antiphase with respect to the I spins. The homonuclear scalar coupling, J_{IK}, is active for the entire constant-time period, T, because both spins are affected equally by a nonselective 180° pulse. Consequently, evolution during the t_1 period is not modulated by homonuclear scalar coupling interactions and the F_1 lineshape does not contain homonuclear multiplet structure. In the present example, this property is not particularly useful because the $2I_zS_y$ operator present during t_1 commutes with the ^{1}H homonuclear scalar coupling Hamiltonian. However, the same property exists for any homonuclear scalar coupling interaction and will be used to great advantage in ^{1}H–^{13}C HSQC spectra of fully ^{13}C-enriched proteins (Section 7.1.5).

Dephasing of the S spin coherence by magnetic field inhomogeneity during the constant-time period is refocused for a time $T - t_1$ by the 180°(S) pulse; consequently, relaxation of the heteronuclear

single-quantum coherence is proportional to $\exp(-R_2T)\exp(-R_{2\text{inhom}}t_1)$, in which R_2 is the homogeneous transverse relaxation rate of the SQ coherence and $R_{2\text{inhom}}$ is the inhomogeneous contribution to the total relaxation rate $R_2^* = R_2 + R_{2\text{inhom}}$. In the constant-time HSQC experiment, $\exp(-R_2T)$ is a multiplicative factor reducing the intensity of the resonance signals, and $\exp(-R_{\text{inhom}}t_1)$ determines the F_1 linewidth (in practice, $R_{\text{inhom}}t_{1\max} \ll 1$ and the F_1 linewidth is determined principally by the apodization function employed). Clearly, $t_{1\max}$ cannot exceed T, and constant-time HSQC experiments invariably require compromise between resolution in F_1 (large values for T to maximize $t_{1\max}$) and sensitivity [small values of T to minimize $\exp(-R_2T)$].

7.1.1.4 Comparison of HMQC and HSQC Spectra Selected regions of the ^{1}H–^{15}N HMQC, HSQC, and constant-time HSQC spectra of

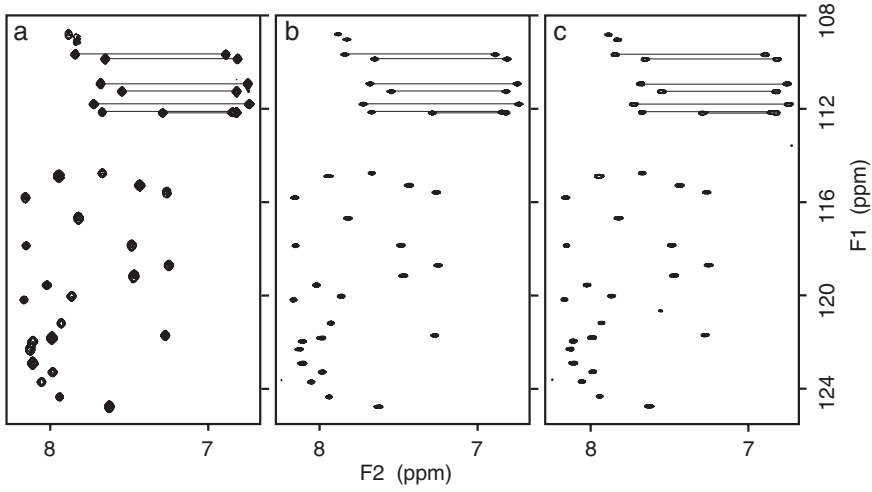

FIGURE 7.2 Comparison of selected regions from ^{1}H–^{15}N heteronuclear correlation spectra of ^{15}N-labeled ubiquitin, recorded using the schemes of Fig. 7.1a–c, respectively. Each spectrum was recorded in approximately the same total time with identical t_1 and t_2 acquisition times (348 and 164 ms, respectively). Each spectrum was processed similarly. No apodization function was applied in the F_1 dimension for the spectra shown in panels a and b; a cosine-bell apodization function was applied in the F_1 dimension of the spectrum shown in panel c. NH_2 correlations are indicated by lines connecting the two nonequivalent proton resonances.

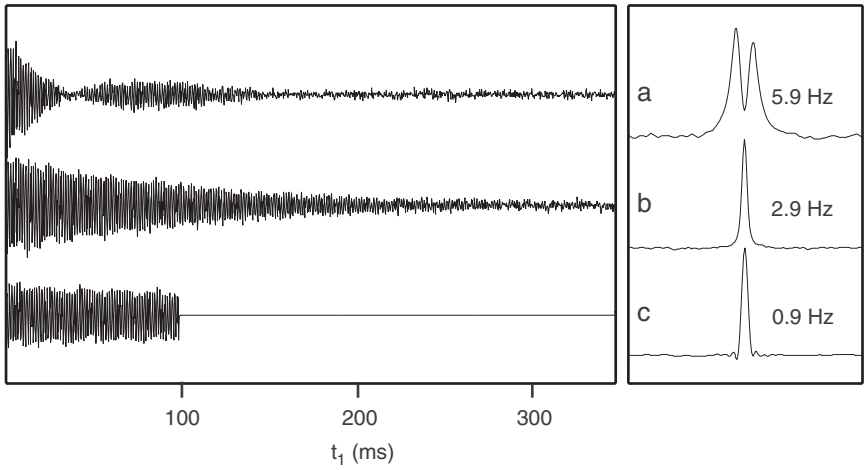

FIGURE 7.3 The t_1 interferograms, and their resulting Fourier transforms, taken through the amide proton resonance of Ile36 in the same ^1H–^{15}N heteronuclear correlation spectra as illustrated in Fig. 7.2a–c, respectively. The F_1 linewidth at half-height is indicated beside each peak. Linewidths were measured by curve fitting the decay of the t_1 interferograms. For peak c, the indicated linewidth represents inhomogeneous broadening.

ubiquitin are compared in Fig. 7.2. The multiplet structure and dispersive contribution to the F_1 lineshapes associated with the homonuclear J coupling is clearly visible in the HMQC spectrum (Fig. 7.2a). The F_1 resolution in the HSQC spectrum (Fig. 7.2b) is clearly superior to the F_1 resolution in the HMQC spectrum.

The different relaxation properties of the HMQC and HSQC experiments are emphasized in Fig. 7.3, which shows the t_1 interferograms through a selected amide ^1H resonance, and their corresponding Fourier transforms, for the spectra shown in Fig. 7.2. For backbone amide moieties in proteins, $d_{CSA(S)}/d_{IS} = 0.055$ (assuming $\Delta\sigma = -160$ ppm for ^{15}N and $B_0 = 11.74$ T) and $d_{IS}/\Sigma d_{Ik} \approx 0.3$. In this calculation, Σd_{Ik} was estimated using a typical value of $\Sigma r_{Ik}^{-6} = 0.027$ Å^{-6} for the distances between a backbone hydrogen atom and the other hydrogen atoms in proteins (*20*). Therefore, $R_{2MQ} \geq \overline{R}_{2S}$, and linewidths are narrower in the F_1 dimension of an ^1H–^{15}N HSQC spectrum than in that of an HMQC spectrum. The observed linewidths in spectra a and b in Fig. 7.3 are consistent with values of 4.9 and 3.0 Hz, respectively, calculated from [7.10] and [7.16] by using $\tau_c = 4.1$ ns.

The dispersive contribution associated with the homonuclear J coupling is clearly visible in the HMQC spectrum (Fig. 7.3a). As expected, the interferogram for the constant-time HSQC experiment (Fig. 7.3c) exhibits very little decay, and the linewidth in the transformed spectrum is dominated by the apodization applied during processing. For ^{1}H–^{13}C methine moieties, $d_{CSA(S)}/d_{IS} = 0.002$ (assuming $\Delta\sigma = 25$ ppm for ^{13}C and $B_0 = 11.74$ T) and $d_{IS}/\Sigma d_{Ik} \approx 1.4$. Therefore, $R_{2MQ} \approx \overline{R}_{2S}$, and linewidth differences in ^{1}H–^{13}C HSQC and ^{1}H–^{13}C HMQC spectra are not as pronounced as for ^{1}H–^{15}N correlations.

7.1.2 Additional Considerations in Heteronuclear Correlation Experiments

Aspects of phase cycling, quadrature detection, multiplet structure, folding or aliasing, and processing schemes that have not been discussed in detail for the basic HMQC and HSQC experiments are presented in the following sections.

7.1.2.1 Phase Cycling and Artifact Suppression The minimum phase cycling required for HMQC and HSQC experiments comprises two steps necessary for *spectral editing* or *isotope filtration* and two steps necessary for frequency discrimination, or quadrature detection, in the indirectly detected dimension (Section 4.3.4).

Frequency discrimination normally is obtained by TPPI, States, or TPPI–States phase cycling (Section 4.3.4.1) of the first $90^{\circ}_{\phi_1}(S)$ pulse in the HMQC and HSQC experiments (Fig. 7.1). In the HSQC experiments (Fig. 7.1b–c), the phase of the $180^{\circ}(S)$ pulses preceding the t_1 period should be phase cycled in concert with the $90^{\circ}_{\phi_1}(S)$ pulse for optimal results (*21*). The initial t_1 sampling delay is adjusted to $1/(2SW_1)$ as described in Section 3.3.2.3 by adjusting $t_1(0)$ such that

$$t_1(0) = 1/(2SW_1) - 4\tau_{90^{\circ}(S)}/\pi \qquad [7.20]$$

for conventional evolution periods (e.g., Fig. 7.1a–b). For the constant-time evolution period of Fig. 7.1c, $t_1(0) = 1/(2SW_1)$.

The isotope filtration phase cycle is critically important for most heteronuclear experiments, because only signals from ^{1}H spins directly attached to the heteronucleus of interest (^{15}N or ^{13}C) are selected. Normally, changes in the coherence order of the S spin between $p_S = 0$ (corresponding to a product operators containing an S_z component) and $p_S = \pm 1$ (corresponding to product operators containing a S_x or S_y

component) are selected in a two-step phase cycle by simultaneously inverting the phase of a $90^\circ(S)$ pulse and the receiver. Signals from I spins that are not scalar coupled to S spins are unaffected by the phase shift of the $90^\circ(S)$ pulse and are canceled by inversion of the receiver phase. Straightforward product operator analysis demonstrates that an isotope filter can be implemented in the HMQC and HSQC (Fig. 7.1) by use of a two-step $(x, -x)$ phase cycle on the $90^\circ_{\phi_1}(S)$ pulse or the $90^\circ_{\phi_2}(S)$ together with an $(x, -x)$ receiver phase cycle. Normally, the first pulse is chosen for the isotope filter phase cycling because a degree of axial peak suppression is obtained as well. Time permitting, both pulses can be cycled independently to give a four-step "double-difference" isotope filter (*22*).

Additional phase cycling is utilized to eliminate artifacts resulting from pulse imperfections. The $180^\circ(I)$ pulse in the middle of the t_1 evolution period of the HMQC experiment (Fig. 7.1a) typically benefits from EXORCYCLE phase cycling (Section 4.3.2.3) to suppress artifacts from imperfect 180° pulses. If a 180° pulse is used simply to invert a longitudinal operator [e.g., the $180^\circ(I)$ pulse applied to I_zS_y in the t_1 period of HSQC experiments], then artifacts caused by pulse imperfections are suppressed by inverting the phase of the 180° pulse in a two-step $(x, -x)$ phase cycle without changing the receiver phase. Time permitting, CYCLOPS phase cycling (Section 4.3.2.3) can be applied to the entire pulse sequence to eliminate quadrature artifacts.

The two-step $(x, -x)$ phase cycle applied to the $180^\circ(I)$ pulse in the t_1 period of the HSQC experiment provides an important example of artifact suppression in heteronuclear correlation experiments. If the pulse has a nominal rotation angle of $\pi + \zeta$, rather than the ideal value of π, then evolution through the t_1 period is given by (for simplicity, Ω_S is assumed to be zero)

$$\begin{aligned}
-2I_zS_y &\xrightarrow{\frac{t_1}{2}} -2I_zS_y\cos(\pi J_{IS}t_1/2) + S_x\sin(\pi J_{IS}t_1/2)\\
&\xrightarrow{\pm(\pi+\zeta)I_x} -2I_zS_y\cos(\pi J_{IS}t_1/2)\cos(\pi+\zeta)\\
&\qquad \pm 2I_yS_y\cos(\pi J_{IS}t_1/2)\sin(\pi+\zeta) + S_x\sin(\pi J_{IS}t_1/2)\\
&\xrightarrow{\frac{t_1}{2}} 2I_zS_y\left\{-\cos^2(\pi J_{IS}t_1/2)\cos(\pi+\zeta) + \sin^2(\pi J_{IS}t_1/2)\right\}\\
&\qquad + S_x\left\{1+\cos(\pi+\zeta)\right\}\cos(\pi J_{IS}t_1/2)\sin(\pi J_{IS}t_1/2)\\
&\qquad \pm 2I_yS_y\cos(\Omega_I t_1/2)\cos(\pi J_{IS}t_1/2)\sin(\pi+\zeta)\\
&\qquad \mp 2I_xS_y\sin(\Omega_I t_1/2)\cos(\pi J_{IS}t_1/2)\sin(\pi+\zeta). \qquad [7.21]
\end{aligned}$$

The first and last terms of the result in [7.21] are converted to observable ^{1}H magnetization by the reverse INEPT sequence:

$$\begin{aligned} &2I_zS_y\{-\cos^2(\pi J_{IS}t_1/2)\cos(\pi+\zeta)+\sin^2(\pi J_{IS}t_1/2)\} \\ &\quad \mp 2I_xS_y\sin(\Omega_I t_1/2)\cos(\pi J_{IS}t_1/2)\sin(\pi+\zeta) \\ &\xrightarrow{\text{INEPT}} -I_x\{-\cos^2(\pi J_{IS}t_1/2)\cos(\pi+\zeta)+\sin^2(\pi J_{IS}t_1/2)\} \\ &\quad \mp I_y\sin(\Omega_I t_1/2)\cos(\pi J_{IS}t_1/2)\sin(\pi+\zeta). \end{aligned} \quad [7.22]$$

This result can be simplified to

$$\begin{aligned} &-I_x\{-\cos^2(\pi J_{IS}t_1/2)\cos(\pi+\zeta)+\sin^2(\pi J_{IS}t_1/2)\} \\ &\quad \mp I_y\sin(\Omega_I t_1/2)\cos(\pi J_{IS}t_1/2)\sin(\pi+\zeta) \\ &= -I_x\{1+\cos(\zeta)\}/2 + I_x\cos(\pi J_{IS}t_1)\{1-\cos(\zeta)\}/2 \\ &\quad \pm I_y\sin(\Omega_I t_1/2)\cos(\pi J_{IS}t_1/2)\sin(\zeta) \\ &= -I_x\{1-\zeta^2/4\} + I_x\cos(\pi J_{IS}t_1)\zeta^2/4 \pm I_y\sin(\Omega_I t_1/2)\cos(\pi J_{IS}t_1/2)\zeta \end{aligned} \quad [7.23]$$

by applying standard trigonometric identities. The last line is obtained by assuming $\zeta \ll 1$. The first term represents the desired heteronuclear correlation resonance peak, with slightly reduced intensity. The second term represents an in-phase doublet split by the heteronuclear scalar coupling constant. The third term generates dispersive doublets at frequencies $+\Omega_I/2$ and $-\Omega_I/2$ (i.e., symmetrically positioned with respect to the main heteronuclear correlation resonance peak), with apparent splitting equal to $J_{IS}/2$ and amplitudes $\zeta/4$. For $\zeta = 20^\circ$ (0.35 radians), the relative amplitudes of the resonance peaks are 0.97, 0.015, and 0.09. The third term in [7.23], which represents the largest artifact, is eliminated by the two-step phase cycle. The second term cannot be eliminated by phase cycling (or field gradient pulses); however, this term normally is small if the pulse lengths are measured carefully.

Artifacts associated with 180° pulses can also be eliminated by using field gradient pulses (Section 4.3.3.2), composite pulses (Section 3.4.3), and adiabatic pulses (Section 3.4.6). Composite and adiabatic pulses are beneficial particularly for the 180°(*S*) pulses during the INEPT sequences of the HSQC experiment (Fig. 7.1b), because optimal inversion of the S_z operator component (over a typically wide spectral width) directly improves the sensitivity of the experiment.

7.1.2.2 ^{13}C Scalar Coupling and Multiplet Structure The preceding analyses of heteronuclear correlation experiments have indicated the

multiplet structure arising due to heteronuclear *IS* and homonuclear *IK* scalar coupling interactions. For proteins enriched in ^{13}C, additional scalar coupling interactions must be considered.

In most of the other experiments designed for application to ^{13}C-labeled proteins, aliphatic $^{13}C^{\alpha}$ and ^{13}CO spins are treated theoretically as different nuclear species because of the large difference in resonance frequencies ($\sim$100 ppm). The $^{13}C^{\alpha}$ or ^{13}CO spins can be decoupled by applying selective 180° pulses or semi-selective decoupling schemes to the ^{13}CO or $^{13}C^{\alpha}$ spins during t_1. However, rf fields applied at aliphatic $^{13}C^{\alpha}$ frequencies can have significant effects at the carbonyl frequencies (and *vice versa*) that must be considered in practice. First, the carbonyl (aliphatic) pulses should minimally excite the aliphatic (carbonyl) spins, either by adjusting the power and duration of rectangular pulses as described in Section 3.4.1 or by using selective pulses (Section 3.4.4). Second, phase errors and frequency shifts caused by off-resonance effects of carbonyl (aliphatic) rf fields applied during aliphatic (carbonyl) ^{13}C evolution periods should be compensated in the pulse sequence whenever possible (Section 3.4.1).

In ^{1}H–^{15}N heteronuclear correlation NMR spectroscopy of $^{15}N/^{13}C$ double-labeled proteins, the ^{13}C–^{15}N scalar coupling interaction must be decoupled. In most instances, decoupling of ^{13}CO–^{15}N and aliphatic ^{13}C–^{15}N interactions is performed independently by using selective 180° pulses or semiselective composite pulse decoupling sequences. In ^{1}H–^{13}C heteronuclear correlation NMR spectroscopy of $^{15}N/^{13}C$ double-labeled proteins, an additional 180°(^{15}N) pulse is applied in the middle of the ^{13}C evolution period, or a broadband ^{15}N decoupling scheme is applied throughout t_1, in order to decouple the ^{15}N and ^{13}C spins.

These methods clearly will not work in the case of homonuclear ^{13}C–^{13}C couplings between aliphatic ^{13}C spins because all aliphatic ^{13}C spins will experience the effect of the inversion pulses. Therefore, the F_1 lineshapes in ^{1}H–^{13}C HSQC and HMQC spectra typically are composed of ^{13}C–^{13}C scalar coupled multiplets. The multiplet structure can be collapsed by using a constant-time ^{13}C evolution period as described in Section 7.1.5 or by homonuclear decoupling techniques (*23*).

7.1.2.3 Folding and Aliasing For a fixed number of t_1 increments, the digital resolution of the F_1 dimension of an HSQC (or other) experiment generally can be increased by reduction of the spectral width to less than the actual maximum frequency range of the resonances of interest. However, if the maximum number of t_1 increments is being utilized in a constant-time experiment ($t_{1\max} = T$), then the digital resolution cannot

be improved because reducing the spectral width requires that the number of t_1 increments be reduced to maintain $t_{1\max} \leq T$.

Whenever the spectral width is reduced, resonance signals from outside the acquired spectral window will be folded or aliased in the NMR spectrum (Sections 3.2.1, and 4.3.4.3). Data acquired with the hypercomplex methods (States or TPPI–States) are aliased, in which resonances upfield (downfield) of the acquired spectral window appear at the low-(high)-field side of the spectrum. Folding, in which resonances upfield (downfield) of the acquired spectral window fold back into the spectrum at the upfield (downfield) edge, occurs for real acquisition (TPPI). If the initial sampling delay in the aliased dimension is set to 1/(2SW), then peaks that have been folded or aliased an odd number of times have opposite phase to those that have not been aliased or have been aliased an even number of times.

The effect of reducing the ^{13}C spectral width is shown schematically in Fig. 7.4 for hypercomplex and real acquisition in t_1. Clearly, the

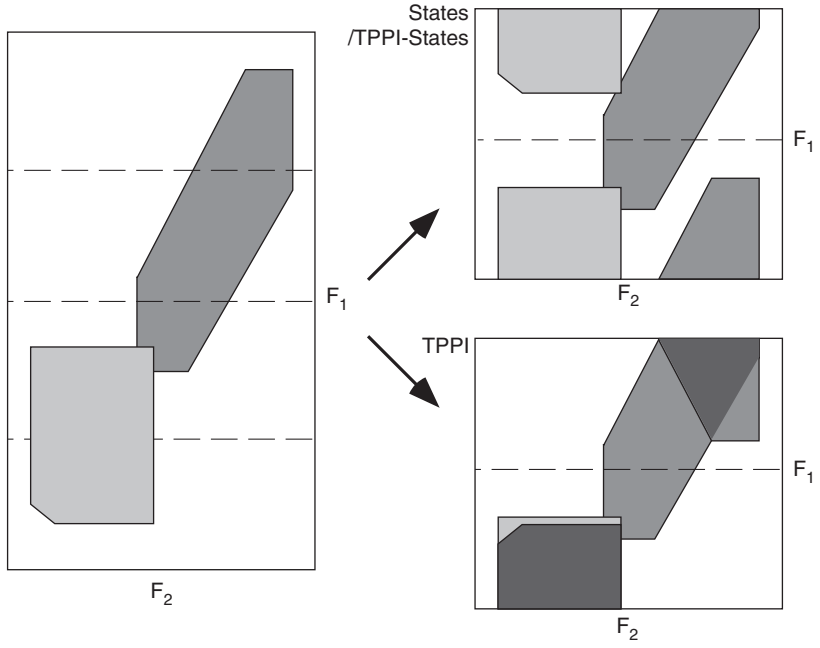

FIGURE 7.4 A schematic illustration of the effect of halving the F_1 spectral width in an ^{1}H–^{13}C heteronuclear correlation experiment, for both hypercomplex (States or TPPI–States) and real (TPPI) acquisition in t_1.

empirical relationship between ^{1}H and ^{13}C chemical shifts in proteins allows extensive aliasing via hypercomplex acquisition in the ^{13}C dimensions of 2D, 3D, and 4D NMR spectra. The ^{13}C spectral width can be readily set to as low as 20 ppm without adversely complicating the interpretation of the spectrum. Each apparent ^{13}C frequency in the final spectrum corresponds to several ^{13}C chemical shifts, separated by intervals equal to the acquired ^{13}C spectral width. Identification of the true ^{13}C chemical shift of a given cross-peak is determined from the associated aliphatic ^{1}H chemical shift together with knowledge of the sequential resonance assignments. Aliasing also can be used advantageously in ^{15}N correlation experiments (particularly to alias upfield Arg $^{15}N^{\varepsilon}$ resonances). When beginning investigations of a new protein, a trial spectrum should be recorded with a wide enough spectral width to encompass the actual resonance positions and enable optimal parameters for folding to be determined.

The use of aliasing is illustrated in practice for the ^{1}H–^{13}C HSQC spectra of ubiquitin in Fig. 7.5. Both experiments were acquired using a simple HSQC pulse sequence (Fig. 7.1b) and the TPPI–States hypercomplex method of quadrature detection in t_1. The improvement in digital resolution can be seen clearly in the aliased spectrum acquired

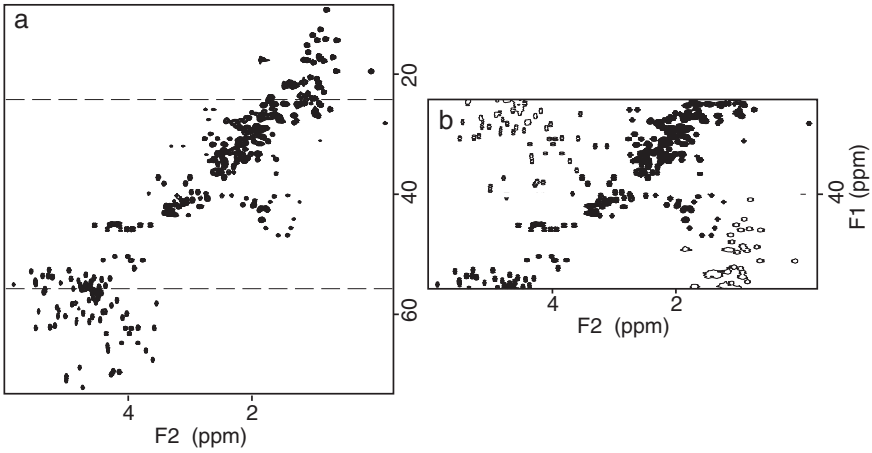

FIGURE 7.5 ^{1}H–^{13}C HSQC spectra of uniformly $^{15}N/^{13}C$-labeled ubiquitin, recorded with F_1 spectral widths of (a) 9090.9 Hz (72.3 ppm) and (b) 3971.4 Hz (31.6 ppm). Negative cross-peaks in panel b, which correspond to resonances that have been aliased in the F_1 dimension, are plotted with a single level only.

with the reduced F_1 spectral width, as more of the homonuclear ^{13}C–^{13}C couplings are resolved in this spectrum.

One of the main advantages of using a narrower ^{13}C spectral width is that a given digital resolution (set by t_{1max}) can be achieved by using fewer t_1 increments. Consequently, for a fixed total acquisition time, more transients can be acquired per increment, more extensive phase cycling can be employed, and data storage requirements are reduced. For given values of t_{1max} and the total acquisition time, reducing the spectral width and increasing the number of transients per increment do not affect sensitivity of the NMR experiment, because proportionally fewer increments are acquired. These features are particularly important when recording 3D and 4D spectra.

7.1.2.4 Processing Heteronuclear Correlation Experiments HMQC, HSQC, and other heteronuclear correlation experiments produce lineshapes that are predominately in-phase and absorptive in both the F_1 and F_2 dimensions. Accordingly, processing these spectra is relatively straightforward and does not require careful optimization of t_{1max} and window functions to avoid self-cancellation of antiphase lineshapes (Section 6.2.1.3). In F_2 (the acquisition dimension), the FID will rarely be truncated, and exponential matched filtering or Lorentzian-to-Gaussian transformation are satisfactory. In the F_1 dimension, similar window functions are satisfactory if the interferograms are not truncated. More commonly, the interferograms will be truncated and Kaiser, Hamming, or cosine bell window functions provide satisfactory apodization (Section 3.3.2.2). Severely truncated data frequently are extended by linear prediction prior to Fourier transformation or are analyzed by maximum entropy reconstruction (Section 3.3.4). Interferograms in constant-time HSQC experiments are ideal for mirror-image linear prediction (Section 3.3.4.1).

7.1.3 DECOUPLED HSQC, SENSITIVITY-ENHANCED HSQC, AND TROSY EXPERIMENTS

Pulse sequences for decoupled HSQC, sensitivity-enhanced HSQC, and TROSY experiments are shown in Fig. 7.6. Each of these pulse sequences contains a reverse polarization scheme that consists of two pulse-interrupted free-precession periods appended to each other (i.e., two INEPT-like sequences separated by mixing pulses). Additional insights into the design of these experiments are obtained by considering them as members of a family of related pulse sequences.

7.1.3.1 The Decoupled HSQC Experiment The basic HSQC experiment transfers coherence from I to S spins in the form of antiphase SQ coherences. In some experiments, net magnetization transfer from I to S spins in the form of in-phase SQ coherence is desirable, either because of the improved linewidth or because of the requirements of subsequent coherence transfer steps in an extended pulse sequence (see Section 7.4.3 for an example) (*10*). A decoupled HSQC experiment that achieves net magnetization transfer is illustrated in Fig. 7.6a. A refocused INEPT sequence (Section 2.7.7.3) is used to transfer I spin polarization to in-phase S magnetization (*24*). The S magnetization evolves during the t_1 evolution period. Continuous ^{1}H decoupling is applied to suppress evolution under the IS scalar coupling Hamiltonian. A reverse refocused INEPT sequence transfers S spin magnetization back to I spin magnetization for detection. A more elegant implementation of this experiment, which does not alter the following discussion, is described by Ottiger and Bax (*25*). In the modified experiment, the pair of 180° pulses in the first $2\tau_1$ period are shifted in a semi-constant-time manner and the pair of 180° pulses in the second $2\tau_1$ period are eliminated. The modified experiment provides increased resolution and requires fewer 180° pulses.

Evolution through the decoupled HSQC pulse sequence for a scalar coupled heteronuclear I_nS spin system can be described as follows (for simplicity, homonuclear scalar coupling to remote ^{1}H spins is ignored):

$$\begin{aligned}
&\sum_{k=1}^{n} I_{kz} \xrightarrow{\frac{\pi}{2}\sum I_{kx}-\tau-\pi\sum I_{kx},\,\pi S_x-\tau-\frac{\pi}{2}\sum I_{ky},\,\frac{\pi}{2}S_x} -\sum_{k=1}^{n} 2I_{kz}S_y \\
&\xrightarrow{\tau_1-\pi\sum I_{kx},\,\pi S_x-\tau_1} nS_x \sin(2\pi J_{IS}\tau_1)\cos^{n-1}(2\pi J_{IS}\tau_1) \\
&\xrightarrow{t_1} nS_x \cos(\Omega_S t_1)\sin(2\pi J_{IS}\tau_1)\cos^{n-1}(2\pi J_{IS}\tau_1) \\
&\xrightarrow{\frac{\pi}{2}\sum I_{ky}-\tau_1-\pi\sum I_{kx},\,\pi S_x-\tau_1} \sum_{k=1}^{n} n2I_{kz}S_y \cos(\Omega_S t_1) \\
&\times \sin^2(2\pi J_{IS}\tau_1)\cos^{2n-2}(2\pi J_{IS}\tau_1) \\
&\xrightarrow{\frac{\pi}{2}\sum I_{kx},\,\frac{\pi}{2}S_x-\tau-\pi\sum I_{kx},\,\pi S_x-\tau} \sum_{k=1}^{n} nI_{kx}\cos(\Omega_S t_1)\Gamma_n^2(2\tau_1),
\end{aligned} \qquad [7.24]$$

in which $2\tau = 1/(2J_{IS})$ and only observable terms arising from in-phase S_x magnetization have been shown. The coherence transfer function,

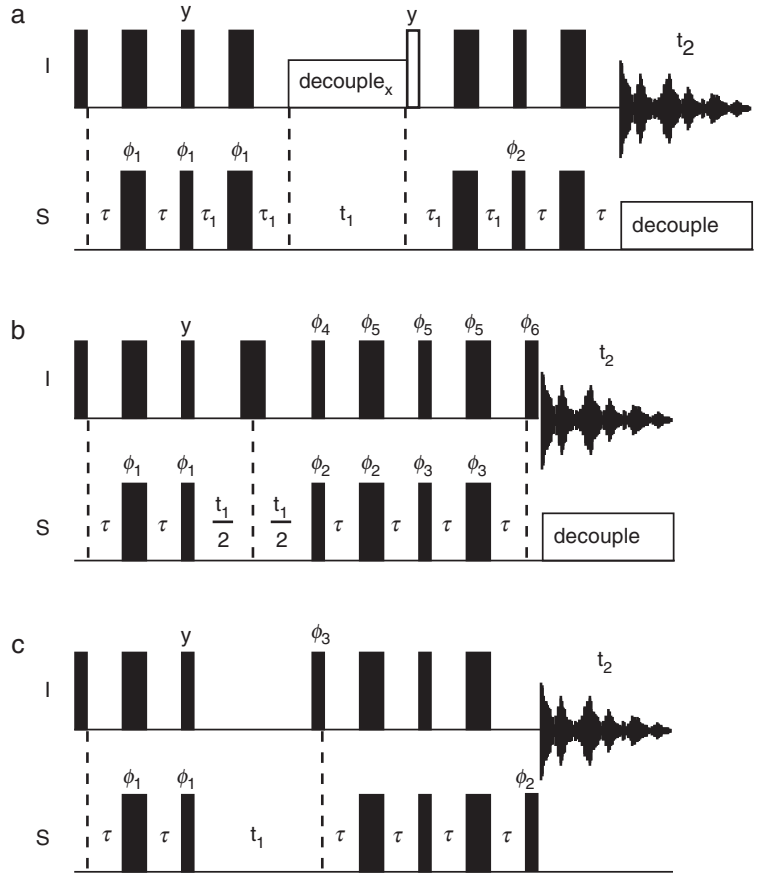

FIGURE 7.6 Pulse sequences for (a) decoupled HSQC, (b) sensitivity-enhanced PEP-HSQC, and (c) TROSY heteronuclear correlation experiments. Thin bars represent 90° pulses and thick bars represent 180° pulses. Pulses are applied with x-phase unless the phase is indicated above the bar. The nominal value for $2\tau = 1/(2J_{IS})$. Decoupling during t_1 in panel a is achieved by using WALTZ-16. Decoupling during t_2 in panels a and b is achieved by using GARP-1, WALTZ-16, or other decoupling sequences. (a) Phase cycling for the decoupled HSQC experiment is $\phi_1 = x, -x$; $\phi_2 = 2(x), 2(-x)$; and receiver $= x, -x, -x, x$. Frequency discrimination is obtained by TPPI, States, or TPPI–States phase cycling of ϕ_1. (b) Phase cycling for the PEP-HSQC experiment can be performed in two ways. In the original version, the phase cycling is $\phi_1 = x, -x$; $\phi_2 = 2(x), 2(-x)$; $\phi_3 = 2(y), 2(-y)$; $\phi_4 = x$; $\phi_5 = y$; $\phi_6 = -x$; and receiver $= x, -x, -x, x$ for the first FID acquired. The second FID is aquired with inversion of ϕ_2. Quadrature detection in the F_1 dimension is performed using the TPPI–States method applied to ϕ_1. In the modified version of the experiment, the phase

$\Gamma_n(t)$, is

$$\Gamma_n(t) = \sin(\pi J_{IS} t) \cos^{n-1}(\pi J_{IS} t) \quad [7.25]$$

and is graphed in Fig. 7.7. Complete refocusing cannot be obtained for I_nS spin systems with $n > 1$ because during the delays, $2\tau_1$, coherences evolve under one active J_{IS} scalar coupling interaction and $n-1$ passive J_{IS} scalar coupling interactions. The relative intensity of the I spin resonance in an IS spin system has a maximum value of 1.0 for $2\tau_1 = 1/(2J_{IS})$. The relative intensity of each I spin resonance in an I_2S spin system has a maximum value of 0.50 for $2\tau_1 = 1/(4J_{IS})$ and is nulled for $2\tau_1 = 1/(2J_{IS})$. The relative intensity for each I spin resonance in an I_3S spin system has a maximum value equal to approximately 0.45 for $2\tau_1 = 1/(5J_{IS})$ and is nulled for $2\tau_1 = 1/(2J_{IS})$. If the I spins are degenerate, as in a methyl moiety, the total signal intensity is obtained by summing the contributions from each I spin. The properties of the coherence transfer function can be used to edit a refocused HSQC experiment according to the I spin multiplicity. A compromise value of $2\tau_1 = 1/(3J_{IS})$ (2.4 ms for $^1J_{CH} = 140$ Hz) yields $\Gamma_n(2\tau_1) = 0.87$, 0.86, and 0.63 for $n = 1$, 2, and 3.

^{1}H decoupling during t_1 is achieved by the use of a composite pulse decoupling scheme (WALTZ-16 or DIPSI-2, for instance). Decoupling must be applied *synchronously*: the decoupling sequence must begin at the same position within the decoupling supercycle for each recorded transient, because evolution of remote ^{1}H spins not scalar coupled to the S spin must be identical during consecutive transients to obtain effective isotope filtration (Section 7.1.2.1).

Evolution under the passive scalar coupling interactions during the delays, $2\tau_1$, generates $2^n - 1$ antiphase product operators in addition to the desired in-phase magnetization. For example, in an I_2S spin system,

---

FIGURE 7.6—*Continued*
cycling is $\phi_1 = x, -x$; $\phi_2 = x, x, y, y$; $\phi_3 = y, y, -x, -x$; $\phi_4 = y, y, x, x$; $\phi_5 = x, x, -y, -y$; $\phi_6 = -y, -y, -x, -x$; and receiver $= x, -x, -x, x$ for the first FID acquired. The second FID is aquired with inversion of ϕ_2. For each t_1 increment, ϕ_1 and the receiver are inverted; no other quadrature detection scheme is required. (c) Four (three) step phase cycling for the TROSY experiment is $\phi_1 = x, y, -x, -y$ (270°, 30°, 150°); $\phi_2 = y$; $\phi_3 = -y$; and receiver $= x, y, -x, -y$ (0°, 240°, 128°) for the first FID acquired. The second FID is acquired with $\phi_1 = x, y, -x, -y$ (270°, 30°, 150°); $\phi_2 = y$; $\phi_3 = -y$; and receiver $= x, -y, -x, y$ (0°, 120°, 240°). Depending on the spectrometer, y and $-y$ phases may need to be interchanged for the TROSY experiment. Processing for PEP-HSQC and TROSY experiments are described in the text.

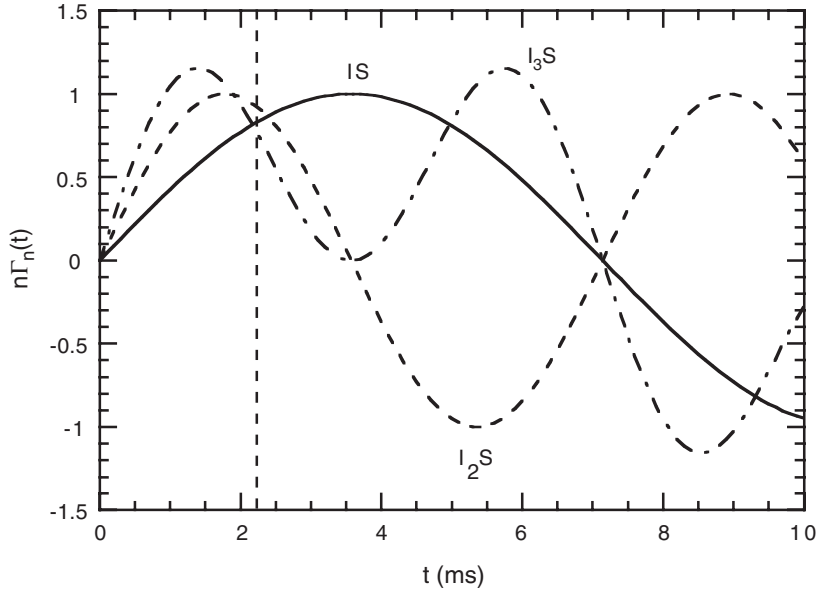

FIGURE 7.7 Plots of the refocused INEPT coherence transfer functions, $n\Gamma_n(t)$, for I_nS spin systems ([7.25]). Results are shown for methine IS (—), methylene I_2S (- - -), and methyl I_3S (- · -) groups with J_{CH} coupling constants of 140 Hz. The dashed vertical line at 2.2 ms indicates the optimal value of t to maximize $\Gamma_n(t)$ simultaneously for methine, methylene, and methyl carbons.

evolution of $-2I_{1z}S_y$ during the $2\tau_1$ delay of the forward refocused INEPT sequence gives

$$\begin{aligned} -2I_{1z}S_y \xrightarrow{\tau_1-\pi\sum I_{kx},\,\pi S_x-\tau_1} & -2I_{1z}S_y\cos(2\pi J_{I_1S}\tau_1)\cos(2\pi J_{I_2S}\tau_1) \\ & +4I_{1z}I_{2z}S_x\cos(2\pi J_{I_1S}\tau_1)\sin(2\pi J_{I_2S}\tau_1) \\ & +2I_{2z}S_y\sin(2\pi J_{I_1S}\tau_1)\sin(2\pi J_{I_2S}\tau_1) \\ & +S_x\sin(2\pi J_{I_1S}\tau_1)\cos(2\pi J_{I_2S}\tau_1). \end{aligned} \quad [7.26]$$

The antiphase terms of the type $I_{1z}S_y$, $I_{2z}S_y$, and $I_{1z}I_{2z}S_x$ present in [7.26] are not efficiently dephased by a highly rf inhomogeneity-compensated composite pulse decoupling scheme (as discussed in Section 3.5, terms such as $4I_{1z}I_{2z}S_x$ are particularly insensitive to rf inhomogeneity). No net rotation of the I_{1z} and I_{2z} operators is expected for an integral number of cycles of an ideal composite pulse decoupling scheme applied to the I

spins (ignoring homonuclear TOCSY transfer); however, the length of the evolution period, t_1, generally will not be equivalent to an integral number of supercycles. If all the pulses of the composite decoupling sequence are applied along the $\pm x$-axis, then the I spin operators experience a net rotation about the x-axis by an angle, α, given by the sum of the flip angles of the pulses in the applied fraction of the final supercycle. Transfer of antiphase S magnetization back to the I spin magnetization by the reverse INEPT sequence depends upon α and therefore is a function of t_1. Subsequent Fourier transformation results in a pattern resembling t_1 noise for the I_2S and I_3S signals. The $90^\circ_y(I)$ pulse immediately following the t_1 period, depicted as an open bar in Fig. 7.6a, suppresses this spurious magnetization transfer by converting the antiphase operators into multiple-quantum operators that are not refocused into observable ^{1}H magnetization by the reverse INEPT sequence.

The F_1 linewidth of a decoupled HSQC spectrum is determined by the relaxation rate of in-phase SQ coherence:

$$\begin{aligned} R_{2S} &= R_2^{IS}(S) + R_2^{\mathrm{CSA}}(S) \\ &= \frac{d_{IS}}{8}\left\{4J(0) + J(\omega_I - \omega_S) + 3J(\omega_S) + 6J(\omega_I) + 6J(\omega_I + \omega_S)\right\} \\ &\quad + \frac{d_{\mathrm{CSA}}}{6}\left\{4J(0) + 3J(\omega_S)\right\}, \end{aligned} \tag{7.27}$$

in which the individual relaxation rate constants are obtained from Tables 5.5 and 5.8 (Chapter 5) and other assumptions are identical to those used in the discussion of the HMQC and HSQC experiments. In the limit of slow overall tumbling, the relaxation rate constant is approximated by

$$R_{2S} = \frac{\tau_c}{5}\left[d_{IS} + \frac{4}{3}d_{\mathrm{CSA}}\right]. \tag{7.28}$$

For backbone amide moieties in proteins, $\overline{R}_{2S} \geq R_{2S}$, because decoupling of the I and S spins during t_1 eliminates broadening due to longitudinal relaxation of I_z. Consequently, narrower linewidths are obtained in decoupled ^{1}H–^{15}N HSQC spectra, compared with conventional HSQC spectra. For example, a linewidth of 2.0 Hz is calculated from [7.28], compared with 3.0 Hz calculated from [7.16], by using $\tau_c = 4.1$ ns. The linewidth differences in conventional and decoupled ^{1}H–^{13}C HSQC spectra are not as pronounced because the C–H dipole–dipole contribution to the transverse relaxation

rate constant is large compared to the H–H dipole–dipole contribution.

To illustrate an analysis (*26*) that will prove very useful in analyzing the sensitivity-enhanced HSQC and TROSY experiments, the following discussion specializes to an *IS* spin system. In this case, $2\tau_1 = 2\tau = 1/(2J_{IS})$ and the $90^\circ_y(I)$ pulse, shown as an open bar in Fig. 7.6a, following the t_1 period can be eliminated. The propagator for the reverse polarization transfer scheme is written as

$$\begin{aligned}
\mathbf{U} &= \exp[-i\mathscr{H}\tau]\exp[-i\pi(I_x+S_x)]\exp[-i\mathscr{H}\tau]\exp\left[-i\left(\tfrac{\pi}{2}\right)(I_x+S_x)\right] \\
&\quad\times \exp[-i\mathscr{H}\tau]\exp[-i\pi(I_x+S_x)]\exp[-i\mathscr{H}\tau] \\
&= \exp\left[-i\left(\tfrac{\pi}{2}\right)2I_zS_z\right]\exp\left[-i\left(\tfrac{\pi}{2}\right)(I_x+S_x)\right]\exp\left[-i\left(\tfrac{\pi}{2}\right)2I_zS_z\right] \\
&= \exp\left[-i\left(\tfrac{\pi}{2}\right)S_x\right]\exp\left[-i\left(\tfrac{\pi}{2}\right)2I_zS_y\right]\exp\left[i\left(\tfrac{\pi}{2}\right)2I_yS_z\right]\exp\left[-i\left(\tfrac{\pi}{2}\right)I_x\right] \\
&= \exp\left[-i\left(\tfrac{\pi}{2}\right)S_x\right]\exp\left[i\left(\tfrac{\pi}{2}\right)S_y\right]\exp\left[-i\left(\tfrac{\pi}{2}\right)S_y\right]\exp\left[-i\left(\tfrac{\pi}{2}\right)2I_zS_y\right] \\
&\quad\times \exp\left[i\left(\tfrac{\pi}{2}\right)2I_yS_z\right]\exp\left[i\left(\tfrac{\pi}{2}\right)I_y\right]\exp\left[-i\left(\tfrac{\pi}{2}\right)I_y\right]\exp\left[-i\left(\tfrac{\pi}{2}\right)I_x\right] \\
&= \exp\left[i\left(\tfrac{\pi}{2}\right)S_y\right]\exp\left[i\left(\tfrac{\pi}{2}\right)S_z\right]\exp\left[-i\pi I^\alpha S_y\right]\exp\left[i\pi I_yS^\alpha\right] \\
&\quad\times \exp\left[i\left(\tfrac{\pi}{2}\right)I_z\right]\exp\left[-i\left(\tfrac{\pi}{2}\right)I_y\right]. \qquad [7.29]
\end{aligned}$$

The two z-rotations in the final result introduce only phase shifts and can be ignored for the present discussion. The $90^\circ_y(I)$ and $90^\circ_{-y}(S)$ rotations do not affect the experiment if the S spin coherence is purely in-phase at the end of the t_1 period and if the detected I spin coherence also is in-phase; the composite pulse decoupling sequences applied during t_1 and t_2 ensure these conditions. Consequently, the part of the propagator responsible for coherence transfer can be written simply as

$$\mathbf{U} = \exp\left[-i\pi I^\alpha S_y\right]\exp\left[i\pi I_yS^\alpha\right]. \qquad [7.30]$$

This propagator corresponds to a selective inversion of coherences (and populations) between the $|\alpha\alpha\rangle$ and $|\beta\alpha\rangle$ eigenstates, followed by a selective inversion between the $|\alpha\alpha\rangle$ and $|\alpha\beta\rangle$ eigenstates. The effects of these rotations are depicted in Fig. 7.8a. The propagator causes the transfers:

$$\begin{aligned}
I^\beta S^- &\xrightarrow{\pi I_yS^\alpha} I^-S^- \xrightarrow{\pi I^\alpha S_y} I^-S^\beta, \\
I^\alpha S^- &\xrightarrow{\pi I_yS^\alpha} I^+S^- \xrightarrow{\pi I^\alpha S_y} I^+S^\alpha. \qquad [7.31]
\end{aligned}$$

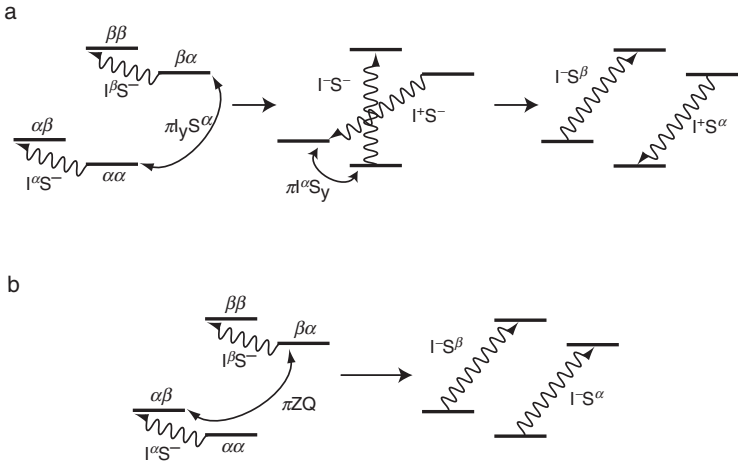

FIGURE 7.8 Energy level representation for reverse polarization transfers for (a) decoupled HSQC and TROSY experiments and (b) a PEP-HSQC experiment. Coherences are represented by wavy lines connecting energy eigenstates. Selective 180° rotations are represented by curved lines and are labeled with the appropriate rotation operator.

The corresponding transfers for the S^+ coherences are found by interchanging the $-$ and $+$ signs:

$$I^\beta S^+ \xrightarrow{\pi I_y S^\alpha} I^+ S^+ \xrightarrow{\pi I^\alpha S_y} I^+ S^\beta,$$
$$I^\alpha S^+ \xrightarrow{\pi I_y S^\alpha} I^- S^+ \xrightarrow{\pi I^\alpha S_y} I^- S^\alpha. \qquad [7.32]$$

Only the operators containing an I^- factor are potentially detectable during t_2; thus, including the effects of chemical shift evolution during t_1 gives

$$I^\beta S^- e^{i\Omega_S t_1} + I^\alpha S^+ e^{-i\Omega_S t_1} \rightarrow I^- S^\beta e^{i\Omega_S t_1} + I^- S^\alpha e^{-i\Omega_S t_1}$$
$$= I^- \cos(\Omega_S t_1) - i2I^- S_z \sin(\Omega_S t_1). \qquad [7.33]$$

The antiphase term is not detectable during t_2, because composite pulse decoupling is utilized. Consequently, in agreement with the preceding product operator analysis, an in-phase, amplitude-modulated signal is recorded. On average, one-half of the signal (the antiphase term) is not detectable in this experiment, which is typical of

amplitude-modulation schemes for frequency discrimination during t_1 of 2D NMR experiments.

7.1.3.2 Sensitivity-Enhanced HSQC In the conventional HSQC experiment (Fig. 7.1b), heteronuclear SQ coherence evolves under the influence of the S spin chemical shift Hamiltonian during the t_1 evolution period to yield *two* orthogonal terms proportional to $2I_zS_y$ and $2I_zS_x$ [7.11]. The second term is not refocused by the reverse INEPT sequence and does not contribute to the final observed magnetization [7.11] (this is essential if amplitude-modulated, pure-phase spectra are to be recorded). Therefore, on average, one-half of the initial I spin polarization does *not* contribute to the detected signal.

Modification of the HSQC experiment to permit refocusing and detection of *both* orthogonal transverse magnetization components forms the basis of a class of heteronuclear correlation experiments, developed originally by Rance and co-workers, that can provide sensitivity improvements by factors of up to $\sqrt{2}$ relative to the conventional experiments (*20*, *27*, *28*). This technology has been denoted "preservation of equivalent pathways" (PEP) (*29*) or "coherence order selective" (COS) (*30*). The principle of the PEP technique for sensitivity improvement will be demonstrated for the PEP-HSQC experiment illustrated in Fig. 7.6b.

The evolution of the density operator for the enhanced PEP-HSQC sequence proceeds exactly as for the conventional HSQC experiment up to the end of the t_1 evolution period in Fig. 7.6b. For an I_nS spin system, the evolution through the remainder of the pulse sequence is given by, for the operators of interest,

$$\begin{aligned}
&2I_zS_y\cos(\Omega_S t_1) - 2I_zS_x\sin(\Omega_S t_1)\\
&\quad\xrightarrow{\frac{\pi}{2}I_x,\frac{\pi}{2}S_x} -2I_yS_z\cos(\Omega_S t_1) + 2I_yS_x\sin(\Omega_S t_1)\\
&\quad\xrightarrow{\tau-\pi I_y,\pi S_x-\tau} -I_x\cos(\Omega_S t_1) + \delta_{1,n}2I_yS_x\sin(\Omega_S t_1)\\
&\quad\xrightarrow{\frac{\pi}{2}I_y,\frac{\pi}{2}S_y} I_z\cos(\Omega_S t_1) - \delta_{1,n}2I_yS_z\sin(\Omega_S t_1)\\
&\quad\xrightarrow{\tau-\pi I_y,\pi S_y-\tau} -I_z\cos(\Omega_S t_1) - \delta_{1,n}I_x\sin(\Omega_S t_1)\\
&\quad\xrightarrow{\frac{\pi}{2}I_{-x}} -I_y\cos(\Omega_S t_1) - \delta_{1,n}I_x\sin(\Omega_S t_1),
\end{aligned} \qquad [7.34]$$

in which $\delta_{1,n} = \cos^{n-1}(2\pi J_{IS}\tau)$ for $2\tau = 1/(2J_{IS})$ results from evolution of the MQ coherence due to passive scalar coupling interactions. The sine-modulated component is stored as multiple-quantum coherence while the cosine-modulated component is refocused to I spin magnetization; subsequently, the cosine-modulated I spin coherence is stored as longitudinal magnetization while the sine-modulated component is refocused to I spin coherence. Refocusing of both orthogonal signal components following t_1 is possible only for $IS\,(n=1)$ spin systems. For example, evolution through the pulse sequence for an I_2S spin system yields

$$
\begin{aligned}
&2I_{1z}S_y\cos(\Omega_S t_1) - 2I_{1z}S_x\sin(\Omega_S t_1)\\
&\xrightarrow{\frac{\pi}{2}I_x,\frac{\pi}{2}S_x} -2I_{1y}S_z\cos(\Omega_S t_1) + 2I_{1y}S_x\sin(\Omega_S t_1)\\
&\xrightarrow{\tau-\pi I_y,\pi S_x-\tau} -I_{1x}\cos(\Omega_S t_1) + 4I_{1y}I_{2z}S_y\sin(\Omega_S t_1)\\
&\xrightarrow{\frac{\pi}{2}I_y,\frac{\pi}{2}S_y} I_{1z}\cos(\Omega_S t_1) + 4I_{1y}I_{2x}S_y\sin(\Omega_S t_1)\\
&\xrightarrow{\tau-\pi I_y,\pi S_y-\tau} -I_{1z}\cos(\Omega_S t_1) - 4I_{1y}I_{2x}S_y\sin(\Omega_S t_1)\\
&\xrightarrow{\frac{\pi}{2}I_{-x}} -I_y\cos(\Omega_S t_1) + 4I_{1z}I_{2x}S_y\sin(\Omega_S t_1). \qquad [7.35]
\end{aligned}
$$

The first term on the last line of [7.35] is observable magnetization; in accordance with [7.34], the second term is unobservable multiple-quantum coherence.

The resultant $-I_y\cos(\Omega_S t_1)$ and $-\delta_{1,n}I_x\sin(\Omega_S t_1)$ terms in [7.34] describe orthogonal in-phase I spin magnetization components that have evolved at the frequency of the S spin during t_1. The final two terms in [7.34] represent superposed observable signals with a 90° phase difference in both dimensions of a 2D spectrum (resulting in phase-twisted lineshapes). In order to separate the two orthogonal terms and obtain purely absorptive lineshapes, a second experiment is performed in which the phase ϕ_2 is inverted. The relevant operator terms are (again beginning with the operators present at time a, given at the

end of [7.11]) as follows:

$$\begin{aligned}
&2I_zS_y\cos(\Omega_S t_1) - 2I_zS_x\sin(\Omega_S t_1)\\
&\quad\xrightarrow{\frac{\pi}{2}I_x,\frac{\pi}{2}S_{-x}} 2I_yS_z\cos(\Omega_S t_1) + 2I_yS_x\sin(\Omega_S t_1)\\
&\quad\xrightarrow{\tau-\pi I_y,\pi S_x-\tau} I_x\cos(\Omega_S t_1) + \delta_{1,n}2I_yS_x\sin(\Omega_S t_1)\\
&\quad\xrightarrow{\frac{\pi}{2}I_y,\frac{\pi}{2}S_y} -I_z\cos(\Omega_S t_1) - \delta_{1,n}2I_yS_z\sin(\Omega_S t_1)\\
&\quad\xrightarrow{\tau-\pi I_y,\pi S_y-\tau} I_z\cos(\Omega_S t_1) - \delta_{1,n}I_x\sin(\Omega_S t_1)\\
&\quad\xrightarrow{\frac{\pi}{2}I_{-x}} I_y\cos(\Omega_S t_1) - \delta_{1,n}I_x\sin(\Omega_S t_1). \qquad [7.36]
\end{aligned}$$

Addition of the two data sets [7.34] and [7.36] gives the single observable term

$$-\delta_{1,n}2I_x\sin(\Omega_S t_1)\varepsilon_{\mathrm{MQ}}, \qquad [7.37]$$

while subtraction of the two data sets yields the single observable term

$$-2I_y\cos(\Omega_S t_1)\varepsilon_I. \qquad [7.38]$$

The data set represented by [7.37] contains only signals from *IS* spin systems, because the extended reverse polarization transfer sequence implements a spin multiplicity filter. The coefficients of 2 in [7.37] and [7.38] arise because two acquisitions have been performed; in practice, each experiment would be recorded with one-half of the total number of transients desired to maintain the same total acquisition time as the conventional experiment. The factors $\varepsilon_{\mathrm{MQ}}$ and ε_I have been introduced in [7.37] and [7.38] to account for the different relaxation rates of the sine- and cosine-modulated components. These factors are given by

$$\varepsilon_{\mathrm{MQ}} = \exp(-2R_{2\mathrm{MQ}}\tau) \qquad [7.39]$$

and

$$\varepsilon_I = \exp(-2R_{1I}\tau), \qquad [7.40]$$

in which $R_{2\mathrm{MQ}}$ is transverse relaxation rate constant for heteronuclear multiple-quantum coherence, and R_{1I} is the longitudinal relaxation rate

constant of the I spin (*28*):

$$\begin{aligned} R_{1I} &= R_1^{IS}(I) + R_1^{IK}(I) + R_1^{\mathrm{CSA}}(I) \\ &= \frac{d_{IS}}{4}\{J(\omega_I - \omega_S) + 3J(\omega_I) + 6J(\omega_I + \omega_S)\} + d_{\mathrm{CSA}(I)}J(\omega_I) \\ &\quad + \frac{1}{4}\sum_k d_{Ik}\{J(0) + 3J(\omega_I) + 6J(2\omega_I)\}. \end{aligned} \quad [7.41]$$

In the limit of slow overall tumbling, the relaxation rate constant is approximated by

$$R_{1I} = \frac{\tau_c}{10}\sum_k d_{Ik}. \quad [7.42]$$

The data sets described by [7.37] and [7.38] differ in phase by 90° in both dimensions. The phase difference in the acquisition dimension can be corrected by applying a 90° zero-order phase correction to the data set represented by [7.38] after processing in F_2. Alternatively, and now more commonly, the phase correction is performed in the time domain by swapping the real and imaginary components of the FID and negating the new imaginary component. The procedure to first add and subtract the data sets followed by time-domain phase correction of one of the resulting data sets is called "Rance–Kay" processing in most NMR data processing programs.

In the original implementation of the PEP-HSQC experiment, either real or hypercomplex acquisition in t_1, by appropriate phase cycling of ϕ_1, is used to obtain two phase-sensitive data sets, corresponding to [7.37] and [7.38]. The data sets are transformed and phased to obtain two 2D heteronuclear correlation spectra with purely absorptive peak shapes in both dimensions. The final sensitivity-enhanced spectrum is obtained by adding the two pure-absorption spectra. The random noise in the two spectra described by [7.37] and [7.38] is uncorrelated (*31*) and increases only by $\sqrt{2}$ in the sensitivity-enhanced spectrum. The achievable sensitivity improvement over a conventional HSQC experiment recorded in the same total time is

$$\varepsilon = \sqrt{2}(\varepsilon_I + \delta_{1,n}\varepsilon_{\mathrm{MQ}})/2, \quad [7.43]$$

which has a maximum value of $\sqrt{2}$ for an IS spin system. The F_1 lineshape of the sensitivity-enhanced HSQC experiment is identical to that of the conventional HSQC experiment because identical spin operators are present during t_1.

In most current implementations of the PEP approach, the two data sets obtained from Rance–Kay processing are treated as a hypercomplex pair for subsequent Fourier transformation in t_1. No additional data acquisitions are utilized for quadrature detection in the indirect dimension. However, processing the hypercomplex data defined by [7.37] and [7.38] yields quadrature artifacts in the F_1 dimension of the spectrum due to the amplitude differences, ε_I and $\delta_{I,n}\varepsilon_{\mathrm{MQ}}$, between the two data sets. The PEP method can be modified, by appropriate phase cycling (see the caption to Fig. 7.6) (*32*), to equalize the relaxation differences between the coherence transfer pathways used to refocus the orthogonal magnetization components. The sine- and cosine-modulated terms that result from addition and subtraction of the data sets acquired using the modified phase cycle are given by

$$-I_x \sin(\Omega_S t_1)\big(\varepsilon_I + \delta_{1,n}\varepsilon_{\mathrm{MQ}}\big), \qquad [7.44]$$

$$-I_y \cos(\Omega_S t_1)\big(\varepsilon_I + \delta_{1,n}\varepsilon_{\mathrm{MQ}}\big), \qquad [7.45]$$

respectively. The two components have identical magnitudes and are treated as a hypercomplex quadrature pair in the t_1 dimension (following a 90° zero-order phase correction in the acquisition dimension of the data described by [7.45]).

Following the same formal discussion presented for the decoupled HSQC experiment, the evolution of an *IS* spin system in the sensitivity-enhanced reverse polarization transfer is considered again. The propagator for the reverse polarization transfer scheme can be written as

$$\begin{aligned}
\mathbf{U} &= \exp\big[-i\left(\tfrac{\pi}{2}\right)I_x\big]\exp[-i\mathscr{H}\tau]\exp\big[-i\pi(I_y+S_y)\big]\exp[-i\mathscr{H}\tau] \\
&\quad\times\exp\big[-i\left(\tfrac{\pi}{2}\right)(I_y+S_y)\big]\exp[-i\mathscr{H}\tau]\exp\big[-i\pi(I_y+S_y)\big]\exp[-i\mathscr{H}\tau] \\
&\quad\times\exp\big[-i\left(\tfrac{\pi}{2}\right)(I_x+S_x)\big] \\
&= \exp\big[i\left(\tfrac{\pi}{2}\right)I_x\big]\exp\big[-i\left(\tfrac{\pi}{2}\right)2I_zS_z\big]\exp\big[-i\left(\tfrac{\pi}{2}\right)(I_y+S_y)\big] \\
&\quad\times\exp\big[-i\left(\tfrac{\pi}{2}\right)2I_zS_z\big]\exp\big[-i\left(\tfrac{\pi}{2}\right)(I_x+S_x)\big] \\
&= \exp\big[i\left(\tfrac{\pi}{2}\right)I_x\big]\exp\big[-i\left(\tfrac{\pi}{2}\right)(I_y+S_y)\big]\exp\big[-i\left(\tfrac{\pi}{2}\right)(I_x+S_x)\big] \\
&\quad\times\exp\big[-i\left(\tfrac{\pi}{2}\right)2I_xS_x\big]\exp\big[-i\left(\tfrac{\pi}{2}\right)2I_yS_y\big] \\
&= \exp\big[i\left(\tfrac{\pi}{2}\right)S_y\big]\exp\big[i\left(\tfrac{\pi}{2}\right)I_z\big]\exp\big[i\left(\tfrac{\pi}{2}\right)S_z\big] \\
&\quad\times\exp\big[-i\left(\tfrac{\pi}{2}\right)2I_xS_x\big]\exp\big[-i\left(\tfrac{\pi}{2}\right)2I_yS_y\big] \\
&= \exp\big[i\left(\tfrac{\pi}{2}\right)S_y\big]\exp\big[i\left(\tfrac{\pi}{2}\right)I_z\big]\exp\big[i\left(\tfrac{\pi}{2}\right)S_z\big]\exp\big[-i\pi\mathrm{ZQ}_y\big]. \qquad [7.46]
\end{aligned}$$

Again, the two z-rotations introduce only phase shifts and can be ignored for the present discussion. In contrast to [7.29], in-phase S spin coherence is not required following t_1. The detected I spin coherence is in-phase because composite pulse decoupling is applied during t_2. Thus, the 90° S_y rotation does not affect evolution of the detected signal. Consequently, the propagator can be written simply as

$$\mathbf{U} = \exp\left[-i\pi \mathrm{ZQ}_y\right]. \qquad [7.47]$$

This propagator corresponds to a selective inversion of coherences (and populations) between the $|\alpha\beta\rangle$ and $|\beta\alpha\rangle$ eigenstates. The effects of these rotations are depicted in Fig. 7.8b. The propagator (ignoring any phase shifts) causes the transfers:

$$\begin{aligned} I^\beta S^- &\xrightarrow{\pi \mathrm{ZQ}_y} iI^- S^\beta, \\ I^\alpha S^- &\xrightarrow{\pi \mathrm{ZQ}_y} -iI^- S^\alpha, \\ I^\beta S^+ &\xrightarrow{\pi \mathrm{ZQ}_y} -iI^+ S^\beta, \\ I^\alpha S^+ &\xrightarrow{\pi \mathrm{ZQ}_y} iI^+ S^\alpha. \end{aligned} \qquad [7.48]$$

The phase factors i and $-i$ are not obtainable from the pictorial description of the ZQ_y rotation and must instead be determined by direct calculation of the product operators. The sign inversion for two of the transfers in [7.48] means that the pulse sequence transfers antiphase S spin coherence to in-phase I spin coherence. Only the operators containing an I^- factor are potentially detectable during t_2; thus, including the effects of chemical shift evolution during t_1 gives

$$I^\alpha S^- e^{i\Omega_S t_1} - I^\beta S^- e^{i\Omega_S t_1} \rightarrow I^- S^\beta e^{i\Omega_S t_1} + I^- S^\alpha e^{i\Omega_S t_1} = I^- e^{i\Omega_S t_1}. \qquad [7.49]$$

In agreement with this product operator analysis, an in-phase, phase-modulated signal is recorded. On average, the detected signal has twice the amplitude, compared to the signal recorded in the amplitude-modulated decoupled HSQC; however, as previously discussed, deconvoluting the phase-modulated signals results in an increase in the noise level by $\sqrt{2}$ and results in a net sensitivity gain of $2/\sqrt{2} = \sqrt{2}$.

The requirement for decoupling during acquisition to ensure that the detected signal is in-phase can be eliminated by inserting a $90^\circ_{-y}(S)$ pulse immediately prior to acquisition. This additional pulse cancels the effect of the 90° S_y rotation in the last line of [7.46]. In fact, this modified

sequence element has been utilized in TROSY experiments by Kay and co-workers (*33*).

7.1.3.3 TROSY Experiment The basic pulse sequence for the original ^1H–^{15}N TROSY (transverse relaxation optimized spectroscopy) experiment is shown in Fig. 7.6c. Rather than performing a detailed product operator analysis of this sequence, the insights obtained in the analyses of the decoupled HSQC and PEP-HSQC experiments will be utilized. The initial part of the TROSY experiment is identical to the HSQC or sensitivity-enhanced HSQC experiments, except that decoupling is not applied during the t_1 period. Consequently, evolution during t_1 is described by

$$\begin{aligned}-2I_zS_y \xrightarrow{t_1} &-2I_zS_y\cos(\Omega_S t_1)\cos(\pi J_{IS}t_1) + 2I_zS_x\sin(\Omega_S t_1)\cos(\pi J_{IS}t_1)\\ &+ S_x\cos(\Omega_S t_1)\sin(\pi J_{IS}t_1) + S_y\sin(\Omega_S t_1)\sin(\pi J_{IS}t_1).\end{aligned} \quad [7.50]$$

The propagator for the reverse polarization transfer scheme can be written as

$$\begin{aligned}\mathbf{U} &= \exp\left[-i\left(\tfrac{\pi}{2}\right)S_y\right]\exp[-i\mathscr{H}\tau]\exp[-i\pi(I_x+S_x)]\exp[-i\mathscr{H}\tau]\\ &\quad\times\exp\left[-i\left(\tfrac{\pi}{2}\right)(I_x+S_x)\right]\exp[-i1\mathscr{H}\tau]\exp[-i\pi(I_x+S_x)]\exp[-i\mathscr{H}\tau]\\ &\quad\times\exp\left[i\left(\tfrac{\pi}{2}\right)I_y\right]\\ &= \exp\left[-i\left(\tfrac{\pi}{2}\right)S_y\right]\exp\left[-i\left(\tfrac{\pi}{2}\right)2I_zS_z\right]\exp\left[-i\left(\tfrac{\pi}{2}\right)(I_x+S_x)\right]\\ &\quad\times\exp\left[-i\left(\tfrac{\pi}{2}\right)2I_zS_z\right]\exp\left[i\left(\tfrac{\pi}{2}\right)I_y\right]\\ &= \exp\left[-i\left(\tfrac{\pi}{2}\right)S_y\right]\exp\left[-i\left(\tfrac{\pi}{2}\right)S_x\right]\exp\left[-i\left(\tfrac{\pi}{2}\right)2I_zS_y\right]\\ &\quad\times\exp\left[i\left(\tfrac{\pi}{2}\right)2I_yS_z\right]\exp\left[-i\left(\tfrac{\pi}{2}\right)I_x\right]\exp\left[i\left(\tfrac{\pi}{2}\right)I_y\right]\\ &= \exp\left[i\left(\tfrac{\pi}{2}\right)S_z\right]\exp\left[-i\left(\tfrac{\pi}{2}\right)S_y\right]\exp\left[-i\left(\tfrac{\pi}{2}\right)2I_zS_y\right]\\ &\quad\times\exp\left[i\left(\tfrac{\pi}{2}\right)2I_yS_z\right]\exp\left[i\left(\tfrac{\pi}{2}\right)I_y\right]\exp\left[i\left(\tfrac{\pi}{2}\right)I_z\right]\\ &= \exp\left[i\left(\tfrac{\pi}{2}\right)S_z\right]\exp\left[-i\pi I^{\alpha}S_y\right]\exp\left[i\pi I_yS^{\alpha}\right]\exp\left[i\left(\tfrac{\pi}{2}\right)I_z\right].\end{aligned} \quad [7.51]$$

The two z-rotations introduce only phase shifts and can be ignored for the present discussion. In contrast to the decoupled HSQC or sensitivity-enhanced HSQC experiments, no unnecessary 90° rotations are present in the propagator; therefore, decoupling is not required during t_1 or t_2. Consequently, the propagator can be written simply as

$$\mathbf{U} = \exp\left[-i\pi I^{\alpha}S_y\right]\exp\left[i\pi I_yS^{\alpha}\right]. \quad [7.52]$$

This propagator is exactly that considered previously for the decoupled HSQC experiment and causes the transfers depicted in Fig. 7.8a and [7.31]–[7.32]. Only the operators containing an I^- factor are potentially detectable during t_2; thus, including the effects of chemical shift evolution during t_1 gives

$$I^\beta S^- e^{i(\Omega_S+\pi J_{IS})t_1} + I^\alpha S^+ e^{-i(\Omega_S-\pi J_{IS})t_1} \rightarrow I^- S^\beta e^{i(\Omega_S+\pi J_{IS})t_1} + I^- S^\alpha e^{-i(\Omega_S-\pi J_{IS})t_1}. \quad [7.53]$$

The transfer from $I^\alpha S^+$ to $I^- S^\alpha$ is suppressed either by phase cycling or by gradient coherence selection (Section 7.1.4.2). Phase cycling of ϕ_1 selects for the coherence order change of the S spin from $p_S = 0$ to -1, while suppressing the coherence order change from $p_S = 0$ to $+1$. In principle, this selection could be obtained using a three-step phase cycle; however, a four-step cycle is normally used for the convenience provided by 90° phase shifts. Both phase cycles are given in the caption to Fig. 7.6c. The net transfer, including the phase cycle, is

$$I^\beta S^- e^{i(\Omega_S+\pi J_{IS})t_1} \rightarrow I^- S^\beta e^{i(\Omega_S+\pi J_{IS})t_1}. \quad [7.54]$$

The full intensity of the $I^- S^\beta$ operator is recorded during acquisition because decoupling is not employed. However, on average, one-half of the signal is recorded in this experiment compared to the sensitivity-enhanced HSQC experiment, resulting in a twofold decrease in overall sensitivity, in the absence of relaxation effects. The resonance correlation peak has frequency coordinates $(\Omega_S + \pi J_{IS}, \Omega_I + \pi J_{IS})$, compared with HSQC spectra, in which the resonance coordinates are (Ω_S, Ω_I).

The final signal in [7.53] is phase modulated in t_1 and is deconvoluted by procedures similar to that used for the PEP-HSQC experiment. To achieve the desired transfer for the second data set required for Rance–Kay processing, two changes are made to the phase cycle. First, the the phase cycling of ϕ_1 is reversed to select for the coherence order change of the S spin from $p_S = 0$ to $+1$, while suppressing the coherence order change from $p_S = 0$ to -1. Second, the phases ϕ_2 and ϕ_3 are shifted by 180°; this is tantamount to inserting a 180°_x pulse on the I spins immediately after t_1 and a 180°_y pulse on the S spins immediately prior to acquisition. The propagator in [7.52] is modified to

$$\mathbf{U} = \exp\left[-i\pi S_y\right] \exp\left[-i\pi I^\alpha S_y\right] \exp\left[i\pi I_y S^\alpha\right] \exp[-i\pi I_x]. \quad [7.55]$$

This propagator results in the desired coherence transfer pathway:

$$I^\beta S^+ \xrightarrow{\pi I_x} I^\alpha S^+ \xrightarrow{\pi I_y S^\beta} I^- S^+ \xrightarrow{\pi I^\alpha S_y} I^- S^\alpha \xrightarrow{\pi S_y} I^- S^\beta, \quad [7.56]$$

with the final result, including chemical shift evolution,

$$I^{\beta}S^{+}e^{-i(\Omega_S+\pi J_{IS})t_1} \rightarrow I^{-}S^{\beta}e^{-i(\Omega_S+\pi J_{IS})t_1}. \qquad [7.57]$$

Equations [7.54] and [7.57] represent the pair of spectra for Rance–Kay processing.

The TROSY experiment is unusual in that the S spin natural abundance magnetization contributes constructively to the signal (in other heteronuclear experiments, the natural spin polarization of the S spin usually is destroyed, prior to the first ^{1}H 90° pulse, by a 90° pulse on the S spin followed by a gradient pulse). Prior to the t_1 period, evolution of the S spin magnetization is described by

$$S_z \rightarrow S_y = -\tfrac{i}{2}(S^{+} - S^{-})(I^{\alpha} + I^{\beta}). \qquad [7.58]$$

Referring to [7.50], the component of the density operator arising from the ^{1}H spin polarization, prior to the t_1 period, is described by

$$-2I_zS_y = \tfrac{i}{2}(S^{+} - S^{-})(I^{\alpha} - I^{\beta}). \qquad [7.59]$$

Comparison of [7.58] and [7.59] shows that the desired operator $S^{-}I^{\beta}$ adds constructively from the initial ^{1}H and ^{15}N polarizations.

As in the PEP-HSQC experiment, differential relaxation of operators present through the reverse polarization transfer affect the final detected resonance in the TROSY spectrum. Examining the effects of relaxation is more straightforward in the Cartesian basis. The initial operator of interest after the t_1 period is $S^{-}I^{\beta} = (E/2 - I_z)(S_x - iS_y)$. Evolution through the reverse polarization transfer, including relaxation, is given by

$$\begin{aligned}
(E/2-I_z)(S_x-iS_y) &\xrightarrow{\frac{\pi}{2}I_{-y}} (E/2+I_x)(S_x-iS_y)\\
&\xrightarrow{2\tau} I_zS_y\exp[-\overline{R}_{2S}2\tau]+I_xS_x\exp[-R_{2MQ}2\tau]\\
&\quad + iI_zS_x\exp[-\overline{R}_{2S}2\tau]-iI_xS_y\exp[-R_{2MQ}2\tau]\\
&\xrightarrow{\frac{\pi}{2}I_x,\frac{\pi}{2}S_x} -I_yS_x\exp[-\overline{R}_{2S}2\tau]+I_xS_x\exp[-R_{2MQ}2\tau]\\
&\quad -iI_yS_x\exp[-\overline{R}_{2S}2\tau]-iI_xS_z\exp[-R_{2MQ}2\tau]\\
&\xrightarrow{2\tau} \tfrac{1}{2}I_x\exp[-(\overline{R}_{2S}+\overline{R}_{2I})2\tau]+I_xS_x\exp[-2R_{2MQ}2\tau]\\
&\quad -iI_yS_x\exp[-(\overline{R}_{2S}+R_{2MQ})2\tau]-\tfrac{i}{2}I_y\exp[-(R_{2MQ}+\overline{R}_{2I})2\tau]\\
&\xrightarrow{\frac{\pi}{2}S_y} \tfrac{1}{2}I_x\exp[-(\overline{R}_{2S}+\overline{R}_{2I})2\tau]-I_xS_z\exp[-2R_{2MQ}2\tau]\\
&\quad + iI_yS_z\exp[-(\overline{R}_{2S}+R_{2MQ})2\tau]-\tfrac{i}{2}I_y\exp[-(R_{2MQ}+\overline{R}_{2I})2\tau], \qquad [7.60]
\end{aligned}$$

in which

$$\begin{aligned}\overline{R}_{2I} &= \tfrac{1}{2}\big[R_2^{IS}(2I^-S_z) + R_2^{IS}(I) + R_1^{\mathrm{CSA}}(S)\big] + R_2^{IK}(I) + R_2^{\mathrm{CSA}}(I) \\ &= \frac{d_{IS}}{8}\big\{4J(0) + J(\omega_I - \omega_S) + 3J(\omega_S) + 3J(\omega_I) + 6J(\omega_I + \omega_S)\big\} \\ &\quad + \frac{d_{\mathrm{CSA}(S)}}{2}J(\omega_S) + \frac{d_{\mathrm{CSA}(I)}}{6}\big\{4J(0) + 3J(\omega_I)\big\} \\ &\quad + \frac{1}{8}\sum_k d_{Ik}\big\{5J(0) + 9J(\omega_I) + 6J(2\omega_I)\big\} \end{aligned} \qquad [7.61]$$

is the relaxation rate constant of the I spin transverse magnetization. In the limit of slow tumbling, this rate constant is approximated by

$$\overline{R}_{2I} = \frac{\tau_c}{5}\left\{d_{IS} + \frac{4}{3}d_{\mathrm{CSA}(I)} + \frac{5}{4}\sum_k d_{Ik}\right\} \qquad [7.62]$$

The operators on the final line in [7.60] can be expressed in the spherical basis as

$$\begin{aligned} I^-S^\beta\{&\exp[-(\overline{R}_{2S} + \overline{R}_{2I})2\tau] + \exp[-2R_{2\mathrm{MQ}}2\tau] + \exp[-(\overline{R}_{2S} + R_{2\mathrm{MQ}})2\tau] \\ &+ \exp[-(R_{2\mathrm{MQ}} + \overline{R}_{2I})2\tau]\}/4 + I^-S^\alpha\{\exp[-(\overline{R}_{2S} + \overline{R}_{2I})2\tau] \\ &- \exp[-2R_{2\mathrm{MQ}}2\tau] - \exp[-(\overline{R}_{2S} + R_{2\mathrm{MQ}})2\tau] \\ &+ \exp[-(R_{2\mathrm{MQ}} + \overline{R}_{2I})2\tau]\}/4 \\ \approx\ & I^-S^\beta\{1 - (\overline{R}_{2S} + \overline{R}_{2I} + 2R_{2\mathrm{MQ}})\tau\} + I^-S^\alpha\{(R_{2\mathrm{MQ}} - \overline{R}_{2I})\tau\}. \end{aligned} \qquad [7.63]$$

The last line of this equation is obtained by expanding the exponentials to first order, assuming that $2\tau R_2\xi \ll 1$, in which $\xi = \{I, S, MQ\}$. This result indicates that when the relaxation rate constants are both large and different, then the desired "TROSY" resonance with frequency coordinates $(\Omega_S + \pi J_{IS}, \Omega_I + \pi J_{IS})$, associated with I^-S^β coherence, has reduced intensity, while an undesired resonance associated with I^-S^α coherence appears in the spectrum with frequency coordinates $(\Omega_S + \pi J_{IS}, \Omega_I - \pi J_{IS})$. A similar analysis shows that the spin operator S^-I^α present after the t_1 period yields an observable operator,

$$I^-S^\alpha \rightarrow I^-S^\beta\{(\overline{R}_{2S} - R_{2\mathrm{MQ}})\tau\}, \qquad [7.64]$$

due to differential relaxation. This transfer yields a correlation with frequency coordinates $(\Omega_S - \pi J_{IS}, \Omega_I + \pi J_{IS})$. Even in the presence of differential relaxation, the resonance correlation at $(\Omega_S - \pi J_{IS}, \Omega_I - \pi J_{IS})$ is efficiently suppressed by the TROSY sequence. Techniques for

additional suppression of these artifactual peaks have been described (*34*, *35*).

7.1.3.4 Comparison of Decoupled HSQC, PEP-HSQC, and TROSY Experiments Selected regions of the ^{1}H–^{15}N decoupled HSQC, sensitivity-enhanced PEP-HSQC, and TROSY spectra of ubiquitin are presented in Fig. 7.9. As predicted by [7.25], the NH_2 resonances are suppressed in the decoupled HSQC pulse sequence; a similar product operator analysis predicts that the NH_2 resonances are suppressed in the TROSY spectrum as well. The relative sensitivity of the three experiments is illustrated by the 1D traces through a selected ^{1}H–^{15}N correlation peak.

7.1.3.5 Relaxation Interference and TROSY Spectra of Larger Proteins TROSY is both a general principle of pulse sequence design and a particular experiment. The concept behind TROSY is

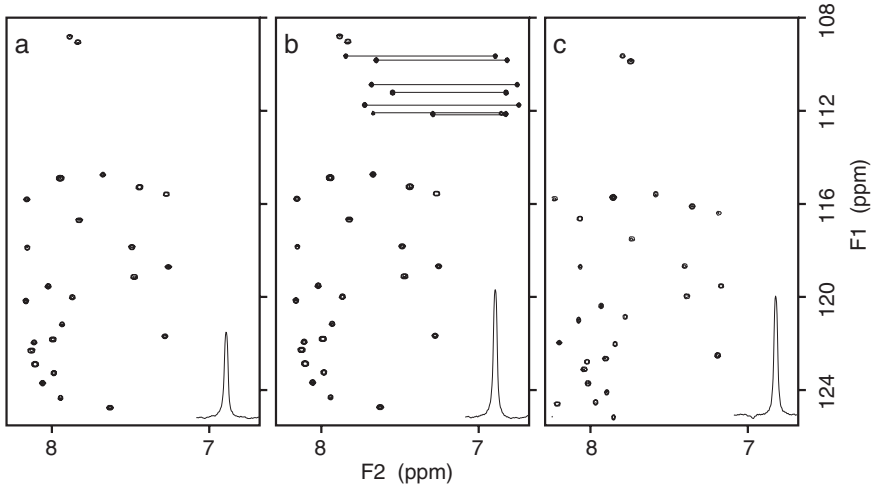

FIGURE 7.9 Comparison of selected regions from ^{1}H–^{15}N heteronuclear correlation spectra of ^{15}N-labeled ubiquitin, recorded using the schemes of Fig. 7.6a–c, respectively. Each spectrum was recorded in approximately the same total time with identical t_1 and t_2 acquisition times and processed similarly. NH_2 correlations are indicated by lines connecting the two nonequivalent proton resonances. A slice parallel to the F_2 axis through a selected resonance is shown in the lower right corner of each spectrum to illustrate the relative sensitivity of the experiments.

that certain coherences (usually specific multiplet components, but also multiple-quantum operators) have smaller transverse relaxation rate constants than do single-quantum operators representing total spin magnetization. Of course, recording only the signal from a subset of multiplet components, rather than the total magnetization, incurs an initial loss of sensitivity. For example, the TROSY experiment for *IS* spin systems, such as $^1H^N$–^{15}N, has one-half the sensitivity of the PEP-HSQC experiment if relaxation is neglected. However, if the selected spin operators have small enough transverse relaxation rate constants, and if $t_{1\max}$ or free-precession delays are long enough, then improved resolution and sensitivity can be obtained, particularly for large macromolecules in which relaxation losses are particularly severe. The application of line narrowing through relaxation interference was anticipated by Griffey and Redfield (*36*). The first TROSY experiment was described by Wüthrich and co-workers and utilized relaxation interference between CSA and dipole–dipole (DD) interactions within the amide $^1H^N$–^{15}N *IS* spin system. Since the original description, TROSY concepts have been developed for other *IS* spin systems (*37*), as well as for I_2S (CH_2) (*38*) and I_3S (CH_3) spin systems (*39*).

Relaxation interference between DD/CSA interactions is discussed in Section 5.4.5. The effect of differential relaxation on the ^1H–^{15}N multiplet components in large proteins at high static magnetic field, where the DD/CSA relaxation interference is most prominent, is shown in Fig. 7.10 for the protein calbindin D_{28k}, with a molecular mass of 30 kDa. The figure shows expansions from a series of heterocorrelation spectra recorded at 800 MHz; in each spectrum, only resonances arising from a single resolved ^1H–^{15}N amide moiety are shown. In Fig. 7.10a, an HSQC spectrum in which decoupling was omitted in both t_1 and t_2 evolution periods is shown. The effects of relaxation interference are manifest in the different intensities of the four multiplet components. The relaxation rate constants for the spin operators contributing to the observed cross-peaks are

$$\begin{aligned} R_2(I^-S^\alpha) &= \overline{R}_{2I} + \eta_{I,IS}, \\ R_2(I^-S^\beta) &= \overline{R}_{2I} - \eta_{I,IS}, \\ R_2(I^\alpha S^-) &= \overline{R}_{2S} + \eta_{S,IS}, \\ R_2(I^\beta S^-) &= \overline{R}_{2S} - \eta_{S,IS}, \end{aligned} \qquad [7.65]$$

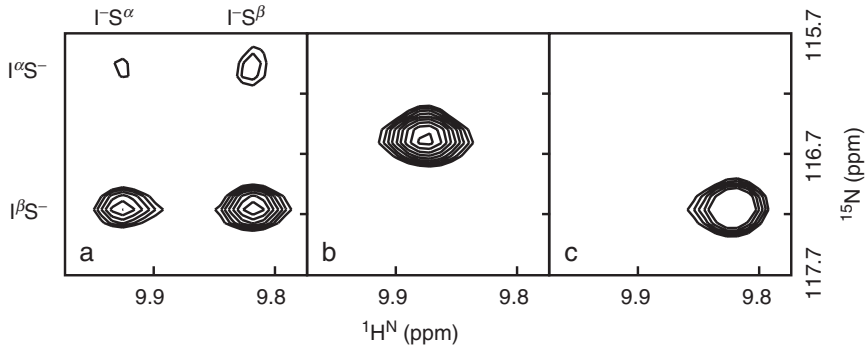

FIGURE 7.10 ^{1}H–^{15}N multiplet structure. A resonance is shown for calbindin D_{28k} recorded at 800 MHz. (a) HSQC spectrum recorded without decoupling in t_1 or t_2 periods to illustrate the differential linewidths of multiplet components. (b) Conventional HSQC spectrum, in which the multiplet components are collapsed to a singlet. (c) TROSY spectrum that selects the narrowest multiplet component.

in which $\eta_{I,IS}$ ($\eta_{S,IS}$) is the transverse CSA/DD relaxation interference rate constant for cross-correlation between the CSA interaction of the I (S) spin and the DD interaction of the IS spin pair [5.145], and $\overline{R}_{2I}$ ($\overline{R}_{2S}$) is the averaged relaxation rate constant for single-quantum coherence of the I (S) spin during free precession. In Fig. 7.10b, a conventional HSQC spectrum is shown. Decoupling in the t_1 and t_2 dimensions suppresses relaxation interference and essentially averages the relaxation rate constants, and consequent intensities, of the multiplet components. In Fig. 7.10c, the TROSY experiment selects the most intense multiplet component, resulting from destructive interference between DD and CSA relaxation during both t_1 and t_2 evolution periods.

An important aspect of TROSY experiments arises from remote ^{1}H–^{1}H dipole–dipole interactions. The narrow TROSY component arises from evolution of $I^{\beta}S^{-}$ during t_1 and $I^{-}S^{\beta}$ during t_2. Both of these operators contain ^{1}H spin components and consequently both $\overline{R}_{2I}$ and $\overline{R}_{2S}$ contain contributions from remote ^{1}H–^{1}H dipole–dipole relaxation. These additional relaxation pathways reduce the line narrowing achievable in the TROSY experiment. As a result, optimal use of TROSY techniques commonly necessitates replacement of remote ^{1}H spins with ^{2}H in order to reduce these dipole–dipole interactions.

7.1.4 Water Suppression and Gradient Enhancement of Heteronuclear Correlation Spectra

The previous sections have outlined the basic coherence transfer and relaxation effects that are important for the most widely utilized two-dimensional heteronuclear correlation experiments. Practical implementations of these techniques, either as two-dimensional methods or for incorporation into higher dimensionality NMR experiments, frequently utilize a number of enhancements to obtain high-quality water suppression and reduced artifacts, particularly by incorporating field gradient pulses. Aspects of water-suppression techniques and gradient coherence selection in heteronuclear correlation spectroscopy are described in the following sections.

7.1.4.1 Solvent Suppression ^{1}H–^{13}C heteronuclear correlation spectra of ^{13}C-labeled proteins normally are recorded using proteins in D_2O solution, and presaturation of the residual HDO solvent resonance usually is satisfactory. The ^{1}H–^{13}C heteronuclear spectra of $^{13}C/^{15}N$-labeled proteins in H_2O solution can be recorded by using presaturation of the solvent resonance; however, pulsed field gradient techniques for solvent suppression are preferable to avoid obscuring $^{1}H^{\alpha}$–$^{13}C^{\alpha}$ correlations. For ^{1}H–^{15}N heteronuclear spectra of ^{15}N- and $^{13}C/^{15}N$-labeled proteins acquired in H_2O solution, presaturation of the solvent signal usually is avoided to minimize solvent saturation transfer to the amide ^{1}H spins that reduces signal intensities (*40–42*).

Although jump–return versions of the HMQC experiment have been designed, the most effective solvent-suppression schemes for ^{1}H–^{15}N heteronuclear NMR spectroscopy incorporate spin lock purge pulses (*43*) or field gradient pulses (*40*, *42*, *44*) (Section 3.7.3) into the HSQC experiment. Use of these techniques is facilitated because evolution under the ^{1}H–^{15}N scalar coupling Hamiltonian provides an efficient mechanism for independently manipulating the protein and solvent resonances. For example, evolution through the initial INEPT sequence of the HSQC experiment yields

$$\begin{aligned} -I_y &\xrightarrow{\tau-\pi I_y,\,\pi S_x-\tau} 2I_xS_z, \\ -W_y &\xrightarrow{\tau-\pi W_y-\tau} -W_y, \end{aligned} \qquad [7.66]$$

in which $I = {}^{1}H^{N}$ and $S = {}^{15}N$ are the solute spins, and W designates the solvent ^{1}H spins. The resulting solute and solvent ^{1}H operators are orthogonal. In these pulse sequence elements, the phase of the 180° pulse

on the ^{1}H spins has been changed to $+y$ compared with the sequences of Fig. 7.1. At this point, a purge pulse applied with x-phase spin-locks the $2I_xS_z$ coherence and dephases the W_y coherence. Alternatively, a 90°_y pulse applied to the ^{1}H spins converts the $2I_xS_z$ coherence into longitudinal two-spin order, $-2I_zS_z$, without affecting the W_y operator. A subsequent z-axis field gradient or homospoil pulse selectively dephases the solvent magnetization without affecting the solute coherence. Finally, if a selective 90°_y pulse is applied to the solvent spins prior to the first nonselective 90°_x pulse, then evolution through the initial INEPT sequence gives

$$\begin{aligned} I_z &\xrightarrow{\frac{\pi}{2}I_x-\tau-\pi I_y,\,\pi S_x-\tau-\frac{\pi}{2}I_y} -2I_zS_z, \\ W_z &\xrightarrow{\frac{\pi}{2}W_y-\tau-\pi W_y-\tau-\frac{\pi}{2}W_y} W_z. \end{aligned} \qquad [7.67]$$

This pulse sequence fragment is the basis for "water flip-back" techniques, because the solvent magnetization is returned to the z-axis by the INEPT sequence; similar concepts are used during other portions of pulse sequences to ensure that the solvent signal remains aligned along the z-axis during the acquisition period.

Examples of the "fast" HSQC pulse sequence and a water flip-back TROSY pulse sequence are shown in Fig. 7.11. In both of these sequences, the water magnetization is transverse during the t_1 period. The gradients labeled g2 dephase and rephase the water magnetization at the beginning and end of the t_1 period to avoid deleterious effects of radiation damping. The water magnetization is returned to the $+z$-axis by the final 90° pulse applied to the I spins. The final 180° pulse applied to the I spins is part of a WATERGATE element, along with the flanking field gradient pulses.

Gradient pulses during periods of free precession, such as the gradient pulses labeled g1 or g3 in sequences a and b in Fig. 7.11 or the gradients g2 in Fig. 7.11b are applied in such manner as to keep transverse water magnetization dephased as much as possible to minimize deleterious radiation damping. Thus, in the sequences shown, the first gradient of the g1 pair is applied immediately after the preceding 90° pulses and the second gradient of the pair is applied immediately before the subsequent 90° pulse.

7.1.4.2 Gradient-Enhanced HSQC and TROSY NMR Spectroscopy Although pulsed field gradients (PFGs) can be used to generate frequency-discriminated pure-absorption spectra by gradient coherence

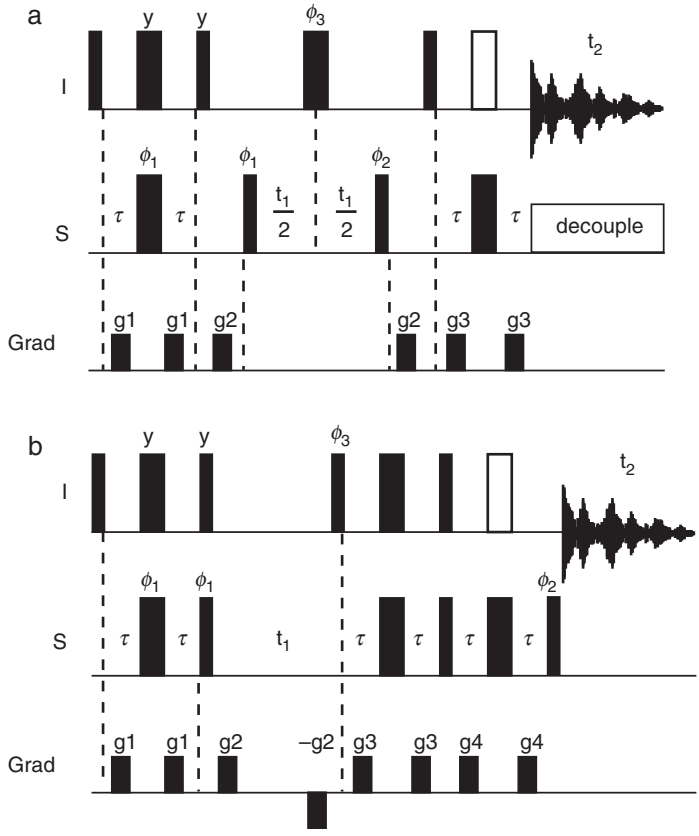

FIGURE 7.11 (a) Fast HSQC and (b) TROSY pulse sequences incorporating water flip-back solvent-suppression schemes. Thin bars represent 90° pulses and thick bars represent 180° pulses. The 180° pulse represented as an open bar is a crafted pulse that leaves the water magnetization unperturbed; 3–9–19, or soft–hard–soft, pulse schemes commonly used for this pulse are described in Section 3.7. Pulses are applied with x-phase unless the phase is indicated above the bar. The nominal value for $2\tau = 1/(2J_{IS})$. (a) Decoupling during t_2 is achieved by using GARP-1, WALTZ-16, or other decoupling sequences. Phase cycling for the fast HSQC experiment is $\phi_1 = x, -x$; $\phi_2 = 2(x), 2(-x)$; $\phi_3 = 4(y), 4(-y)$; and receiver $= x, -x, -x, x$. (b) Phase cycling for the TROSY experiment is $\phi_1 = x, y, -x, -y$; $\phi_2 = y$; $\phi_3 = -y$; and receiver $= x, y, -x, -y$ for the first FID acquired. The second FID is acquired with $\phi_1 = x, y, -x, -y$; $\phi_2 = y$; $\phi_3 = -y$; and receiver $= x, -y, -x, y$. The two data sets are stored separately and then combined as described in the text. Depending on the spectrometer, y and $-y$ phases may need to be interchanged for the TROSY experiment.

selection, a signal-to-noise loss of $2^{1/2}$ normally is incurred relative to techniques employing phase cycling (TPPI or hypercomplex methods) (Section 4.3.4.2). Kay and co-workers showed that pulsed field gradients can be used for coherence selection in a PEP-HSQC experiment without sacrificing sensitivity (*45*). A PFG-PEP-HSQC experiment is shown in Fig. 7.12a. Coherence selection is obtained using gradient pulses g3 and g6; the other gradient pulses are used to suppress artifacts associated with the 180° pulses (Section 4.3.3.2). The sequence also incorporates water flip-back techniques for solvent suppression. The evolution of the density operator for the PFG-PEP-HSQC sequence proceeds exactly as for the conventional HSQC experiment up to the end of the t_1 period in Fig. 7.12a. Evolution through the first spin echo period yields

$$\begin{aligned} &2I_zS_y\cos(\Omega_S t_1) - 2I_zS_x\sin(\Omega_S t_1) \\ &\qquad \xrightarrow{\delta_1-\pi S_x-\delta_1} -2I_zS_y\cos[\Omega_S t_1+\phi_S(z)] - 2I_zS_x\sin[\Omega_S t_1+\phi_S(z)], \end{aligned} \tag{7.68}$$

in which $\phi_S(z)$ is the spatially dependent phase acquired by the S spin coherence during the gradient pulse g3. The PEP reverse INEPT sequence yields

$$\begin{aligned} &-2I_zS_y\cos[\Omega_S t_1+\phi_S(z)] - 2I_zS_x\sin[\Omega_S t_1+\phi_S(z)] \\ &\qquad \xrightarrow{\text{PEP}} I_y\cos[\Omega_S t_1+\phi_S(z)]\varepsilon_I - \delta_{1,n}I_x\sin[\Omega_S t_1+\phi_S(z)]\varepsilon_{\text{MQ}}. \end{aligned} \tag{7.69}$$

Following the second spin echo period and gradient pulse g_6, the I spin coherences acquire a spatially dependent phase $\phi_I(z)$. If the gradient pulses are adjusted such that $\phi_S(z)=\phi_I(z)$, the resulting observable magnetization is

$$\left\{I_y\cos(\Omega_S t_1) - I_x\sin(\Omega_S t_1)\right\}\left(\varepsilon_I+\delta_{1,n}\varepsilon_{\text{MQ}}\right)/2. \tag{7.70}$$

Imbalance between the two coherence transfer pathways is suppressed by the N/P selection of the second field gradient pulse. To deconvolute the orthogonal magnetization components, a second acquisition is performed in which the phase of the $90^\circ_{\phi_2}(S)$ pulse immediately following the t_1 evolution period is inverted and the sign of gradient g_6 is reversed so that $\phi_S(z)=-\phi_I(z)$. The resulting observable magnetization is given by

$$\left\{-I_y\cos(\Omega_S t_1) - I_x\sin(\Omega_S t_1)\right\}\left(\varepsilon_I+\delta_{1,n}\varepsilon_{\text{MQ}}\right)/2. \tag{7.71}$$

Addition and subtraction of these two data sets yield results equivalent to [7.44] and [7.45]. The resulting phase-sensitive PFG-PEP-HSQC

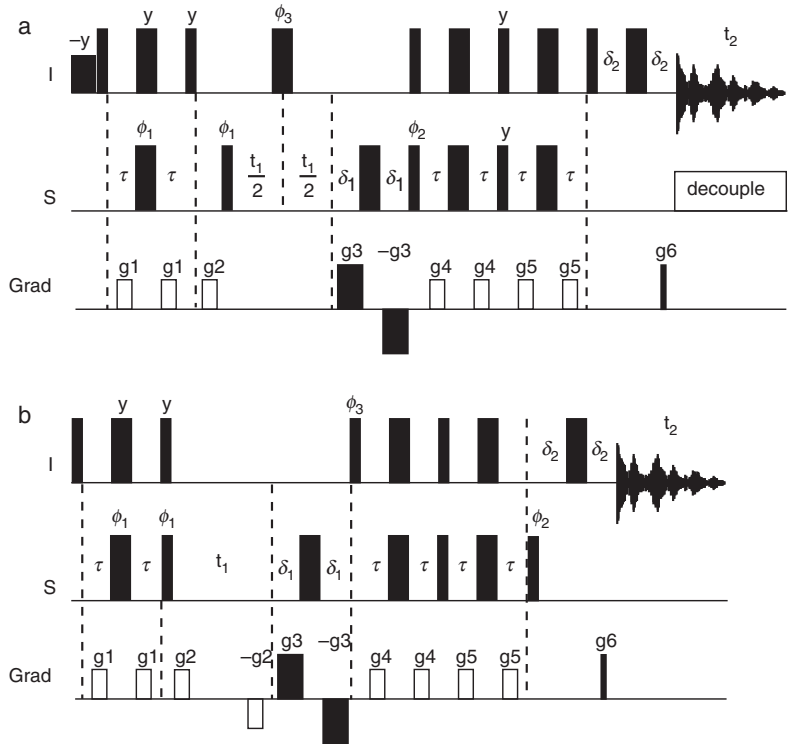

FIGURE 7.12 Pulse sequence for the (a) PFG-PEP-HSQC and (b) PFG-TROSY experiments. Thin bars represent 90° pulses and thick bars represent 180° pulses. Pulses are applied with x-phase unless the phase is indicated above the bar. The short thick bar represents a water-selective soft 90° pulse. The nominal value for $2\tau = 1/(2J_{IS})$; delays δ_1 and δ_2 are long enough to encompass the gradients. Gradient coherence selection is performed using g3 and g6 (black); other gradients (white) are for artifact suppression. Gradients g3 are applied as a pair in order to minimize the delay δ_1. (a) Decoupling during t_2 is achieved by using GARP-1, WALTZ-16, or other decoupling sequences. The phase cycling for the PFG-PEP-HSQC experiment is $\phi_1 = x, -x$; $\phi_2 = x$; and receiver $= x, -x$ for the first FID acquired. The second FID is acquired with inversion of ϕ_2 and gradient g6. For each t_1 increment, ϕ_1 and the receiver are inverted; no other quadrature detection scheme is required. (b) Phase cycling for the TROSY experiment is $\phi_1 = x, -x$; $\phi_2 = y$; $\phi_3 = -y$; and receiver $= x, -x$ for the first FID acquired. The second FID is acquired with $\phi_1 = x, -x$; $\phi_2 = y$; $\phi_3 = -y$; and receiver $= x, -x$. The gradient g6 also is inverted for the second FID. Depending on the spectrometer, y and $-y$ phases may need to be interchanged for the TROSY experiment. For both PFG-PEP-HSQC and PFG-TROSY, the two data sets are stored separately and then combined as described in the text.

spectrum has the same nominal sensitivity as does the phase-cycled PEP-HSQC spectrum, or *double* the sensitivity of a conventional PFG-HSQC spectrum. The $2^{1/2}$ sensitivity loss associated with coherence selection by pulsed field gradients is recovered *and* the nominal $2^{1/2}$ PEP sensitivity enhancement is obtained independently in the PFG-PEP-HSQC experiment. The gradient-enhanced pulse sequence is necessarily longer than the PEP-HSQC experiment, because the gradient pulses required for coherence selection are placed within spin echoes in order to refocus chemical shift evolution. The sensitivity of the PFG-PEP-HSQC experiment is reduced relative to the PEP-HSQC experiment by a factor of $\exp[-2\delta_1 R_{2S} - 2\delta_2 R_{2I}]$, in which R_{2S} and R_{2I} are the relaxation rate constants for the S and I spin coherence present during the spin echo periods (*46*).

The same considerations can be applied to the TROSY experiment. A PFG-TROSY experiment is shown in Fig. 7.12b. In addition to gradient coherence selection, this sequence also incorporates water flip-back solvent suppression.

7.1.5 THE CONSTANT-TIME ^{1}H–^{13}C HSQC EXPERIMENT

As noted in Section 7.1.2.2, multiplet structure in the F_1 dimension of conventional ^{1}H–^{13}C HSQC or HMQC spectra arises from aliphatic homonuclear ^{13}C–^{13}C scalar coupling interactions. The multiplet structure can be eliminated by using a constant-time ^{13}C evolution period (*18*, *19*). The constant-time ^{1}H–^{13}C HSQC (CT-HSQC) experiment illustrated in Fig. 7.13 differs from the pulse sequence of Fig. 7.1c by addition of ^{15}N coherent decoupling throughout the constant-time period T and addition of two carbonyl 180° pulses. Evolution under the ^{13}CO–^{13}C scalar coupling Hamiltonian is refocused during the initial t_1 fraction of the constant-time evolution period by the 180° pulse applied to the carbonyl spins, and during the remaining fraction of the constant-time period, $T - t_1$, by the 180° pulse applied to the aliphatic carbon spins. The ^{13}C–^{13}C scalar coupling interaction between the S spin and n other aliphatic ^{13}C spins, R, with coupling constant J_{CC}, is active during the entire period T. The net evolution of $2I_zS_y$ coherence during T is obtained by generalizing [7.19]:

$$-2I_zS_y \xrightarrow{T} -2I_zS_y \cos(\Omega_S t_1)\cos^n(\pi J_{CC}T) + 2I_zS_x \sin(\Omega_S t_1)\cos^n(\pi J_{CC}T) + \text{antiphase terms.} \qquad [7.72]$$

The antiphase terms (of the form $4I_zS_xR_{1z}$ and $8I_zS_yR_{1z}R_{2z}$, etc.) are not converted back to observable ^{1}H magnetization by the reverse INEPT sequence following the constant-time evolution period, and can be ignored. The ^{13}C magnetization present at the end of the constant-time evolution period is modulated only by its chemical shift during t_1; therefore, cross-peaks in the 2D correlation spectrum appear as singlets in the F_1 dimension.

To achieve effective decoupling of the $^{13}C^{\alpha}$–^{13}CO scalar coupling interaction, the rectangular 180°(^{13}C) pulse applied during T of Fig. 7.13 has a field strength given by $\gamma B_1 = \Omega/\sqrt{3}$, where Ω is the offset between the ^{13}CO and aliphatic ^{13}C carrier frequencies, and selective shaped 180°(^{13}CO) pulses are used (Section 7.1.2.2). The second 180°(^{13}CO)

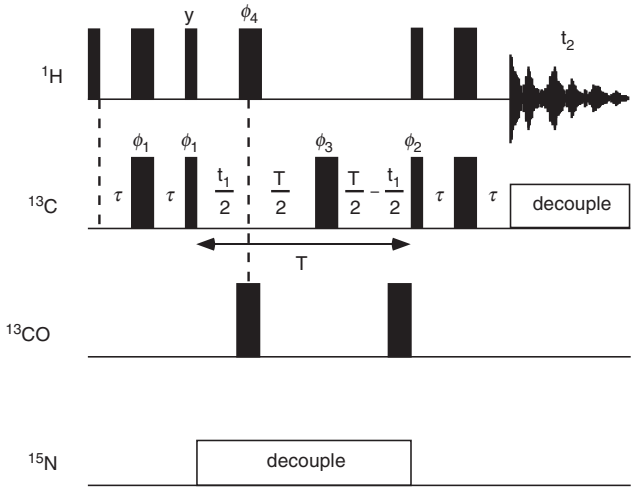

FIGURE 7.13 Pulse sequences for the ^{1}H–^{13}C constant-time HSQC experiment. Thin bars represent 90° pulses and thick bars represent 180° pulses. Pulses are applied with x-phase unless the phase is indicated above the bar. The nominal value for $2\tau = 1/(2J_{IS})$, $T = n/J_{CC}$, and $n = 1$ or 2. The first and last 180°(^{13}C) pulses are best applied as composite pulses of the type $90^\circ_x 180^\circ_y 90^\circ_x$, or other broadband inversion pulse, in order to minimize resonance offset and rf inhomogeneity effects. The ^{15}N decoupling during the constant-time evolution period is accomplished using a WALTZ-16 or DIPSI-2 decoupling scheme, and ^{13}C decoupling during the t_2 ^{1}H data acquisition period is accomplished with a GARP-1 or other decoupling scheme. The phase cycle is $\phi_1 = x, -x$; $\phi_2 = 8(x), 8(-x)$; $\phi_3 = 2(x), 2(y), 2(-x), 2(-y)$; $\phi_4 = 16(y), 16(-y)$; and receiver $= 2(x, -x, -x, x), 2(-x, x, x, -x)$; if required, this 32-step phase cycle can be reduced by a factor of two by eliminating cycling of ϕ_4. Frequency discrimination is obtained by TPPI, States, or TPPI–States phase cycling of ϕ_1.

pulse has no effect on the product operator analysis of the pulse sequence and serves to refocus aliphatic ^{13}C evolution caused by the off-resonance effects of the first 180°(^{13}CO) pulse. If the second selective 180°(^{13}CO) pulse were omitted, the resulting spectrum would have a frequency-dependent phase error in the F_1 dimension (Section 3.4.1). The $^{13}C^{\alpha}$–^{13}CO scalar coupling interaction is not active during the 2τ INEPT delays, so the aliphatic ^{13}C pulses may be applied at full power to maximize excitation of the aliphatic spins.

The 180°(^{13}CO) pulses can be applied in an alternative sequence:

$$(T-t_1)/4-180^\circ(^{13}CO)-(T-t_1)/4-180^\circ(^{13}C)-$$
$$(T+t_1)/4-180^\circ(^{13}CO)-(T+t_1)/4. \qquad [7.73]$$

In this case, the $^{13}C^{\alpha}$ operators of interest are in-phase with respect to the $^{13}C^{\alpha}$–^{13}CO scalar coupling when the 180°(^{13}C) pulse is applied. Consequently, this pulse can be applied at full power to obtain optimal inversion of aliphatic 180°(^{13}C) spins.

The uniformity of one-bond aliphatic ^{13}C–^{13}C couplings (J_{CC} ranges from 32 to 40 Hz) facilitates optimization of the length of T to maximize the $\cos^n(\pi J_{CC}T)$ factor in [7.72]. The experiment also can provide information on the number of aliphatic carbons attached to a given ^{13}C nucleus. As can be seen from [7.72], if $T = 1/J_{CC}$, the sign of the ^{13}C magnetization will be opposite for carbons coupled to an odd, relative to an even, number of other aliphatic carbons. If, on the other hand, $T = 2/J_{CC}$, all cross-peaks will have the same sign.

The resolution enhancement and spectral editing features of the CT-HSQC experiment are illustrated in Fig. 7.14, which compares ^{1}H–^{13}C HSQC spectra of uniformly $^{15}N/^{13}C$-labeled ubiquitin acquired using the conventional HSQC sequence of Fig. 7.1b with spectra acquired using the CT-HSQC scheme of Fig. 7.13 and constant-time evolution periods, T, of 27 and 54 ms. Expansions of the $^{1}H^{\alpha}$–$^{13}C^{\alpha}$ regions of the spectra are shown in Fig. 7.15. The conventional HSQC spectrum (Fig. 7.14a) and the CT-HSQC spectrum acquired with $T = 54$ ms (Fig. 7.14c) were recorded with identical digital resolution in the t_1 dimension (480 complex t_1 data points were acquired with $t_{1max} = 52.8$ ms), while the CT-HSQC spectrum acquired using $T = 27$ ms (Fig. 7.14b) was recorded with one-half the digital resolution of the other two experiments (240 complex t_1 data points were acquired with $t_{1max} = 26.4$ ms). Each spectrum was zero-filled to give a final F_1 digital resolution of 8.9 Hz.

The resolution obtained using $T = 2/J_{CC} \approx 54$ ms is clearly greater than that obtained using $T = 1/J_{CC} \approx 27$ ms. However, ^{13}C transverse

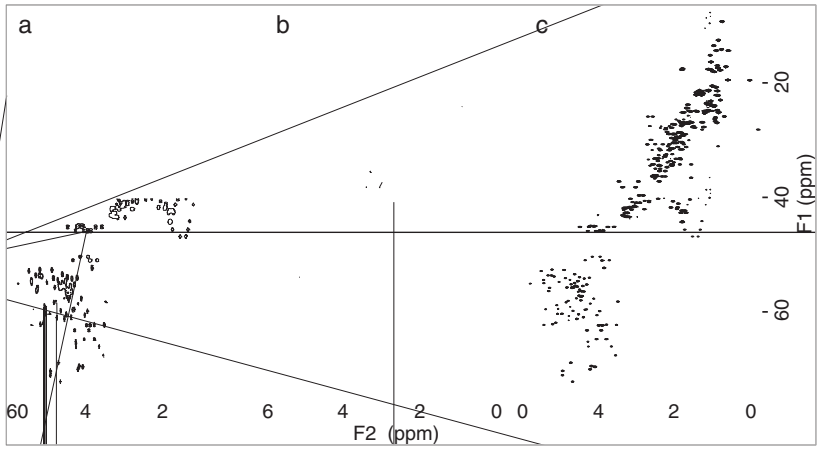

relaxation during the constant-time period attenuates the observable signal by a factor of $\exp(-R_2T)$. For proteins larger than ubiquitin, this attenuation can be significant, even for $T = 27$ ms. To obtain the maximum ^{13}C resolution, the maximum number of t_1 increments must be acquired. In 3D or 4D experiments, the number of increments in the indirectly detected dimensions is limited by the time available for total acquisition of the spectrum and ^{13}C constant-time evolution periods are limited practically to 27 ms.

7.2 Heteronuclear-Edited NMR Spectroscopy

Heteronuclear-edited NMR experiments represent the simplest use of heteronuclear spins to facilitate NMR spectroscopy of larger proteins (*1*, *2*). Three- and four-dimensional heteronuclear-edited NMR experiments resolve cross-peaks between ^{1}H spins according to the chemical shift of the heteronuclei bonded directly to the ^{1}H spins.

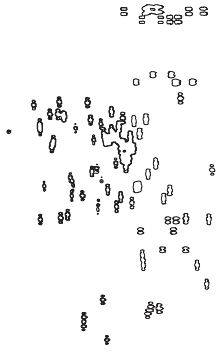

A 3D heteronuclear-edited experiment consists of a homonuclear pulse sequence, usually a NOESY (Section 6.6.1) or TOCSY (Section 6.5) experiment, and an HSQC (or HMQC) pulse sequence (Section 7.1) catenated as discussed in Section 4.5 (*47*). A 4D heteronuclear-edited NOESY experiment consists of the catenation of a homonuclear NOESY pulse sequence and two HSQC (or HMQC) building blocks.

7.2.1 3D NOESY–HSQC Spectroscopy

The basic I–S ($I = {}^{1}\mathrm{H}$, and $S = {}^{13}\mathrm{C}$ or ${}^{15}\mathrm{N}$) NOESY–HSQC experiment is illustrated in Fig. 7.16 (*48–50*). Up until time a, the sequence is a homonuclear NOESY experiment (Section 6.6.1) with S spin decoupling during the t_1 evolution period. Decoupling of the J_{IS} coupling interaction is achieved by application of a $180^\circ(S)$ pulse at the midpoint of t_1 (illustrated), or by application of a composite decoupling pulse scheme throughout t_1. The $90^\circ(I)$ pulse immediately preceding time a is equivalent to the first $90^\circ(I)$ pulse in the HSQC experiment, and the remainder of the pulse sequence following time a is identical to the HSQC experiment (Fig. 7.1b). The product operator treatment of the NOESY–HSQC experiment is obtained by catenating the results for the NOESY and HSQC experiments. For example, for two ${}^{1}\mathrm{H}$ spins I and K and a heteronuclear S spin

that is scalar coupled only to the I spin, evolution through the pulse sequence is given by

$$
\begin{aligned}
I_z + K_z &\xrightarrow{\frac{\pi}{2}(I_x+K_x)-t_1/2-\pi S_x-t_1/2-\frac{\pi}{2}(I_x+K_x)} I_z \cos(\Omega_I t_1) \prod_\eta \cos\left(\pi J_{I\eta} t_1\right) \\
&\qquad + K_z \cos(\Omega_K t_1) \prod_\lambda \cos(\pi J_{K\lambda} t_1) \\
&\xrightarrow{\tau_m} I_z \Bigg\{ a_{II}(\tau_m) \cos(\Omega_I t_1) \prod_\eta \cos\left(\pi J_{I\eta} t_1\right) \\
&\qquad + a_{IK}(\tau_m) \cos(\Omega_K t_1) \prod_\lambda \cos(\pi J_{K\lambda} t_1) \Bigg\} \\
&\xrightarrow{\frac{\pi}{2}(I_x+K_x)-\tau-\pi(I_x+K_x),\, \pi S_x-\tau-\frac{\pi}{2}(I_y+K_y),\, \frac{\pi}{2}S_x} \\
&\qquad - 2I_z S_y \Bigg\{ a_{II}(\tau_m) \cos(\Omega_I t_1) \prod_\eta \cos\left(\pi J_{I\eta} t_1\right) \\
&\qquad + a_{IK}(\tau_m) \cos(\Omega_K t_1) \prod_\lambda \cos(\pi J_{K\lambda} t_1) \Bigg\} \\
&\xrightarrow{t_2/2-\pi(I_x+K_x)-t_2/2} 2I_z S_y \cos(\Omega_S t_2) \Bigg\{ a_{II}(\tau_m) \cos(\Omega_I t_1) \prod_\eta \cos\left(\pi J_{I\eta} t_1\right) \\
&\qquad + a_{IK}(\tau_m) \cos(\Omega_K t_1) \prod_\lambda \cos(\pi J_{K\lambda} t_1) \Bigg\} \\
&\xrightarrow{\frac{\pi}{2}(I_x+K_x),\, \frac{\pi}{2}S_x-\tau-\pi(I_x+K_x),\, \pi S_x-\tau} -I_x \cos(\Omega_S t_2) \Bigg\{ a_{II}(\tau_m) \cos(\Omega_I t_1) \\
&\qquad \times \prod_\eta \cos\left(\pi J_{I\eta} t_1\right) + a_{IK}(\tau_m) \cos(\Omega_K t_1) \prod_\lambda \cos(\pi J_{K\lambda} t_1) \Bigg\},
\end{aligned}
\qquad [7.74]
$$

in which $2\tau = 1/(2J_{IS})$, $a_{II}(\tau_m)$ and $a_{IK}(\tau_m)$ are transfer functions for dipolar cross-relaxation (Sections 5.1.2 and 5.4.1), homonuclear scalar coupling interactions of the I and K spins with other ^{1}H spins are represented by terms containing $J_{I\eta}$ and $J_{K\lambda}$, and only terms leading to observable signals are derived. Magnetization originating on the K spin that is not transferred to the I spin during the NOESY mixing

period is suppressed by the HSQC isotope filter. If the K spins were coupled to S spins, then analogous detectable K_x coherence terms would appear in [7.74]. The complete magnetization transfer pathway can be abbreviated as follows:

$$\begin{matrix} K_i & \overset{\text{NOE}}{\longrightarrow} & I_j & \overset{^1J_{IS}}{\longrightarrow} & S_j & \overset{^1J_{IS}}{\longrightarrow} & I_j. \\ (t_1) & & & & (t_2) & & (t_3) \end{matrix} \qquad [7.75]$$

Coherence transfer steps are indicated above the arrows, and the locations of the independent t_1, t_2, and t_3 evolution periods are indicated on the second line.

In order to obtain sufficient digital resolution in the 3D experiment, a large number of (t_1, t_2) experiments are required (typically 128×32 complex data points are acquired in t_1 and t_2, respectively), therefore only a limited number of transients can be recorded for every (t_1, t_2) value if the entire experiment is to be completed in a reasonable time period. As a consequence, a short phase cycle must be utilized and incorporation of pulsed field gradients for artifact suppression is a powerful approach for reducing the length of the requisite phase cycle (Section 7.2.4.3). Using the eight-step phase cycle illustrated in Fig. 7.16, a 3D spectrum can be acquired in 3–4 days. A shorter phase cycle can be obtained by eliminating the axial peak suppression phase cycle, ϕ_1.

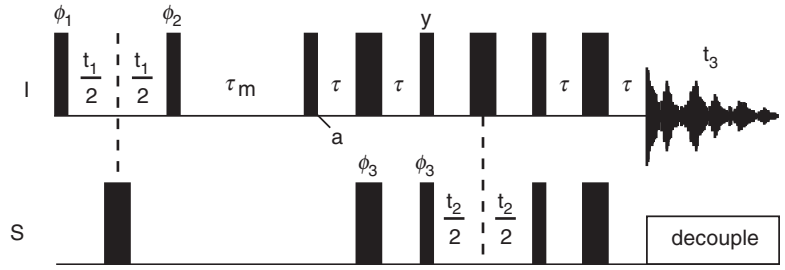

FIGURE 7.16 Pulse sequence for the 3D ^{1}H–^{15}N NOESY–HSQC experiment. Thin bars represent 90° pulses and thick bars represent 180° pulses. Pulses are applied with x-phase unless the phase is indicated above the bar. The nominal value for $2\tau = 1/(2J_{IS})$ and τ_m is the mixing time. The phase cycling is $\phi_1 = 2(x)$, $2(-x)$; $\phi_2 = 4(x)$, $4(-x)$; $\phi_3 = x, -x$; and receiver $= x, -x, -x, x, -x, x, x, -x$. Quadrature detection in the t_1 and t_2 dimensions is achieved by incrementing independently the phases ϕ_1 and ϕ_3, respectively, and the receiver phase, in a TPPI, States, or TPPI–States manner.

Quadrature detection in the t_1 and t_2 dimensions is achieved by shifting the phases of ϕ_1 and ϕ_3 independently in a TPPI or TPPI–States manner.

Processing NOESY–HSQC spectra follows the general methods outlined in Section 6.6.1.3 for processing NOESY spectra and Section 7.1.2.4 for processing HSQC spectra, apart from the more limited resolution of the F_1 and F_2 dimensions. In the final 3D spectrum, the $F_1(^1H)$–$F_3(^1H)$ projection corresponds to the $F_1(^1H)$–$F_2(^1H)$ region of a conventional 2D ^1H–^1H NOESY spectrum, and the $F_2(S)$–$F_3(^1H)$ projection corresponds to the $F_1(S)$–$F_2(^1H)$ dimensions of a 2D HSQC (or HMQC) correlation spectrum, as illustrated schematically in Fig. 7.17.

The NOESY–HSQC pulse sequence illustrated in Fig. 7.16 can be simplified by replacing the HSQC sequence with the HMQC sequence. From the previous discussion of the HSQC and HMQC experiments, such simplification may appear to be undesirable due to the superior resolution and relaxation properties of the HSQC experiment. However, the resolution in the heteronuclear dimension of a 3D experiment is typically limited by the digital resolution, so the detrimental effect of using the HMQC sequence is not as great in the 3D as in the 2D case. In addition, the simple HSQC sequence can be replaced with any of the variant heteronuclear correlation pulse sequences (decoupled HSQC, constant-time HSQC, PEP-HSQC, TROSY) as desired.

7.2.1.1 3D ^1H–^{15}N NOESY–HSQC Presaturation of the solvent resonance normally is avoided in ^1H–^{15}N NOESY–HSQC NMR spectroscopy of ^{15}N-labeled proteins. Instead, water suppression is achieved by incorporating spin lock purge pulses or field gradient pulses into the pulse sequence, as discussed in Section 7.1.4. The use of these techniques avoids saturation of the $^1H^{\alpha}$ spins and allows observation of important $^1H^N$–$^1H^{\alpha}$ cross-peaks.

The advantage of not presaturating the water resonance in the ^1H–^{15}N NOESY–HSQC experiment is illustrated clearly by Fig. 7.18, which shows selected regions of $F_2(^{15}N)$ slices of a 3D NOESY–HSQC spectrum of ubiquitin compared with the equivalent regions from a 2D homonuclear NOESY spectrum. Several $^1H^{\alpha}$–$^1H^N$ cross-peaks can be seen close to the water resonance position in the NOESY–HSQC spectrum (Fig. 7.18, a and b), but are not observable in the 2D homonuclear NOESY spectrum acquired using presaturation of the water resonance (Fig. 7.18c). These cross-peaks would be difficult to observe if presaturation of the water resonance had been utilized in the 3D NOESY–HSQC experiment.

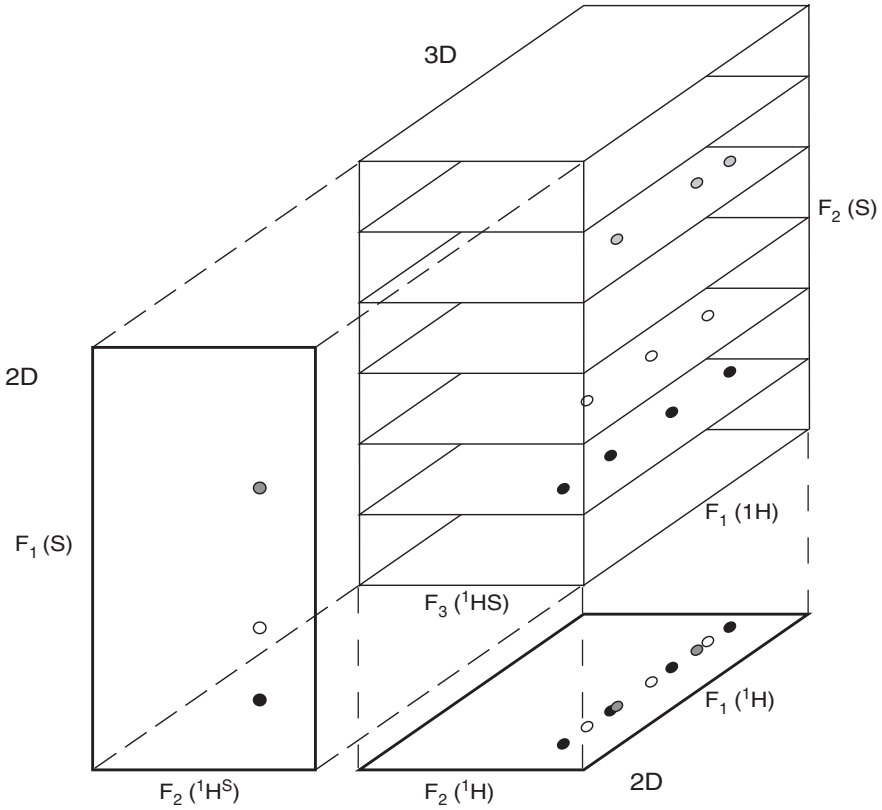

FIGURE 7.17 A schematic illustration showing the relationship between a 3D heteronuclear-edited spectrum and 2D homonuclear and heteronuclear correlation spectra. Cross-peaks representing three different spin systems, with degenerate $^1H^S$ chemical shifts, but differing S spin chemical shifts, are indicated. The 3D spectrum is represented as a series of $F_1(^1H)$–$F_3(^1H^S)$ slices edited by the chemical shift of the directly attached S spins along the F_2 axis.

The phase cycle of ϕ_1 necessary for coherence selection and for frequency discrimination in F_1 results in a different state of the water magnetization for different values of ϕ_1. When $\phi_1 = x$, the water magnetization is given by $-W_z$ at the start of the mixing period. When $\phi_1 = -x$, the state of the water magnetization is W_z. When the phase of ϕ_1 is shifted to $\pm y$ for quadrature detection, the state of the water magnetization is described by $\pm W_x$. The extent of radiation damping during τ_m is very different for these different operators; thus, the quality

the different transients.
the phases of ϕ_1 by 45°
he start of the mixing
spect to the z-axis and
or different transients.
plied during τ_m should
ow maximal radiation

ring t_1, only magnetiza-
s retained for detection
served in the spectrum
nus, the $F_1(^1H)$–$F_3(^1H)$

projection of the 3D spectrum corresponds to the $F_1(^1H)$–$F_2(^1H^N)$ region of a conventional 2D ^1H–^1H NOESY spectrum.

7.2.1.2 3D ^1H–^{13}C NOESY–HSQC The ^1H–^{13}C NOESY–HSQC experiment, which typically is acquired in D_2O solution, provides NOE correlations between aliphatic ^1H spins (and between aliphatic and aromatic ^1H spins). In a ^{13}C-edited NOESY–HSQC spectrum the $F_1(^1H)$–$F_3(^1H)$ projection corresponds to the $F_1(^1H)$–$F_2(^1H^{aliphatic})$ region of a conventional 2D ^1H–^1H NOESY spectrum acquired in D_2O solution, and the $F_2(^{13}C)$–$F_3(^1H)$ projection corresponds to the 2D HSQC (or HMQC) correlation spectrum [$F_1(^{13}C)$–$F_2(^1H)$] (*52*).

For uniformly ^{13}C-labeled proteins, the NOESY–HSQC experiment illustrated in Fig. 7.16 is modified to include ^{13}CO decoupling during the t_2 evolution period by using a selective composite pulse decoupling scheme such as SEDUCE-1 (*52*). Aliphatic ^{13}C decoupling during the ^1H t_1 evolution period can be accomplished by using a composite pulse decoupling scheme or, more simply, a composite 180°(^{13}C) pulse.

If the ^{13}C-edited NOESY–HSQC experiment utilizes a conventional HSQC sequence (Figs. 7.1b and 7.16), then the maximum t_2 acquisition time must be kept shorter than $1/(2J_{CC})$ in order to avoid sensitivity losses due to resolution of the J_{CC} couplings in the F_2 dimension, unless homonuclear decoupling is used (*23*). This constraint usually is not limiting in a 3D experiment. For example, on an 800-MHz spectrometer, if 48 complex points are to be acquired in the t_2 dimension with an F_2 spectral width of 30–35 ppm, then the value of t_{2max} will range from 8.0 to 6.9 ms, compared with $1/(2J_{CC}) = 14$ ms. Of course, the CT-HSQC sequence (Fig. 7.13) also can be incorporated into the ^1H–^{13}C NOESY–HSQC experiment in order to completely eliminate line broadening due to J_{CC} scalar coupling (Section 7.1.5).

Assignment of NOE cross-peaks in a 3D ^1H–^{13}C NOESY–HSQC spectrum is greatly aided by the symmetry present in the spectrum. For two proximal spins, H_1 and H_2, NOE cross-peaks are expected at $[F_1(^1H_1), F_2(^{13}C_2), F_3(^1H_2)]$ and at $[F_1(^1H_2), F_2(^{13}C_1), F_3(^1H_1)]$. By searching the 3D spectrum for such symmetry-related peaks, the ^{13}C chemical shifts associated with both ^1H spins involved in the NOE interaction can therefore be identified. Knowledge of all four chemical shifts can potentially lead to an unambiguous NOE assignment. An example in which identification of the symmetry-related peak aids NOE assignment is included in Fig. 7.19, which shows selected regions from $F_1(^1H)$–$F_3(^1H)$ slices of a 3D ^1H–^{13}C NOESY–HSQC spectrum of ^{13}C-labeled ubiquitin, together with the equivalent region from

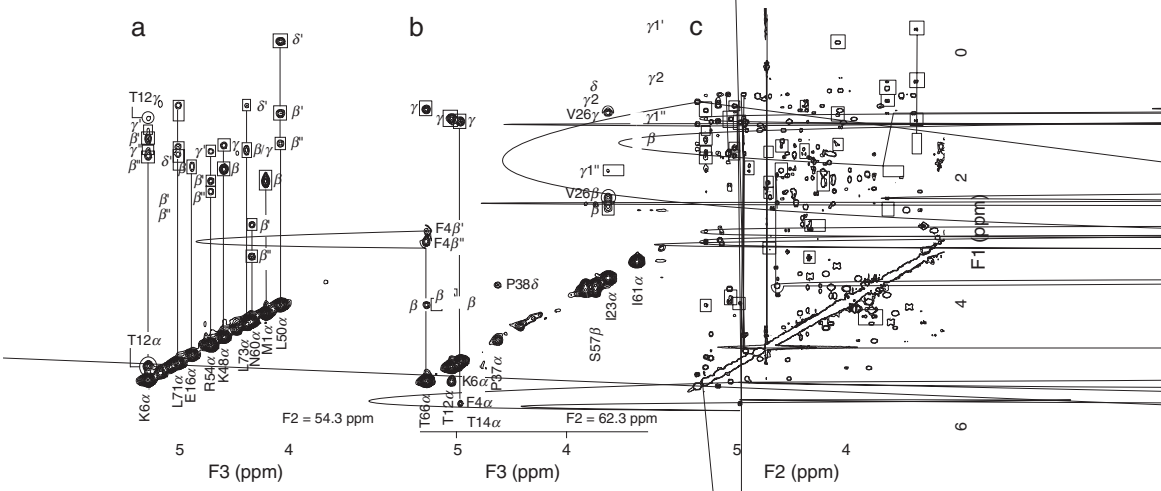

FIGURE 7.19 Selected $F_1(^1H)$–$F_3(^1H^{\alpha})$ regions from a 3D ^1H–^{13}C NOESY–HSQC spectrum of ^{13}C-labeled ubiquitin in D_2O solution at $F_2(^{13}C)$ chemical shifts of 54.3 ppm (a) and 30.2/62.3 ppm (b), and the corresponding region from a 2D homonuclear NOESY spectrum (c) acquired using an unlabeled sample of ubiquitin in D_2O solution. Intraresidue NOEs are indicated by a box while interresidue NOEs are indicated by ellipses. The Lys6($^1H^{\alpha}$)–Thr12($^1H^{\alpha}$) cross-peak discussed in the text is located in the lower left region of each spectrum.

a homonuclear ^1H–^1H NOESY spectrum of ubiquitin. The cross-peak between Lys6($^1H^{\alpha}$) and Thr12($^1H^{\alpha}$) is ambiguous in the homonuclear NOESY spectrum due to degeneracy of the $^1H^{\alpha}$ chemical shifts of Lys6 and Thr66; the presence of this cross-peak in Fig. 7.19a at the $F_3(^1H)$ chemical shift of Lys6, and its absence in Fig. 7.19b at the $F_3(^1H)$ chemical shift of Thr66, clearly support the assignment indicated.

7.2.2 3D TOCSY–HSQC SPECTROSCOPY

The description of the ^1H–^{15}N NOESY–HSQC experiment given in the preceding section also applies to the ^1H–^{15}N TOCSY–HSQC experiment, with the exception that the NOESY mixing period is replaced by a TOCSY isotropic mixing sequence (*1*, *49*, *50*). The information obtained from a 3D ^1H–^{15}N TOCSY–HSQC spectrum is the same as that obtained from the $F_1(^1H)$–$F_2(^1H^N)$ region of a conventional 2D ^1H–^1H TOCSY spectrum, but, as illustrated schematically in Fig. 7.17, it is edited in a third dimension according to the ^{15}N chemical shift associated with the amide $^1H^N$. In addition to providing intraresidue

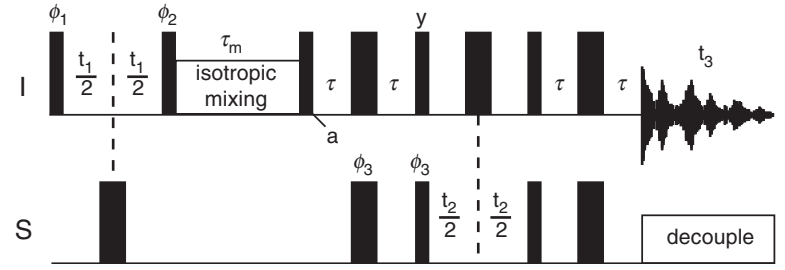

FIGURE 7.20 Pulse sequence for the 3D ^{1}H–^{15}N TOCSY–HSQC experiment. DIPSI-2rc isotropic mixing is used during τ_m. Other experimental details are as given in Fig. 7.16.

correlations that are important for the sequential assignment process, the ^{1}H–^{15}N TOCSY–HSQC experiment may be used to obtain qualitative estimates of $^3J_{H^\alpha H^\beta}$ coupling constants from the relative intensities of well-resolved $^1H^N$–$^1H^\beta$ cross-peaks in spectra acquired with short mixing times (<35 ms) (*53*).

A pulse sequence for an ^{1}H–^{15}N TOCSY–HSQC experiment is shown in Fig. 7.20. Following the initial ^{1}H t_1 evolution period, a 90°(^{1}H) pulse returns the frequency-labeled magnetization to the $\pm z$-axis for the isotropic mixing period. The DIPSI-2rc isotropic mixing sequence (*54*) transfers ^{1}H magnetization from aliphatic spins to the corresponding intraresidue amide ^{1}H spins, while minimizing rotating-frame NOE effects. The 90°(^{1}H) pulse following the mixing sequence rotates the resulting z-magnetization back into the transverse plane, and is therefore analogous to the first pulse in an HSQC experiment, as already discussed for the ^{1}H–^{15}N NOESY–HSQC experiment. The remainder of the sequence is equivalent to an ^{1}H–^{15}N HSQC experiment. The complete magnetization transfer pathway is

$$\underset{(t_1)}{I_i} \xrightarrow{\text{TOCSY}} I_j \xrightarrow{^1J_{IS}} \underset{(t_2)}{S_j} \xrightarrow{^1J_{IS}} \underset{(t_3)}{I_j}. \qquad [7.76]$$

Sample F_1(^{1}H)–F_3(^{1}H) planes from a TOCSY–HSQC spectrum of ubiquitin are compared with the equivalent region of a homonuclear TOCSY spectrum in Fig. 7.21. An analogous ^{1}H–^{13}C TOCSY–HSQC experiment, for use with protein D_2O solutions, might also be designed. However, a significantly more sensitive experiment, which relies on coherence transfer via the large and uniform ^{13}C–^{13}C J couplings, rather than the smaller ^{1}H–^{1}H J couplings, gives the same information.

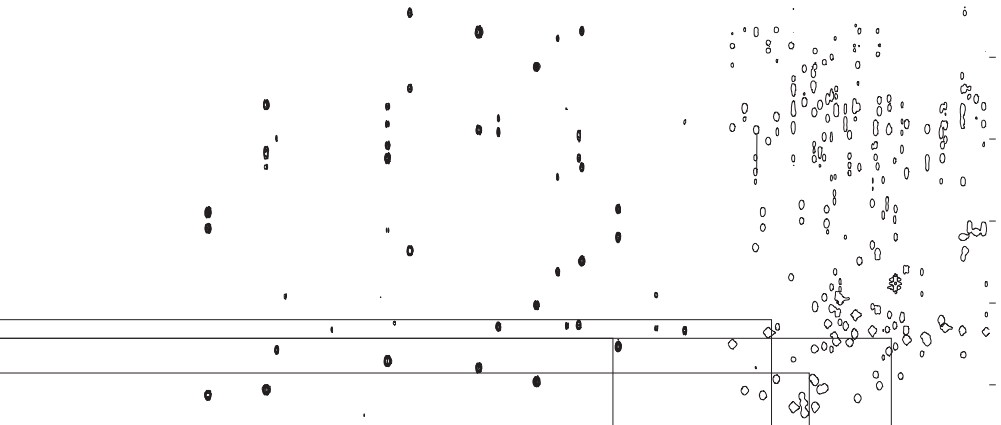

These experiments, the HCCH–TOCSY, and the related HCCH–COSY, are discussed in Section 7.3.

7.2.3 3D HSQC–NOESY and HSQC–TOCSY Experiments

NOESY and HSQC (or HMQC) pulse sequences conceivably could be combined in the reverse order to yield an HSQC–NOESY (or HMQC–NOESY) experiment, illustrated in Fig. 7.22 (*55*). In this experiment, the F_1 and F_3 dimensions are exchanged relative to the NOESY–HSQC experiment; thus, the $F_1(^1H)$–$F_2(S)$ projection corresponds to the 2D HSQC (or HMQC) correlation spectrum, and the $F_1(^1H)$–$F_3(^1H)$ projection corresponds to the $F_1(^1H)$–$F_2(^1H)$ region of a conventional 2D ^1H–^1H NOESY spectrum. Similarly, in an HSQC–TOCSY (or HMQC–TOCSY) experiment, the $F_1(^1H)$–$F_2(S)$ projection corresponds to the 2D HSQC (or HMQC) correlation spectrum, and the $F_1(^1H)$–$F_3(^1H)$ projection corresponds to the $F_1(^1H)$–$F_2(^1H)$ region of a conventional 2D ^1H–^1H TOCSY spectrum.

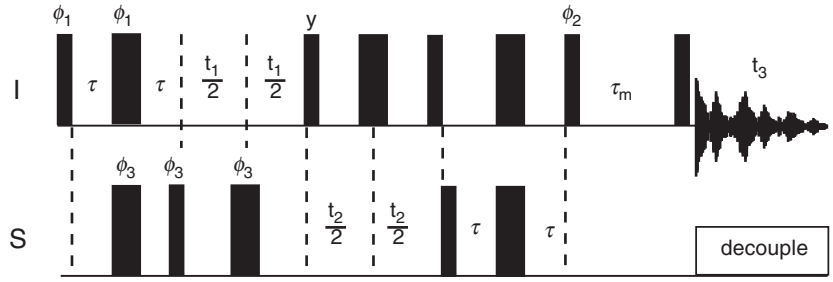

FIGURE 7.22 HSQC–NOESY pulse sequence. Thin bars represent 90° pulses and thick bars represent 180° pulses. Pulses are applied with x-phase unless the phase is indicated above the bar. The nominal value for $2\tau = 1/(2J_{IS})$ and τ_m is the mixing time. The phase cycling is $\phi_1 = x, -x$; $\phi_2 = x, x, -x, -x$; $\phi_3 = 4(x)$, $4(-x)$; and receiver $= x, -x, -x, x, -x, x, x, -x$. Quadrature detection in the t_1 and t_2 dimensions is achieved by incrementing independently the phases ϕ_1 and ϕ_3, respectively, and the receiver phase, in a TPPI, States, or TPPI–States manner.

The coherence transfer pathway is given by

$$\underset{(t_1)}{I_i} \xrightarrow{{}^1J_{IS}} \underset{(t_2)}{S_i} \xrightarrow{{}^1J_{IS}} I_i \xrightarrow{\text{NOESY/TOCSY}} \underset{(t_3)}{I_j}. \qquad [7.77]$$

For ^{15}N-labeled proteins, these experiments have two advantages compared to the ^{1}H–^{15}N NOESY–HSQC and ^{1}H–^{15}N TOCSY–HSQC experiments (the differences are much less pronounced for ^{1}H–^{13}C heteronuclear-edited experiments). First, the ^{1}H–^{1}H planes in HSQC–NOESY and HSQC–TOCSY experiments have higher digital resolutions than do the corresponding planes in NOESY–HSQC and TOCSY–HSQC experiments for a given experimental time, because the full ^{1}H spectral width is digitized during t_3 rather than during t_1 and the narrower H^N spectral region is digitized in t_1 rather than in t_3. Second, narrower F_1 linewidths result from evolution of heteronuclear multiple-quantum coherence during t_1 rather than of ^{1}H single quantum coherence (Section 7.1.1). However, the HSQC–NOESY and HSQC–TOCSY experiments have the disadvantage that a number of $^1H^N(F_1)$–$^1H^\alpha(F_3)$ cross-peaks may be obscured by the intense residual water peak, unless very efficient water suppression can be obtained using field gradient pulses (Section 3.7.3).

PEP sensitivity enhancement cannot be incorporated into the HSQC–NOESY experiment because the orthogonal magnetization

components following t_2 cannot be converted simultaneously to longitudinal magnetization during the NOESY mixing period. In contrast, PEP sensitivity enhancement can be incorporated *independently* into the HSQC and TOCSY portions of the HSQC–TOCSY pulse sequence, which yields a theoretical sensitivity improvement of 2 compared to the conventional HSQC–TOCSY or TOCSY–HSQC experiment (*56*, *57*).

7.2.4 HMQC–NOESY–HMQC EXPERIMENTS

Although the 3D heteronuclear-edited NOESY spectra previously discussed offer a vast improvement in resolution relative to 2D homonuclear NOESY spectra, the possibility of ambiguity still remains. One limitation of the 3D heteronuclear-edited NOESY experiments is that NOE correlations cannot be observed between ^{1}H spins with degenerate chemical shifts, because these cross-peaks are coincident with the more intense *autocorrelation* or "diagonal" peak. Observation of such NOEs, which occur between both aromatic and aliphatic ^{1}H spins in 3D ^{1}H–^{13}C NOESY–HSQC spectra and between amide ^{1}H spins (particularly in proteins with a high helical content) in ^{1}H–^{15}N NOESY–HSQC spectra, is important for both resonance assignment and protein structure determination. Indeed, NOEs between aliphatic ^{1}H spins make up the majority of NOEs observed for proteins, and identification of as many of these NOEs as possible is essential. Additionally, in an ^{1}H–^{15}N NOESY–HSQC experiment, ambiguities related to $^1H^N$ chemical shift degeneracy are removed provided that either the $^1H^N$ or ^{15}N chemical shifts of a given amide group can be resolved; however, ambiguities associated with overlap in the aliphatic ^{1}H region remain. Therefore, even if a given amide–aliphatic NOE cross-peak is fully resolved in the 3D ^{1}H–^{15}N NOESY–HSQC spectrum, unambiguous assignment on the basis of the aliphatic ^{1}H chemical shift alone may be impossible.

HMQC–NOESY–HMQC NMR spectroscopy provides a solution to these problems (analogous HSQC–NOESY–HSQC experiments are discussed in Section 9.1.8) (*58*). These experiments are derived conceptually by overlapping HMQC–NOESY and NOESY–HMQC experiments or by catenating two HMQC experiments and a NOESY experiment. As the experiment names indicate, a ^{15}N/^{15}N HMQC–NOESY–HMQC combines ^{1}H–^{15}N HMQC, ^{1}H–^{1}H NOESY, and ^{1}H–^{15}N HMQC sequences; a ^{13}C/^{15}N HMQC–NOESY–HMQC combines ^{1}H–^{13}C HMQC, ^{1}H–^{1}H NOESY, and ^{1}H–^{15}N HMQC sequences; and a ^{13}C/^{13}C HMQC–NOESY–HMQC combines ^{1}H–^{13}C HMQC, ^{1}H–^{1}H NOESY, and ^{1}H–^{13}C HMQC sequences. For the case

of two ^{1}H spins, I_1 and I_2, covalently bonded to two heteronuclei, S_1 and S_2, the first HMQC experiment correlates spins I_1 and S_1, magnetization is exchanged between I_1 and I_2 during the NOESY mixing period, and the second HMQC experiment correlates I_2 and S_2. Thus, each NOE cross-peak can be identified by up to four (two ^{1}H and two heteronuclear) chemical shifts in four independent frequency dimensions in 4D versions of these experiments. In some instances, 3D versions of the HMQC–NOESY–HMQC experiments that correlate S_1, S_2, and I_2 in the three frequency dimensions are satisfactory, provided that the S_1 resonances are well-resolved (see Section 7.2.5).

7.2.4.1 3D $^{15}N/^{15}N$ HMQC–NOESY–HMQC The 3D ^{1}H–^{15}N HMQC–NOESY–HMQC experiment illustrated in Fig. 7.23 is used to detect NOEs between amide ^{1}H spins with degenerate chemical shifts. In this experiment, the heteronuclear chemical shifts are labeled in the F_1 and F_2 dimensions, and the ^{1}H chemical shift is detected in the F_3 dimension (*59*, *60*). The initial part of this experiment, between points *a* and *b*, is equivalent to an HMQC sequence (less the t_2 acquisition period) (Fig. 7.1a), and generates, at time *b*, transverse $^1H^N$ magnetization that is modulated by the chemical shift of its attached ^{15}N nucleus as a function of t_1 [7.2]. The following 90°(^{1}H) pulse regenerates $^1H^N$ *z*-magnetization, which is transferred by cross-relaxation to proximal ^{1}H spins during the NOESY mixing time, τ_m. The second HMQC sequence converts any $^1H^N$ magnetization present following τ_m into heteronuclear multiple-quantum coherence for indirect detection of the associated ^{15}N

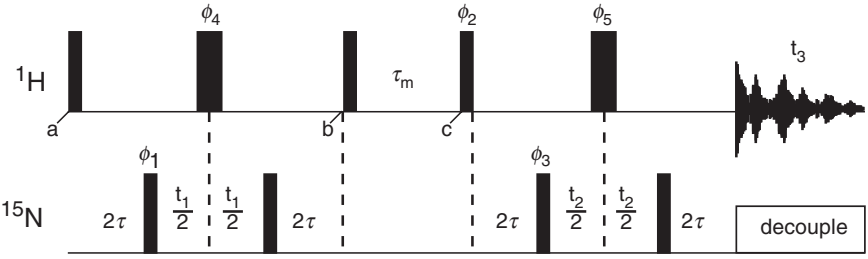

FIGURE 7.23 Pulse sequence for the 3D ^{1}H–^{15}N HMQC–NOESY–HMQC experiment. Experimental details are similar to those given in Fig. 7.16. The phase cycling is $\phi_1 = x, -x$; $\phi_2 = 4(x), 4(-x)$; $\phi_3 = 2(x), 2(-x)$; $\phi_4 = 8(y), 8(-y)$; $\phi_5 = 16(y), 16(-y)$; and receiver $= x, -x, -x, x, -x, x, x, -x$. Quadrature detection in the t_1 and t_2 dimensions is achieved by incrementing independently the phases ϕ_1, and ϕ_3, respectively, and the receiver phase, in a TPPI, States, or TPPI–States manner.

chemical shifts during t_2 and direct detection of the $^1H^N$ frequencies during the acquisition period, t_3. The delays $2\tau = 1/(2^1J_{NH})$. The magnetization transfer pathway is

$$\begin{matrix} {}^1H_i^N & \xrightarrow{{}^1J_{NH}} & {}^{15}N_i & \xrightarrow{{}^1J_{NH}} & {}^1H_i^N & \xrightarrow{NOE} & {}^1H_j^N & \xrightarrow{{}^1J_{NH}} & {}^{15}N_j & \xrightarrow{{}^1J_{NH}} & {}^1H_j^N \\ & & (t_1) & & & & & & (t_2) & & (t_3) \end{matrix}. \quad [7.78]$$

The 32-step phase cycle given in Fig. 7.23 is rather long by 3D standards, but because the digital resolution in the heteronuclear dimensions need not be as great as in ^1H dimensions, the total acquisition time can still be limited to ~4 days. Typically, the acquired 3D matrix comprises $64(t_1) \times 32(t_2) \times 512(t_3)$ complex data points. The first four steps of the phase cycle select signals that have arisen via $^1H^N$ multiple-quantum coherence, while the third step (the first and second set of four transients) eliminates artifacts that arise from single-quantum ^1H magnetization present during τ_m. The phase cycling of the two $180°(^1H)$ pulses simply serves to eliminate artifacts that result from imperfections in these pulses. If desired, phase cycling of these two pulses can be eliminated in order to reduce the overall experiment time, or to increase the digital resolution in the t_2 dimension by acquiring more increments with fewer transients per increment.

7.2.4.2 4D $^{13}C/^{15}N$ HMQC–NOESY–HMQC The pulse sequence for the 4D $^{13}C/^{15}N$ HMQC–NOESY–HMQC experiment (*61*) is illustrated in Fig. 7.24. Conceptually, the experiment simply comprises a NOESY mixing period between two HMQC sequences; the first HMQC sequence is tuned to ^1H–^{13}C couplings and the second is tuned to ^1H–^{15}N couplings. Magnetization is therefore transferred from ^{13}C-attached aliphatic ^1H spins to ^{15}N–attached amide ^1H spins via the following pathway:

$$\begin{matrix} {}^1H_i & \xrightarrow{{}^1J_{CH}} & {}^{13}C_i & \xrightarrow{{}^1J_{CH}} & {}^1H_i & \xrightarrow{NOE} & {}^1H_j^N & \xrightarrow{{}^1J_{NH}} & {}^{15}N_j & \xrightarrow{{}^1J_{NH}} & {}^1H_j^N \\ & & (t_1) & & (t_2) & & & & (t_3) & & (t_4) \end{matrix}. \quad [7.79]$$

Between times *a* and *b* in Fig. 7.24, the basic pulse sequence is similar to a 2D ^1H–^{13}C HMQC experiment (Section 7.1.1.1), except that the t_2 acquisition time of the 2D experiment has been substituted with an incremental t_2 evolution period for indirect detection of the aliphatic ^1H chemical shifts. The $180°(^{13}C)$ decoupling pulse applied in the middle of the t_2 evolution period should be applied as a broadband inversion composite pulse, such as $90°_x180°_y90°_x$, in order to minimize resonance

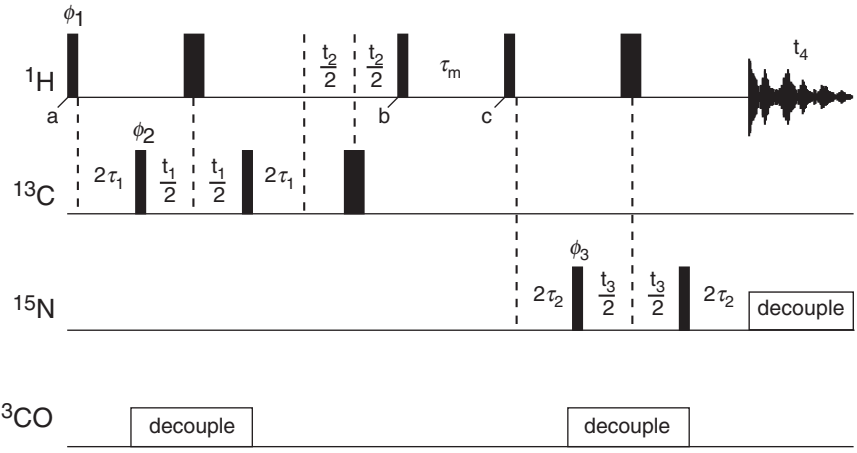

FIGURE 7.24 Pulse sequence for the 4D $^{13}C/^{15}N$ HMQC–NOESY–HMQC experiment. The nominal values for $2\tau_1 = 1/(2J_{CH})$ and $2\tau_2 = 1/(2J_{NH})$. The 180°(^{13}C) decoupling pulse in the middle of the t_2 evolution period is applied as a broadband inversion composite pulse, such as $90^\circ_x 180^\circ_y 90^\circ_x$, in order to minimize resonance offset effects. Other experimental details are similar to those given in Fig. 7.16. The phase cycling is $\phi_1 = x$; $\phi_2 = x, -x$; $\phi_3 = 2(x), 2(-x)$; receiver $= x, -x, -x, x$. Quadrature detection in the t_1, t_2, and t_3 dimensions is achieved by incrementing independently the phases ϕ_2, ϕ_1, and ϕ_3, respectively, and the receiver phase, in a TPPI, States, or TPPI–States manner.

offset effects. The delays $2\tau_1 = 1/(2^1J_{CH})$. The 90°(^{1}H) pulse immediately following the initial ^{1}H–^{13}C HMQC sequence rotates the transverse ^{1}H magnetization to the z-axis. During the subsequent NOESY mixing time, τ_m, magnetization can be transferred to proximal ^{1}H spins via dipolar couplings. The remainder of the pulse sequence, following time c, represents an ^{1}H–^{15}N HMQC sequence, with indirect detection of the ^{15}N chemical shift during t_3, and, finally, detection of $^1H^N$ during the acquisition time t_4. The delays $2\tau_2 = 1/(2^1J_{NH})$. Decoupling of the ^{13}CO spins during t_1 and t_3 can be achieved using a suitable low-power composite pulse decoupling scheme, such as SEDUCE-1, as indicated in Fig. 7.24, or by application of selective 180°(^{13}CO) pulses at the midpoint of the evolution periods. Alternatively, ^{13}CO decoupling may be omitted all together, because t_{1max} and t_{3max} always are much less than $1/(2J_{C^\alpha CO})$ and$1/(2J_{NCO})$, respectively, and therefore evolution of these couplings do not greatly reduce sensitivity.

In a 4D experiment, every effort must be made to maximize the digital resolution, but at the same time keep the total acquisition time

within reasonable bounds. The minimum phase cycling requires two steps for each heteronuclear filter, therefore the four-step phase cycle given in Fig. 7.24 is used. The double heteronuclear filtering in this experiment is very efficient at removing artifacts, including the intense "diagonal peaks" corresponding to magnetization that has not been transferred from a ^{13}C-attached ^{1}H spin to an ^{15}N-attached ^{1}H spin during the NOESY mixing time.

The initial t_1, t_2, and t_3 sampling delays are adjusted to 1/(2SW) as described in Sections 3.3.2.3 and 7.1.2.1. Alternatively, the initial value of t_2 can be set to zero if a compensatory delay equal in duration to the 180°(^{13}C) composite pulse is inserted prior to the first 90°(^{13}C) pulse (*61*). In this case, the 180°(^{1}H) pulse in the middle of t_1 refocuses the evolution during the delay and the 180°(^{13}C) composite pulse.

Quadrature detection in the t_1, t_2, and t_3 dimensions is achieved by shifting the phases of ϕ_1, ϕ_2, and ϕ_3 independently in a TPPI–States manner. A typical acquisition comprises 8–16(t_1) × 64(t_2) × 8–16(t_3) × 128–256(t_4) complex data points. Processing of four-dimensional NMR experiments is discussed in Section 7.2.4.4.

Pulsed field gradients may be applied with particular advantage in the 4D ^{13}C/^{15}N HMQC–NOESY–HSQC experiment to suppress artifacts, eliminate the H_2O signal, and select for the coherence transfer pathway involving ^{15}N magnetization (*62*). Gradient coherence selection is coupled with the PEP sensitivity improvement technology discussed earlier (Section 7.1.4.2) to decrease the number of phase cycle steps by a factor of two relative to the nongradient experiment. The shorter phase cycle allows spectra to be recorded with increased resolution for a given total acquisition time.

7.2.4.3 4D ^{13}C/^{13}C HMQC–NOESY–HMQC The pulse sequence for the 4D ^{13}C/^{13}C HMQC–NOESY–HMQC experiment (*63*, *64*) illustrated in Fig. 7.25 consists of a NOESY mixing period between two ^{1}H–^{13}C HMQC sequences. The delays $2\tau = 1/(2^{1}J_{CH})$. Magnetization is transferred via the following pathway:

$$^{1}\mathrm{H}_i \xrightarrow{^{1}J_{CH}} \underset{(t_1)}{^{13}\mathrm{C}_i} \xrightarrow{^{1}J_{CH}} \underset{(t_2)}{^{1}\mathrm{H}_i} \xrightarrow{\mathrm{NOE}} {}^{1}\mathrm{H}_j \xrightarrow{^{1}J_{CH}} \underset{(t_3)}{^{13}\mathrm{C}_j} \xrightarrow{^{1}J_{CH}} \underset{(t_4)}{^{1}\mathrm{H}_j}. \qquad [7.80]$$

Suppression of undesired coherence transfer pathways is more difficult in the 4D ^{13}C/^{13}C HMQC–NOESY–HMQC experiment than in the in the ^{13}C/^{15}N HMQC–NOESY–HMQC experiment (*63*). In particular, artifact peaks observed along the pseudo-diagonal with $F_2(^{1}\mathrm{H}) = F_4(^{1}\mathrm{H})$ and $F_1(^{13}\mathrm{C}) \neq F_3(^{13}\mathrm{C})$ would otherwise render identification of genuine

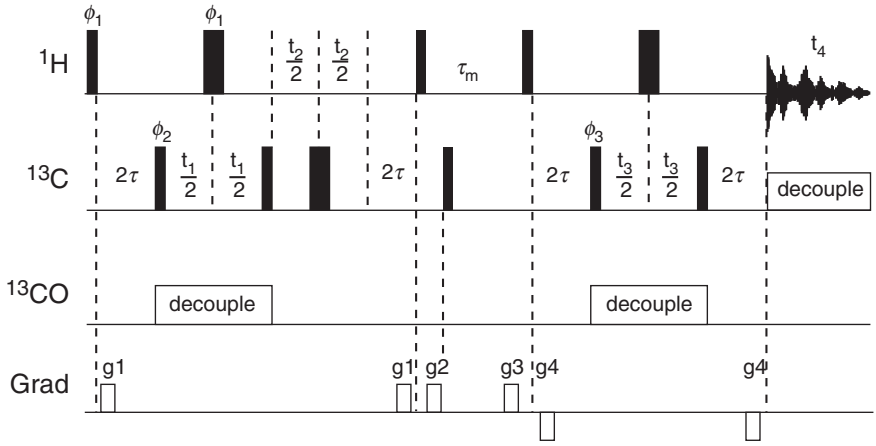

FIGURE 7.25 Pulse sequence for the 4D $^{13}C/^{13}C$ HMQC–NOESY–HMQC experiment. The 180°(^{13}C) decoupling pulse in the middle of the t_2 evolution period is applied as a broadband inversion composite pulse, such as $90^\circ_x 180^\circ_y 90^\circ_x$, in order to minimize resonance offset effects. Gradients are used for artifact suppression (Section 3.6). Other experimental details are similar to those given in Fig. 7.16. The phase cycling is $\phi_1 = x$; $\phi_2 = x, -x$; $\phi_3 = 2(x), 2(-x)$; receiver $= x, -x, -x, x$. Quadrature detection in the t_1, t_2, and t_3 dimensions is achieved by incrementing independently the phases ϕ_2, ϕ_1, and ϕ_3, respectively, and the receiver phase, in a TPPI, States, or TPPI–States manner.

NOEs between ^{1}H spins with degenerate chemical shifts extremely difficult, if not impossible, in the 4D $^{13}C/^{13}C$ HMQC–NOESY–HMQC experiment.

The pulse sequence shown in Fig. 7.25 incorporates field gradient pulses designed to eliminate spurious magnetization transfer pathways without requiring lengthy pulse phase cycles (*64*). The gradient pulses are used only for artifact suppression and are positioned within existing delays in the pulse sequence; consequently, sensitivity of the experiment is not compromised by the use of gradient pulses. The gradient g2 eliminates any transverse coherences present during τ_m and the 90°(^{13}C)–g3 sequence element eliminates any heteronuclear two-spin order ($2I_zS_z$). Unlike the 4D $^{13}C/^{15}N$ HMQC–NOESY–HSQC experiment (*62*), the PEP sensitivity improvement scheme (Section 7.1.3.2) does not compensate completely for the sensitivity loss associated with coherence selection by pulsed field gradients because, in addition to CH groups, CH_2 and CH_3 moieties must be detected (i.e., ^{13}C spins with $n > 1$ attached ^{1}H spins) (*30*).

The four steps of the phase cycle correspond to independent cycling of the 90°(^{13}C) pulses at the beginning of the HMQC periods, in a fashion identical to that of the ^{13}C/^{15}N HMQC–NOESY–HMQC experiment already discussed; phase cycling of these pulses provides isotope filtration and eliminates axial peaks in the F_1 and F_3 dimensions. The phase cycle can be shortened to two steps by eliminating phase cycling of the second 90°(^{13}C) pulse. In this case, no isotope filtering is used after the NOESY mixing period; therefore, axial peaks occur at the edges of the spectrum in the F_3 dimension.

The initial t_1, t_2, and t_3 sampling delays are adjusted to 1/(2SW) as described in Sections 3.3.2.3 and 7.1.2.1. Alternatively, the initial value of t_2 can be set to zero if a compensatory delay equal in duration to the 180°(^{13}C) pulse is inserted prior to the first 90°(^{13}C) pulse (*61*). In this case, the 180°(^{1}H) pulse in the middle of t_1 refocuses the evolution during the delay and the 180°(^{13}C) pulse. Quadrature detection in the t_1, t_2, and t_3 dimensions is achieved by shifting the phases of ϕ_1, ϕ_2, and ϕ_3 independently in a TPPI–States manner. A typical acquisition is limited to $16(t_1) \times 64(t_2) \times 16(t_3) \times 128\text{–}256(t_4)$ complex data points, resulting in an acquisition time of 3.5 days using the two-step phase cycle. Processing of four-dimensional NMR experiments is discussed in Section 7.2.4.4.

7.2.4.4 Processing 4D HMQC–NOESY–HMQC Spectra The acquired digital resolution in the indirectly detected dimensions of a 4D HMQC–NOESY–HMQC spectrum is necessarily low in order to keep the overall measuring time within reasonable limits (less than 7–8 days). In particular, the heteronuclear dimensions are limited to only 8–16 complex points (or slightly more if gradient-enhanced pulse sequences are used). Resolution enhancement of the severely truncated heteronuclear signals (t_1 and t_3) by either linear prediction or maximum entropy reconstruction (Section 3.3.4) is essential.

In maximum-entropy reconstruction, the time-domain data for the ^{1}H dimensions, t_2 and t_4, are completely processed first, including apodization, zero-filling, Fourier transformation, and phasing. The imaginary parts of F_2 and F_4 are discarded following these initial steps. The heteronuclear (t_1, t_3) planes [for each (t_2, t_4) pair] are processed by using a two-dimensional maximum-entropy algorithm to directly yield the final 4D spectrum (Section 3.3.4.2).

Analogously to maximum-entropy processing, a two-dimensional linear prediction algorithm ideally would be used to increase the resolution in the (t_1, t_3) planes (*65*). However, as pointed out by Zhu and Bax, 2D linear prediction requires enormous amounts of computing

TABLE 7.1
Summary of Steps Used in Processing 4D $^{13}C/^{15}N$ and $^{13}C/^{13}C$-Edited NOESY Data Sets[a]

Step	Computation performed
1	Fourier transform in t_3(^{13}C or ^{15}N) dimension
2	Apodization, zero-filling, Fourier transformation, and phasing in t_2(^{1}H) and t_4(^{1}H) dimensions
3	Linear prediction of t_1(^{13}C) time-domain data
4	Apodization, zero-filling, Fourier transformation, and phasing in t_1(^{13}C) dimension
5	Inverse Fourier transformation in t_3(^{13}C or ^{15}N) dimension
6	Linear prediction of t_3(^{13}C or ^{15}N) time-domain data
7	Apodization, zero-filling, Fourier transformation, and phasing in t_3(^{13}C or ^{15}N) dimension

[a]Adapted from Clore et al. (*63*).

time and is therefore (presently at least) impractical for 4D data sets. Instead, one-dimensional linear prediction routines are used to extend the time-domain data independently in both the t_1 and t_3 dimensions (*63*, *66*) by using the protocol presented in Table 7.1.

A data set containing $8(t_1) \times 64(t_2) \times 8(t_3) \times 128(t_4)$ complex data points typically is processed by the maximum-entropy reconstruction or linear prediction protocols to give a final spectrum comprising $32 \times 128 \times 32 \times 256$ real data points.

7.2.5 RELATIVE MERITS OF 3D AND 4D HETERONUCLEAR-EDITED NOESY SPECTROSCOPY

The number of cross-peaks observable in these 3D and 4D heteronuclear-edited NOESY spectra is the same as is present in the 2D homonuclear NOESY spectra. Each ^{1}H–^{1}H NOE cross-peak in a 2D NOESY spectrum is separated into a third dimension by the chemical shift of the heteronucleus attached to one ^{1}H spin and, for 4D spectroscopy, into a fourth dimension by the chemical shift of the heteronucleus directly attached to the other ^{1}H spin. Therefore, the increased resolution associated with the extension to three or four dimensions is not accompanied by any increase in the complexity of the spectrum (unlike homonuclear 3D NMR spectroscopy; Section 6.7). In addition, the sensitivity of the 3D and 4D NOESY experiments is relatively high, even

for larger proteins, because the through-bond coherence transfer steps are highly efficient (the heteronuclear couplings involved, $^1J_{CH}$ and $^1J_{NH}$, are significantly larger than the linewidths).

Generally, equivalent information can be obtained from a set of complementary three-dimensional NMR experiments or a single four-dimensional experiment. For example, the information content of the two 3D ^{1}H–^{15}N NOESY–HSQC and 3D ^{13}C/^{15}N HMQC–NOESY–HMQC experiments theoretically is equivalent to that of a single 4D ^{13}C/^{15}N-edited HMQC–NOESY–HMQC experiment. However, no direct correlation can made between the aliphatic ^{1}H and ^{13}C chemical shifts using the two 3D experiments, so the possibility of ambiguity remains, particularly as the two 3D experiments would be acquired at different times (with possible slight variations in conditions). On the other hand, the two three-dimensional NMR experiments can be acquired with much greater resolutions in the indirect dimensions than can the four-dimensional experiment, which facilitates more accurate determination of resonance frequencies. Assuming complete ^{1}H, ^{15}N, and ^{13}C assignments are available, the 4D ^{13}C/^{15}N-edited HMQC–NOESY–HMQC and 4D ^{13}C/^{13}C-edited HMQC–NOESY–HMQC experiments allow assignment of virtually all observable NOEs, because they eliminate most of the problems associated with resonance overlap.

7.3 ^{13}C–^{13}C Correlations: The HCCH–COSY and HCCH–TOCSY Experiments

The HCCH–COSY (*67–69*) (^{1}H–^{13}C–^{13}C–^{1}H correlation spectroscopy) and HCCH–TOCSY (*70*, *71*) (^{1}H–^{13}C–^{13}C–^{1}H total correlation spectroscopy) experiments are used in the assignment of aliphatic ^{1}H and ^{13}C resonances of ^{13}C-labeled proteins. These experiments allow dispersion of the 2D ^{1}H–^{1}H COSY or TOCSY spectra into a third (or fourth) ^{13}C frequency dimension by utilizing three magnetization transfer steps: first from an ^{1}H to its directly attached ^{13}C nucleus via the $^1J_{CH}$ coupling (~140 Hz), then from the ^{13}C to neighboring ^{13}C nuclei via the $^1J_{CC}$ couplings (32–40 Hz), and, finally, from ^{13}C back to the directly attached ^{1}H spins via the $^1J_{CH}$ coupling. For larger proteins the three-step magnetization transfer is significantly more efficient than is transferring ^{1}H magnetization in a single step using the unresolved ^{1}H–^{1}H J couplings. In the HCCH–COSY experiment, ^{13}C magnetization transfer is achieved by using a 90° ^{13}C COSY mixing pulse (in analogous fashion to the 90° ^{1}H COSY mixing pulse in the ^{1}H–^{1}H COSY

experiment discussed in Section 6.2.1.1), so that magnetization is transferred only from a ^{13}C nucleus to its directly bound neighbors; in the HCCH–TOCSY experiment, transfer is achieved by isotropic mixing of the ^{13}C spins, resulting in both direct and multiple-relayed magnetization transfers along the carbon side chain.

The amino acid spin system considered in the following sections consists of K (noncarbonyl) carbon spins, C^k for $k = 1, \ldots, K$, and a carbonyl spin, C'. Carbon spin C^1 has M directly bonded ^1H spins, H^1_m for $m = 1$ to M, and carbon spin C^k has N^k directly bonded ^1H spins, H^k_n for $n = 1$ to N^k. The ^1H and ^{13}C Larmor frequencies are Ω_{H^k} and Ω_{C^k}, respectively. The one-bond ^1H–^{13}C scalar coupling constants are designated as J_{CH}. The ^{13}C–^{13}C scalar coupling constants are designated as $J_{C^jC^k}$, and J_{C^kCO}; these interactions can be one bond or multiple bond, depending on the context. Homonuclear ^1H–^1H scalar coupling interactions are unresolved in larger proteins and are not considered explicitly. For simplicity, the ^{15}N–$^{13}C^\alpha$ scalar coupling Hamiltonian is not considered. If desired, ^{15}N decoupling can be achieved by applying a composite pulse decoupling sequence during ^{13}C evolution periods. The free-precession Hamiltonian for the C^1 spin is given by

$$\mathscr{H}_1 = \Omega_{C^1} C^1_z + \sum_{m=1}^{M} 2\pi J_{CH} H^1_{mz} C^1_z + \sum_{k=2}^{K} 2\pi J_{C^1C^k} C^1_z C^k_z + 2\pi J_{C^1CO} C^1_z C'_z. \quad [7.81]$$

A similar Hamiltonian can be written for any other C^k. The net evolution through the HCCH–COSY and HCCH–TOCSY experiments is summarized as

$$\sum_{m=1}^{M} H^1_m \xrightarrow[(t_1)]{^1J_{CH}} C^1 \xrightarrow[(t_2)]{^1J_{CC}} C^k \xrightarrow[(t_3)]{^1J_{CH}} \sum_{n=1}^{N^k} H^k_n. \quad [7.82]$$

Carbon nuclei C^1 and C^k ($k = 2$) are directly covalently bonded in the HCCH–COSY experiment (this restriction does not apply to the HCCH–TOCSY experiment). As a concrete example, if C^1 is the $^{13}C^\alpha$ spin, and C^2 is the $^{13}C^\beta$ spin of isoleucine, then $K = 5$, $M = 1$, $N_2 = 1$, C^3 is the $^{13}C^{\gamma 1}$ spin, C^4 is the $^{13}C^{\gamma 2}$ spin, C^5 is the $^{13}C^\delta$ spin, $J_{C^1C^2}$ is a one-bond scalar coupling constant, $J_{C^1C^k}$ for $k > 2$ are (negligible) two- or three-bond scalar coupling constants, $J_{C^2C^3}$ and $J_{C^2C^4}$ are one-bond scalar coupling constants, $J_{C^2C^5}$ is a (negligible) two-bond

scalar coupling constant, J_{C^1CO} is a one-bond scalar coupling constant, and J_{C^2CO} is a (negligible) two-bond scalar coupling constant.

7.3.1 HCCH–COSY

Figure 7.26a illustrates a simple HCCH–COSY pulse sequence (*67–69*). The basic principles behind this, and other, HCCH-type

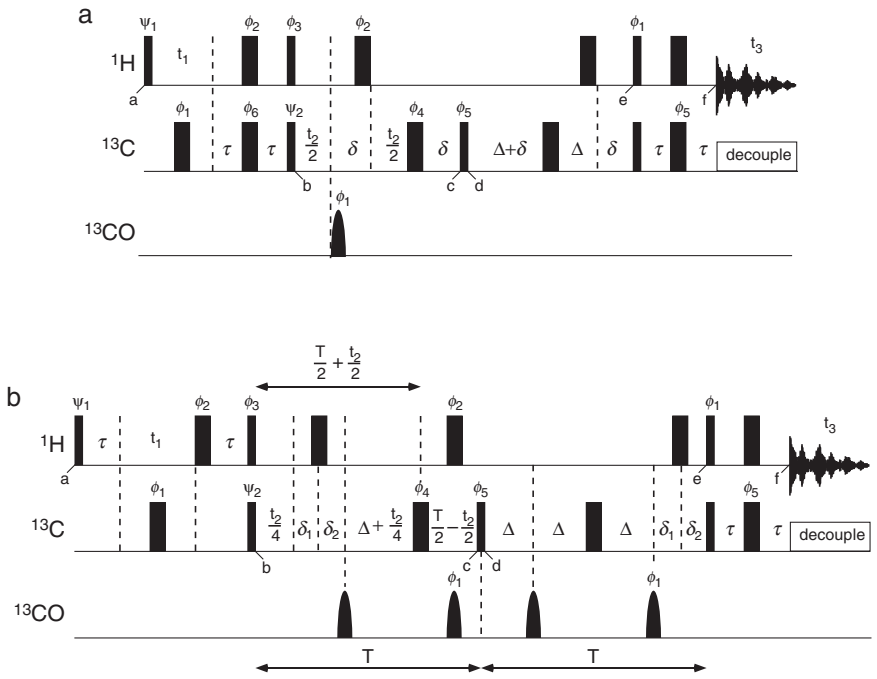

FIGURE 7.26 Pulse sequences for the 3D HCCH–COSY (a) and constant-time HCCH–COSY (b) experiments. Thin and thick rectangular bars represent 90° and 180° pulses, respectively. Rounded bars represent selective 180° pulses applied to ^{13}CO spins. Pulses are applied with x-phase unless the phase is indicated above the bar. Values for delays are discussed in the text. The phase cycling for both experiments is $\Psi_1 = x$; $\Psi_2 = x$; $\phi_1 = 8(x), 8(-x)$; $\phi_2 = 4(x), 4(y), 4(-x), 4(-y)$; $\phi_3 = y, -y$; $\phi_4 = 2(x), 2(y), 2(-x), 2(-y)$; $\phi_5 = 4(x), 4(-x)$; $\phi_6 = 2(x), 2(-x)$; and receiver $= x, -x, -x, x, 2(-x, x, x, -x), x, -x, -x, x$. Quadrature detection in the t_1 and t_2 dimensions is achieved by incrementing independently the phases Ψ_1 and Ψ_2, respectively, and the receiver phase, in a TPPI–States manner.

experiments are described here using the product operator formalism. Several shortcomings of this particular pulse sequence are alleviated in a constant-time version of the experiment (Fig. 7.26b).

The experiment begins at time a in Fig. 7.26a with longitudinal magnetization of the H^1_{mz} spins. At the end of the ^{1}H evolution period, t_1, this magnetization is transferred to the attached carbon via an INEPT sequence. The 180°(^{13}C) decoupling pulse in the middle of t_1 ensures that the ^{1}H spins effectively are decoupled from ^{13}C spins during this evolution period. A composite pulse (90°_x–180°_y–90°_x) is used to minimize resonance offset and rf inhomogeneity effects. For $2\tau = 1/(2J_{\mathrm{CH}})$ the magnetization at time b is given by

$$\sigma_b = \sum_{m=1}^{M} 2H^1_{mz}C^1_y \cos(\Omega_{H^1} t_1). \qquad [7.83]$$

Between points b and c, only the Hamiltonian for the C^1 spin need be considered because σ_b commutes with the Hamiltonian for spin C^2. The propagator for the pulse sequence is given by

$$\begin{aligned}\mathbf{U} &= \exp(-i\mathscr{H}_1\delta)\exp\left(-i\pi\sum_{k=1}^{K}C^k_x\right)\exp(-i\mathscr{H}_1 t_2/2)\exp\left(-i\pi\sum_{m=1}^{M}H^1_{mx}\right)\\ &\quad\times\exp(-i\mathscr{H}_1\delta)\exp\left(-i\pi C'_x\right)\exp(-i\mathscr{H}_1 t_2/2)\\ &= \exp\left(-i\sum_{m=1}^{M}4\pi J_{\mathrm{CH}}\delta H^1_{mz}C^k_z\right)\exp\left(-i\sum_{k=2}^{K}2\pi J_{C^1C^k}(2\delta+t_2)C^1_zC^k_z\right)\\ &\quad\times\exp(i\Omega_{C^1}t_2)\exp\left(-i\pi\sum_{k=1}^{K}C^k_x\right)\exp\left(-i\pi\sum_{m=1}^{M}H^1_{mx}\right)\exp\left(-i\pi C'_x\right),\end{aligned} \qquad [7.84]$$

in which the last line is obtained by applying [2.121]. The positioning of the ^{1}H and ^{13}C 180° pulses between points b and c results in proton decoupling during t_2. The $^{13}C^\alpha$ spins are decoupled from ^{13}CO spins during the entire $t_2+2\delta$ delay. The 180°(^{13}C) pulse refocuses chemical shift evolution during the two δ delays. The magnetization at time c is described by

$$\begin{aligned}\sigma_c = &\left\{-C^1_x\cos[\pi J_{C^1C^2}(t_2+2\delta)] - 2C^1_yC^2_z\sin[\pi J_{C^1C^2}(t_2+2\delta)]\right\}\\ &\times\cos(\Omega_{H^1}t_1)\cos(\Omega_{C^1}t_2)\Pi_1(t_2+2\delta)M\Gamma_M(2\delta),\end{aligned} \qquad [7.85]$$

in which $\Gamma_n(t)$ is given by [7.25] (for $J_{IS} = J_{CH}$), and

$$\Pi_j(t) = \prod_{k=3}^{K} \cos(\pi J_{C^j C^k} t) \qquad [7.86]$$

encapsulates the effect of passive ^{13}C–^{13}C couplings to spin C^j. Only terms that result in observable magnetization have been included in [7.86]. The 90°(^{13}C) pulse following time point c transfers the antiphase C^1 magnetization into antiphase C^2 magnetization in a COSY-like manner, giving, at time d,

$$\sigma_d = \left\{ -C_x^1 \cos[\pi J_{C^1C^2}(t_2 + 2\delta)] + 2C_z^1 C_y^2 \sin[\pi J_{C^1C^2}(t_2 + 2\delta)] \right\}$$
$$\times \cos(\Omega_{H^1} t_1) \cos(\Omega_{C^1} t_2) \Pi_1(t_2 + 2\delta) M \Gamma_M(2\delta). \qquad [7.87]$$

During the subsequent time interval, $2\Delta + 2\delta$, between points d and e, the propagator is

$$\mathbf{U} = \exp(-i[\mathscr{H}_1 + \mathscr{H}_2]\delta) \exp\left(-i\pi \sum_{m=1}^{M} H_{mx}^1 \right) \exp\left(-i\pi \sum_{n=1}^{N_2} H_{nx}^2 \right)$$
$$\times \exp(-i[\mathscr{H}_1 + \mathscr{H}_2]\Delta) \exp\left(-i\pi \sum_{k=1}^{K} C_x^k \right) \exp(-i[\mathscr{H}_1 + \mathscr{H}_2][\delta + \Delta])$$
$$= \exp\left(-i \sum_{m=1}^{M} 4\pi J_{\mathrm{CH}} \delta H_{mz}^1 C_z^1 \right) \exp\left(-i \sum_{n=1}^{N_2} 4\pi J_{\mathrm{CH}} \delta H_{nz}^2 C_z^2 \right)$$
$$\times \exp\left(-i \sum_{k=3}^{K} 4\pi J_{C^1C^k}(\delta + \Delta) C_z^1 C_z^k \right) \exp\left(-i \sum_{k=3}^{K} 4\pi J_{C^2C^k}(\delta + \Delta) C_z^2 C_z^k \right)$$
$$\times \exp\left(-i 4\pi J_{C^1C^2}(\delta + \Delta) C_z^1 C_z^2 \right)$$
$$\times \exp\left(-i\pi \sum_{k=1}^{K} C_x^k \right) \exp\left(-i\pi \sum_{m=1}^{M} H_{mx}^1 \right) \exp\left(-i\pi \sum_{n=1}^{N_2} H_{nx}^2 \right). \qquad [7.88]$$

The magnetization at time e is described by

$$\sigma_e = \left\{ -\sum_{m=1}^{M} 2H_{mz}^{1} C_y^1 \cos[\pi J_{C^1C^2}(t_2 + 2\delta)] \right.$$
$$\times \cos[2\pi J_{C^1C^2}(\delta + \Delta)]\Pi_1(2\delta + 2\Delta)\Gamma_M(2\delta)$$
$$- \sum_{n=1}^{N_2} 2H_{nz}^{2} C_y^2 \sin[\pi J_{C^1C^2}(t_2 + 2\delta)]$$
$$\left. \times \sin[2\pi J_{C^1C^2}(\delta + \Delta)]\Pi_2(2\delta + 2\Delta)\Gamma_{N_2}(2\delta) \right\}$$
$$\times \cos(\Omega_{H^1} t_1) \cos(\Omega_{C^1} t_2)\Pi_1(t_2 + 2\delta)M\Gamma_M(2\delta). \qquad [7.89]$$

The remainder of the experiment is a reverse INEPT sequence. At the start of the detection period, f, the magnetization is described by

$$\sigma_f = \left\{ \sum_{m=1}^{M} 2H_{mx}^{1} \cos[\pi J_{C^1C^2}(t_2 + 2\delta)] \right.$$
$$\times \cos[2\pi J_{C^1C^2}(\delta + \Delta)]\Pi_1(2\delta + 2\Delta)\Gamma_M(2\delta)$$
$$+ \sum_{n=1}^{N_2} 2H_{nx}^{2} \sin[\pi J_{C^1C^2}(t_2 + 2\delta)]$$
$$\left. \times \sin[2\pi J_{C^1C^2}(\delta + \Delta)]\Pi_2(2\delta + 2\Delta)\Gamma_{N_2}(2\delta) \right\}$$
$$\times \cos(\Omega_{H^1} t_1) \cos(\Omega_{C^1} t_2)\Pi_1(t_2 + 2\delta)M\Gamma_M(2\delta). \qquad [7.90]$$

For carbons with at least one passive coupling partner, ^{13}C–^{13}C coherence transfer is optimized by setting $2\Delta + 2\delta = 1/(4^1J_{CC})$. To maximize both $\Gamma_M(2\delta)$ and $\Gamma_{N_2}(2\delta)$ simultaneously for methine, methylene, and methyl carbons, $2\delta \approx 2.2$ ms (Fig. 7.7). The first term in [7.90] represents the autocorrelation or "diagonal peak" and the second term represents the cross-peak resulting from coherence transfer from the H_m^1 protons to the H_n^2 protons by the pathway [7.82].

The principal disadvantage to this pulse sequence is that the efficiency of ^{13}C–^{13}C magnetization transfer between J-coupled carbons depends on t_2 via $\sin[\pi J_{C^1C^2}(t_2 + 2\delta)]\Pi_1(t_2 + 2\delta)$. This has three consequences: (*i*) magnetization transfer is not maximal, (*ii*) the lineshape in the ^{13}C dimension (F_2) is not purely absorptive because the term $2\pi J_{C^1C^2}\delta \approx 0.24$ radians (14°) represents a phase shift, and (*iii*) the lineshape in F_2 is a multiplet with the active $J_{C^1C^2}$ coupling antiphase and passive $J_{C^2C^x}$

couplings in-phase. The antiphase, partially dispersive, character of the lineshape reduces sensitivity and resolution of the spectrum.

7.3.2 CONSTANT-TIME HCCH–COSY

The ^{13}C–^{13}C magnetization transfer can be optimized independently of t_2, and the multiplet structure in the F_2 dimension can be collapsed, by using the constant-time HCCH–COSY experiment shown in Fig. 7.26b (*69*). The same spin system is considered.

The modified ^{1}H evolution period and INEPT sequence between time points *a* and *b* in the constant-time HCCH–COSY pulse sequence reduce the number of 180°(^{13}C) pulses from two to one; reducing the number of 180°(^{13}C) pulses reduces artifacts from pulse imperfections (*72*). Ignoring artifacts and relaxation, the magnetization at time *b* is identical to the magnetization present at time *b* of the original HCCH–COSY experiment [7.83]. This modification also could be incorporated into the original pulse sequence (Fig. 7.26a).

Between points *b* and *c*, the propagator for the pulse sequence is given by

$$\begin{aligned}\mathbf{U} &= \exp(-i\mathscr{H}_1(T-t_2)/4)\exp\left(-i\pi\sum_{m=1}^{M}H_{mx}^{1}\right)\\ &\quad\times\exp\left(-i\pi C_x'\right)\exp(-i\mathscr{H}_1(T-t_2)/4)\\ &\quad\times\exp\left(-i\pi\sum_{k=1}^{K}C_x^k\right)\exp(-i\mathscr{H}_1(t_2/4+\Delta))\exp(-i\pi C_x')\exp(-i\mathscr{H}_1\delta_2)\\ &\quad\times\exp\left(-i\pi\sum_{m=1}^{M}H_{mx}^{1}\right)\exp(-i\mathscr{H}_1(t_2/4+\delta_1))\\ &= \exp\left(-i\sum_{m=1}^{M}4\pi J_{\mathrm{CH}}\delta_2 H_{mz}^{1}C_z^1\right)\exp\left(-i\sum_{k=2}^{K}2\pi J_{C^1C^k}TC_z^1C_z^k\right)\\ &\quad\times\exp(i\Omega_{C^1}t_2)\exp\left(-i\pi\sum_{k=1}^{K}C_x^k\right)\end{aligned} \qquad [7.91]$$

for $\Delta = T/4 = \delta_1 + \delta_2$ and $2\delta_2 = 2.2$ ms. Evolution due to ^{13}C–^{13}C scalar coupling interactions occurs during the entire constant-time evolution period, while C^1 chemical shift evolution proceeds during t_2 only. The selective 180°(CO) pulses remove the effects of one-bond ^{13}C–^{13}CO scalar coupling interaction (selective pulses also can be applied

simultaneously to the aromatic ^{13}C spins to remove the effects of scalar coupling between the $^{13}C^{\beta}$ and $^{13}C^{\gamma}$ spins of aromatic residues). The duration of the selective pulses must be minimized in order to maximize the attainable resolution, for a given value of T. The magnetization present at time c is described by

$$\sigma_c = \left\{ C_x^1 \cos(\pi J_{C^1C^2} T) + 2C_y^1 C_z^2 \sin(\pi J_{C^1C^2} T) \right\} \times \cos(\Omega_{H^1} t_1) \cos(\Omega_{C^1} t_2) \Pi_1(T) M \Gamma_M(2\delta_2). \quad [7.92]$$

Magnetization transfer through the remainder of the sequence is essentially the same as for the non-constant-time version of the experiment. At the start of the final acquisition period, f, the magnetization is described by

$$\sigma_f = \left\{ -\sum_{m=1}^{M} H_{mx}^1 \cos^2(\pi J_{C^1C^2} T) \Pi_1(T) \Gamma_M(2\delta_2) - \sum_{n=1}^{N_2} H_{nx}^2 \sin^2(\pi J_{C^1C^2} T) \Pi_2(T) \Gamma_N(2\delta_2) \right\} \times \cos(\Omega_{H^1} t_1) \cos(\Omega_{C^1} t_2) \Pi_1(T) M \Gamma_M(2\delta_2). \quad [7.93]$$

Magnetization transfer between scalar-coupled carbons is independent of t_2 and can be optimized by setting the duration of T. The maximum t_2 acquisition time, and therefore digital resolution, is limited to be less than T, while values of T significantly longer than $1/(4J_{CC})$ reduce sensitivity due to the passive carbon couplings. In practice, a value of $T \sim 7.8$ ms gives close to optimal transfer and sufficient digital resolution in the ^{13}C dimension (if the spectral width is chosen to give appropriate aliasing of resonances in this dimension; Section 7.1.2.3). At the same time, purely absorptive, singlet Lorenztian lineshapes are obtained in the F_2 dimension.

Figure 7.27 shows an example $F_1(^1H)$–$F_3(^1H)$ slice from a constant-time HCCH-COSY spectrum of ^{13}C-labeled ubiquitin. The F_2 spectral width is only ~32 ppm; therefore, aliasing has occurred and the displayed slice corresponds to two ^{13}C chemical shifts (30.2 and 62.3 ppm). Those resonances that have been aliased in the $F_2(^{13}C)$ dimension have phase opposite to the phase of those that have not been aliased.

7.3.3 HCCH–TOCSY

The HCCH–TOCSY experiment (*70*, *71*) is similar to the HCCH–COSY experiment, except that the 90°(^{13}C) mixing pulse is replaced

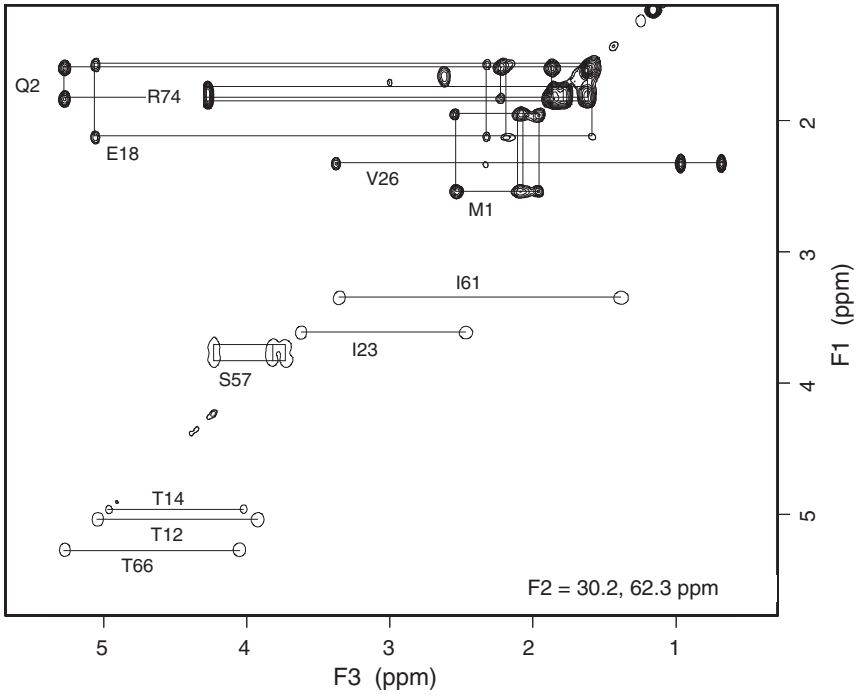

FIGURE 7.27 A selected $F_1(^1H)$–$F_3(^1H)$ slice from a constant-time HCCH–COSY spectrum of ^{13}C-labeled ubiquitin in D_2O solution, acquired using the pulse sequence illustrated in Fig. 7.26b. Negative cross-peaks, which correspond to resonances that have been aliased in the $F_2(^{13}C)$ dimension, are plotted with a single level only; these peaks have $F_2(^{13}C)$ chemical shifts of 62.3 ppm. The labels indicate the assignment in the $F_1(^1H)$ and $F_2(^{13}C)$ dimensions.

by an isotropic mixing scheme that results in both direct and relayed magnetization transfer along the carbon side chain. The HCCH–TOCSY pulse sequence illustrated in Fig. 7.28 combines features from the two HCCH–COSY pulse sequences (a and b, Fig. 7.26). A version of the HCCH–TOCSY experiment incorporating field gradient pulses for artifact and solvent suppression has been described (*73*).

Up to time *b*, the HCCH–TOCSY sequence is equivalent to that in Fig. 7.26b, and the magnetization present at time *b* is described by [7.83]. The following sequence, up to time *c*, is equivalent to that in Fig. 7.26a, and the relevant magnetization present at time *c* is given by [7.85]. The short (~2 ms) spin lock (SL) "trim-pulse" applied along the *x*-axis

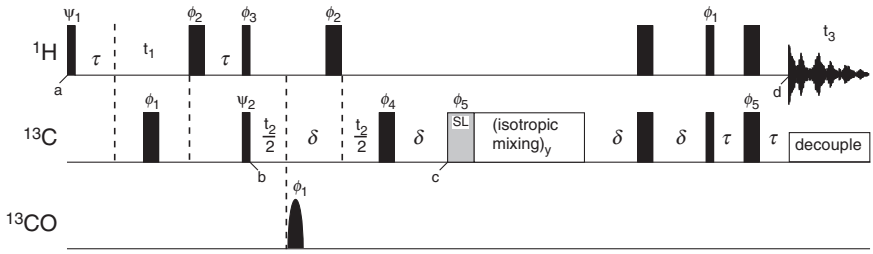

FIGURE 7.28 Pulse sequence for the HCCH–TOCSY experiment. Thin and thick rectangular bars represent 90° and 180° pulses, respectively. Rounded bars represent selective 180° pulses applied to ^{13}CO spins. Pulses are applied with x-phase unless the phase is indicated above the bar. Values for delays are discussed in the text. The phase cycling for this experiment is $\Psi_1 = x$; $\Psi_2 = x$; $\phi_1 = 8(x), 8(-x)$; $\phi_2 = 4(x), 4(y), 4(-x), 4(-y)$; $\phi_3 = y, -y$; $\phi_4 = 2(x), 2(y), 2(-x), 2(-y)$; $\phi_5 = 4(x), 4(-x)$; and receiver $= x, -x, -x, x, 2(-x, x, x, -x), x, -x, -x, x$. Quadrature detection in the t_1 and t_2 dimensions is achieved by incrementing independently the phases Ψ_1 and Ψ_2, respectively, and the receiver phase, in a TPPI–States manner.

following time c defocuses the $2C_y^1C_z^k$ antiphase coherence that is not parallel to the effective field. The subsequent isotropic mixing sequence (Section 4.2.1.2) transfers the in-phase C_x^1 magnetization to its neighbors within the carbon spin system, via the ^{13}C–^{13}C scalar coupling interactions. The remainder of the experiment comprises a refocused reverse INEPT sequence that transfers the in-phase ^{13}C magnetization back to the attached protons for detection. The final magnetization prior to acquisition is given by

$$\sigma_d = \left\{ \sum_{m=1}^{M} H_{mx}^1 \Pi_1(2\delta) \Gamma_M(2\delta) a_{11}(\tau_m) + \sum_{k=2}^{K} \sum_{n=1}^{N} H_{nx}^k \Pi_2(2\delta) \Gamma_N(2\delta) a_{1k}(\tau_m) \right\}$$
$$\times \cos(\Omega_{H^1} t_1) \cos(\Omega_{C^1} t_2) \cos[\pi J_{C^1C^2}(t_2 + 2\delta)] \cos(2\pi J_{C^1C^2}\delta)$$
$$\times \Pi_1(t_2 + 2\delta) M \Gamma_M(2\delta), \qquad [7.94]$$

in which $a_{11}(\tau_m)$ and $a_{1k}(\tau_m)$ are the isotropic mixing coefficients and τ_m is the mixing time.

An efficient broadband isotropic mixing scheme, such as DIPSI or FLOPSY sequences (*74–77*), must be used for the HCCH–TOCSY

experiment, because the ^{13}C chemical shifts are dispersed over a wide frequency range; use of FLOPSY requires addition of a *z*-filter to the pulse sequence (*78*). The rate of coherence transfer from one carbon to its neighbor depends on the magnitude of the effective scalar coupling during the mixing time. For coupled ^{13}C spins with significantly different chemical shifts (e.g., Thr $^{13}C_\beta$ and $^{13}C_\gamma$; Ala $^{13}C_\alpha$ and $^{13}C_\beta$), the magnitude of the effective coupling can be reduced substantially and the rate of ^{13}C magnetization transfer during the isotropic mixing period is reduced correspondingly.

To determine the optimum ^{13}C isotropic mixing time to be used in an HCCH–TOCSY experiment, rates of the carbon–carbon magnetization transfer must be known for the amino acid spin systems of interest. Calculations for the DIPSI-3 sequence (*71*, *79*) indicate that an isotropic mixing time of 20–35 ms is optimal for the observation of ^{13}C relayed connectivities. Figure 7.29 shows the calculated net

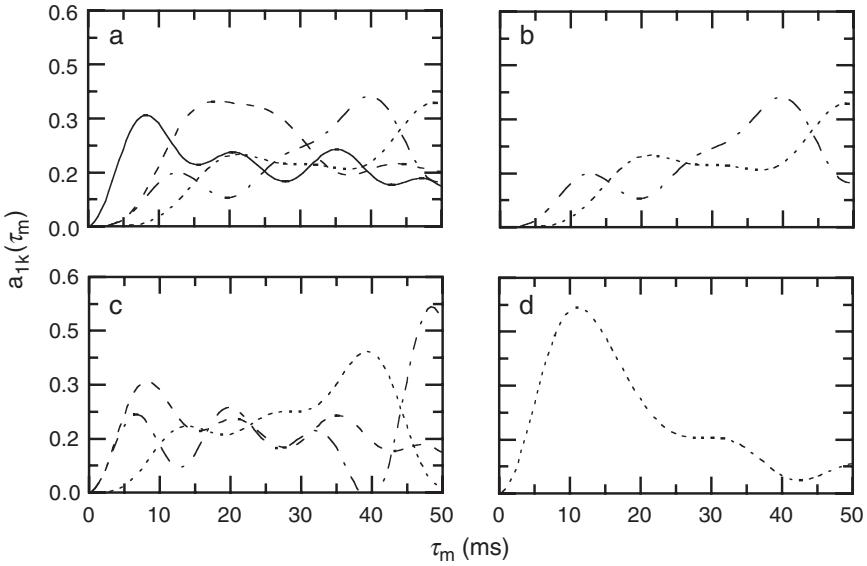

FIGURE 7.29 Isotropic mixing for ^{13}C spins in isoleucine. Transfer functions for ideal isotropic mixing under the strong coupling Hamiltonian are shown for magnetization transfer for magnetization originating on the (a) $^{13}C^\alpha$, (b) $^{13}C^\beta$, (c) $^{13}C^{\gamma 2}$, and (d) $^{13}C^{\gamma 1}$ spins. The curves for the destination spins are (—) C^β, (- - -) $C^{\gamma 2}$, (- · -) $C^{\gamma 1}$, and (· · · ·) C^δ. The one-bond scalar coupling constants were assumed to be 35 Hz. Relaxation and resonance offset effects have been neglected.

intraresidue ^{13}C–^{13}C magnetization transfer for an isoleucine amino acid spin system as a function of the mixing time during an ideal isotropic sequence.

Selected regions from an HCCH–TOCSY spectrum of ^{13}C-labeled ubiquitin, illustrating the assignment of the side chain resonances of Ile23, are shown in Fig. 7.30. Cross-peaks corresponding to $^{13}C^{\alpha}$, $^{13}C^{\gamma 2}$, and $^{13}C^{\delta}$ in the F_2 dimension have been aliased, and have phase opposite to the cross-peaks corresponding to $^{13}C^{\beta}$ and $^{13}C^{\gamma 1}$. The low intensity of the $^{1}H^{\alpha}$–$^{1}H^{\gamma 1}$ and $^{1}H^{\gamma 2}$–$^{1}H^{\gamma 1}$ correlations in this 22.5-ms mixing time HCCH–TOCSY spectrum is to be expected from Fig. 7.29.

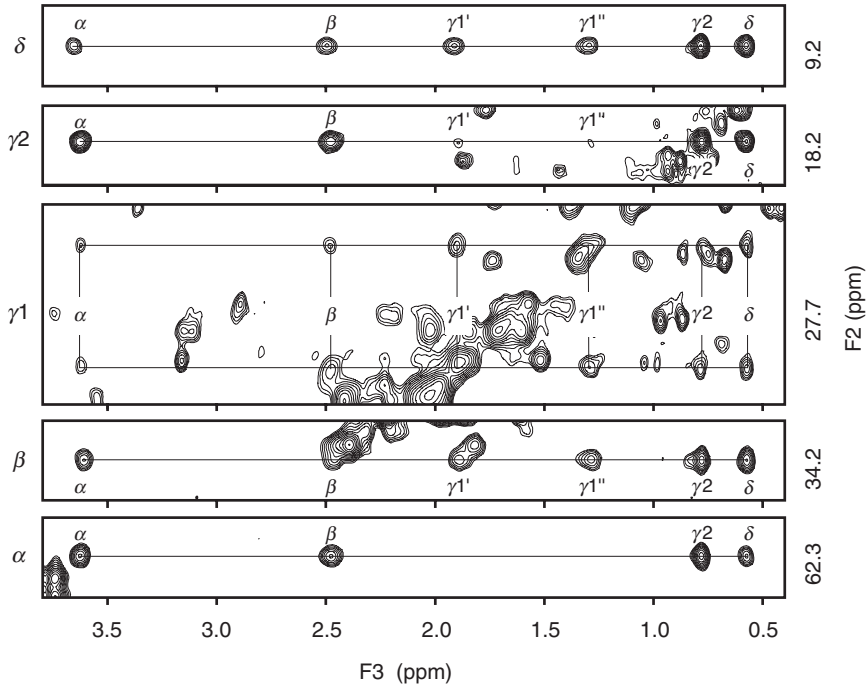

FIGURE 7.30 Selected regions from $F_2(^{13}C)$ slices of a 22.5-ms mixing-time 3D HCCH–TOCSY spectrum of ^{13}C-labeled ubiquitin, showing correlations originating from the $^{1}H^{\alpha}$, $^{1}H^{\beta}$, $^{1}H^{\gamma 1}$, $^{1}H^{\gamma 2}$, and $^{1}H^{\delta}$ of Ile23. Isotropic mixing was achieved using a DIPSI-2 sequence with a 7.7-kHz rf field strength.

7.4 3D Triple-Resonance Experiments

Three- and four-dimensional heteronuclear triple-resonance experiments correlate backbone $^{1}H^{N}$, ^{15}N, $^{1}H^{\alpha}$, $^{13}C^{\alpha}$, and ^{13}CO (and side chain $^{1}H^{\beta}$ and $^{13}C^{\beta}$) spins using one-bond and two-bond scalar coupling interactions. These experiments constitute an alternative to the classical sequential resonance assignment strategy based on observation of characteristic short-range NOEs (Chapter 10). A large number of triple-resonance pulse schemes (*7*) have been published since the original description of this approach in application to calmodulin (16.7 kDa), by Bax and co-workers in 1990 (*80*, *81*). Using these methods, assignments of $^{13}C/^{15}N$-labeled proteins up to ~30 kDa can be achieved routinely. Using extensions of these techniques for $^{2}H/^{13}C/^{15}N$-labeled proteins (Section 9.1), backbone, $^{13}C^{\beta}$, and side chain methyl (Ile, Leu, Val) assignments have been achieved for malate synthase G (81.4 kDa) (*82*, *83*).

The nomenclature established for triple-resonance experiments is more or less systematic. The spins that are frequency labeled during the indirect evolution periods or the acquisition period are listed using HN, N, HA, CA, CO, HB, and CB to represent the $^{1}H^{N}$, ^{15}N, $^{1}H^{\alpha}$, $^{13}C^{\alpha}$, ^{13}CO, $^{1}H^{\beta}$, and $^{13}C^{\beta}$ spins. Spins through which coherence is transferred, but not frequency labeled, are given in parentheses. For example, a triple-resonance experiment utilizing the following coherence transfers,

$$\underset{}{^{1}H^{N}} \rightarrow \underset{(t_1)}{^{15}N} \rightarrow {}^{13}CO \rightarrow \underset{(t_2)}{^{13}C^{\alpha}} \rightarrow {}^{13}CO \rightarrow {}^{15}N \rightarrow \underset{(t_3)}{^{1}H^{N}}, \qquad [7.95]$$

might be called an (HN)N(CO)CA(CO)(N)HN experiment. However, this unwieldy moniker can be shortened using the following conventions. First, the experiment is a so-called out-and-back pulse sequence in which the initially excited proton spin and the detected proton spin are identical. Omitting the back-transfer steps from the name yields the shorter form, HNN(CO)CA, without introducing ambiguity, because the $^{13}C^{\alpha}$ usually is not the detected spin and the presence of a back-transfer pathway to the $^{1}H^{N}$ spin thereby is implied. Second, the designation of the $^{1}H^{N}$ spin is redundant, because the transfer from $^{1}H^{N} \leftrightarrow {}^{15}N$ is the only available step. Thus, $^{1}H^{N}$ can be abbreviated as H without confusion to yield the final name HN(CO)CA for this experiment. This abbreviated name describes equally well an experiment

that rearranges the labeling periods as

$$^{1}H^{N} \rightarrow {}^{15}N \rightarrow {}^{13}CO \rightarrow {}^{13}C^{\alpha} \rightarrow {}^{13}CO \rightarrow {}^{15}N \rightarrow {}^{1}H^{N}. \qquad [7.96]$$
$$(t_1) \qquad (t_2) \quad (t_3)$$

The order in which the frequency labeling is performed is easily determined from the pulse sequence. A four-dimensional version of this experiment that includes a CO evolution period would be designated HNCOCA.

Table 7.2 summarizes the correlations that are observed, and the scalar couplings utilized for coherence transfer, in several useful triple-resonance experiments. These experiments offer alternative ways of establishing sequential backbone connectivities, and at least two and often more independent pathways can be found to support a given sequential assignment, without any knowledge of the spin system type. Knowledge of some of the spin systems involved is required to "align" the assignments with the protein amino acid sequence; this information is obtained from the HCCH–COSY and HCCH–TOCSY experiments (Section 7.3), from an ^{1}H–^{15}N TOCSY–HSQC experiment (Section 7.2.2), or from knowledge of $^{13}C^{\alpha}$ and $^{13}C^{\beta}$ chemical shifts. Assignment strategies using triple resonance experiments are summarized in Chapter 10.

The experiments listed in Table 7.2 are discussed in more detail herein to demonstrate the basic principles of triple-resonance NMR spectroscopy. The set of experiments presented is certainly not complete, and new and improved triple-resonance pulse sequences, based on the principles described herein, continue to be published. In the following discussion, the nuclear spins of the ith amino acid residue are designated H_i^N for the amide ^{1}H spin, N_i for the amide ^{15}N spin, H_i^{κ} and C_i^{κ} for aliphatic ^{1}H and ^{13}C spins ($\kappa = \alpha$, β, etc.), and C_i' for the carbonyl ^{13}C spin. One-bond scalar coupling constants are designated J_{CH}, J_{NH}, $J_{C^{\kappa}C^{\eta}}$ (κ, $\eta = \alpha$, β, γ, etc.), $J_{C^{\alpha}CO}$, and J_{NCO} (interresidue ^{15}N–^{13}CO scalar coupling). Intraresidue and interresidue $^{13}C^{\alpha}$–^{15}N scalar coupling constants are designated $^{1}J_{C^{\alpha}N}$ and $^{2}J_{C^{\alpha}N}$, respectively. Aspects of data acquisition and processing common to all triple-resonance NMR experiments are discussed in Section 7.4.6.

7.4.1 A PROTOTYPE TRIPLE-RESONANCE EXPERIMENT: HNCA

The HNCA experiment correlates the amide $^{1}H^{N}$ and ^{15}N chemical shifts with the intraresidue $^{13}C^{\alpha}$ shift, by making use of the relatively small one-bond ^{15}N–$^{13}C^{\alpha}$ scalar coupling (7–11 Hz) to establish

Table 7.2
Triple-Resonance Experiments Used for Sequential Resonance Assignment[a]

Experiment	Correlations observed	Magnetization transfer	J couplings[b]	Ref.
HNCA	$^{1}H_i^N - {}^{15}N_i - {}^{13}C_i^{\alpha}$ $^{1}H_i^N - {}^{15}N_i - {}^{13}C_{i-1}^{\alpha}$	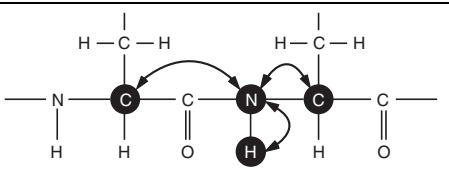	$^{1}J_{NH}$ $^{1}J_{NC^{\alpha}}$ $^{2}J_{NC^{\alpha}}$	*81*, *84*, *86*
HN(CO)CA	$^{1}H_i^N - {}^{15}N_i - {}^{13}C_{i-1}^{\alpha}$	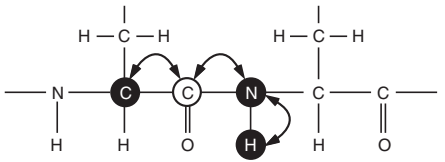	$^{1}J_{NH}$ $^{1}J_{NCO}$ $^{1}J_{C^{\alpha}CO}$	*84*, *89*
H(CA)NH	$^{1}H_i^{\alpha} - {}^{15}N_i - {}^{1}H_i^N$ $^{1}H_i^{\alpha} - {}^{15}N_{i+1} - {}^{1}H_{i+1}^N$	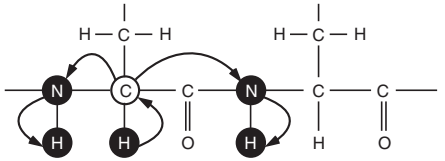	$^{1}J_{C^{\alpha}H^{\alpha}}$ $^{1}J_{NC^{\alpha}}$ $^{2}J_{NC^{\alpha}}$ $^{1}J_{NH}$	*72*

(*continued*)

TABLE 7.2
continued

Experiment	Correlations observed	Magnetizatio	lings[b]	Ref.
HNCO	$^{1}H_{i}^{N} - {}^{15}N_{i} - {}^{13}CO_{i-1}$	— —		

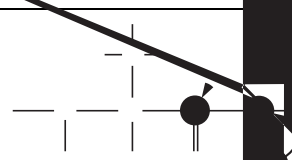

CBCANH	$^{13}C_i^{\beta}/^{13}C_i^{\alpha} - {}^{15}N_i - {}^{1}H_i^{N}$ $^{13}C_i^{\beta}/^{13}C_i^{\alpha} - {}^{15}N_{i+1} - {}^{1}H_{i+1}^{N}$	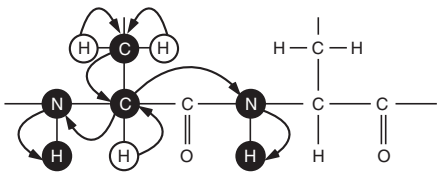	$^{1}J_{CH}$ $^{1}J_{C^{\alpha}C^{\beta}}$ $^{1}J_{NC^{\alpha}}$ $^{2}J_{NC^{\alpha}}$ $^{1}J_{NH}$	*98*
HNCACB	$^{13}C_i^{\beta}/^{13}C_i^{\alpha} - {}^{15}N_i - {}^{1}H_i^{N}$ $^{13}C_{i-1}^{\beta}/^{13}C_{i-1}^{\alpha} - {}^{15}N_i - {}^{1}H_i^{N}$	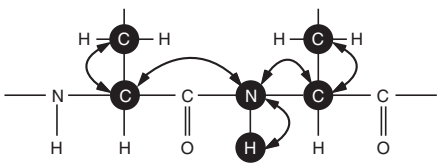	$^{1}J_{C^{\alpha}C^{\beta}}$ $^{1}J_{NC^{\alpha}}$ $^{2}J_{NC^{\alpha}}$ $^{1}J_{NH}$	*105*

[a]Only the experiments analyzed in the text are listed. A more extensive tabulation of triple-resonance (and other) NMR experiments is presented elsewhere (*7, 157*).
[b]$^{1}J_{NH} \sim 91$ Hz, $^{1}J_{NC^{\alpha}} \sim 7$–11 Hz, $^{2}J_{NC^{\alpha}} \sim 4$–9 Hz, $^{1}J_{NCO} \sim 15$ Hz, $^{1}J_{C^{\alpha}CO} \sim 55$ Hz, $^{1}J_{CH}$ ($^{1}J_{C^{\alpha}H^{\alpha}}$,$^{1}J_{C^{\beta}H^{\beta}}$) ~ 140 Hz, $^{1}J_{C^{\alpha}C^{\beta}} \sim 35$ Hz.

correlations between the ^{15}N and $^{13}C^{\alpha}$ spins (*81*, *84*). In addition, this experiment also provides sequential connectivities by transferring coherence from the ^{15}N spins to the $^{13}C^{\alpha}$ of the preceding residue via the interresidue two-bond ^{15}N–$^{13}C^{\alpha}$ scalar coupling, which can be as large as 9 Hz. The HNCA experiment utilizes "out-and-back" coherence transfer, in which the $^{1}H^{N}$ magnetization excited initially in the pulse sequence also is detected during t_3. A simple HNCA pulse sequence (*81*) is illustrated in Fig. 7.31a. Analysis of this pulse sequence using the product operator formalism reveals the basic principles of triple-resonance NMR spectroscopy. Figure 7.31 also includes more sophisticated versions of the same experiment that overcome several shortcomings of the original. The more advanced pulse sequences utilize many of the concepts introduced elsewhere in this text and serve to illustrate the iterative process by which NMR experiments are refined.

7.4.1.1 A Simple HNCA Experiment The design of the HNCA pulse sequence shown in Fig. 7.31a is particularly straightforward and evolution through the sequence can be evaluated by inspection. Magnetization originating on amide $^{1}H^{N}$ spins is transferred to the directly attached ^{15}N spins via an INEPT sequence. For $2\tau = 1/(2J_{NH})$, the resulting antiphase ^{15}N magnetization at time *a* in Fig. 7.31a is represented by

$$\sigma_a = -2H_{iz}^{N}N_{iy}. \qquad [7.97]$$

The ^{15}N chemical shift evolution proceeds during the subsequent t_1 evolution period. Evolution due to scalar coupling interactions between the ^{15}N spin and $^{1}H^{N}$, $^{13}C^{\alpha}$, and ^{13}CO spins is eliminated by 180° refocusing pulses applied in the middle of the t_1 period. The magnetization present at time *b* is described by

$$\sigma_b = -2H_{iz}^{N}N_{iy}\cos(\Omega_{N_i}t_1). \qquad [7.98]$$

Omitting the 180°(^{13}CO) pulse from the experiment introduces an additional $\cos(\pi J_{NCO}t_1)$ factor in [7.98]; fortunately, this does not greatly attenuate the signal because the maximum acquisition time in the ^{15}N dimension (t_{1max}) is typically chosen to be less than $1/(2J_{NCO})$. Indeed, the original description of this experiment did not include ^{13}CO decoupling in t_1 (*81*).

Following t_1 evolution, the ^{15}N magnetization becomes antiphase with respect to the coupled $^{13}C^{\alpha}$ spins during the delay δ. Evolution due to ^{1}H–^{15}N couplings also proceeds during this delay; therefore,

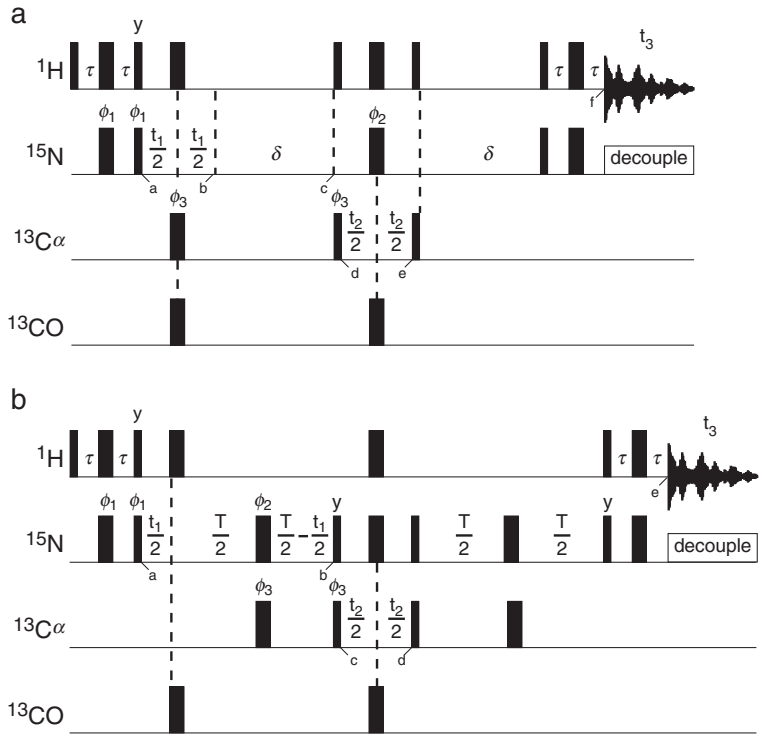

FIGURE 7.31 Pulse sequences for the HNCA experiment. Thin and thick rectangular bars represent 90° and 180° pulses, respectively. Pulses are applied with x-phase unless the phase is indicated above the bar. Short, wide rectangles are selective soft pulses applied at the frequency of the water resonance. Field gradient pulses shown as open bars are used for artifact and water suppression; field gradient pulses shown as filled bars are used for coherence selection. Values for delays are discussed in the text. (a) A non-constant-time HNCA experiment, with phase cycling $\phi_1 = x, -x$; $\phi_2 = 4(x), 4(y), 4(-x), 4(-y)$; $\phi_3 = 2(x), 2(-x)$; and receiver $= x, -x, -x, x, -x, x, x, -x$. (b) A constant-time HNCA experiment with phase cycling $\phi_1 = x, -x$; $\phi_2 = 4(x), 4(y), 4(-x), 4(-y)$; $\phi_3 = 2(x), 2(-x)$; and receiver $= x, -x, -x, x, -x, x, x, -x$. (c) An ^{1}H-decoupled constant-time HNCA experiment with phase cycling $\phi_1 = x, -x$; $\phi_2 = 4(x), 4(y), 4(-x), 4(-y)$; $\phi_3 = 2(x), 2(-x)$; and receiver $= x, -x, -x, x, -x, x, x, -x$. In sequences a–c, quadrature detection in the t_1 and t_2 dimensions is achieved by incrementing independently the phases ϕ_1 and ϕ_3, respectively, and the receiver phase, in a TPPI–States manner. (d) A PFG-PEP-HNCA experiment with phase cycling $\phi_1 = x, -x$; $\phi_2 = 2(x), 2(-x)$; $\phi_3 = 4(x), 4(-x)$; $\phi_4 = x$ plus the correction for off-resonance phase shift caused by the 180°(^{13}CO) pulse during t_2; $\phi_5 = x$; and receiver $= x, -x, -x, x$ for the first FID acquired. The phase $\phi_5 = -x$ and the gradient g2 is inverted for the second FID. The 90° pulses flanking decoupling periods are applied with the same field strength as the decoupling sequence. The delay δ_2 is longer than g5. The data are acquired and processed as described for the PFG-PEP-HSQC experiment (Section 7.1.4.2).

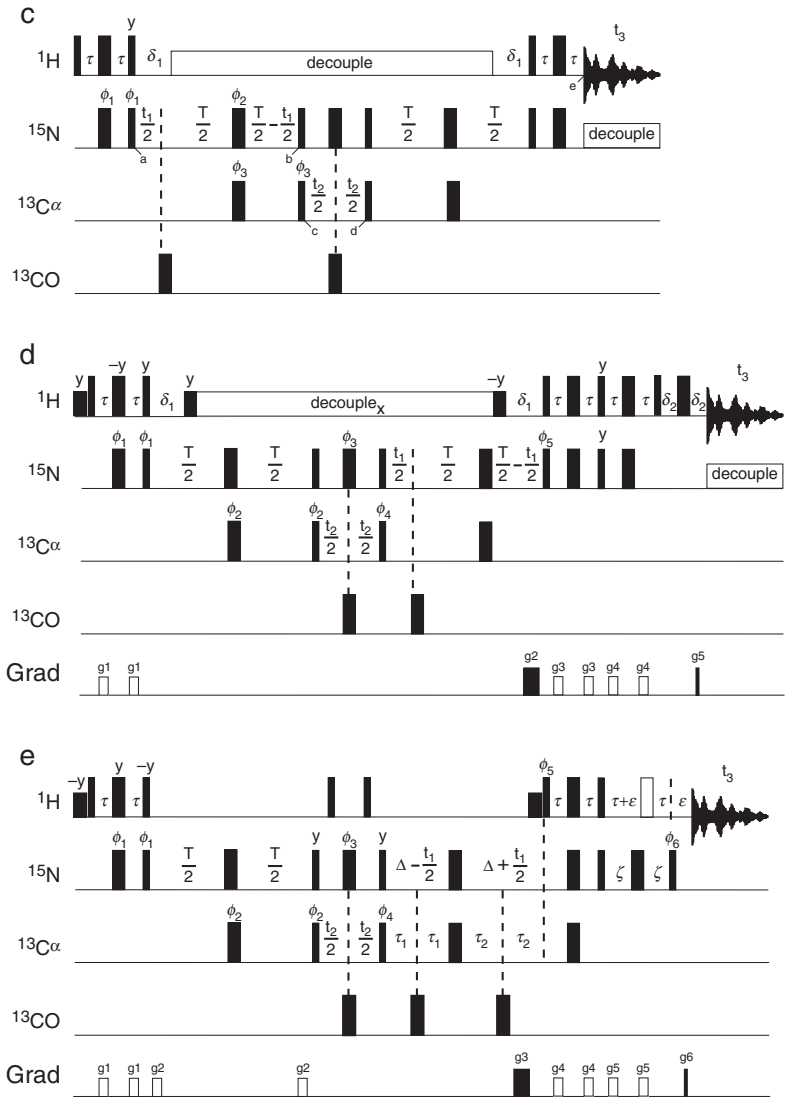

FIGURE 7.31—*Continued*
(e) A PFG-TROSY-HNCA experiment with phase cycling $\phi_1 = x, -x$; $\phi_2 = 2(x)$, $2(-x)$; $\phi_3 = 4(x)$, $4(-x)$; $\phi_5 = y$; $\phi_6 = -y$; and receiver $= x, -x, -x, x$ for the first FID acquired. The second FID is acquired with $\phi_1 = x, -x$; $\phi_5 = y$; $\phi_6 = -y$; and receiver $= x, -x$. The gradient g3 also is inverted for the second FID. Depending on the spectrometer, y and $-y$ phases may need to be interchanged. The 180° pulse represented as an open bar leaves the water magnetization unperturbed; 3–9–19, or soft–hard–soft, pulse schemes commonly used for this pulse are described in Section 3.7. The delays $\Delta = T/2 - \tau$, ε is longer than g6, and $\zeta = \tau + \varepsilon/2$. The data are acquired and processed as described for the PFG-TROSY experiment (Section 7.1.4.2).

the duration of δ is restricted to be an integral multiple of $1/J_{NH}$, so that the ^{15}N magnetization is antiphase with respect to its coupled proton at the end of the delay. Scalar coupling evolution involving the ^{13}CO spins is refocused by the 180°(^{13}CO) pulse in the middle of the t_2 evolution period. Ignoring evolution of the ^{13}CO scalar coupling interactions, the relevant components of the density operator present at time c are given by

$$\sigma_c = \left\{4H_{iz}^N N_{ix} C_{iz}^\alpha \Gamma_1(\delta) + 4H_{iz}^N N_{ix} C_{(i-1)z}^\alpha \Gamma_2(\delta)\right\} \cos(\Omega_{N_i} t_1) \cos(\pi J_{NH}\delta), \quad [7.99]$$

in which $\Gamma_1(t)$ and $\Gamma_2(t)$ are coherence transfer functions for intra- and interresidue scalar connectivities between the ^{15}N and $^{13}C^\alpha$ spins, respectively:

$$\begin{aligned} \Gamma_1(t) &= \sin(\pi^1 J_{C^\alpha N} t) \cos(\pi^2 J_{C^\alpha N} t), \\ \Gamma_2(t) &= \cos(\pi^1 J_{C^\alpha N} t) \sin(\pi^2 J_{C^\alpha N} t). \end{aligned} \quad [7.100]$$

As shown in Fig. 7.32, these functions have two relatively broad maxima centered around 28 and 35 ms for α-helical and β-sheet structures, respectively (*85*). As shown in Fig. 7.33, the total amplitudes of the operators in [7.99], $\Gamma_1(\delta)\cos(\pi J_{NH}\delta)$ and $\Gamma_2(\delta)\cos(\pi J_{NH}\delta)$, have maxima for δ equal to ~22 ms and ~33 ms. The positions of these maxima correspond to $2/J_{NH}$ and $3/J_{NH}$, respectively, and are not significantly affected by the small variations of the $^{13}C^\alpha$–^{15}N coupling constants with local secondary structure. In order to minimize relaxation losses, the value of δ is set to ~22 ms, for which $\cos(\pi J_{NH}\delta) \approx 1$.

The 90° pulses applied to both ^1H and $^{13}C^\alpha$ spins immediately following point c create multiple-quantum three-spin $^1H^N$–^{15}N–$^{13}C^\alpha$ coherence represented by

$$\sigma_d = \left\{4H_{iy}^N N_{ix} C_{iy}^\alpha \Gamma_1(\delta) + 4H_{iy}^N N_{ix} C_{(i-1)y}^\alpha \Gamma_2(\delta)\right\} \cos(\Omega_{N_i} t_1) \cos(\pi J_{NH}\delta). \quad [7.101]$$

During the subsequent t_2 evolution period, both ^1H and ^{15}N chemical shifts are refocused by the 180° pulses applied to these spins; effectively, the three-spin coherence evolution depends only on the $^{13}C^\alpha$ chemical shift. The three-spin coherence does not evolve under the influence of the active scalar couplings between the spins (Section 2.7.5). Application of the 180°(^{13}CO) pulse at the midpoint of the t_2 evolution period, however, ensures that evolution due to ^{13}CO scalar coupling is refocused; the

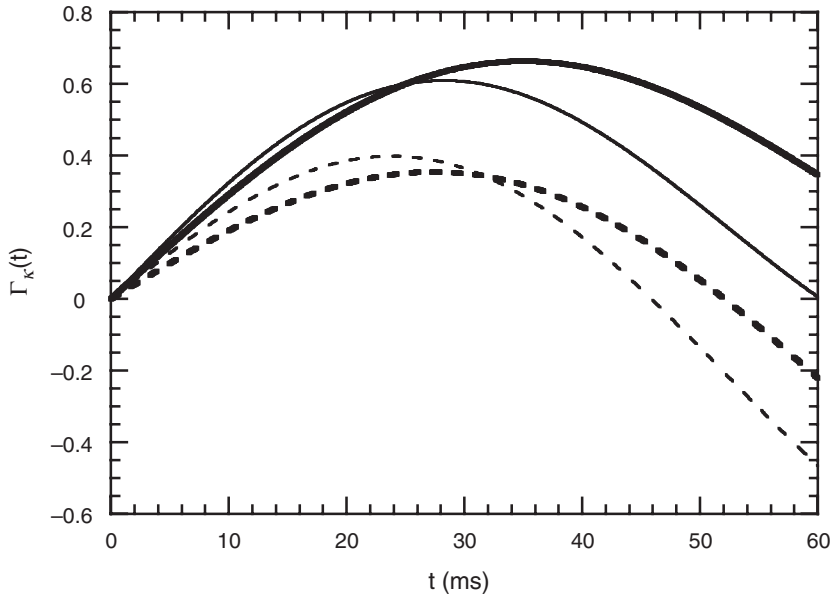

FIGURE 7.32 Plots of the HNCA coherence transfer functions, $\Gamma_k(t)$, for (—) $k=1$ or (- - -) $k=2$ [7.100]. Thin and thick lines represent the results for α-helical and β-sheet conformations, respectively. Nominal values of $^1J_{C^\alpha N}$ and $^2J_{C^\alpha N}$ for an α-helical conformation are assumed to be 9.6 and 6.4 Hz, respectively, and in a β-sheet conformation are assumed to be 10.9 and 8.3 Hz, respectively (*85*).

small F_2 phase errors resulting from the off-resonance effects of the 180°(^{13}CO) pulse are readily corrected when processing the data (Section 3.4.1). The scalar coupling interactions between $^{13}C^\alpha$ and $^{13}C^\beta$ spins do, however, remain active during the t_2 evolution period. At the end of the t_2 period, e, the magnetization is described by

$$\sigma_e = \left\{4H_{iy}^N N_{ix} C_{iy}^\alpha \cos(\Omega_{C_i^\alpha} t_2)\Gamma_1(\delta) + 4H_{iy}^N N_{ix} C_{(i-1)y}^\alpha \cos(\Omega_{C_{i-1}^\alpha} t_2)\Gamma_2(\delta)\right\} \times \cos(\Omega_{N_i} t_1) \cos(\pi J_{C^\alpha C^\beta} t_2) \cos(\pi J_{NH}\delta). \quad [7.102]$$

Alternatively, the antiphase ^{15}N magnetization present at time c can be transferred into antiphase $^{13}C^\alpha$ magnetization by application of 90° pulses to the ^{15}N and $^{13}C^\alpha$ spins, rather than to the ^{1}H and $^{13}C^\alpha$ spins as described. This alternative method, which is illustrated in the next

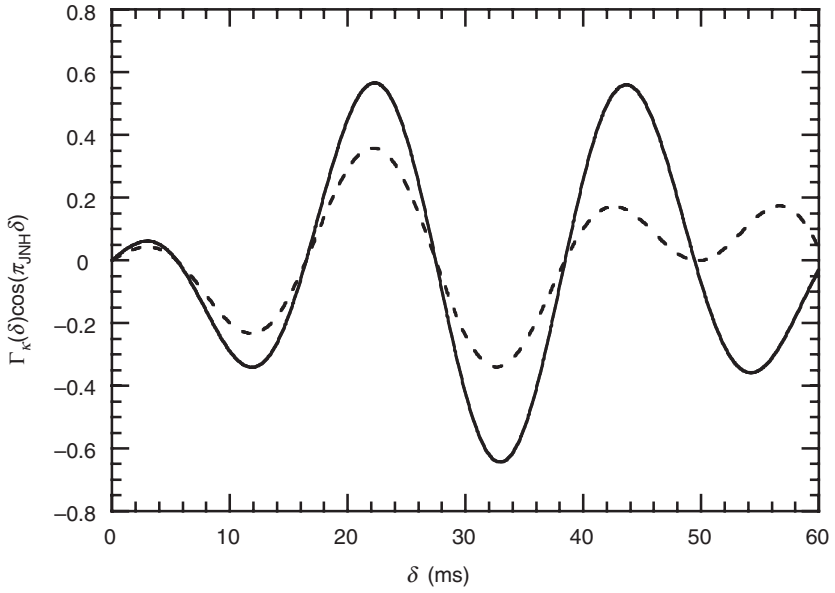

FIGURE 7.33 Plots of the HNCA coherence transfer functions, $\Gamma_k(\delta)\cos(\pi J_{NH}\delta)$ for (—) $k=1$ or (- - -) $k=2$. The plots were calculated for $^1J_{C^\alpha N}$ and $^2J_{C^\alpha N}$, coupling constants of 10 and 7 Hz, respectively, and a J_{NH} coupling constant of 91 Hz.

section for a constant-time version of the HNCA experiment, might be thought to offer a distinct advantage because the signal decay in the t_2 dimension is determined by the transverse relaxation rate of single-quantum $^{13}C^\alpha$ coherence rather than the three-spin $^1H^N$–^{15}N–$^{13}C^\alpha$ multiple-quantum coherence. However, as discussed by Grzesiek and Bax (*84*), the $^{13}C^\alpha$ spins remain coupled to the $^{13}C^\beta$ spins during the t_2 evolution period [7.102], and the acquisition time in the t_2 dimension is therefore kept shorter than $1/(2J_{C^\alpha C^\beta})$, about 8–10 ms in practice. Over this time period, the difference in the intrinsic relaxation rates of transverse $^{13}C^\alpha$ magnetization and three-spin $^1H^N$–^{15}N–$^{13}C^\alpha$ coherence is of little consequence, and the two methods of transferring coherence from ^{15}N to $^{13}C^\alpha$ are equivalent.

The magnetization present following the t_2 evolution period [7.102] is transferred back to observable $^1H^N$ magnetization by the pathway reverse of that described previously, with the exception that the t_1 evolution period is omitted. The 90° pulses immediately following point *e* convert the three-spin $^1H^N$–^{15}N–$^{13}C^\alpha$ coherence back into antiphase ^{15}N magnetization, which rephases with respect to its coupled $^{13}C^\alpha$ spin

during the delay δ. The ^{15}N remains antiphase with respect to its coupled amide ^{1}H because, as already discussed, the duration of δ is set to be an integral multiple of $1/J_{NH}$. The final series of pulses represent a reverse INEPT sequence and result in observable $^{1}H^{N}$ magnetization described by

$$\sigma_f = H_{ix}^{N}\Big\{\cos(\Omega_{C_i^{\alpha}} t_2)\Gamma_1^2(\delta) + \cos(\Omega_{C_{i-1}^{\alpha}} t_2)\Gamma_2^2(\delta)\Big\} \times \cos(\Omega_N t_1)\,\cos(\pi J_{C^{\alpha}C^{\beta}} t_2)\,\cos(\pi J_{NH}\delta). \qquad [7.103]$$

A representative $F_2(^{13}C^{\alpha})$–$F_3(^{1}H^{N})$ slice from an HNCA spectrum of $^{15}N/^{13}C$-labeled ubiquitin is shown in Fig. 7.34. The observed $^{1}H^{N}$–$^{13}C^{\alpha}$ correlations are labeled according to the $^{13}C^{\alpha}$ resonance; in this example, the stronger correlations correspond to the intraresidue connectivities while the weaker correlations correspond to sequential interresidue connectivities. Empirically, average values of $^{1}J_{C^{\alpha}N} > {}^{2}J_{C^{\alpha}N}$; however, the ranges of intra- and interresidue scalar coupling constants observed in proteins overlap, and intensities of the resonance peaks can be affected by differences in relaxation rates. Consequently, identification of the intra- and interresidue connectivities on the basis of resonance intensities in the HNCA experiment is not infallible.

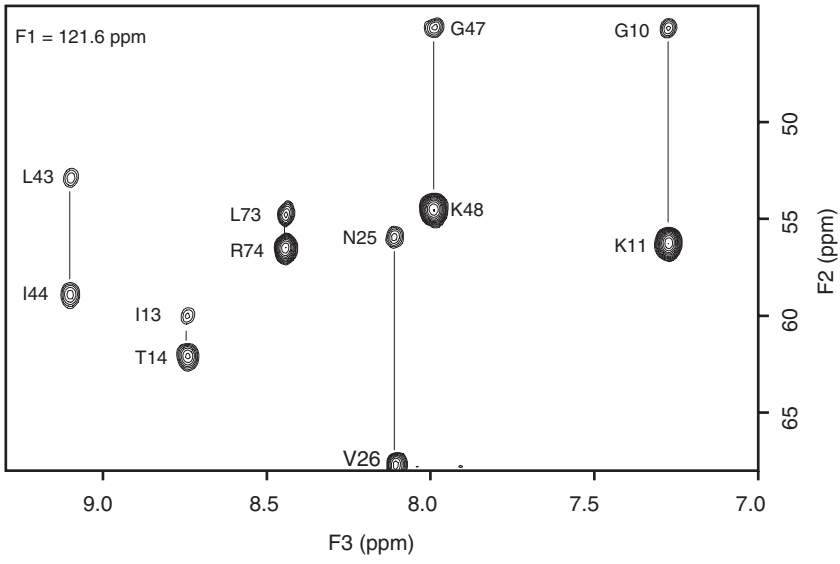

FIGURE 7.34 A selected $F_2(^{13}C^{\alpha})$–$F_3(^{1}H^{N})$ slice, at an $F_1(^{15}N)$ chemical shift of 121.6 ppm, from an HNCA spectrum of $^{15}N/^{13}C$-labeled ubiquitin.

7.4.1.2 The CT-HNCA Experiment The modified version of the HNCA experiment illustrated in Fig. 7.31b includes a "constant-time" period during which evolution of the ^{15}N chemical shift and evolution of the ^{15}N–$^{13}C^{\alpha}$ scalar coupling interaction occur simultaneously. In the original HNCA experiment (Fig. 7.31a), the ^{15}N chemical shift, and ^{15}N–$^{13}C^{\alpha}$ scalar coupling evolution periods are independent. The main advantage of the constant-time evolution scheme, as discussed in detail here, is a reduction in relaxation losses and a concomitant improvement in sensitivity.

During the first part of the CT-HNCA experiment, magnetization originating on amide ^{1}H spins is transferred to their directly attached ^{15}N spins via an INEPT sequence, in a fashion identical to that of the original experiment discussed previously. The magnetization present at time *a* in Fig. 7.31b is therefore represented by [7.97].

Between points *a* and *b*, the pulse sequence is similar to the constant-time periods used in the constant-time HSQC (Section 7.1.1.3) and constant-time ^{1}H–^{13}C HSQC (Section 7.1.5) experiments. By similar reasoning, evolution due to the ^{15}N–$^{13}C^{\alpha}$ scalar coupling interaction ($^{1}J_{C^{\alpha}N}$,$^{2}J_{C^{\alpha}N}$) occurs during the entire constant-time evolution period, T, while ^{15}N chemical shift evolution proceeds only during t_1. The ^{15}N spins are effectively decoupled from both the ^{1}H and ^{13}CO spins by the application of 180° pulses to these nuclei; consequently, the ^{15}N magnetization remains antiphase with respect to its coupled ^{1}H spin. The magnetization at time *b* is described by

$$\sigma_b = \left\{4H_{iz}^{N}N_{ix}C_{iz}^{\alpha}\Gamma_1(T) + 4H_{iz}^{N}N_{ix}C_{(i-1)z}^{\alpha}\Gamma_2(T)\right\}\cos(\Omega_{N_i}t_1), \qquad [7.104]$$

in which $\Gamma_1(T)$ and $\Gamma_2(T)$ are the coherence transfer functions [7.100]. If relaxation during T is ignored, then intraresidue coherence transfer is optimized by selecting T to maximize $\Gamma_1(T)$ (Fig. 7.32). The amplitude of the signal is further reduced, however, by a factor of $\exp(-RT)$, in which R is the average relaxation rate constant for the $H_{iz}^{N}N_{ix}C_{iz}^{\alpha}$ operator. In practice, T is typically chosen to be between 22 and 28 ms.

The magnetization present at the end of the constant-time delay, T, is transferred by the simultaneous ^{15}N and $^{13}C^{\alpha}$ 90° pulses into antiphase $^{13}C^{\alpha}$ magnetization at time *c*,

$$\sigma_c = \left\{4H_{iz}^{N}N_{iz}C_{iy}^{\alpha}\Gamma_1(T) + 4H_{iz}^{N}N_{iz}C_{(i-1)y}^{\alpha}\Gamma_2(T)\right\}\cos(\Omega_{N_i}t_1). \qquad [7.105]$$

The three 180° pulses applied at the midpoint of the t_2 evolution period serve to refocus ^{1}H, ^{15}N, and ^{13}CO scalar coupling evolution. The $^{13}C^{\alpha}$ and $^{13}C^{\beta}$ spins are scalar coupled during t_2; thus, the acquisition time

in the t_2 dimension should be shorter than $1/(2J_{C^\alpha C^\beta})$, or about 8–10 ms in practice. At the end of the t_2 evolution period, point d, the relevant operators are

$$\sigma_d = \left\{4H_{iz}^N N_{iz} C_{iy}^\alpha \cos(\Omega_{C_i^\alpha} t_2)\Gamma_1(T) + 4H_{iz}^N N_{iz} C_{(i-1)y}^\alpha \cos(\Omega_{C_{i-1}^\alpha} t_2)\Gamma_2(T)\right\} \times \cos(\Omega_{N_i} t_1) \cos(\pi J_{C^\alpha C^\beta} t_2). \quad [7.106]$$

This magnetization is then transferred back into observable amide ^{1}H magnetization by the pathway reverse of that described previously. At the beginning of the acquisition period, the observable magnetization is described by

$$\sigma_e = H_{ix}^N \left\{\cos(\Omega_{C_i^\alpha} t_2)\Gamma_1^2(T) + \cos(\Omega_{C_{i-1}^\alpha} t_2)\Gamma_2^2(T)\right\} \cos(\Omega_{N_i} t_1) \cos(\pi J_{C^\alpha C^\beta} t_2). \quad [7.107]$$

For $T = \delta$, this expression is identical to that previously derived, [7.103], for the original non-constant-time version of the HNCA experiment. As already mentioned, however, the advantage of the constant-time evolution scheme is found when relaxation effects are considered. In the original HNCA experiment (Fig. 7.31a), signal decays as t_1 increases; in the CT-HNCA experiment (Fig. 7.31b), signal does not decay as t_1 increases. For $T = \delta$, the gain in sensitivity that can be obtained from using the constant-time evolution scheme is approximately

$$\mathscr{S} = \frac{t_{1\max}}{\int_0^{t_{1\max}} \exp(-t_1 \overline{R}_{2N})\, dt_1} = \frac{t_{1\max} \overline{R}_{2N}}{1 - \exp(-t_{1\max} \overline{R}_{2N})}, \quad [7.108]$$

in which $\overline{R}_{2N}$ is the transverse relaxation rate of the antiphase ^{15}N magnetization ($2H_{iz}^N N_{iy}$) present during the t_1 evolution period of the non-constant-time experiment [7.16], and $t_{1\max}$ is the maximum duration of the t_1 evolution period. As with any constant-time evolution scheme, $t_{1\max}$ is limited to be less than (or equal to) the constant-time period, T. For ubiquitin, $\overline{R}_{2N} \approx 9.9\ s^{-1}$ (calculated as described in Section 7.1.1.2 for $\tau_c = 4.1$ ns), and for $t_{1\max} = 18.6$ ms, [7.108] predicts a sensitivity gain of 10% in the constant-time experiment. Larger gains would be expected for larger proteins with larger relaxation rate constants.

7.4.1.3 The Decoupled CT-HNCA Experiment The sensitivity of the above CT-HNCA experiment (and related pulse sequences) can be

further increased by the introduction of synchronous broadband ^{1}H decoupling (*84*, *86*), as illustrated in Fig. 7.31c. The magnetization present at time *a* in Fig. 7.31c is represented by [7.97]. At the end of the first delay, $\delta_1 = 1/(2J_{NH})$, the ^{15}N magnetization is refocused to be in-phase with respect to its attached proton. Application of synchronous broadband ^{1}H decoupling (WALTZ-16 or DIPSI-2, for instance) prevents the creation of any ^{15}N or ^{13}C quantum states that are antiphase with respect to the attached ^{1}H spin. Contributions to the ^{15}N and ^{13}C linewidths from ^{1}H longitudinal relaxation are therefore eliminated, because both ^{15}N and ^{13}C transverse magnetization remains in-phase (Section 7.1.3.1). The resulting decrease in the apparent R_{2N} and R_{2C} relaxation rate constants reduces the signal loss caused by ^{15}N and ^{13}C transverse relaxation during delays between the two ^{1}H–^{15}N INEPT sequences. The magnetization at time *c* is therefore described by

$$\sigma_c = \{-2N_{iz}C^{\alpha}_{iy}\Gamma_1(T) - 2N_{iz}C^{\alpha}_{(i-1)y}\Gamma_2(T)\}\cos(\Omega_{N_i}t_1). \qquad [7.109]$$

This expression can be compared directly with [7.101] and [7.105] from the HNCA and CT-HNCA experiments, respectively, which contain multiple-quantum ($4H^N_{iy}N_{ix}C^{\alpha}_{iy}$) or antiphase ($4H^N_{iz}N_{iz}C^{\alpha}_{iy}$) states with respect to ^{1}H spins. At the end of the t_2 evolution period, point *d*, the relevant operators are

$$\sigma_d = \{-2N_{iz}C^{\alpha}_{iy}\cos(\Omega_{C^{\alpha}_i}t_2)\Gamma_1(T) - 2N_{iz}C^{\alpha}_{(i-1)y}\cos(\Omega_{C^{\alpha}_{i-1}}t_2)\Gamma_2(T)\}$$
$$\times \cos(\Omega_{N_i}t_1)\cos(\pi J_{C^{\alpha}C^{\beta}}t_2). \qquad [7.110]$$

This magnetization is then transferred back into observable amide ^{1}H magnetization by the reverse pathway. The magnetization prior to acquisition, point *e*, is described by [7.107].

7.4.1.4 The Gradient-Enhanced HNCA Experiment The HNCA and many other triple resonance experiments include an indirect evolution period for amide ^{15}N spins and detect amide proton spins during the acquisition period. These experiments are particularly easy to modify for coherence selection using pulsed field gradients and PEP sensitivity enhancement (Section 7.1.4.2). A pulse sequence for a decoupled PFG-PEP-HNCA experiment is shown in Fig. 7.31d (a nongradient PEP-HNCA could be designed as well). This experiment is very similar to the experiment shown in Fig. 7.31c, with the following exceptions: (*i*) ^{15}N frequency labeling is performed during the second period, *T*, rather than during the first; (*ii*) the reverse INEPT sequence of Fig. 7.31c

is replaced by a PEP reverse INEPT sequence; (*iii*) field gradient pulses are used for coherence selection and quadrature detection in the ^{15}N evolution period; (*iv*) pulsed field gradient pulses are used to suppress artifacts associated with 180° pulses; (*v*) water flip-back solvent suppression is incorporated; and (*vi*) the off-resonance phase shift caused by the 180°(^{13}CO) pulse during t_2 is corrected by adjusting the phase ϕ_4. The 90°_y pulse prior the ^1H decoupling sequence rotates the water magnetization from the $+z$-axis to the $+x$-axis so that the water magnetization is spin-locked by the decoupling rf field. The 90°_{-y} pulse returns the water magnetization to the $+z$-axis at the end of the decoupling period. Acquisition and processing of the PFG-PEP-HNCA experiment are performed as described for the PFG-PEP-HSQC experiment (Section 7.1.4.2).

7.4.1.5 The Gradient-Enhanced TROSY–HNCA Experiment A PFG-TROSY–HNCA experiment is shown in Fig. 7.31e (a nongradient TROSY–HNCA could be designed as well). This experiment is derived from the PFG-PEP-HNCA by omitting the ^1H decoupling field and replacing the PEP reverse polarization transfer scheme with the TROSY pulse sequence element. Decoupling of the ^1H–$^{13}C^\alpha$ scalar coupling interaction during t_2 is performed with 180°(^1H) pulses applied at $t_2/4$ and $3t_2/4$; the net 0° rotation avoids interconversion of the ^1H I^α and I^β spin operators, which would destroy the TROSY effect. For ^2H-labeled proteins, the ^1H decoupling pulses can be omitted, and composite pulse decoupling applied to the ^2H spins during t_2 when the $^{13}C^\alpha$ magnetization is transverse. The sequence incorporates two enhancements compared to the PFG-PEP-HNCA and the originally proposed TROSY–HNCA (*87*, *88*). First, the TROSY element begins with a 90°(^1H) pulse, but no ^{15}N pulse. Consequently, the refocusing period for the ^{15}N–$^{13}C^\alpha$ scalar coupling interaction can be extended into the first 2τ period of the TROSY element by adding a 180°($^{13}C^\alpha$) pulse. This shortens the overall length of the pulse sequence by 2τ, with consequent reduction in relaxation losses. Second, the TROSY element ends with a 90°(^{15}N) pulse, but no ^1H pulse. Consequently, the refocusing gradient g6 can be accommodated by shifting the final 180°(^1H) pulse as shown in Fig. 7.31e, rather than by incorporating an additional spin echo element as in Fig. 7.31d. This change reduces the number of 180° pulses. More importantly, the final 180° pulse is crafted to leave the water magnetization unperturbed (Section 3.7.3) so that the water magnetization is never inverted during the reverse polarization transfer. Acquisition and processing of the PFG-TROSY–HNCA experiment is performed as described for the PFG-TROSY experiment (Section 7.1.4.2).

7.4.2 A Complementary Approach: The HN(CO)CA Experiment

The HN(CO)CA experiment provides sequential correlations between the amide ^{1}H and ^{15}N chemical shifts of one amino acid residue and the $^{13}C^{\alpha}$ chemical shift of the preceding residue by transferring coherence via the intervening ^{13}CO spin (*84*, *89*). The same sequential information is obtained from the HNCA experiment (Section 7.4.1); however, the HNCA experiment does not always distinguish intraresidue and interresidue connectivities because the $^{1}J_{C^{\alpha}N}$ and $^{2}J_{C^{\alpha}N}$ coupling constants can be of comparable magnitude or the intraresidue and interresidue $^{13}C^{\alpha}$ chemical shifts may be coincidentally degenerate. The HN(CO)CA experiment circumvents these problems by providing sequential correlations exclusively. In addition, the sensitivity of the HN(CO)CA experiment is greater than that of the HNCA for larger proteins, because the relay of magnetization via the one-bond J_{NCO} and $J_{C^{\alpha}CO}$ scalar coupling interactions is more efficient compared to transfer via the relatively small $^{2}J_{C^{\alpha}N}$ scalar coupling interaction.

The salient features of the CT-HN(CO)CA experiment illustrated in Fig. 7.35 are discussed here. Following the initial INEPT-type transfer of magnetization from the amide $^{1}H^{N}$ spins to their directly attached ^{15}N spins, the magnetization present at time *a* in Fig. 7.35 is represented by

$$\sigma_a = -2H_{iz}N_{iy} \qquad [7.111]$$

for $2\tau = 1/(2J_{NH})$.

During the subsequent constant-time evolution period, $2\delta_1 = 2(\delta_2 + \delta_3)$, the propagator is

$$\begin{aligned}\mathbf{U} &= \exp\left(-i\tfrac{\pi}{2}C'_{(i-1)x}\right)\exp\left(-i\tfrac{\pi}{2}N_{ix}\right)\exp[-i\mathscr{H}(\delta_1 - t_1/2)]\exp\left(-i\pi C'_{(i-1)x}\right)\\ &\quad\times\exp(-i\pi N_{ix})\exp[-i\mathscr{H}\delta_2]\exp\left(-i\pi\sum H^{\kappa}_{kx}\right)\exp[-i\mathscr{H}\delta_3]\\ &\quad\times\exp\left(-i\pi\sum C^{\kappa}_{kx}\right)\exp[-i\mathscr{H}t_1/2]\\ &= \exp\left(-i\tfrac{\pi}{2}C'_{(i-1)x}\right)\exp\left(-i\tfrac{\pi}{2}N_{ix}\right)\exp\ -i4\pi\end{aligned}$$

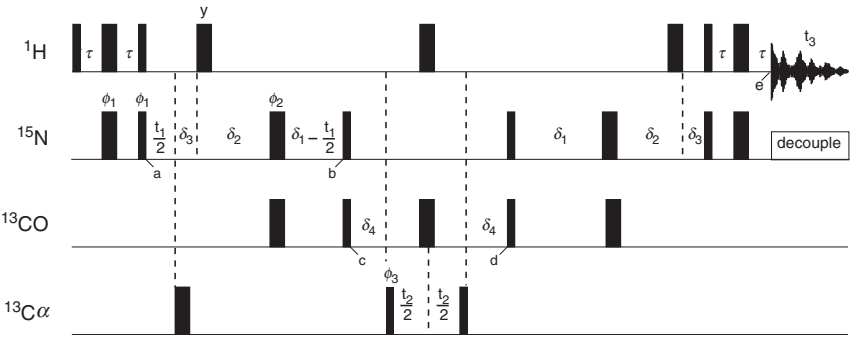

FIGURE 7.35 Pulse sequence for a constant-time HN(CO)CA experiment. Values of delays are described in the text. Other experimental details are similar to those given in Fig. 7.31. The phase cycle is $\phi_1 = x, -x$; $\phi_2 = 4(x), 4(y), 4(-x), 4(-y)$; $\phi_3 = 2(x), 2(-x)$; and receiver $= x, -x, -x, x, -x, x, x, -x$. Quadrature detection in the t_1 and t_2 dimensions is achieved by incrementing independently the phases ϕ_1 and ϕ_3, respectively, and the receiver phase, in a TPPI–States manner.

in which $\exp\left(-i\pi \sum H_{kx}^{\kappa}\right)$ represents a nonselective proton 180° pulse and $\exp\left(-i\pi \sum C_{kx}^{\kappa}\right)$ represents a nonselective carbon 180° pulse (with summations over k and κ implied), only chemical shift and scalar coupling interactions affecting the ^{15}N spin have been included in the Hamiltonian, and the last line is obtained by using [2.121]. Evolution due to ^{1}H–^{15}N coupling occurs only during $2\delta_3$, while evolution due to ^{15}N–^{13}CO coupling occurs during the entire period, $2\delta_1$. For $2\delta_3 = 1/(2J_{\mathrm{NH}})$, the antiphase ^{15}N operator is refocused to become in-phase with respect to the amide ^{1}H$^{\mathrm{N}}$ spin at the end of the constant-time period. Chemical shift evolution of the ^{15}N coherence occurs only during t_1. The duration of the constant-time evolution period, $2\delta_1$, can be adjusted from $1/(3J_{\mathrm{NCO}})$ to $1/(2J_{\mathrm{NCO}})$, independently of the ^{1}H–^{15}N coupling evolution period, $2\delta_3$, as required to minimize relaxation losses. Typically, $2\delta_1 \approx 22$ ms $[1/(3J_{\mathrm{NCO}})]$. The magnetization present at time b is described by

$$\sigma_b = 2N_{iy}C'_{(i-1)_z} \cos(\Omega_{N_i} t_1) \sin(2\pi J_{\mathrm{NCO}}\delta_1) \sin(2\pi J_{\mathrm{NH}}\delta_3). \qquad [7.113]$$

The pair of simultaneous 90° pulses transfer [7.113] into antiphase carbonyl magnetization, given at time c,

$$\sigma_c = -2N_{iz}C'_{(i-1)_y} \cos(\Omega_{N_i} t_1) \sin(2\pi J_{\mathrm{NCO}}\delta_1) \sin(2\pi J_{\mathrm{NH}}\delta_3). \qquad [7.114]$$

The product operator in [7.114] is in-phase with respect to the amide $^1H^N$ spin. If this ^{13}CO magnetization were antiphase, then its transverse relaxation rate (and the relaxation rates of the product operators during t_2) would be increased due to contributions from proton longitudinal relaxation, and the signal observed would be correspondingly decreased. This would be the case if the amide $^1H^N$ spins were decoupled during the constant-time evolution period, as in the CT-HNCA experiment [7.104].

During the subsequent δ_4–t_2–δ_4 period, the ^{13}CO spin is correlated with its attached $^{13}C^\alpha$ spin in an HMQC-like manner. Ignoring evolution due to couplings between $^{13}C^\alpha$ and ^{15}N, which are relatively small in magnitude, and between ^{13}CO and ^1H spins, which are not refocused by the 180° pulses at the midpoint of t_2, the coherence present at time *d* is

$$\sigma_d = -2N_{iz}C'_{(i-1)y}\cos(\Omega_{N_i}t_1)\cos(\Omega_{C^\alpha_{i-1}}t_2)\cos(\pi J_{C^\alpha C^\beta}t_2) \times \sin^2(\pi J_{C^\alpha CO}\delta_4)\sin(2\pi J_{NCO}\delta_1)\sin(2\pi J_{NH}\delta_3). \quad [7.115]$$

The delay δ_4 is set from $1/(3J_{C^\alpha CO})$ to $1/(2J_{C^\alpha CO})$. The $^{13}C^\alpha$ and $^{13}C^\beta$ spins remain coupled during t_2; therefore, in order to avoid sensitivity losses due to resolved $J_{C^\alpha C^\beta}$ scalar couplings in the F_2 dimension, the t_2 acquisition time must be shorter than $1/(2J_{C^\alpha C^\beta})$, or about 8–10 ms in practice. The off-resonance effect of the 180°(^{13}CO) pulse in the middle of the t_2 evolution period results in a small frequency-dependent phase shift in this dimension, which can be corrected approximately during data processing (Section 3.4.1). Magnetization is transferred back along the same pathway to yield the observable magnetization at time *e*:

$$\sigma_e = H^N_{ix}\cos(\Omega_{N_i}t_1)\cos(\Omega_{C^\alpha_{i-1}}t_2)\cos(\pi J_{C^\alpha C^\beta}t_2) \times \sin^2(\pi J_{C^\alpha CO}\delta_4)\sin^2(2\pi J_{NCO}\delta_1)\sin^2(2\pi J_{NH}\delta_3). \quad [7.116]$$

As in the HNCA experiment, the sensitivity of the HN(CO)CA experiment can be improved by the use of synchronous broadband proton decoupling after the antiphase term at time *a* [7.111] has been allowed to refocus and by incorporating PEP sensitivity enhancement.

A representative $F_2(^{13}C^\alpha)$–$F_3(^1H^N)$ slice from an HN(CO)CA spectrum of $^{15}N/^{13}C$-labeled ubiquitin is shown in Fig. 7.36. This slice was taken at the same $F_1(^{15}N)$ chemical shift as for the $F_2(^{13}C^\alpha)$–$F_3(^1H^N)$ slice from the HNCA spectrum of ubiquitin shown in Fig. 7.34. By comparison of these spectra, the interresidue correlations in the HNCA

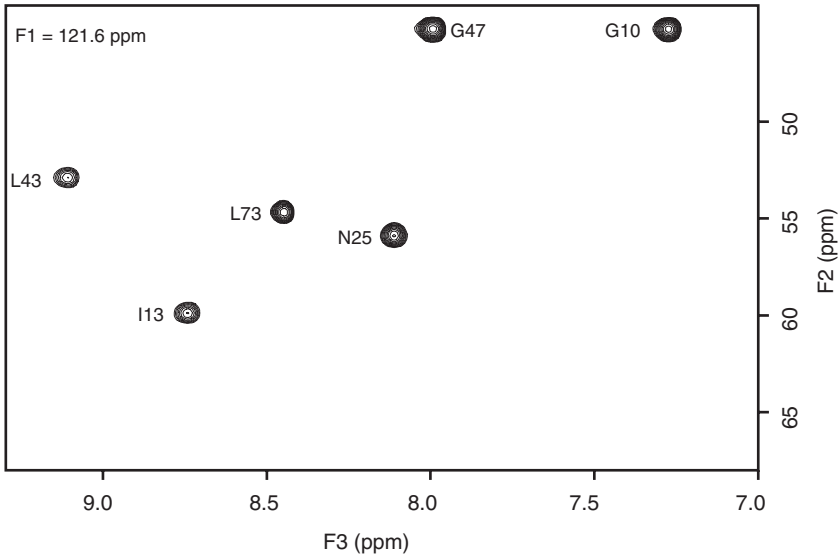

FIGURE 7.36 A selected $F_2(^{13}C^{\alpha})$–$F_3(^{1}H^{N})$ slice, at an $F_1(^{15}N)$ chemical shift of 121.6 ppm, from an HN(CO)CA spectrum of $^{15}N/^{13}C$-labeled ubiquitin. This slice may be compared directly with the equivalent region from the HNCA spectrum of ubiquitin illustrated in Fig. 7.34.

spectrum can be unambiguously distinguished from the intraresidue correlations, because only the interresidue connectivities are observed in the HN(CO)CA experiment.

7.4.3 A STRAIGHT-THROUGH TRIPLE-RESONANCE EXPERIMENT: H(CA)NH

The H(CA)NH experiment (*72*) correlates $^{1}H^{\alpha}$ chemical shifts with intraresidue amide ^{1}H and ^{15}N chemical shifts, by making use of the one-bond ^{15}N–$^{13}C^{\alpha}$ J coupling (7–11 Hz). This experiment also provides sequential connectivities by transferring coherence from the $^{13}C^{\alpha}$ spins to the ^{15}N of the following residue via the interresidue two-bond ^{15}N–$^{13}C^{\alpha}$ J coupling (4–9 Hz). The H(CA)NH experiment differs fundamentally from the HNCA experiment because one-way "straight-through" or "out-and-stay" transfer of magnetization from $^{1}H^{\alpha}$ to ^{15}N spins is obtained via successive through-bond transfer between the directly coupled $^{1}H^{\alpha}$–$^{13}C^{\alpha}$, $^{13}C^{\alpha}$–^{15}N, and ^{15}N–$^{1}H^{N}$ pairs. At each

transfer step, net magnetization transfer (rather than coherence transfer to antiphase spin states) must be obtained using refocused INEPT sequences. A product operator description of the H(CA)NH experiment illustrated in Fig. 7.37 is given in the following discussion.

Beginning with longitudinal $^1H^\alpha$ magnetization at point a ($\sigma_a = H_{iz}^\alpha$), transverse $^1H^\alpha$ magnetization is frequency labeled during t_1 and transferred in an INEPT-like manner to its directly attached $^{13}C^\alpha$, to yield at point b

$$\sigma_b = 2H_{iz}^\alpha C_{iy}^\alpha \cos(\Omega_{H_i^\alpha} t_1) \qquad [7.117]$$

for $2\tau_1 = 1/(2J_{CH})$ (~ 3.5 ms). The identical concatenated t_1 evolution period and INEPT magnetization transfer scheme were used in the CT-HCCH–COSY experiment (Fig. 7.26b).

Following the simultaneous 90° ^1H and $^{13}C^\alpha$ pulses, the antiphase $^{13}C^\alpha$ magnetization, [7.117], is refocused with respect to the $^1H^\alpha$ spins during the period $2\delta_1$, while dephasing due to ^{15}N–$^{13}C^\alpha$ one-bond and two-bond scalar couplings, and $^{13}C^\alpha$–$^{13}C^\beta$ one-bond scalar coupling occurs during $2\delta_2$. For $^{13}C^\alpha$ directly coupled to a single proton (i.e., all

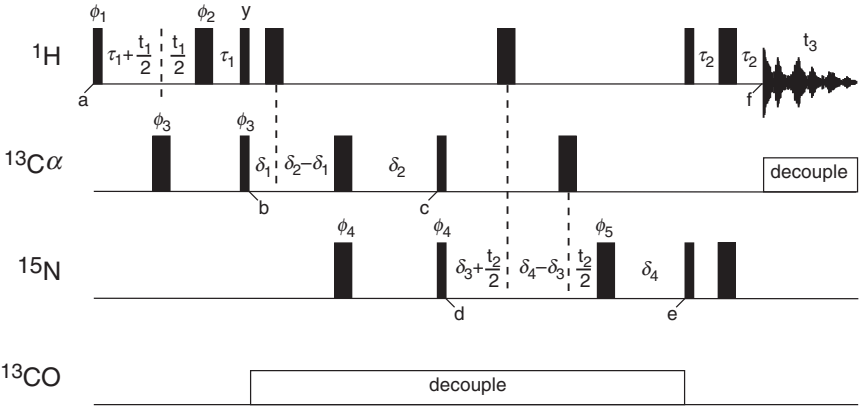

FIGURE 7.37 Pulse sequence for a constant-time H(CA)NH experiment. Values of delays are described in the text. Other experimental details are similar to those given in Fig. 7.31. The phase cycle is $\phi_1 = x, -x$; $\phi_2 = 16(x), 16(-x)$; $\phi_3 = 2(x), 2(-x)$; $\phi_4 = 4(x), 4(-x)$; $\phi_5 = 8(x), 8(y), 8(-x), 8(-y)$; and receiver $= x, -x, -x, x, 2(-x, x, x, -x), x, -x, -x, x$. Quadrature detection in the t_1 and t_2 dimensions is achieved by incrementing independently the phases ϕ_1 and ϕ_4, respectively, and the receiver phase, in a TPPI–States manner.

amino acids except glycine), the relevant components of the density operator at point c are

$$\sigma_c = \left\{-2C^{\alpha}_{iy}N_{iz}\Gamma_1(2\delta_2) - 2C^{\alpha}_{iy}N_{(i+1)z}\Gamma_2(2\delta_2)\right\} \times \cos(\Omega_{H^{\alpha}_i}t_1)\,\sin(2\pi J_{\mathrm{CH}}\delta_1)\,\cos(2\pi J_{\mathrm{C^{\alpha}C^{\beta}}}\delta_2), \qquad [7.118]$$

in which the coherence transfer functions, $\Gamma_1(t)$ and $\Gamma_2(t)$, are given by [7.100]. The optimal value of $2\delta_1 = 1/(2J_{\mathrm{CH}})$. Intraresidue coherence transfer is optimized by selecting δ_2 to maximize

$$\Gamma_{\alpha}(2\delta_2) = \Gamma_1(2\delta_2)\,\cos\left(2\pi J_{\mathrm{C^{\alpha}C^{\beta}}}\delta_2\right)\,\exp\left(-2R_{2C^{\alpha}_i}\delta_2\right), \qquad [7.119]$$

in which $R_{2C^{\alpha}_i}$ is the $^{13}C^{\alpha}$ transverse relaxation rate. This function, which is plotted in Fig. 7.38, has a maximum value for $\delta_2 = 12$ to 13 ms.

The 90°($^{13}C^{\alpha}$) and 90°(^{15}N) pulses immediately following point c transfer the antiphase ^{13}C coherence into antiphase ^{15}N coherence at point d:

$$\sigma_d = \left\{2C^{\alpha}_{iz}N_{iy}\Gamma_1(2\delta_2) + 2C^{\alpha}_{iz}N_{(i+1)y}\Gamma_2(2\delta_2)\right\}\,\cos(\Omega_{H^{\alpha}_i}t_1) \times \sin(2\pi J_{\mathrm{CH}}\delta_1)\,\cos(2\pi J_{\mathrm{C^{\alpha}C^{\beta}}}\delta_2). \qquad [7.120]$$

During the subsequent evolution period between points d and e, the propagator is

$$\begin{aligned}\mathbf{U} &= \exp[-i\mathscr{H}\delta_4]\,\exp\left(-i\pi\sum N_{kx}\right)\,\exp[-i\mathscr{H}t_2/2]\,\exp\left(-i\pi\sum C^{\alpha}_{kx}\right) \times \exp[-i\mathscr{H}(\delta_4-\delta_3)]\,\exp\left(-i\pi\sum H^{\kappa}_{kx}\right)\,\exp[-i\mathscr{H}(\delta_3+t_2/2)] \\ &= \sum\left\{\exp\left(-i4\pi J_{\mathrm{NH}}\delta_3 H^{N}_{kz}N_{kz}\right).\exp\left(-i4\pi^{1}J_{\mathrm{C^{\alpha}N}}C^{\alpha}_{kz}N_{kz}\right) \times \exp\left(-i4\pi 2J_{\mathrm{C^{\alpha}N}}C^{\alpha}_{(k-1)z}N_{kz}\right)\,\exp\left(-i\Omega_{N_k}t_2N_{kz}\right)\right\} \\ &\quad\times\exp\left(-i\pi\sum N_{kx}\right)\,\exp\left(-i\pi\sum C^{\alpha}_{kx}\right)\,\exp\left(-i\pi\sum H^{\kappa}_{kx}\right),\end{aligned} \qquad [7.121]$$

in which only chemical shift and scalar coupling interactions affecting the ^{15}N spins have been included in the Hamiltonian, and the last line is obtained by using [2.121]. The antiphase ^{15}N coherences refocus with respect to the active ^{15}N–^{13}C scalar coupling and dephase due to passive ^{15}N–^{13}C scalar coupling during $2\delta_4$. Thus, $2C^{\alpha}_{iz}N_{iy}$ refocuses under the intraresidue $^{1}J_{\mathrm{C^{\alpha}N}}$ scalar coupling interaction and dephases under the $^{2}J_{\mathrm{C^{\alpha}N}}$ scalar coupling to the $^{13}C^{\alpha}$ spin of the preceding residue, while

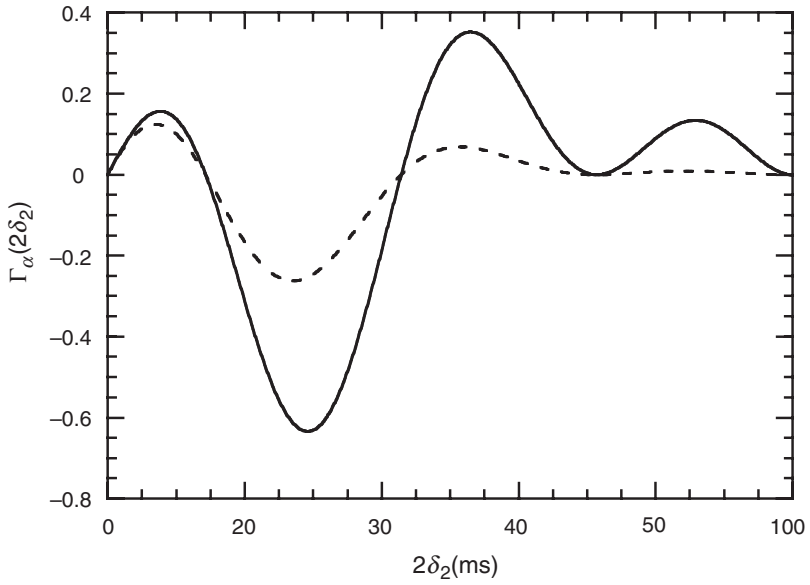

FIGURE 7.38 Plots of the H(CA)NH coherence transfer function, $\Gamma_\alpha(2\delta_2)$ [7.119], for $^1J_{C^{\alpha 1}N}$, $^2J_{C^{\alpha 2}N}$, and $^1J_{C^\alpha C^\beta}$ coupling constants of 10, 7, and 35 Hz, respectively. The solid line corresponds to the transfer function in the absence of relaxation, while the dashed line includes the relaxation term $\exp(-2R_{2C^\alpha}\delta_2)$ for $^{13}C^\alpha$ linewidths of $1/(\pi T_{2C^\alpha}) = 10$ Hz.

$2C^\alpha_{iz}N_{(i+1)y}$ refocuses under the interresidue scalar coupling interaction and dephases due to the intraresidue coupling. The ^{15}N magnetization also defocuses with respect to the amide proton during the time period $2\delta_3$. The relevant coherences present at point e are described by

$$\begin{aligned}\sigma_e = &\Big\{-2H^N_{iz}N_{iy}\cos(\Omega_{N_i}t_2)\Gamma_1(2\delta_2)\Gamma_1(2\delta_4).\\ &-2H^N_{(i+1)z}N_{(i+1)y}\cos(\Omega_{N_{i+1}}t_2)\Gamma_2(2\delta_2)\Gamma_2(2\delta_4)\Big\}\\ &\times\cos(\Omega_{H^\alpha_i}t_1)\sin(2\pi J_{NH}\delta_3)\sin(2\pi J_{CH}\delta_1)\cos(2\pi J_{C^\alpha C^\beta}\delta_2). \quad [7.122]\end{aligned}$$

Intraresidue coherence transfer through this segment of the experiment is maximized by setting $2\delta_3 = 1/(2J_{NH})$ ($\sim$5.4 ms), and by adjusting $2\delta_4$ to maximize $\Gamma_1(2\delta_4)$. This transfer function is identical to that plotted in Fig. 7.32 for the HNCA experiment [7.100]. When ^{15}N transverse relaxation, R_{2N}, is considered, a value of $2\delta_4$ of $\sim$23 ms is close to optimal.

The final INEPT step in the pulse sequence transfers the antiphase ^{15}N magnetization to in-phase $^{1}H^{N}$ magnetization to yield, at time f,

$$\sigma_f = \left\{ H_{ix}^{N} \cos(\Omega_{N_i} t_2)\Gamma_1(2\delta_2)\Gamma_1(2\delta_4) + H_{(i+1)x}^{N} \cos(\Omega_{N_{i+1}} t_2)\Gamma_2(2\delta_2)\Gamma_2(2\delta_4) \right\} \times \cos(\Omega_{H_i^{\alpha}} t_1) \sin(2\pi J_{CH}\delta_1) \cos(2\pi J_{C^{\alpha}C^{\beta}}\delta_2), \quad [7.123]$$

for $2\tau_2 = 1/(2J_{NH})$. Thus, magnetization that originated as $^{1}H^{\alpha}$ magnetization has been transferred to and is detected as amide $^{1}H^{N}$ magnetization.

A representative $F_1(^{1}H^{\alpha})$–$F_3(^{1}H^{N})$ slice from an H(CA)NH spectrum of $^{15}N/^{13}C$-labeled ubiquitin is shown in Fig. 7.39. The observed $^{1}H^{N}$–$^{1}H^{\alpha}$ correlations are labeled according to the $^{1}H^{\alpha}$ resonance. In this example, the stronger correlation corresponds to the intra-residue connectivities while the weaker correlation corresponds to sequential interresidue connectivities. Identification of the intra- and interresidue connectivities on the basis of resonance intensities in the H(CA)NH experiment has the same caveats as given for the HNCA experiment (Section 7.4.1).

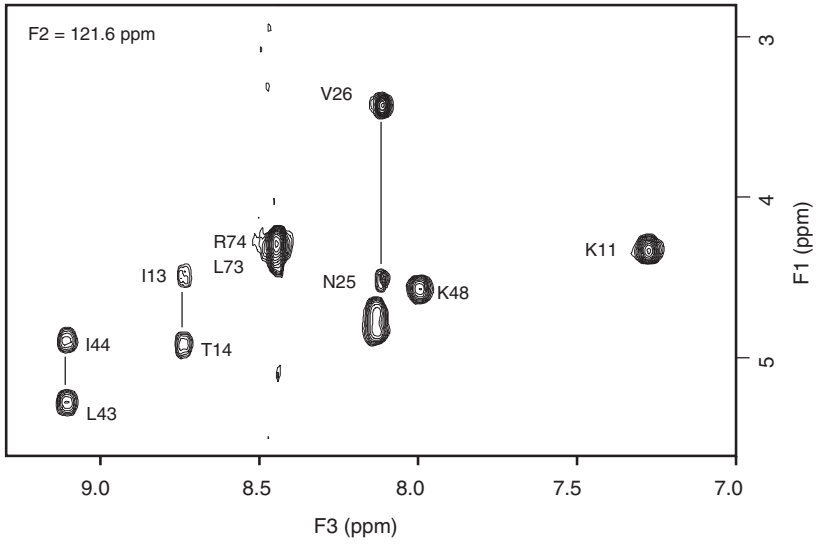

FIGURE 7.39 A selected $F_1(^{1}H^{\alpha})$–$F_3(^{1}H^{N})$ slice, at an $F_2(^{15}N)$ chemical shift of 121.6 ppm, from an H(CA)NH spectrum of $^{15}N/^{13}C$-labeled ubiquitin. Resonances from Gly10 and Gly47 are suppressed for $2\delta_1 = 1/(2J_{CH})$.

7.4.4 BACKBONE CORRELATIONS WITH THE ^{13}CO SPINS

The HNCA, HN(CO)CA, and H(CA)NH experiments illustrate many of the principles utilized in triple-resonance NMR spectroscopy. These experiments alone usually are not sufficient to establish complete backbone sequential connectivities, and do not indicate the enormous variety of triple-resonance experiments that have been developed (*7*). The HNCA and HN(CO)CA provide correlations between $^{1}H^{N}$, ^{15}N, and $^{13}C^{\alpha}$ spins. The HNCO and HN(CA)CO experiments provide analogous correlations between the $^{1}H^{N}$, ^{15}N, and ^{13}CO spins. These experiments are presented briefly in this section.

7.4.4.1 HNCO The HNCO experiment correlates the amide $^{1}H^{N}$ and ^{15}N chemical shifts of one amino acid with the ^{13}CO chemical shift of the preceding residue, by using the one-bond ^{15}N–^{13}CO J coupling ($\sim$15 Hz) to establish the sequential correlation (*81*, *84*). The sequential connectivities provided by this experiment are particularly useful when used in conjunction with interresidue connectivities provided by the HN(CA)CO (Section 7.4.4.2) and HCACO (*81*, *90*) experiments. A detailed description of alternative pulse sequences for the HNCO experiment has been given by Muhandiram and Kay (*33*, *88*, *91*).

The CT-HNCO pulse sequence illustrated in Fig. 7.40 is analogous to the CT-HNCA and CT-HN(CO)CA experiments. The CT-HNCO substitutes an evolution period for the carbonyl spins instead of the HMQC-type magnetization transfer from the ^{13}CO to the $^{13}C^{\alpha}$ spins used in the HN(CO)CA experiment. The important coherences present at times *a*–*e* of the pulse sequence are

$$\sigma_a = -2H_{iz}^{N}N_{iy}, \qquad [7.124]$$

$$\sigma_b = 2N_{iy}C'_{(i-1)z}\cos(\Omega_{N_i}t_1)\sin(\pi J_{\mathrm{NCO}}T)\sin(\pi J_{\mathrm{NH}}T), \qquad [7.125]$$

$$\sigma_c = -2N_{iz}C'_{(i-1)y}\cos(\Omega_{N_i}t_1)\sin(\pi J_{\mathrm{NCO}}T)\sin(\pi J_{\mathrm{NH}}T), \qquad [7.126]$$

$$\sigma_d = -2N_{iz}C'_{(i-1)y}\cos(\Omega_{N_i}t_1)\cos(\Omega_{CO_{i-1}}t_2)\sin(\pi J_{\mathrm{NCO}}T)\sin(\pi J_{\mathrm{NH}}T), \qquad [7.127]$$

$$\sigma_e = H_{ix}^{N}\cos(\Omega_{N_i}t_1)\cos(\Omega_{CO_{i-1}}t_2)\sin(\pi J_{\mathrm{NCO}}T)\sin(\pi J_{\mathrm{NH}}T) \times \sin(2\pi J_{\mathrm{NCO}}\delta_1)\sin(2\pi J_{\mathrm{NH}}\delta_3), \qquad [7.128]$$

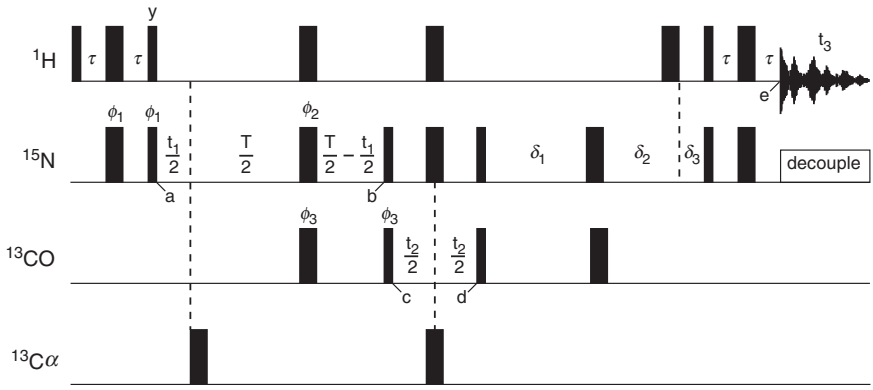

FIGURE 7.40 Pulse sequence for a constant-time HNCO experiment. Values of delays are described in the text. Other experimental details are similar to those given in Fig. 7.31. The phase cycle is $\phi_1 = x, -x$; $\phi_2 = 4(x), 4(y), 4(-x), 4(-y)$; $\phi_3 = 2(x), 2(-x)$; and receiver $= x, -x, -x, x, -x, x, x, -x$. Quadrature detection in the t_1 and t_2 dimensions is achieved by incrementing independently the phases ϕ_1 and ϕ_3, respectively, and the receiver phase, in a TPPI–States manner.

in which $2\tau = 1/(2J_{NH})$, $2\delta_1 = 2(\delta_2+\delta_3)$, and $2\delta_3 = 1/(2J_{NH})$. Typically, $2\delta_1 \approx 1/(3J_{NCO})$ (22 ms) instead of $1/(2J_{NCO})$ to reduce relaxation losses. The time T must be an odd multiple of $1/(2J_{NH})$ [e.g., $5/(2J_{NH}) = 27$ ms] to ensure that the ^{15}N magnetization is in-phase with respect to the amide proton spins at the end of the constant-time evolution period.

In contrast to the CT-HNCA experiment (Fig. 7.31b), antiphase ^{15}N magnetization present at *a* rephases with respect to the $^1H^N$ spins under the influence of the ^{15}N–^{1}H coupling during the constant-time evolution period. Therefore, evolution of the $2N_{iz}C'_{(i-1)y}$ coherence during t_2 does not contain contributions from relaxation of the amide proton spin. The constant-time evolution scheme described here also differs from that described in Section 7.4.2 for the HN(CO)CA experiment, in which the duration of the constant-time period was not limited to be an odd multiple of $1/(2J_{NH})$. Either scheme may be used in each experiment, because if relaxation effects are ignored, the final results are very similar. The sensitivity of this scheme may be further improved by the use of synchronous broadband proton decoupling in a way analogous to that for the decoupled CT-HNCA experiment.

7.4.4.2 HN(CA)CO The HN(CA)CO experiment provides intra-residue correlations between the amide ^{1}H, ^{15}N, and ^{13}CO chemical

shifts by using the one-bond ^{15}N–$^{13}C^{\alpha}$ and $^{13}C^{\alpha}$–^{13}CO J couplings to transfer coherence (*92*). In addition, this experiment can also provide sequential connectivities from the ^{15}N spins to the ^{13}CO of the preceding residue via the interresidue two-bond ^{15}N–$^{13}C^{\alpha}$ J coupling. When used in conjunction with the HNCO experiment, which gives the sequential correlations only (Section 7.4.4.1), the HN(CA)CO experiment provides a method for sequentially assigning the amide ^{1}H, ^{15}N, and ^{13}CO resonances.

A constant-time version of a HN(CA)CO pulse-sequence is illustrated in Fig. 7.41. The important product operator terms at times *a–f* of the pulse sequence are given by

$$\sigma_a = -2H_{iz}^{N}N_{iy}, \qquad [7.129]$$

$$\sigma_b = \left\{2N_{iy}C_{iz}^{\alpha}\Gamma_1(T) + 2N_{iy}C_{(i-1)z}^{\alpha}\Gamma_2(T)\right\}\cos(\Omega_{N_i}t_1), \qquad [7.130]$$

$$\sigma_c = \left\{-2N_{iz}C_{iy}^{\alpha}\Gamma_1(T) - 2N_{iz}C_{(i-1)y}^{\alpha}\Gamma_2(T)\right\}\cos(\Omega_{N_i}t_1), \qquad [7.131]$$

$$\sigma_d = \left\{4N_{iz}C_{iz}^{\alpha}C_{iy}'\Gamma_1(T) + 4N_{iz}C_{(i-1)z}^{\alpha}C_{(i-1)y}'\Gamma_2(T)\right\}\cos(\Omega_{N_i}t_1)\Gamma_3(2\delta_2), \qquad [7.132]$$

$$\sigma_e = \left\{4N_{iz}C_{iz}^{\alpha}C_{iy}'\cos(\Omega_{CO_i}t_2)\Gamma_1(T) + 4N_{iz}C_{(i-1)z}^{\alpha}C_{(i-1)y}'\cos(\Omega_{CO_{i-1}}t_2)\Gamma_2(T)\right\}\cos(\Omega_{N_i}t_1)\Gamma_3(2\delta_2), \qquad [7.133]$$

$$\sigma_f = H_{ix}^{N}\left\{\cos(\Omega_{CO_i}t_2)\Gamma_1^2(T).+\cos(\Omega_{CO_{i-1}}t_2)\Gamma_2^2(T)\right\}\cos(\Omega_{N_i}t_1)\Gamma_3^2(2\delta_2), \qquad [7.134]$$

in which $\delta = 1/(2J_{NH})$, and the coherence transfer functions, $\Gamma_1(t)$ and $\Gamma_2(t)$, are given by [7.100] and

$$\Gamma_3(t) = \sin(\pi J_{C^{\alpha}CO}t)\cos(\pi J_{C^{\alpha}C^{\beta}}t). \qquad [7.135]$$

As with the CT-HNCA experiment, the length of the constant-time evolution period, T, is typically chosen to be between 22 and 28 ms (Section 7.4.1.2). A value of 3.0–3.5 ms is optimal for δ_2.

The CT-HN(CA)CO pulse sequence illustrated in Fig. 7.41 differs slightly from the originally reported sequence (*92*), in which a refocused INEPT sequence (Section 2.7.7.3) is used to generate in-phase ^{15}N

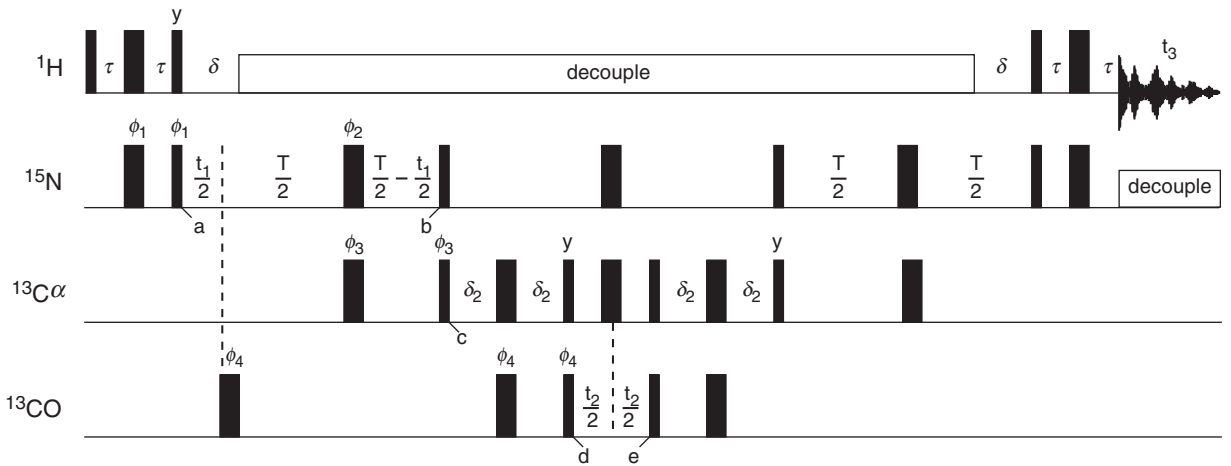

FIGURE 7.41 Pulse sequence for a constant-time HN(CA)CO experiment. Values of delays are described in the text. Other experimental details are similar to those given in Fig. 7.31. The phase cycle is $\phi_1 = x, -x$; $\phi_2 = 8(x), 8(y), 8(-x), 8(-y)$; $\phi_3 = 2(x), 2(-x)$; $\phi_4 = 4(x), 4(-x)$; and receiver $= x, -x, -x, x, 2(-x), x, x, -x\ x, -x, -x, x$. Quadrature detection in the t_1 and t_2 dimensions is achieved by incrementing independently the phases ϕ_1 and ϕ_4, respectively, and the receiver phase, in a TPPI–States manner.

magnetization prior to the constant-time evolution period, and to convert in-phase ^{15}N magnetization back into detectable ^{1}H magnetization immediately prior to acquisition. The experiment discussed here achieves the same magnetization state at times *b* and *e* (ignoring relaxation effects), but does so in less total evolution time and with four less 180° pulses; for these reasons, the sequence presented here is likely to be more sensitive than the originally proposed sequence.

The main shortcoming of the HN(CA)CO experiment is the low sensitivity that results from rapid relaxation of the transverse $^{13}C^{\alpha}$ magnetization during the delays δ_2. For $^{2}H/^{13}C/^{15}N$-labeled proteins, TROSY–HN(CA)CO experiments are substantially more sensitive because of the smaller dipolar $^{2}H–^{13}C^{\alpha}$ interaction (*88*). For $^{13}C/^{15}N$-labeled proteins, the straight-through (HCA)CONH experiment is more sensitive than the HN(CA)CO experiment (*93–95*).

7.4.5 CORRELATIONS WITH THE C^{β}/H^{β} SPINS

The triple-resonance experiments discussed thus far provide sequential connectivities along the peptide backbone. The HCCH experiments (Section 7.3) provide connectivities of the aliphatic side chains of individual amino acid residues. Complete assignments can be obtained if the backbone assignments and the side chain assignments can be connected using either the $^{1}H^{\alpha}$ or the $^{13}C^{\alpha}$ spins. Congestion in the $^{1}H^{\alpha}–^{13}C^{\alpha}$ region of the spectrum often renders this approach difficult. One solution to the problem combines HCCH-type magnetization transfer from the side chain to the $^{13}C^{\alpha}$ spin (using either COSY or TOCSY transfers) with a "straight-through" magnetization transfer from the $^{13}C^{\alpha}$ spin to the amide moiety of the following residue (*96–105*). The side chain assignments are connected thereby to the more highly resolved amide $^{1}H^{N}$ and ^{15}N spins. Two such experiments, CBCA(CO)NH and CBCANH, are discussed in the following sections. These straight-through experiments have out-and-back analogs, the HN(CO)CACB and HNCACB experiments. The HNCACB is discussed in the following sections as well. These experiments frequency label the ^{15}N magnetization as one of the dimensions of the 3D spectrum. The CBCACO(N)H (*106*) and CO_H(N)CACB (*107*) experiments frequency label the ^{13}CO magnetization rather than the ^{15}N magnetization to resolve resonance correlations overlapped in CBCA(CO)NH and HNCACB spectra. Correlations to side chain resonances beyond $^{1}H^{\beta}$ and $^{13}C^{\beta}$ are discussed in Sections 9.1.6 and 9.1.7.

The topology of the amino acid spin system affects coherence transfer in the CBCA(CO)NH, CBCANH, and HNCACB experiments

more strongly than do the triple-resonance experiments that only correlate backbone spins. In the following discussion, b is the number of $^{13}C^{\beta}$ nuclei in the spin system, g is number of resonant aliphatic $^{13}C^{\gamma}$ nuclei in the spin system, m is the number of $^{1}H^{\alpha}$ spins, and n is the number of $^{1}H^{\beta}$ spins in the spin system. The value of b is 0 for glycine and 1 for all other amino acids; the value of g is 0 for alanine, aspartic acid, asparagine, cysteine, and serine, 2 for valine and isoleucine, and 1 for all other residues (aromatic $^{13}C^{\gamma}$ spins may be perturbed by the aliphatic ^{13}C pulses); m is 2 for glycine and 1 for all other amino acids; and n is one for valine, isoleucine, and threonine and 2 for all other amino acids.

7.4.5.1 CBCA(CO)NH The CBCA(CO)NH experiment correlates both the $^{13}C^{\alpha}$ and the $^{13}C^{\beta}$ resonances of an amino acid residue with the amide ^{1}H and ^{15}N resonances of the following residue (*97*). These correlations are extremely useful if significant $^{13}C^{\alpha}$–$^{1}H^{\alpha}$ chemical shift degeneracy exists. In addition, the $^{13}C^{\alpha}$ and $^{13}C^{\beta}$ chemical shifts provide information on the type of amino acid preceding each amide (Chapter 10). As with the HCA(CO)N and HN(CO)CA experiments, interresidue correlations are established by transferring coherence via the intervening ^{13}CO spin. The pulse sequence for the CBCA(CO)NH experiment, which incorporates two constant-time evolution periods, is illustrated in Fig. 7.42. The relevant components of the density operator at the indicated time points in the pulse sequence are given by

$$\sigma_a = -2H_{iz}^{\alpha}C_{iy}^{\alpha} - 2H_{iz}^{\beta}C_{iy}^{\beta}, \qquad [7.136]$$

$$\sigma_b = C_{ix}^{\alpha}\cos(\Omega_{C_i^{\alpha}}t_1)\cos^{b}(\pi J_{C^{\alpha}C^{\beta}}T_{AB})m\Gamma_m(\delta_1) + 2C_{iy}^{\beta}C_{iz}^{\alpha}\cos(\Omega_{C_i^{\beta}}t_1)\sin(\pi J_{C^{\alpha}C^{\beta}}T_{AB})\cos^{g}(\pi J_{C^{\beta}C^{\gamma}}T_{AB})n\Gamma_n(\delta_1), \qquad [7.137]$$

$$\sigma_c = C_{ix}^{\alpha}\cos(\Omega_{C_i^{\alpha}}t_1)\cos^{b}(\pi J_{C^{\alpha}C^{\beta}}T_{AB})m\Gamma_m(\delta_1) - 2C_{iz}^{\beta}C_{iy}^{\alpha}\cos(\Omega_{C_i^{\beta}}t_1)\sin(\pi J_{C^{\alpha}C^{\beta}}T_{AB})\cos^{g}(\pi J_{C^{\beta}C^{\gamma}}T_{AB})n\Gamma_n(\delta_1), \qquad [7.138]$$

$$\sigma_d = 2C_{iy}^{\alpha}C'_{iz}\cos(\Omega_{C_i^{\alpha}}t_1)\cos^{b}(\pi J_{C^{\alpha}C^{\beta}}T_{AB})m\Gamma_m(\delta_1)\Gamma_{1A}(\delta_2) + 2C_{iy}^{\alpha}C'_{iz}\cos(\Omega_{C_i^{\beta}}t_1)\sin(\pi J_{C^{\alpha}C^{\beta}}T_{AB})\cos^{g}(\pi J_{C^{\beta}C^{\gamma}}T_{AB})n\Gamma_n(\delta_1)\Gamma_{1B}(\delta_2), \qquad [7.139]$$

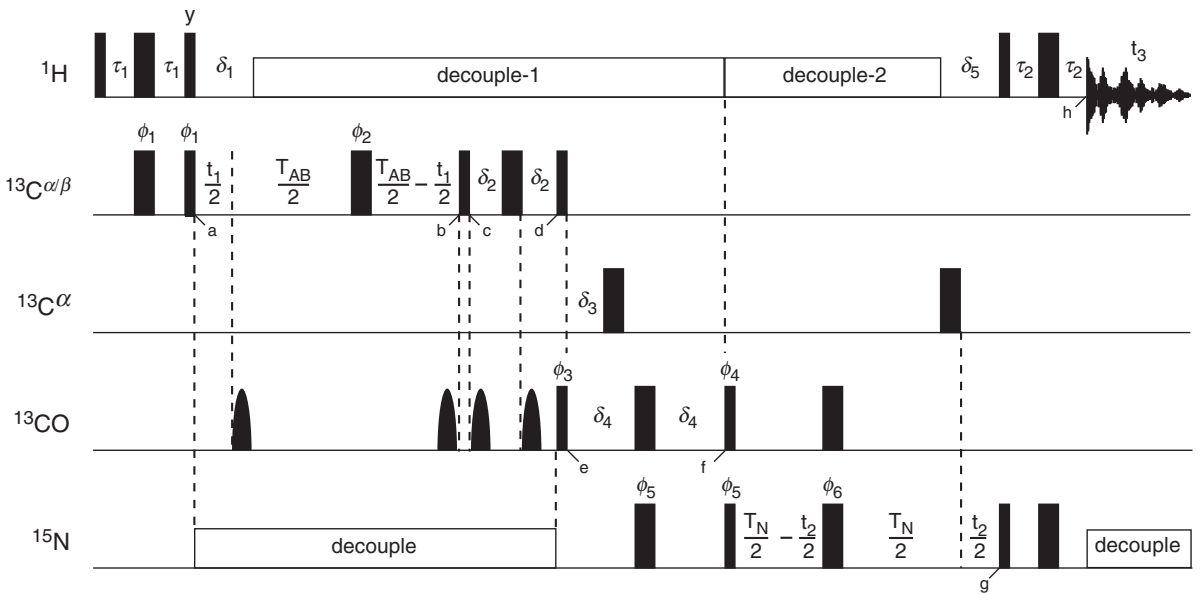

FIGURE 7.42 Pulse sequence for the CBCA(CO)NH experiment. Values of delays are described in the text. Rounded bars represent selective 180° pulses applied to ^{13}CO spins. Other experimental details are similar to those given in Fig. 7.31. The phase cycle is $\phi_1 = x, -x$; $\phi_2 = 8(x), 8(y), 8(-x), 8(-y)$; $\phi_3 = 4(x), 4(-x)$; $\phi_4 = x$ plus the off-resonance phase error calculated using [3.88] (see text); $\phi_5 = 2(x), 2(-x)$; $\phi_6 = 8(x), 8(-x)$; and receiver $= x, -x, -x, x, 2(-x, x, x, -x), x, -x, -x, x$. Quadrature detection in the t_1 and t_2 dimensions is achieved by incrementing independently the phases ϕ_1 and ϕ_5, respectively, and the receiver phase, in a TPPI–States manner.

$$\sigma_e = -2C^{\alpha}_{iz}C'_{iy}\cos(\Omega_{C^{\alpha}_i}t_1)\cos^b(\pi J_{C^{\alpha}C^{\beta}}T_{AB})m\Gamma_m(\delta_1)\Gamma_{1A}(\delta_2)$$
$$- 2C^{\alpha}_{iz}C'_{iy}\cos(\Omega_{C^{\beta}_i}t_1)\sin(\pi J_{C^{\alpha}C^{\beta}}T_{AB})$$
$$\times \cos^g(\pi J_{C^{\beta}C^{\gamma}}T_{AB})n\Gamma_n(\delta_1)\Gamma_{1B}(\delta_2), \qquad [7.140]$$

$$\sigma_f = 2C'_{iy}N_{(i+1)z}\Big\{\cos(\Omega_{C^{\alpha}_i}t_1)\cos^b(\pi J_{C^{\alpha}C^{\beta}}T_{AB})m\Gamma_m(\delta_1)\Gamma_{1A}(\delta_2)$$
$$+ \cos(\Omega_{C^{\beta}_i}t_1)\sin(\pi J_{C^{\alpha}C^{\beta}}T_{AB})\cos^g(\pi J_{C^{\beta}C^{\gamma}}T_{AB})n\Gamma_n(\delta_1)\Gamma_{1B}(\delta_2)\Big\}$$
$$\times \Gamma_2(\delta_3,\delta_4), \qquad [7.141]$$

$$\sigma_g = 2H^N_{(i+1)z}N_{(i+1)y}\Big\{\cos(\Omega_{C^{\alpha}_i}t_1)\cos^b(\pi J_{C^{\alpha}C^{\beta}}T_{AB})m\Gamma_m(\delta_1)\Gamma_{1A}(\delta_2)$$
$$+ \cos(\Omega_{C^{\beta}_i}t_1)\sin(\pi J_{C^{\alpha}C^{\beta}}T_{AB})\cos^g(\pi J_{C^{\beta}C^{\gamma}}T_{AB})n\Gamma_n(\delta_1)\Gamma_{1B}(\delta_2)\Big\}$$
$$\times \cos(\Omega_{N_{i+1}}t_2)\sin(\pi J_{NCO}T_N)\Gamma_2(\delta_3,\delta_4), \qquad [7.142]$$

$$\sigma_h = H^N_{(i+1)x}\Big\{\cos(\Omega_{C^{\alpha}_i}t_1)\cos^b(\pi J_{C^{\alpha}C^{\beta}}T_{AB})m\Gamma_m(\delta_1)\Gamma_{1A}(\delta_2)$$
$$+ \cos(\Omega_{C^{\beta}_i}t_1)\sin(\pi J_{C^{\alpha}C^{\beta}}T_{AB})\cos^g(\pi J_{C^{\beta}C^{\gamma}}T_{AB})n\Gamma_n(\delta_1)\Gamma_{1B}(\delta_2)\Big\}$$
$$\times \cos(\Omega_{N_{i+1}}t_2)\sin(\pi J_{NCO}T_N)\Gamma_2(\delta_3,\delta_4), \qquad [7.143]$$

in which $2\tau_1 = 1/(2J_{CH})$, $T_{AB} \approx 6.6$ ms to maximize coherence transfer for both $^{13}C^{\alpha}$ and $^{13}C^{\beta}$ spins, $T_N = 22$ ms, and $\delta_5 = 2\tau_2 = 1/(2J_{NH})$. The magnitudes of the coherence transfer functions, $\Gamma_n(\delta_1)$ and $\Gamma_m(\delta_1)$, are optimized for $\delta_1 = 2.2$ ms ([7.25] and Fig. 7.7). The magnitudes of the coherence transfer functions,

$$\Gamma_{1A}(\delta_2) = \cos^n(2\pi J_{C^{\alpha}C^{\beta}}\delta_2)\sin(2\pi J_{C^{\alpha}CO}\delta_2),$$
$$\Gamma_{1B}(\delta_2) = \sin(2\pi J_{C^{\alpha}C^{\beta}}\delta_2)\sin(2\pi J_{C^{\alpha}CO}\delta_2), \qquad [7.144]$$

are optimized simultaneously by setting $\delta_2 \approx 3.7$ ms. The coherence transfer function $\Gamma_2(\delta_3,\delta_4)$ is

$$\Gamma_2(\delta_3,\delta_4) = \sin(2\pi J_{C^{\alpha}CO}\delta_3)\sin(2\pi J_{NCO}\delta_4), \qquad [7.145]$$

in which $\delta_4 \approx 1/(6J_{NCO})$ to $1/(4J_{NCO})$, as required to minimize relaxation losses, and $\delta_3 = 1/(4J_{C^{\alpha}CO})$ ($\sim$4.5 ms). In the original description of

this experiment, a value of $\delta_4 = 11.4$ ms was demonstrated to be suitable for a 31-kDa protein (*97*).

All $^{13}C^{\alpha/\beta}$ pulses in the CBCA(CO)NH experiment are applied near the center of the $^{13}C^{\alpha}$ and $^{13}C^{\beta}$ chemical shift range in order to maximize excitation of the $^{13}C^{\alpha}$ and $^{13}C^{\beta}$ spins, and the power of these pulses is adjusted in order to minimize their effect on the ^{13}CO spins (i.e., for 90° pulses, $\gamma B_1 = \Omega/\sqrt{15}$, and for 180° pulses, $\gamma B_1 = \Omega/\sqrt{3}$; Section 3.4.1). The two 180°($^{13}C^{\alpha}$) pulses in this experiment are applied in the center of the $^{13}C^{\alpha}$ chemical shift region to maximize their effect on these nuclei, and the power of these pulses is adjusted such that they do not perturb the ^{13}CO spins (i.e., $\gamma B_1 = \Omega/\sqrt{3}$; Section 3.4.1). At time *f* the position of the ^{1}H carrier (and hence the frequency of the ^{1}H broadband decoupling) is shifted from the water resonance to the center of the amide region.

The second shaped selective 180°(^{13}CO) pulse, applied immediately before time *b*, serves to eliminate phase error induced by the off-resonance effects of the first such pulse on the transverse ^{13}C magnetization (Section 3.4.1), and thus ensures pure cosinusoidal modulation in the t_1 dimension. The 180°($^{13}C^{\alpha}$) pulse applied between time points *e* and *f* results in a change in the ^{13}CO phase due to the off-resonant effect of this pulse (Section 3.4.1). This phase error, which can be approximated using [3.88], can be compensated for by an adjustment of the phase of the 90°(^{13}CO) pulse immediately following time *f* (ϕ_6); the phase of this pulse should be set to *x* plus the off-resonance phase error, in order to fully transfer ^{13}CO magnetization to the ^{15}N spins.

Selected $F_2(^{15}N)$ slices from a CBCA(CO)NH spectrum of ubiquitin are shown in Fig. 7.43. Two resonances are observed at the $F_1(^{13}C)$ frequencies of the $^{13}C^{\alpha}$ and $^{13}C^{\beta}$ spins of residue *i* and the $F_3(^{1}H_N)$ frequency of residue $i+1$ for all amino acid residues except glycine (which has only a single resonance corresponding the $^{13}C^{\alpha}$ spin).

With relatively minor modifications, the CBCA(CO)NH experiment can be converted to an experiment that correlates the $^{1}H^{N}$ and ^{15}N resonances of one residue with the $^{1}H^{\alpha}$ and $^{1}H^{\beta}$ resonances of the preceding residue; such a pulse scheme has been called the HBHA(CBCACO)NH experiment (*96*). However, this experiment alone does not provide unambiguous assignment of the $^{1}H^{\alpha}$ and $^{1}H^{\beta}$ resonances to amino acid type, because such assignments generally cannot be made on the basis of ^{1}H chemical shifts alone.

7.4.5.2 CBCANH The CBCANH experiment correlates the $^{13}C^{\alpha}$ and $^{13}C^{\beta}$ resonances with the amide ^{1}H and ^{15}N resonances of the same residue and the amide ^{1}H and ^{15}N resonances of the succeeding residue

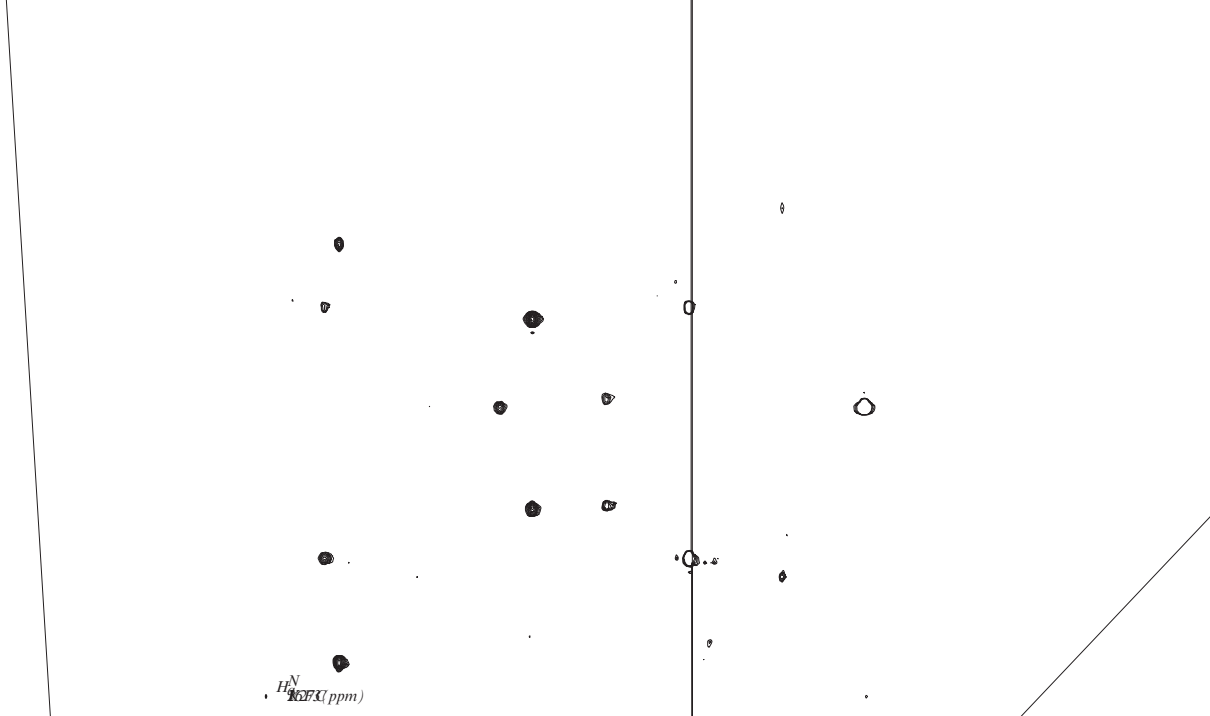

via the $^{1}J_{C^{\alpha}N}$ and $^{2}J_{C^{\alpha}N}$ couplings, respectively (*98*). For proteins up to ~20 kDa, this experiment alone can provide virtually complete sequential assignment of the $^{1}H^{N}$, ^{15}N, $^{13}C^{\alpha}$, and $^{13}C^{\beta}$ resonances, because in addition to the sequential connectivities, the $^{13}C^{\alpha}$ and $^{13}C^{\beta}$ chemical shifts provide information on the amino acid type. The pulse sequence for the CBCANH experiment is illustrated in Fig. 7.44. As with the closely related CBCA(CO)NH experiment already discussed, the CBCANH experiment utilizes two constant-time evolution periods.

The evolution in the CBCANH experiment up to time *c* (Fig. 7.44) is identical to that found for the CBCA(CO)NH experiment (Fig. 7.42). The magnetization present at times *a*, *b*, and *c* in Fig. 7.44 is therefore described by operators [7.136], [7.137], and [7.138], respectively. The relevant components of the density operator at the time points *d*–*g*

in the pulse sequence are given by

$$\begin{aligned}\sigma_d = {} & 2C_{iy}^{\alpha}N_{iz}\Big\{\cos(\Omega_{C_i^a}t_1)\,\cos^b(\pi J_{C^\alpha C^\beta}T_{AB})m\Gamma_m(\delta_1)\Gamma_{1A}(\delta_2)\\ & +\cos(\Omega_{C_i^\beta}t_1)\,\sin(\pi J_{C^\alpha C^\beta}T_{AB})\,\cos^g(\pi J_{C^\beta C^\gamma}T_{AB})n\Gamma_n(\delta_1)\Gamma_{1B}(\delta_2)\Big\}\\ & +2C_{iy}^{\alpha}N_{(i+1)z}\Big\{\cos(\Omega_{C_i^a}t_1)\,\cos^b(\pi J_{C^\alpha C^\beta}T_{AB})m\Gamma_m(\delta_1)\Gamma_{2A}(\delta_2)\\ & +\cos(\Omega_{C_i^\beta}t_1)\,\sin(\pi J_{C^\alpha C^\beta}T_{AB})\,\cos^g(\pi J_{C^\beta C^\gamma}T_{AB})n\Gamma_n(\delta_1)\Gamma_{2B}(\delta_2)\Big\},\end{aligned} \tag{7.146}$$

$$\begin{aligned}\sigma_e = {} & -2C_{iz}^{\alpha}N_{iy}\Big\{\cos(\Omega_{C_i^a}t_1)\,\cos^b(\pi J_{C^\alpha C^\beta}T_{AB})m\Gamma_m(\delta_1)\Gamma_{1A}(\delta_2)\\ & +\cos(\Omega_{C_i^\beta}t_1)\,\sin(\pi J_{C^\alpha C^\beta}T_{AB})\,\cos^g(\pi J_{C^\beta C^\gamma}T_{AB})n\Gamma_n(\delta_1)\Gamma_{1B}(\delta_2)\Big\}\\ & -2C_{iz}^{\alpha}N_{(i+1)y}\Big\{\cos(\Omega_{C_i^a}t_1)\,\cos^b(\pi J_{C^\alpha C^\beta}T_{AB})m\Gamma_m(\delta_1)\Gamma_{2A}(\delta_2)\\ & +\cos(\Omega_{C_i^\beta}t_1)\,\sin(\pi J_{C^\alpha C^\beta}T_{AB})\,\cos^g(\pi J_{C^\beta C^\gamma}T_{AB})n\Gamma_n(\delta_1)\Gamma_{2B}(\delta_2)\Big\},\end{aligned} \tag{7.147}$$

$$\begin{aligned}\sigma_f = {} & 2H_{iz}^{N}N_{iy}\Big\{\cos(\Omega_{C_i^a}t_1)\,\cos^b(\pi J_{C^\alpha C^\beta}T_{AB})m\Gamma_m(\delta_1)\Gamma_{1A}(\delta_2)\\ & +\cos(\Omega_{C_i^\beta}t_1)\,\sin(\pi J_{C^\alpha C^\beta}T_{AB})\,\cos^g(\pi J_{C^\beta C^\gamma}T_{AB})n\Gamma_n(\delta_1)\Gamma_{1B}(\delta_2)\Big\}\\ & \times\cos\big(\Omega_{N_i}t_2\big)\Gamma_1(T_N)\\ & +2H_{(i+1)z}^{N}N_{(i+1)y}\Big\{\cos(\Omega_{C_i^a}t_1)\,\cos^b(\pi J_{C^\alpha C^\beta}T_{AB})m\Gamma_m(\delta_1)\Gamma_{2A}(\delta_2)\\ & +\cos(\Omega_{C_i^\beta}t_1)\,\sin(\pi J_{C^\alpha C^\beta}T_{AB})\,\cos^g(\pi J_{C^\beta C^\gamma}T_{AB})n\Gamma_n(\delta_1)\Gamma_{2B}(\delta_2)\Big\}\\ & \times\cos\big(\Omega_{N_{i+1}}t_2\big)\Gamma_2(T_N),\end{aligned} \tag{7.148}$$

$$\begin{aligned}\sigma_g = {} & H_{ix}^{N}\Big\{\cos(\Omega_{C_i^a}t_1)\,\cos^b(\pi J_{C^\alpha C^\beta}T_{AB})m\Gamma_m(\delta_1)\Gamma_{1A}(\delta_2)\\ & +\cos(\Omega_{C_i^\beta}t_1)\,\sin(\pi J_{C^\alpha C^\beta}T_{AB})\,\cos^g(\pi J_{C^\beta C^\gamma}T_{AB})n\Gamma_n(\delta_1)\Gamma_{1B}(\delta_2)\Big\}\\ & \times\cos\big(\Omega_{N_i}t_2\big)\Gamma_1(T_N)\\ & +H_{(i+1)x}^{N}\Big\{\cos(\Omega_{C_i^a}t_1)\,\cos^b(\pi J_{C^\alpha C^\beta}T_{AB})m\Gamma_m(\delta_1)\Gamma_{2A}(\delta_2)\\ & +\cos(\Omega_{C_i^\beta}t_1)\,\sin(\pi J_{C^\alpha C^\beta}T_{AB})\,\cos^g(\pi J_{C^\beta C^\gamma}T_{AB})n\Gamma_n(\delta_1)\Gamma_{2B}(\delta_2)\Big\}\\ & \times\cos\big(\Omega_{N_{i+1}}t_2\big)\Gamma_2(T_N).\end{aligned} \tag{7.149}$$

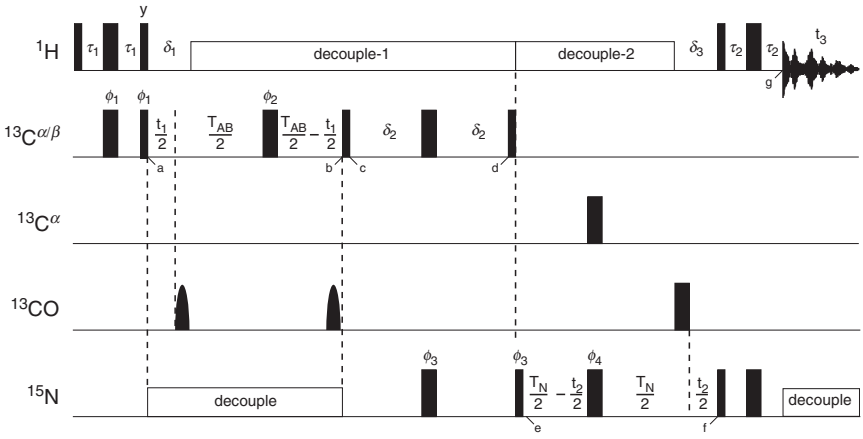

FIGURE 7.44 Pulse sequence for the CBCANH experiment. Values of delays are described in the text. Rounded bars represent selective 180° pulses applied to ^{13}CO spins. Other experimental details are similar to those given in Fig. 7.31. The phase cycle is $\phi_1 = x, -x$; $\phi_2 = 4(x), 4(y), 4(-x), 4(-y)$; $\phi_3 = 2(x), 2(-x)$; $\phi_4 = 8(x), 8(-x)$; receiver $= x, -x, -x$, x, $-x$, x, x, $-x$. Quadrature detection in the t_1 and t_2 dimensions is achieved by incrementing independently the phases ϕ_1 and ϕ_3, respectively, and the receiver phase, in a TPPI–States manner.

The coherence transfer functions $\Gamma_{1A}(\delta_2)$, $\Gamma_{2A}(\delta_2)$, $\Gamma_{1B}(\delta_2)$, and $\Gamma_{2B}(\delta_2)$ are given by

$$\begin{aligned}
\Gamma_{1A}(\delta_2) &= \sin(2\pi {}^1J_{C^\alpha N}\delta_2)\cos(2\pi {}^2J_{C^\alpha N}\delta_2)\cos^n(2\pi J_{C^\alpha C^\beta}\delta_2),\\
\Gamma_{2A}(\delta_2) &= \cos(2\pi {}^1J_{C^\alpha N}\delta_2)\sin(2\pi {}^2J_{C^\alpha N}\delta_2)\cos^n(2\pi J_{C^\alpha C^\beta}\delta_2),\\
\Gamma_{1B}(\delta_2) &= \sin(2\pi {}^1J_{C^\alpha N}\delta_2)\cos(2\pi {}^2J_{C^\alpha N}\delta_2)\sin(2\pi J_{C^\alpha C^\beta}\delta_2),\\
\Gamma_{2B}(\delta_2) &= \cos(2\pi {}^1J_{C^\alpha N}\delta_2)\sin(2\pi {}^2J_{C^\alpha N}\delta_2)\sin(2\pi J_{C^\alpha C^\beta}\delta_2).
\end{aligned} \qquad [7.150]$$

The magnitudes of these transfer functions are optimized simultaneously by setting δ_2 to 11 ms, as indicated in Fig. 7.45. The coherence transfer functions $\Gamma_1(T_N)$ and $\Gamma_2(T_N)$ are given by [7.100]. As indicated by Fig. 7.32, $\Gamma_1(T_N)$ is maximized by setting T_N to between 22 and 28 ms. Following time d, the position of the ^{1}H carrier and hence the frequency of the ^{1}H broadband decoupling is shifted from the water resonance to the center of the amide region. As usual, the 180°($^{13}C^{\alpha/\beta}$) pulse power is adjusted such that it does not perturb the ^{13}CO spins.

Each given amide proton will have correlations to its intraresidue $^{13}C^\alpha$ and $^{13}C^\beta$ nuclei and to the $^{13}C^\alpha$ and $^{13}C^\beta$ of the preceding residue.

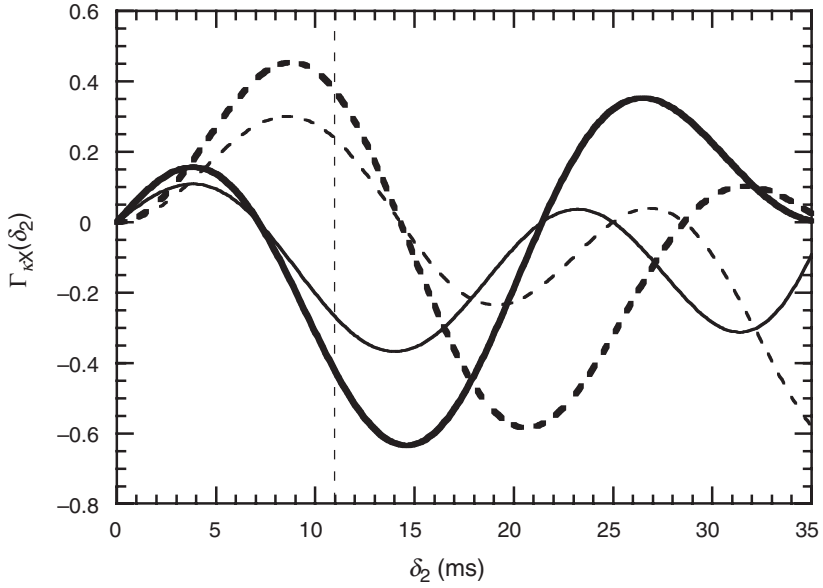

FIGURE 7.45 Plots of the CBCANH coherence transfer functions, $\Gamma_{1A}(\delta_2)$ (—, thick), $\Gamma_{2A}(\delta_2)$ (—, thin), $\Gamma_{1B}(\delta_2)$ (- - -, thick), and $\Gamma_{2B}(\delta_2)$ (- - -, thin) [7.150], for $^1J_{C^\alpha N^1}$, $^2J_{C^\alpha N^2}$, and $^1J_{C^\alpha C^\beta}$ coupling constants of 10, 7, and 35 Hz, respectively. The dashed vertical line at 11 ms indicates the optimal value of δ_2 to maximize all four transfer functions simultaneously.

With the exception of glycine residues, for which the exponent b is 0, the $\Gamma_{1A}(\delta_2)$ and $\Gamma_{2A}(\delta_2)$ functions have signs opposite to the sign of $\Gamma_{1B}(\delta_2)$ and $\Gamma_{2B}(\delta_2)$ (Fig. 7.45). This feature is helpful in the final spectrum because the $^{13}C^\alpha$ resonances of glycines and all $^{13}C^\beta$ resonances have opposite phase relative to the other $^{13}C^\alpha$ resonances. This feature of the CBCANH is particularly useful for discriminating between the $^{13}C^\alpha$ and $^{13}C^\beta$ resonances of serine and threonine residues, which resonate in the same spectral region. A CBCANH spectrum of ubiquitin is shown in Fig. 7.46. Identification of the intra- and interresidue connectivities on the basis of resonance intensities in the CBCANH experiment is subject to the same uncertainties as discussed for the HNCA experiment (Section 7.4.1).

As with the CBCA(CO)NH experiment, relatively minor modifications can be made to the CBCANH experiment, to produce an experiment that provides correlations to the $^1H^\alpha$ and $^1H^\beta$ resonances rather than to the $^{13}C^\alpha$ and $^{13}C^\beta$ resonances; this experiment has been called the HBHA(CBCA)NH experiment (*99*). In contrast to the

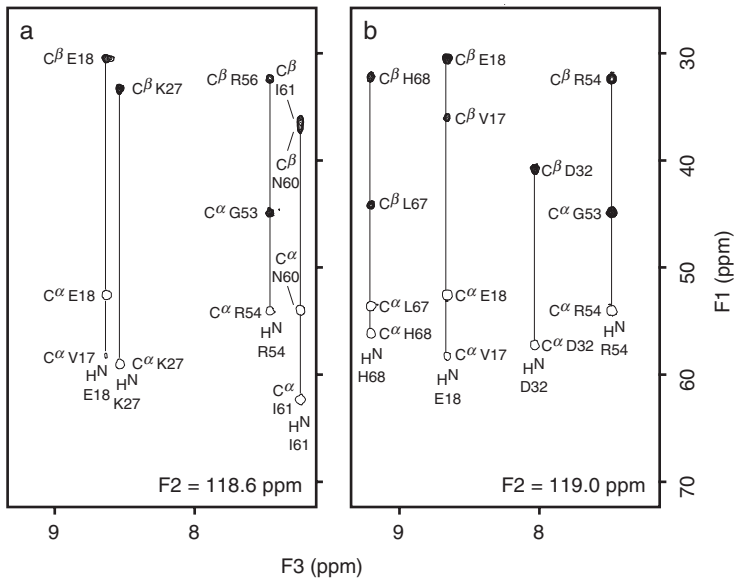

FIGURE 7.46 CBCANH spectrum of ubiquitin. Selected (adjacent) $F_1(^{13}C)$–$F_3(^1H^N)$ slices from a 3D CBCANH spectrum of $^{15}N/^{13}C$-labeled ubiquitin at $F_2(^{15}N)$ chemical shifts of (a) 118.6 ppm and (b) 119.0 ppm. Correlations to $^{13}C^{\beta}$ nuclei and the $^{13}C^{\alpha}$ of glycines are plotted with multiple contours while those to the remaining $^{13}C^{\alpha}$ nuclei, which have opposite phase, are plotted with a single contour. Cross-peak assignments are indicated.

HBHA(CBCACO)NH experiment (*96*), the $^1H^{\alpha}$ and $^1H^{\beta}$ resonances in an HBHA(CBCA)NH spectrum are easily identified, as they have opposite phase (the $^1H^{\alpha}$ resonances of glycine residues also have phase opposite to those of all other $^1H^{\alpha}$ resonances).

7.4.5.3 HNCACB Shortly after development of the straight-through CBCANH experiment, the out-and-back HNCAB experiment was developed as an alternative approach for obtaining correlations between the amide moiety and the $^{13}C^{\alpha}$ and $^{13}C^{\beta}$ spins. The HNCACB has two advantages compared with the earlier approach: (*i*) the time for which transverse ^{13}C magnetization is present is shorter, resulting in increased sensitivity, and (*ii*) the experiment is applicable to larger proteins in which carbon sites have been perdeuterated. A pulse sequence for the HNCACB experiment is shown in Fig. 7.47. This pulse sequence shares many aspects of the decoupled HNCA experiment discussed in Section 7.4.1.3.

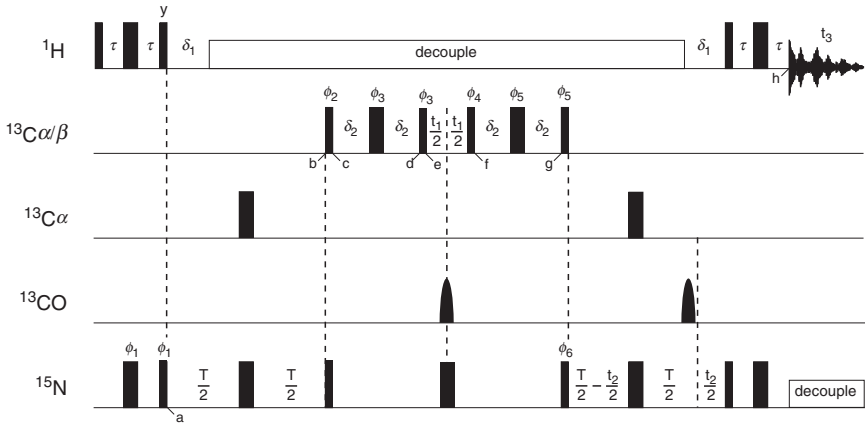

FIGURE 7.47 Pulse sequence for the HNCACB experiment. Values of delays are described in the text. Rounded bars represent selective 180° pulses applied to ^{13}CO spins. Other experimental details are similar to those given in Fig. 7.31. The phase cycle is $\phi_1 = x, -x$; $\phi_2 = 2(x), 2(-x)$; $\phi_3 = y$; $\phi_4 = y$; $\phi_5 = x$; $\phi_6 = 4(x), 4(-x)$; receiver $= x, -x, -x, x, -x, x, x, -x$. Quadrature detection during t_1 is obtained by TPPI–States protocol applied to pulse phases ϕ_2, ϕ_3, and the receiver. Quadrature detection during t_2 is obtained by TPPI–States protocol applied to pulse phases ϕ_6 and the receiver. The phase rotation induced by the nonresonant effects of the 180° pulse applied to the ^{13}CO spins during t_1 can be compensated by adding a correction to pulse phases ϕ_4 and ϕ_5 (Section 3.4.1).

At point *a*, the density operator is given by

$$\sigma_a = -2H_{iz}^N N_{iy} \qquad [7.151]$$

for $\tau = 1/(4J_{\mathrm{NH}})$. This operator is converted during the subsequent T period to

$$\sigma_b = -2N_{iy}C_{iz}^{\alpha}\Gamma_1(T) - 2N_{iy}C_{(i-1)z}^{\alpha}\Gamma_2(T) \qquad [7.152]$$

at point *b*, in which $\Gamma_1(T)$ and $\Gamma_2(T)$ are given in [7.100]. As in the decoupled HNCA experiment, $T = 22$–28 ms and $\delta_1 = 1/(2J_{\mathrm{NH}})$. Antiphase coherence with respect to the ^{15}N spin is converted to antiphase coherence with respect to the $^{13}C^{\alpha}$ spins at point *c* by the simultaneous 90°(^{15}N) and 90°($^{13}C^{\alpha}$) pulses:

$$\sigma_c = 2N_{iz}C_{iy}^{\alpha}\Gamma_1(T) + 2N_{iz}C_{(i-1)y}^{\alpha}\Gamma_2(T). \qquad [7.153]$$

During the following $2\delta_2$ element, the $J_{C^\alpha C^\beta}$ scalar coupling is active because the 180° pulse is nonselective for the $^{13}C^\alpha$ and $^{13}C^\beta$ spins (in practice, this pulse frequently is applied as a composite element to obtain the best possible inversion). Evolution under the scalar coupling Hamiltonian yields, at point *d*,

$$\begin{aligned}\sigma_d = &-2N_{iz}C^\alpha_{iy}\Gamma_1(T)\cos^{b_i}(2\pi J_{C^\alpha C^\beta}\delta_2) + b_i 4N_{iz}C^\alpha_{ix}C^\beta_{iz}\Gamma_1(T)\sin(2\pi J_{C^\alpha C^\beta}\delta_2)\\ &- 2N_{iz}C^\alpha_{(i-1)y}\Gamma_2(T)\cos^{b_{i-1}}(2\pi J_{C^\alpha C^\beta}\delta_2)\\ &+ b_{i-1}4N_{iz}C^\alpha_{(i-1)x}C^\beta_{(i-1)z}\Gamma_2(T)\sin(2\pi J_{C^\alpha C^\beta}\delta_2),\end{aligned} \quad [7.154]$$

in which b_i is the number of C^β spins within the *i*th spin system ($b_i = 0$ for glycine residues and 1 for other residues). The relative magnitudes of the two- and three-spin operators are determined by the value of δ_2. If $\delta_2 = 1/(8J_{C^\alpha C^\beta})$, then the magnitudes of the operators are approximately equal and correlations to both the $^{13}C^\alpha$ and the $^{13}C^\beta$ spins are observed in the final spectrum. If $\delta_2 = 1/(4J_{C^\alpha C^\beta})$, then the magnitudes of the two-spin operators are approximately zero and correlations to $^{13}C^\beta$ spins are observed in the final spectrum with maximum magnitude (ignoring the effects of relaxation). However, the longer δ_2 delay incurs significant relaxation losses from transverse relaxation of the $^{13}C^\alpha$ spins and, except for very small proteins, is most often utilized for perdeuterated proteins.

The 90°_y pulse following point *d* generates the coherences

$$\begin{aligned}\sigma_e = &-2N_{iz}C^\alpha_{iy}\Gamma_1(T)\cos^{b_i}(2\pi J_{C^\alpha C^\beta}\delta_2) - b_i 4N_{iz}C^\alpha_{iz}C^\beta_{ix}\Gamma_1(T)\sin(2\pi J_{C^\alpha C^\beta}\delta_2)\\ &- 2N_{iz}C^\alpha_{(i-1)y}\Gamma_2(T)\cos^{b_{i-1}}(2\pi J_{C^\alpha C^\beta}\delta_2)\\ &- b_{i-1}4N_{iz}C^\alpha_{(i-1)z}C^\beta_{(i-1)x}\Gamma_2(T)\sin(2\pi J_{C^\alpha C^\beta}\delta_2),\end{aligned} \quad [7.155]$$

which evolve under the free-precession Hamiltonian during the t_1 period. The 90°_y pulse after the t_1 period yields, at point *f*,

$$\begin{aligned}\sigma_f = &-2N_{iz}C^\alpha_{iy}\Gamma_1(T)\cos^{b_i}(2\pi J_{C^\alpha C^\beta}\delta_2)\cos(\Omega_{C^\alpha_i}t_1)\cos^{b_i}(\pi J_{C^\alpha C^\beta}t_1)\\ &+ b_i 4N_{iz}C^\alpha_{ix}C^\beta_{iz}\Gamma_1(T)\sin(2\pi J_{C^\alpha C^\beta}\delta_2)\cos(\Omega_{C^\beta_i}t_1)\cos^{b_i}(\pi J_{C^\alpha C^\beta}t_1)\\ &\times\cos^{g_i}(\pi J_{C^\alpha C^\gamma}t_1) - 2N_{iz}C^\alpha_{(i-1)y}\Gamma_2(T)\cos^{b_{i-1}}(2\pi J_{C^\alpha C^\beta}\delta_2)\cos(\Omega_{C^\alpha_{i-1}}t_1)\\ &\times\cos^{b_{i-1}}(\pi J_{C^\alpha C^\beta}t_1) + b_{i-1}4N_{iz}C^\alpha_{(i-1)x}C^\beta_{(i-1)z}\Gamma_2(T)\sin(2\pi J_{C^\alpha C^\beta}\delta_2)\\ &\times\cos(\Omega_{C^\beta_{i-1}}t_1)\cos^{b_{i-1}}(\pi J_{C^\alpha C^\beta}t_1)\cos^{g_{i-1}}(\pi J_{C^\alpha C^\gamma}t_1),\end{aligned} \quad [7.156]$$

in which g_i is the number of C^{γ} spins within the ith spin system. The maximum value of t_1 is set relatively short (<10 ms) to avoid resolving homonuclear ^{13}C scalar coupling multiplets.

The preceding operators are refocused during the second $2\delta_2$ period to yield, at point g,

$$\begin{aligned}\sigma_g = {} & 2N_{iz}C^{\alpha}_{iy}\Gamma_1(T)\cos^{b_i}(\pi J_{C^{\alpha}C^{\beta}}t_1)\{\cos^{2b_i}(2\pi J_{C^{\alpha}C^{\beta}}\delta_2)\cos(\Omega_{C^{\alpha}_i}t_1) \\ & - b_i\sin^2(2\pi J_{C^{\alpha}C^{\beta}}\delta_2)\cos(\Omega_{C^{\beta}_i}t_1)\cos^{g_i}(\pi J_{C^{\alpha}C^{\gamma}}t_1)\} \\ & + 2N_{iz}C^{\alpha}_{(i-1)y}\Gamma_2(T)\cos^{b_{i-1}}(\pi J_{C^{\alpha}C^{\beta}}t_1)\{\cos^{2b_{i-1}}(2\pi J_{C^{\alpha}C^{\beta}}\delta_2)\cos(\Omega_{C^{\alpha}_{i-1}}t_1) \\ & - b_{i-1}\sin^2(2\pi J_{C^{\alpha}C^{\beta}}\delta_2)\cos(\Omega_{C^{\beta}_{i-1}}t_1)\cos^{g_{i-1}}(\pi J_{C^{\alpha}C^{\gamma}}t_1)\}.\end{aligned} \quad [7.157]$$

The relative signs of the terms in brackets indicate that the correlation peaks for $^{13}C^{\alpha}$ and $^{13}C^{\beta}$ spins have opposite signs in the final HNCACB spectrum. This feature facilitates distinguishing such correlations. However, unlike most triple-resonance experiments, if $\delta_2 = 1/(8J_{C^{\alpha}C^{\beta}})$, then the initial signal intensity is approximately zero when $t_1 = 0$. The remainder of the pulse sequence frequency labels the coherences with the ^{15}N chemical shift during a constant-time evolution period and transfers the resulting coherence to the $^{1}H^{N}$ spin for detection. The final operator of interest prior to acquisition, at point h, is

$$\begin{aligned}\sigma_h = {} & H^{N}_{ix}\cos(\Omega_{N_i}t_2)\{\Gamma_1^2(T)\cos^{2b_i}(2\pi J_{C^{\alpha}C^{\beta}}\delta_2)\cos(\Omega_{C^{\alpha}_i}t_1)\cos^{b_i}(\pi J_{C^{\alpha}C^{\beta}}t_1) \\ & - b_i\Gamma_1^2(T)\sin^2(2\pi J_{C^{\alpha}C^{\beta}}\delta_2)\cos(\Omega_{C^{\beta}_i}t_1)\cos^{b_i}(\pi J_{C^{\alpha}C^{\beta}}t_1)\cos^{g_i}(\pi J_{C^{\alpha}C^{\gamma}}t_1) \\ & + \Gamma_2^2(T)\cos^{2b_{i-1}}(2\pi J_{C^{\alpha}C^{\beta}}\delta_2)\cos(\Omega_{C^{\alpha}_{i-1}}t_1)\cos^{b_{i-1}}(\pi J_{C^{\alpha}C^{\beta}}t_1) \\ & - b_{i-1}\Gamma_2^2(T)\sin^2(2\pi J_{C^{\alpha}C^{\beta}}\delta_2)\cos(\Omega_{C^{\beta}_{i-1}}t_1)\cos^{b_{i-1}}(\pi J_{C^{\alpha}C^{\beta}}t_1) \\ & \times\cos^{g_{i-1}}(\pi J_{C^{\alpha}C^{\gamma}}t_1)\}.\end{aligned} \quad [7.158]$$

An HNCACB spectrum of ubiquitin is shown in Fig. 7.48. Identification of the intra- and interresidue connectivities on the basis of resonance intensities in the HNCACB experiment is subject to the same uncertainties discussed for the HNCA experiment (Section 7.4.1).

In combination, the HBHA(CBCA)NH, HBHA(CBCACO)NH, CBCANH, and CBCA(CO)NH experiments can provide complete sequential assignments of the $^{1}H^{N}$, ^{15}N, $^{1}H^{\alpha}$, $^{13}C^{\alpha}$, $^{1}H^{\beta}$, and $^{13}C^{\beta}$ resonances for proteins up to about 20 kDa. A major limitation of the CBCANH and HBHA(CBCA)NH experiments, however, is that they are relatively insensitive. The sensitivity of these two experiments

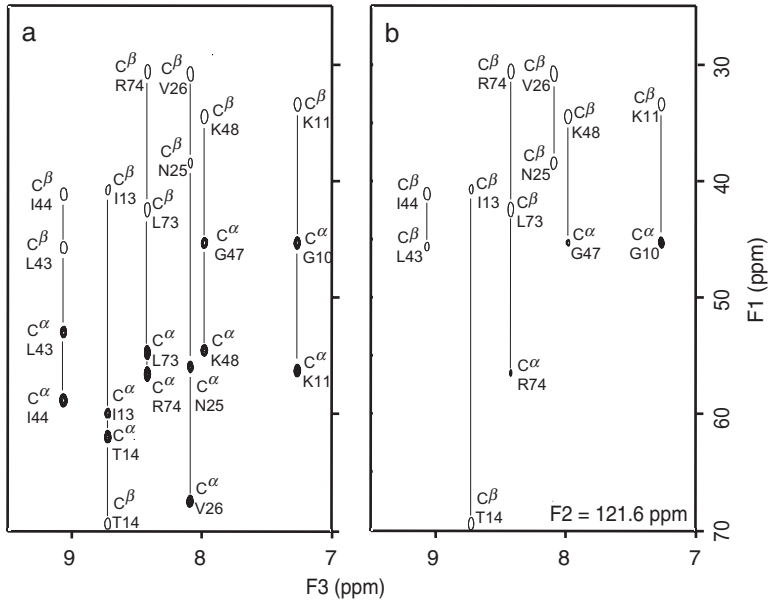

FIGURE 7.48 HNCACB spectrum of ubiquitin. Selected $F_1(^{13}C)$–$F_3(^1H^N)$ slices from 600-MHz 3D HNCACB spectra of $^{15}N/^{13}C$-labeled ubiquitin at an $F_2(^{15}N)$ chemical shift of 121.6 ppm. (a) $\delta_2 = 3.5$ ms to obtain correlations to both $^{13}C^{\alpha}$ and $^{13}C^{\beta}$ spins. (b) $\delta_2 = 7.0$ ms to obtain correlations primarily to the $^{13}C^{\beta}$ spins. Correlations to $^{13}C^{\alpha}$ nuclei are plotted with multiple contours while those to the $^{13}C^{\beta}$ nuclei, which have opposite phase, are plotted with a single contour. Cross-peak assignments are indicated.

is limited by the transverse relaxation rate of $^{13}C^{\alpha}$ magnetization. For larger proteins (>20 kDa), observation of a complete set of interresidue correlations is therefore unlikely. For larger proteins that have been perdeuterated at carbon sites, the HNCACB and HN(CO)CACB experiments (*5*) are preferable (see Chapter 9).

7.4.6 ADDITIONAL CONSIDERATIONS FOR TRIPLE-RESONANCE EXPERIMENTS

Unless otherwise noted above, $^{13}C^{\alpha}$ (^{13}CO) pulses are applied with the transmitter frequency in the middle of the $^{13}C^{\alpha}$ (^{13}CO) region of the spectrum. The field strengths of the $^{13}C^{\alpha}$ 90° and 180° pulses

are adjusted to minimally excite the ^{13}CO spins (i.e., $\gamma B_1 = \Omega/\sqrt{15}$ or $\Omega/\sqrt{3}$ for 90° and 180° pulses, respectively, in which Ω is the frequency difference between the $^{13}C^{\alpha}$ and ^{13}CO spectral regions; Section 3.4.1). Similarly, the ^{13}CO pulses are applied as selective shaped pulses or as weak rectangular pulses, with field strengths adjusted such that the $^{13}C^{\alpha}$ spins remain unperturbed. Nonresonant effects of the ^{13}CO pulses are compensated using the techniques presented in Section 3.4.1 and as discussed in the descriptions of individual triple-resonance experiments.

Frequency discrimination in indirectly detected dimensions usually is achieved using the TPPI–States protocol (Section 4.3.4.1). The phase shifts are applied to *all* the pulses preceding the evolution period that are applied to the spin whose coherence is being frequency labeled. Normally, the initial value of the sampling delay is adjusted to exactly 1/(2SW) as described in Section 3.3.2.3.

Most triple-resonance experiments (particularly constant-time versions) yield in-phase absorptive lineshapes. Consequently, the discussion of processing HSQC spectra (Section 7.1.2.4) is applicable. The data are truncated in the t_1 and t_2 dimensions of triple-resonance experiments and linear prediction or maximum entropy reconstruction usually will be utilized. A secondary problem is that most experiments using a non-constant-time frequency labeling of the $^{13}C^{\alpha}$ spins contain a contribution from passive coupling to the $^{13}C^{\beta}$ spins. In these cases, the total acquisition time is limited to less than $1/(2J_{CC})$ to avoid resolution of the scalar coupling and loss of sensitivity. The effect of the coupling can be eliminated by multiplication of the interferogram by the function $\cos^{-1}(\pi J_{CC} t_1)$ or $\cos^{-1}(\pi J_{CC} t_2)$ as relevant prior to linear prediction or maximum entropy reconstruction.

The preceding analyses of triple-resonance NMR experiments have focused on 3D versions of the experiments; however, most of the 3D experiments can be converted into 4D experiments by inserting an additional evolution period. Generally, equivalent information can be obtained from a pair of complementary three-dimensional NMR experiments or a single four-dimensional experiment. The greater resolution in the indirect dimensions of 3D experiments, compared with 4D experiments, facilitates more accurate determination of resonance frequencies during the assignment process (Chapter 10). However, 4D triple resonance experiments have the advantage that assignments are obtained from a single spectrum, whereas the two 3D experiments would be acquired at different times (with possible slight variations in conditions). In practice, a mix of 3D and 4D experiments typically would be used in obtaining resonance assignments.

7.5 Measurement of Scalar Coupling Constants

Homo- and heteronuclear three-bond J coupling constants are important for establishing local backbone and side chain conformations in proteins; in particular, information on the backbone dihedral angle ϕ and the side chain torsion angle χ_1 can be obtained from measurement of such coupling constants. Measurement of $^3J_{H^NH^\alpha}$ and $^3J_{H^\alpha H^\beta}$ from homonuclear spectra either by direct methods (i.e., direct measurement or iterative fitting of in-phase or antiphase splittings; Section 6.2.1.5) or from homonuclear E.COSY spectra (Section 6.3.3) was discussed in the preceding chapter. For larger proteins, accurate measurement of homonuclear J couplings by these methods is difficult because the couplings involved are smaller than the proton resonance linewidths. In recent years, a large number of alternative experiments to measure three-bond J coupling constants from isotopically labeled protein samples have been published, elucidating how to circumvent these problems. The new methods may be classified into three distinct categories: (*i*) direct measurement of resolved J couplings from heteronuclear-edited spectra (*108*, *109*), (*ii*) E.COSY-like methods for measurement of unresolved J couplings, in which a well-resolved ^1J coupling in one dimension of an *n*D experiment allows resolution of two components of the cross-peaks that are separated by the ^3J coupling of interest (*110–132*), and (*iii*) quantitative J correlation, in which the coupling constant is determined from the intensity ratio of two cross-peaks (*133–141*).

A great deal of similarity exists among the different published experiments within these three experimental categories. The most common schemes for measurement of homo- and heteronuclear three-bond J coupling constants to date are based on the E.COSY principle; an example of this class of experiment, designed to measure $^3J_{H^NH^\alpha}$ coupling constants, is discussed in the following section. An alternative method for measurement of $^3J_{H^NH^\alpha}$ coupling constants using the quantitative J correlation class of experiments is discussed later.

7.5.1 HNCA-*J* EXPERIMENT

The first example of a heteronuclear triple-resonance correlation experiment to measure $^3J_{H^NH^\alpha}$ coupling constants using the heteronuclear E.COSY principle was an HNCA-J experiment (*111*, *112*). Indeed, this was also the first HNCA-type experiment to be published. Further modification of the original sequence (*113–117*) has led to the HNCA-J experiment illustrated in Fig. 7.49 (*110*, *118*). The basic

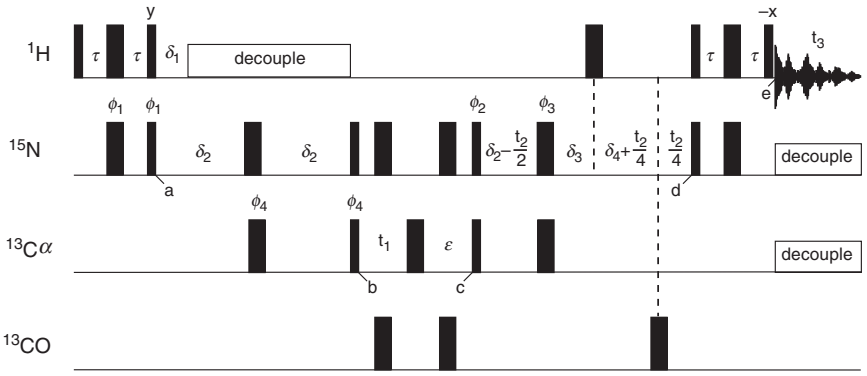

FIGURE 7.49 Pulse sequence for the HNCA-*J* experiment. Values of delays are described in the text. Other experimental details are similar to those given in Fig. 7.31. The phase cycle is $\phi_1 = x, -x$; $\phi_2 = 2(x), 2(-x)$; $\phi_3 = 8(x), 8(y), 8(-x), 8(-y)$; $\phi_4 = 4(x), 4(-x)$; and receiver $= x, -x, -x, x, 2(-x, x, x, -x), x, -x, -x, x$. Quadrature detection in the t_1 and t_2 dimensions is achieved by incrementing independently the phases ϕ_4 and ϕ_2, respectively, and the receiver phase, in a TPPI–States manner.

principle behind this E.COSY-like experiment is identical to that described previously for the homonuclear E.COSY experiment (Section 6.3.3): the $^{13}C^{\alpha}$ and $^{1}H^{N}$ spins are correlated without disturbing the spin state of the $^{1}H^{\alpha}$ nucleus. As a result, the large one-bond $J_{C^{\alpha}H^{\alpha}}$ coupling resolved in one dimension allows the $^{3}J_{H^{N}H^{\alpha}}$ coupling to be measured in another dimension. The (optional) ^{15}N dimension simply improves the spectral resolution by separating the $^{13}C^{\alpha}$–$^{1}H^{N}$ correlations into a third dimension. A more detailed product operator description of the HNCA-*J* experiment is given in the following discussion.

The HNCA-*J* experiment illustrated in Fig. 7.49 begins by transferring magnetization originating on amide protons to their directly bonded ^{15}N nuclei via an INEPT sequence. For $2\tau = 1/(2J_{NH})$, the magnetization present at time *a* is represented by

$$\sigma_a = -2H_z^N N_y. \qquad [7.159]$$

A second INEPT sequence transfers the ^{15}N magnetization to its coupled $^{13}C^{\alpha}$ spins. In addition, the ^{15}N magnetization refocuses to become in-phase with respect to its attached proton during the delay $\delta_1 = 1/(2J_{NH})$. Application of synchronous broadband ^{1}H decoupling (WALTZ-16 or DIPSI-2, for instance) after δ_1 ensures that the ^{15}N spin

remains decoupled from its attached proton. As with the previously discussed triple-resonance experiments (Section 7.4.6), the power and duration of the $^{13}C^{\alpha}$ pulses are adjusted so that they do not perturb the ^{13}CO spins (Section 3.4.1). Focusing on the intraresidue correlations, and ignoring the interresidue correlations, the relevant component of the density operator at time b is given by

$$\sigma_b = -2N_z C_y^{\alpha} \Gamma_1(2\delta_2), \qquad [7.160]$$

in which the coherence transfer function $\Gamma_1(2\delta_2)$ is given by [7.100]. For the purpose of measuring the $^3J_{H^NH^{\alpha}}$ coupling, $2\delta_2$ is adjusted to optimize $\Gamma_1(2\delta_2)$ for intraresidue coherence transfer only; after allowing for the additional relaxation term, $\exp(-2\delta_2 R_{2N})$, $2\delta_2$ is typically set to 20–30 ms.

At this stage, [7.160] is rewritten using a mixture of Cartesian operators for the ^{15}N spin and single-element operators for the $^{13}C^{\alpha}$ and $^1H^{\alpha}$ spins (Section 2.7.2) to give

$$\sigma_b = -N_z[C_y^{\alpha} H^{\alpha}(\alpha) - C_y^{\alpha} H^{\alpha}(\beta)]\Gamma_1(2\delta_2), \qquad [7.161]$$

in which $H^{\alpha}(\alpha)$ and $H^{\alpha}(\beta)$ correspond to the $|\alpha\rangle$ and $|\beta\rangle$ spin states of the ^1H nucleus, respectively. Thus, $C_y^{\alpha} H^{\alpha}(\alpha)$ and $C_y^{\alpha} H^{\alpha}(\beta)$ represent the $^{13}C^{\alpha}$ spins whose attached $^1H^{\alpha}$ spins are in the $|\alpha\rangle$ and $|\beta\rangle$ states. Using [2.218], $C_y^{\alpha} H^{\alpha}(\alpha)$ and $C_y^{\alpha} H^{\alpha}(\beta)$ can be expanded to give the equivalent Cartesian representations:

$$C_y^{\alpha} H^{\alpha}(\alpha) = C_y^{\alpha}(H_z^{\alpha} + \tfrac{1}{2}\mathbf{E}) = C_y^{\alpha} H_z^{\alpha} + \tfrac{1}{2} C_y^{\alpha} \qquad [7.162]$$

and

$$C_y^{\alpha} H^{\alpha}(\beta) = C_y^{\alpha}(H_z^{\alpha} - \tfrac{1}{2}\mathbf{E}) = C_y^{\alpha} H_z^{\alpha} - \tfrac{1}{2} C_y^{\alpha}. \qquad [7.163]$$

Evolution of the single-element operators can be followed either by using the product operator rules or, more simply, by direct matrix manipulation using the matrix representations given in Table 2.2, together with the relationships given in [7.162] and [7.163].

Following time b, the $^{13}C^{\alpha}$ chemical shift evolves without proton decoupling during t_1. The application of $180^{\circ}(^{15}N)$ and $180^{\circ}(^{13}CO)$ pulses at the midpoint of the t_1 evolution period ensures decoupling of these spins; however, the passive scalar coupling interactions between $^{13}C^{\alpha}$ and $^{13}C^{\beta}$ spins evolve during this period. The $180^{\circ}(^{13}C^{\alpha})$ and

$180°(^{13}CO)$ pulses applied following t_1 and prior to time c provide a method to compensate for the off-resonance effect of the first $180°(^{13}CO)$ pulse on the transverse $^{13}C^{\alpha}$ magnetization (Section 3.4.1). The $180°(^{15}N)$ pulse applied in the middle of the ε delay decouples the $^{13}C^{\alpha}$ and ^{15}N spins. Setting the delay ε equivalent to the initial value of $t_1(t_1(0))$ ensures that no phase correction is necessary in the F_1 dimension; need only be long enough to accommodate the $180°(^{13}CO)$ pulse. The relevant components of the density operator present at time c are described by

$$\sigma_c = -N_z\Big\{C_y^{\alpha}H^{\alpha}(\alpha)\cos[(\Omega_{C^{\alpha}} + \pi J_{C^{\alpha}H^{\alpha}})t_1] - C_y^{\alpha}H^{\alpha}(\beta)\cos[(\Omega_{C^{\alpha}} - \pi J_{C^{\alpha}H^{\alpha}})t_1]\Big\}\cos(\pi J_{C^{\alpha}C^{\beta}}t_1)\Gamma_1(\delta_2). \quad [7.164]$$

The frequencies of the two multiplet components now are separated in the F_1 dimension by the large one-bond $J_{C^{\alpha}H^{\alpha}}$ scalar coupling constant. During the remainder of the experiment, the spin states of the $^1H^{\alpha}$ nuclei effectively are unchanged, and the two correlations observed in the F_1 dimension are treated separately.

Following time c, the antiphase $^{13}C^{\alpha}$ magnetization is transferred back to ^{15}N by the simultaneous $90°$ $^{13}C^{\alpha}$ and ^{15}N pulses. During the following constant-time evolution period of length $2\delta_2$, in which $\delta_2 = \delta_3 + \delta_4$, and $2\delta_4 = 1/(2J_{NH})$, the antiphase ^{15}N magnetization refocuses with respect to $^{13}C^{\alpha}$ (during $2\delta_2$) and dephases with respect to its attached $^1H^N$ (during $2\delta_4$). The ^{15}N chemical shift evolution proceeds during t_2 only. The magnetization present at time d is thus represented by

$$\sigma_d = N_y\Big\{H_z^N H^{\alpha}(\alpha)\cos[(\Omega_{C^{\alpha}} + \pi J_{C^{\alpha}H^{\alpha}})t_1] - H_z^N H^{\alpha}(\beta)\cos[(\Omega_{C^{\alpha}} - \pi J_{C^{\alpha}H^{\alpha}})t_1]\Big\}\cos(\Omega_N t_2)\cos(\pi J_{C^{\alpha}C^{\beta}}t_1)\Gamma_1^2(2\delta_2). \quad [7.165]$$

The final set of pulses represents a reverse INEPT sequence that transfers the antiphase magnetization back into observable $^1H^N$ magnetization. Note that the inclusion of the final $90°(^1H)$ pulse results in zero net rotation of the $^1H^{\alpha}$ spins (and all other protons not directly bound to ^{15}N) between times b and e. In addition, this pulse also returns any $^1H^N$ magnetization that is not aligned along the x-axis to the z-axis, and thus effectively purges phase errors resulting from the $^3J_{H^NH^{\alpha}}$ coupling that is active during the τ delays (Section 7.1.1.2).

For $2\tau = 1/(2J_{\mathrm{NH}})$, the magnetization present at time e is described by

$$\sigma_e = \tfrac{1}{2}\{H_x^N H^\alpha(\alpha)\cos[(\Omega_{C^\alpha} + \pi J_{C^\alpha H^\alpha})t_1] - H_x^N H^\alpha(\beta)\cos[(\Omega_{C^\alpha} - \pi J_{C^\alpha H^\alpha})t_1]\}\cos(\Omega_N t_2)\cos(\pi J_{C^\alpha C^\beta} t_1)\Gamma_1^2(2\delta_2). \quad [7.166]$$

During acquisition, ^{15}N spins are decoupled from the $^1\mathrm{H}^\mathrm{N}$ spins. Decoupling of the ^{13}C spins ($^{13}\mathrm{C}^\alpha$ and ^{13}CO) also is desirable in order to remove the effects of the small $^2J_{\mathrm{H^NC}^\alpha}$, $^2J_{\mathrm{H^NCO}}$, and $^3J_{\mathrm{H^NC}^\alpha}$ couplings. The coherences represented by σ_e evolve under the chemical shift Hamiltonian during t_3 to yield an observable signal, after forming the trace with the observation operator, proportional to

$$\tfrac{1}{4}\{\cos[(\Omega_{C^\alpha} + \pi J_{C^\alpha H^\alpha})t_1]\exp[i(\Omega_{H^N} - \pi^3 J_{\mathrm{H^NH}^\alpha})t_3] + \cos[(\Omega_{C^\alpha} - \pi J_{C^\alpha H^\alpha})t_1]\exp[i(\Omega_{H^N} + \pi^3 J_{\mathrm{H^NH}^\alpha})t_3]\} \times \cos(\Omega_N t_2)\cos(\pi J_{C^\alpha C^\beta} t_1)\Gamma_1^2(2\delta_2). \quad [7.167]$$

From [7.167], two components corresponding to the $|\alpha\rangle$ and $|\beta\rangle$ spin states of $^1\mathrm{H}^\alpha$ are observed for each intraresidue $F_1(^{13}\mathrm{C}^\alpha)$–$F_3(^1\mathrm{H}^\mathrm{N})$ cross-peak. The F_1 displacement of the two components corresponds to $^1J_{\mathrm{CH}}$ and the F_3 displacement corresponds to $^3J_{\mathrm{H^NH}^\alpha}$.

The E.COSY principle requires that the $^1\mathrm{H}^\alpha$ nuclear spin does not change spin states between the t_1 and t_3 time periods. In practice, nuclear spin relaxation exchanges the $^1\mathrm{H}^\alpha$ spin between states $|\alpha\rangle$ and $|\beta\rangle$ with two consequences: (*i*) relaxation during the t_3 period results in self-decoupling of the spins (Section 5.4.2), and (*ii*) relaxation during the fixed time period between *b* and *d* results in the superposition of the E.COSY and natural multiplet structures in the final spectrum. Both effects mediated by spin relaxation reduce the size of the apparent $^3J_{\mathrm{H^NH}^\alpha}$ scalar coupling constant.

Measurement of $^3J_{\mathrm{H^NH}^\alpha}$ by the heteronuclear E.COSY technique is illustrated for a cross peak from a selected $F_2(^{15}\mathrm{N})$ slice in the HNCA-*J* spectrum of ubiquitin in Fig. 7.50. The asymmetry in the peak shape is a consequence of relaxation between points *b* and *d* in the pulse sequence, as discussed above.

7.5.2 HNHA EXPERIMENT

An alternative method to the HNCA-*J* experiment for measurement of $^3J_{\mathrm{H^NH}^\alpha}$ coupling constants relies on a quantitative analysis of the

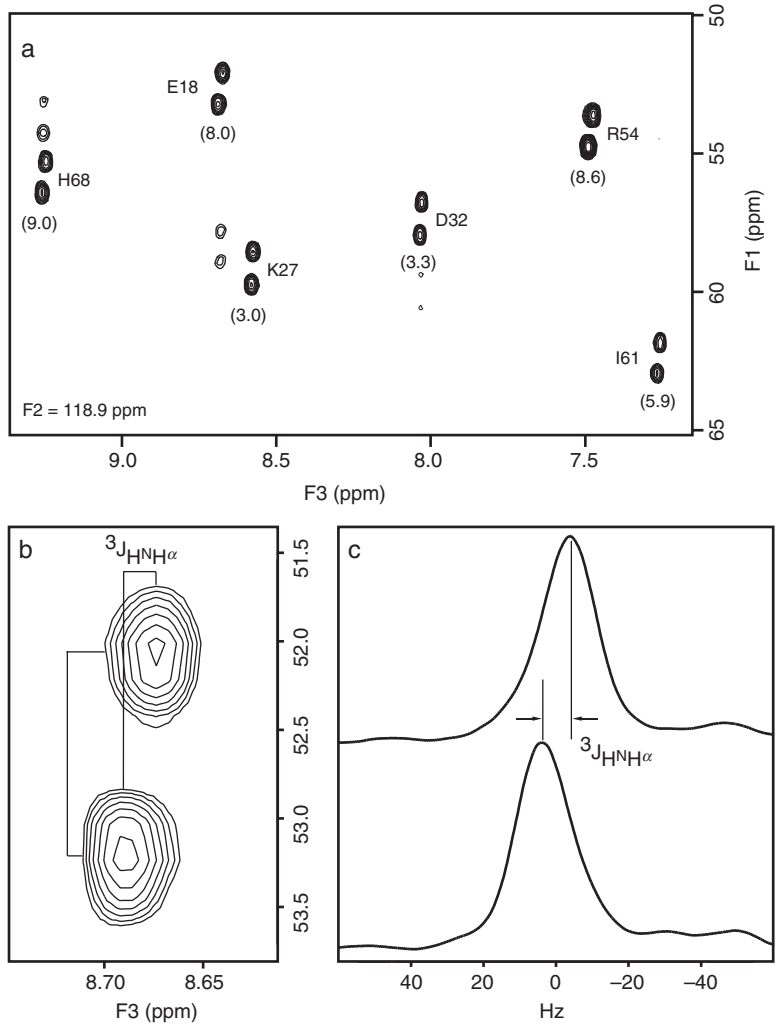

FIGURE 7.50 (a) A selected $F_1(^{13}C^{\alpha})$–$F_3(^1H^N)$ slice, at an $F_1(^{15}N)$ chemical shift of 118.9 ppm, from a HNCA-J spectrum of $^{15}N/^{13}C$-labeled ubiquitin. The intraresidue cross-peaks are labeled with the residue name and the measured $^3J_{H^NH^\alpha}$ coupling constants are in parentheses. The weaker, unlabeled cross-peaks are due to interresidue correlations. The E.COSY-like cross-peak pattern is highlighted in panel b for the cross-peak of Glu18. The $^3J_{H^NH^\alpha}$ coupling constants were determined as illustrated in panel c, which shows rows taken through the maxim of the two cross-peak components of Glu18. The peak displacements were measured following inverse Fourier transformation, zero-filling to 16,384 points, and retransformation.

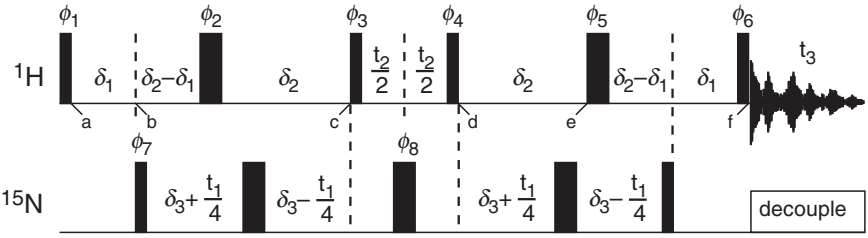

FIGURE 7.51 Pulse sequence for the HNHA experiment. The delay δ_1 is set to 4.5 ms, the delay δ_2 is set to 13.05 ms, and $2\delta_3 = 2\delta_2 - \delta_1$. Other experimental details are similar to those given in Fig. 7.31. The phase cycle is $\phi_1 = x$; $\phi_2 = 4(x)$, $4(-x)$, $4(y)$, $4(-y)$; $\phi_3 = x, -x$; $\phi_4 = 2(x)$, $2(-x)$; $\phi_5 = 4(x)$, $4(y)$, $4(-x)$, $4(-y)$; $\phi_6 = y, -y$; $\phi_7 = x$; $\phi_8 = 16(x)$, $16(y)$; and receiver $= 4(x)$, $8(-x)$, $4(x)$, $4(-x)$, $8(x)$, $4(-x)$. Quadrature detection in the t_1 and t_2 dimensions is achieved by incrementing independently the phases ϕ_3 and ϕ_7, respectively, and the receiver phase, in a TPPI–States manner.

diagonal to cross-peak intensity ratio in an ^{15}N-edited ^{1}H$^{\mathrm{N}}$–^{1}H$^{\alpha}$ correlation experiment. This technique is referred to as the HNHA experiment because the intraresidue ^{1}H$^{\mathrm{N}}$, ^{15}N, and ^{1}H$^{\alpha}$ resonances are correlated by using the pulse sequence illustrated in Fig. 7.51 (*133*). A description of this experiment using the product operator formalism is given in the following discussion.

The initial part of the pulse sequence transfers ^{1}H$^{\mathrm{N}}$ magnetization to heteronuclear multiple-quantum coherence in an HMQC-type manner, giving, at time *b*,

$$\sigma_b = 2H_x^N N_y \sin(\pi J_{\mathrm{NH}} \delta_1). \qquad [7.168]$$

In addition, the transverse ^{1}H$^{\mathrm{N}}$ magnetization present at time *a* dephases due to homonuclear ^{1}H$^{\mathrm{N}}$–^{1}H$^{\alpha}$ J coupling that is active for a total duration $2\delta_2$, between times *a* and *c*. Chemical shift evolution of the ^{15}N spins occurs in a constant-time period between points *b* and *c* ($2\delta_3$) for a duration of $t_1/2$. The multiple-quantum coherence does not evolve under the influence of the active ^{1}H$^{\mathrm{N}}$–^{15}N coupling during the constant-time period (Section 2.7.5). The magnetization present at time *c* can therefore be represented by

$$\sigma_c = \left\{-2H_x^N N_y \cos(2\pi^3 J_{\mathrm{H^N H^\alpha}} \delta_2) - 4H_y^N H_z^\alpha N_y \sin(2\pi^3 J_{\mathrm{H^N H^\alpha}} \delta_2)\right\} \times \cos(\Omega_N t_1/2) \sin(\pi J_{\mathrm{NH}} \delta_1). \qquad [7.169]$$

The subsequent 90°(^{1}H) pulse converts the antiphase $^1H^N$ magnetization to antiphase $^1H^\alpha$ magnetization. Following a short t_2 evolution period, the antiphase $^1H^\alpha$ terms are converted back to antiphase $^1H^N$ magnetization to give, at time d,

$$\sigma_d = \{-2H_x^N N_y \cos(\Omega_{H^N} t_2) \cos(2\pi^3 J_{H^N H^\alpha} \delta_2) - 4H_y^N H_z^\alpha N_y \cos(\Omega_{H^\alpha} t_2) \sin(2\pi^3 J_{H^N H^\alpha} \delta_2)\} \cos(\Omega_N t_1/2) \sin(\pi J_{NH} \delta_1). \quad [7.170]$$

During the following rephasing period, between time points d and f, the ^{15}N chemical shift evolution is continued for an additional period $t_1/2$, the $^1H^N$–$^1H^\alpha$ J coupling is again active, and the ^{15}N–$^1H^N$ MQ coherence is converted back to observable $^1H^N$ magnetization. The observable magnetization present at time f is represented by

$$\sigma_f = -H_y^N \{-\cos(\Omega_{H^N} t_2) \cos^2(2\pi^3 J_{H^N H^\alpha} \delta_2) + \cos(\Omega_{H^\alpha} t_2) \sin^2(2\pi^3 J_{H^N H^\alpha} \delta_2)\} \times \cos(\Omega_N t_1) \sin^2(\pi J_{NH} \delta_1). \quad [7.171]$$

The 90°(^{1}H) purge pulse applied immediately before acquisition ensures that only in-phase $^1H^N$ magnetization contributes to the observed signal. This analysis has neglected the effects of heteronuclear J_{NH^α} two- and three-bond couplings that are active for limited parts of the pulse sequence. In the first part of the sequence (i.e., prior to t_2 between times b and c), these couplings are active for a fraction corresponding to $2\delta_3 - t_1/2 - \delta_1$. In the latter part of the experiment, the J_{NH^α} couplings are active for a time $2\delta_3 + t_1/2 - \delta_1$ if $t_1/2 < \delta_1$, and for $2\delta_3 - t_1/2 + \delta_1$ if $t_1/2 > \delta_1$. The effects of these couplings are identical for both terms in [7.171] and can be accounted for by the inclusion of additional cosine terms; for instance, for $t_1/2 < \delta_1$, the $^2J_{NH^\alpha}$ coupling contributes the following terms to the observed magnetization:

$$\cos[\pi^2 J_{NH^\alpha}(2\delta_3 - t_1/2 - \delta_1)] \cos[\pi^2 J_{NH^\alpha}(2\delta_3 + t_1/2 - \delta_1)]. \quad [7.172]$$

Analogous expressions can be written for $t_1/2 > \delta_1$, and for the $^3J_{NH^\alpha}$ couplings. In practice, however, these coupling constants are small, such that $2\delta_3 \ll 1/J_{NH^\alpha}$, and therefore have little effect on the observed intensity.

Equation [7.171] indicates that two peaks, an autocorrelation or "diagonal" peak at $F_1(^{15}N)$–$F_2(^1H^N)$–$F_3(^1H^N)$ and a cross-peak at $F_1(^{15}N)$–$F_2(^1H^\alpha)$–$F_3(^1H^N)$, with opposite phase will be observed for each

amino acid spin system (except glycine). The lineshapes of these peaks in the F_1 and F_3 dimensions are determined by identical factors. The intrinsic linewidths of the diagonal and cross-peaks in the F_2 dimension, however, are determined by the relaxation rates of the transverse $^1H^N$ and $^1H^\alpha$ magnetization present during t_2. If the lineshapes of the diagonal and cross-peaks in F_2 dimension are assumed to be identical (but see later for a discussion of relaxation rates), the intensity ratio of these peaks then provides a measure of the magnitude of the $^3J_{H^NH^\alpha}$ coupling constant,

$$\frac{S_{\text{cross}}}{S_{\text{diagonal}}} = -\frac{\sin^2(2\pi^3 J_{H^NH^\alpha}\delta_2)}{\cos^2(2\pi^3 J_{H^NH^\alpha}\delta_2)} = -\tan^2(2\pi^3 J_{H^NH^\alpha}\delta_2). \qquad [7.173]$$

In practice, the intensity of the cross-peak resonance is reduced relative to the "diagonal" resonance because the antiphase component of the $4H_y^N H_z^\alpha N_y$ operator leads to faster relaxation during the $2\delta_2$ periods compared with the pure multiple-quantum $2H_x^N N_y$ operator. Ignoring cross-correlation, to a first approximation, the relaxation rates of the two operators are given by

$$R_2(2H_x^N N_y) = R_{2H^N} + R_{2\text{MQ}}, \qquad [7.174]$$

$$R_2(4H_y^N H_z^\alpha N_y) = R_{2H^N} + R_{2\text{MQ}} + R_{1H^\alpha}. \qquad [7.175]$$

The time dependence of the in-phase and antiphase operators during the $2\delta_2$ delays, including relaxation effects, is a problem identical to that presented in Section 5.4.2 for relaxation in a scalar-coupled spin system. Using the results presented in Section 5.4.2,

$$\frac{S_{\text{cross}}}{S_{\text{diagonal}}} = -\left\{\frac{\tan\left[(1-\chi^2)^{1/2}\zeta\right]}{(1-\chi^2)^{1/2} + \chi\tan\left[(1-\chi^2)^{1/2}\zeta\right]}\right\}^2, \qquad [7.176]$$

in which the dimensionless parameters, χ and ζ, are given by

$$\chi = R_{1H^\alpha}/\left(2\pi^3 J_{H^NH^\alpha}\right), \qquad \zeta = 2\pi^3 J_{H^NH^\alpha}\delta_2. \qquad [7.177]$$

Equation [7.176] reduces to [7.173] as expected if χ approaches zero. If R_{1H^α} is known from experimental measurements or from calculations, then [7.176] can be solved numerically to determine values of $^3J_{H^NH^\alpha}$ that are more accurate than those determined from [7.173]. A graph of the differences between the actual value of $^3J_{H^NH^\alpha}$ and the apparent values calculated using [7.173] is shown in Fig. 7.52. As shown, the effect of

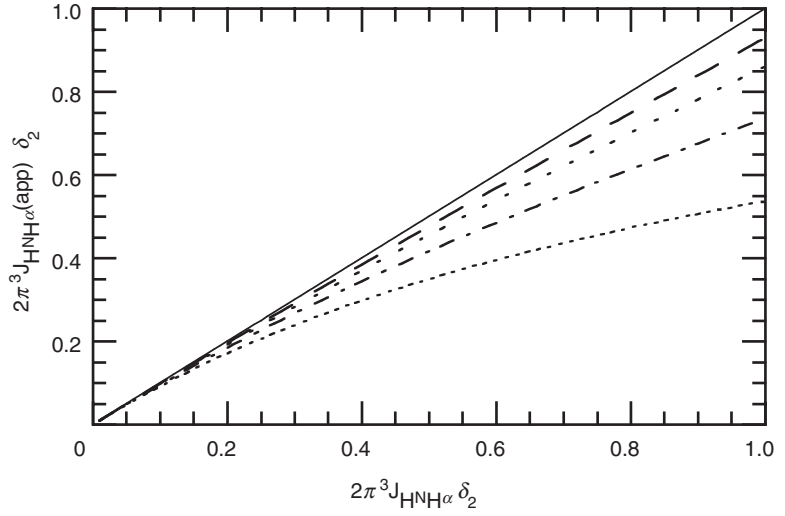

FIGURE 7.52 Effects of relaxation on the HNHA experiment. The apparent coupling constant calculated using [7.173] is plotted (in dimensionless units) versus the actual coupling constant calculated using [7.176] (also in dimensionless units). Results are shown for $\chi = R_{1H^\alpha}/(2\pi J_{H^NH^\alpha})$ equal to (—) 0, (– –) 0.1, (- - -) 0.2, (· – ·) 0.4 and (· · ·) 0.8.

relaxation is always to reduce the apparent scalar coupling constant measured using [7.173].

A selected $F_1(^{15}N)$ slice of an HNHA spectrum of ubiquitin is shown in Fig. 7.53. Results obtained for $^3J_{H^NH^\alpha}$ from COSY, HNCA-*J*, and HNHA experiments are summarized in Table 7.3. As shown, the values of $^3J_{H^NH^\alpha}$ obtained from COSY spectra are consistently larger than values obtained from HNCA-*J* or HNHA spectra. Values obtained from the HNHA experiment using [7.176] are approximately 7.5% larger than values obtained using [7.173].

7.6 Measurement of Residual Dipolar Coupling Constants

Residual dipolar couplings (RDCs) between pairs of NMR active nuclei provide structural and dynamical information that is not strictly local in nature. In particular, RDCs between directly bonded nuclei provide restraints on the orientation of the internuclear vector in the molecular alignment frame (Section 10.2.1.4).

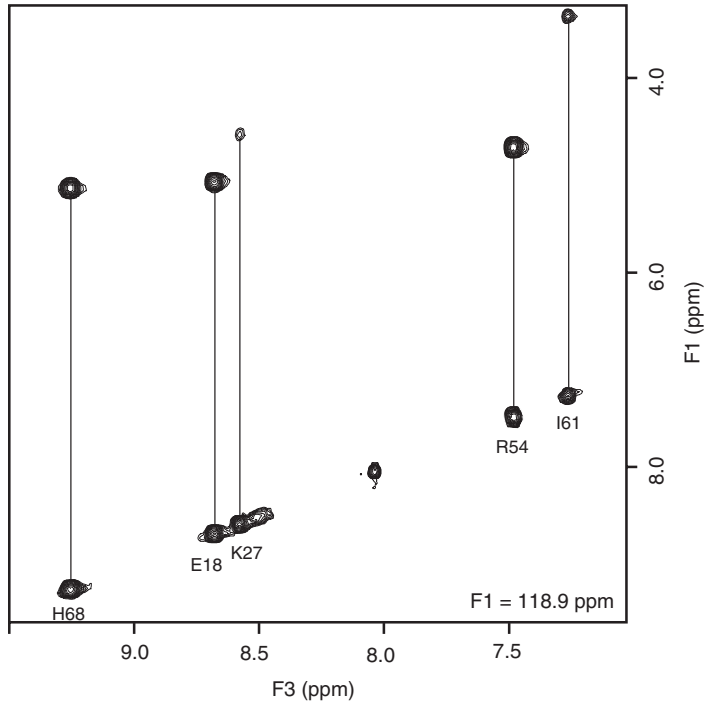

FIGURE 7.53 HNHA spectrum of ubiquitin. A selected $F_2(^1\mathrm{H})$–$F_3(^1\mathrm{H}^{\mathrm{N}})$ slice, at an $F_1(^{15}\mathrm{N})$ chemical shift of 118.9 ppm, from an HNHA spectrum of ^{15}N-labeled ubiquitin acquired with $\delta_1 = 4.5$ ms and $2\delta_2 = 26.1$ ms. The intraresidue peaks are labeled with their residue names. The cross-peaks have phase opposite to the phase of "diagonal" peaks. From the ratios of cross-peak to "diagonal" peak intensity, the following uncorrected $^3J_{\mathrm{H^N H^\alpha}}$ coupling constant values were obtained: His68, 8.9 Hz; Glu18, 8.2 Hz; Lys27, 3.1 Hz; Arg54, 8.5 Hz; Ile61, 6.4 Hz.

Dipolar couplings, although a major source of structural information in solid-state NMR, are not normally observed for proteins in solution because rotational diffusion in an isotropic solution environment averages the traceless dipole coupling tensor to zero. However, in 1982, Bothner-By and co-workers demonstrated that small heme-like molecules, possessing large anisotropic magnetic susceptibilities, adopted preferred orientations with respect to the main static field (*142*). This so-called molecular alignment demonstrated that dipolar couplings would not always average to zero in solution NMR studies. In 1995, Prestegard and co-workers, studying the protein

TABLE 7.3
$^3J_{H^NH^\alpha}$ Scalar Coupling Constants[a]

Residue	COSY	HNCA-*J*	HNHA (uncorrected)	HNHA (corrected)
Glu18	9.3	8.0	8.2	8.8
Lys27	4.8	3.0	3.1	3.4
Asp32	4.3	3.3	3.4	3.7
Arg54	9.7	8.6	8.5	9.2
Ile61	6.9	5.9	6.7	7.3
His68	9.8	9.0	8.9	9.6

[a]All values are given in Hertz. Scalar coupling constants were determined from COSY spectra by line fitting (Section 6.2.1.5). HNCA-*J* results were measured from the spectrum as illustrated in Fig. 7.50. Uncorrected HNHA results were calculated from [7.173]. Corrected HNHA results were calculated from [7.176], assuming $R_1(H^\alpha) = 6.4\ s^{-1}$.

cyanometmyoglobin at high magnetic field strengths (up to 750 MHz), demonstrated that this alignment mechanism resulted in measurable one-bond $^1H^N$–^{15}N RDCs (*143*). Cyanometmyoglobin, because of the heme moiety, has a very highly anisotropic paramagnetic susceptibility. In fact, most proteins have a measurable, albeit very small, anisotropic magnetic susceptibility tensor. Bax and co-workers have accurately measured one-bond $^1H^N$–^{15}N dipolar couplings in human ubiquitin (*144*). In this diamagnetic protein, magnetic alignment results from the sum of the anisotropic magnetic susceptibility contributions of the backbone peptide bonds and the aromatic side chains. The $^1H^N$–^{15}N RDCs were determined by fitting resonance intensities from a series of $^1J_{NH}$ amplitude-modulated 2D spectra collected at ^1H frequencies of 360, 500, and 600 MHz. The measured residual couplings in ubiquitin are very small, ranging from −0.09 to +0.10 Hz.

A major breakthrough in the measurement of dipolar couplings was realized with the introduction of anisotropic media for macromolecular alignment (*145*). The first such method used a dilute aqueous liquid crystalline phase of discotic phospholipid micelles consisting of a 1:2.9 ratio of dihexanoyl phosphatidylcholine (DHPC) and dimyristoyl phosphatidylcholine (DMPC). These lipids form bicelles and a liquid crystalline phase over a narrow concentration and temperature range (*145*). Macromolecules dissolved in this medium experience a small degree of alignment due to steric and electrostatic interactions with the bicelle phase. The degree of alignment is adjusted, by variation in the concentration of the liquid crystalline phase, so that only dipolar

couplings between closely spaced nuclei give measurable dipolar couplings. If alignment is too strong, then the resulting spectra become impossible to interpret because of the large number of RDCs present, the degradation of the lineshape due to unresolved RDCs and anisotropic chemical shifts, and the increased transverse relaxation rate constants (which are essentially population averages of the rate constants for the free protein and the protein interacting with the bicelle). RDCs for proteins properly aligned in such media are several orders of magnitude larger than are couplings measured based on the alignment caused by the inherent magnetic susceptibility anisotropy of a diamagnetic protein.

Numerous media for obtaining tunable molecular alignment have been introduced and a comprehensive listing is provided in the review article by Prestegard and co-workers (*146*). No single alignment medium is universal and the search for alignment media suitable for a given protein is an empirical process. Many bicellar media based on various cocktails of amphiphilic molecules have been described as providing improved physical properties, including increased chemical stability, broader temperature ranges over which alignment is obtained, and modified surface electrostatics, compared to DMPC/DHPC bicelles. The alignment media developed by Rückert and Otting (*147*) based on *n*-alkyl-poly(ethylene glycol)/*n*-alkyl alcohol mixtures meet these objectives and are compatible with many proteins. Two effective approaches for obtaining molecular alignment — filamentous phage and polyacrylamide gels — are distinctly different from the bicellar media, and are discussed briefly here.

The Pf1 filamentous bacteriophage has been widely adopted as an alignment medium (*148*, *149*). The Pf1 bacteriophage particle has a diameter of ~60 Å and a length of ~20,000 Å. The coat protein, which packages the phage DNA, forms an α-helical structure that is parallel to the long axis of the phage particle. This organization is believed to be the reason for the large magnetic susceptibility anisotropy and the alignment of the particle in the magnetic field. Phage particles have many favorable properties for use as alignment media. The particles stably align over a range of concentrations, pH, temperatures, and salt concentrations. In addition, they are fully aligned at all magnetic fields used for protein NMR studies. Furthermore, the solutions formed using precious protein samples are stable over long periods of time and the phage and protein can be separated and retrieved by ultracentrifugation (*148*). Molecular alignment also can be achieved using compressed or stretched polyacrylamide gels (*150*, *151*). Anisotropy results from the mechanical forces of stretching or compressing the gel and as a consequence, unlike the other media already discussed,

alignment is independent of the orientation with respect to the static magnetic field. Procedures for compressing or stretching the gel inside the NMR tube have been described (*150–152*).

As described by [2.328], the RDC between two nuclear spins has the same form as the weak scalar coupling Hamiltonian; thus, the RDC simply adds to the conventional scalar coupling splitting observed in an NMR spectrum. Figure 7.54 illustrates the effect of molecular alignment on the apparent coupling and lineshape in an ^{1}H–^{15}N HSQC spectrum of ubiquitin, recorded without decoupling during t_1. In the absence of bicelles, the peak separation results from the $^{1}J_{NH}$ scalar coupling with a magnitude of approximately 93 Hz (the coupling constant is known to be negative). As the concentration of bicelles is increased, the apparent peak separation, given by $^{1}J_{NH} + D_{NH}$, changes and values both smaller and larger than $^{1}J_{NH}$ are observed, depending on whether the RDC is positive or negative for a particular N–H moiety.

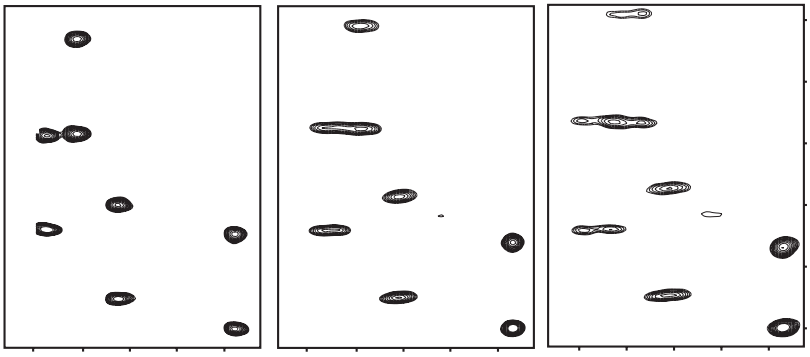

The magnitude of the RDCs scales linearly over the range of concentrations of bicelles for the three spectra shown in Fig. 7.54. As the degree of alignment increases, ^{1}H–^{1}H dipolar couplings also increase and eventually become comparable to or larger than the $^3J_{HH}$ scalar couplings. As a result, the apparent linewidth in the ^{1}H dimension increases, leading to reduced sensitivity and increased overlap. For this example, the lineshape is only slightly degraded in the spectrum recorded for the sample containing 4.5% volume fraction of the liquid crystalline phase, while the RDCs, on the order of 10 Hz, are easily measurable from the difference in splitting between the isotropic and aligned samples. The increased degradation in the lineshape in the ^{1}H dimension of the spectra shown in Fig. 7.54, compared with the ^{15}N dimension, is the reason that measuring the RDCs from the splitting in the ^{15}N dimension usually is preferable, even though the ^{1}H acquisition dimension has higher digital resolution.

Because the RDC adds to the scalar coupling constant, experimental techniques discussed in Section 7.5 for measuring heteronuclear scalar coupling constants and in Chapter 6 for measuring homonuclear scalar coupling constants are equally applicable for measuring RDCs. In particular, numerous techniques based on the E.COSY (frequency domain) and quantitative *J*-correlation (time-domain) approaches have been developed. Pulse sequence development for measuring RDCs is directed toward maximizing precision and accuracy, particularly for large proteins and for small coupling constants. Experimental methods for measuring RDCs have been tabulated by Prestegard and co-workers (*146*).

The simple method of recording an HSQC spectrum without decoupling during either the t_1 or t_2 evolution periods, used in Fig. 7.54, doubles the number of resonance correlations in the spectrum, and resonance overlap represents a severe limitation in practical applications. One approach to reduce spectral crowding separates the two doublet components into different subspectra using the IPAP (in-phase/antiphase) technique introduced by Bax and co-workers (*153*). A pulse sequence for the ^{1}H–^{15}N IPAP HSQC experiment is shown in Fig. 7.55. Product operator analysis of the IP and AP experiments shows that the density operators immediately prior to acquisition are given by, respectively,

$$\begin{aligned}\sigma_{IP} &= \cos(\Omega_N t_1)\,\cos(\pi J_{NH}^{app} t_1) I_x, \\ \sigma_{AP} &= \exp(-\overline{R}_{2S}\Delta)\,\sin(\pi J_{NH}^{app}\Delta)\,\sin(\Omega_N t_1)\,\sin(\pi J_{NH}^{app} t_1) I_x,\end{aligned} \qquad [7.178]$$

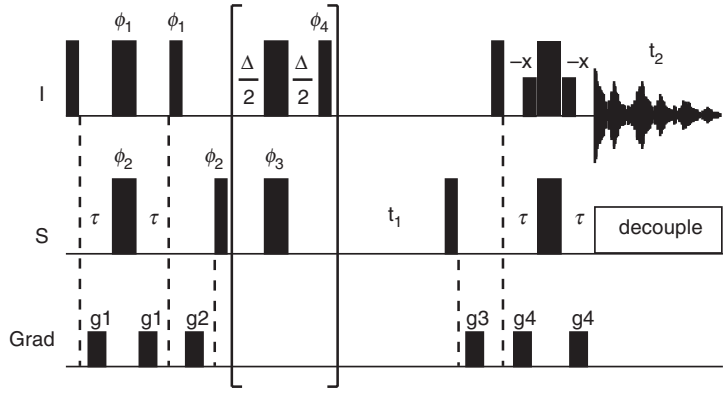

FIGURE 7.55 Pulse scheme of the IPAP ^{15}N–^{1}H HSQC experiment. Thin and thick rectangular bars represent 90° and 180° pulses, respectively. Pulses are applied with x-phase unless the phase is indicated above the bar. Short, wide rectangles are selective soft pulses applied at the frequency of the water resonance. Field gradient pulses are used for artifact and water suppression. The sequence element shown in brackets is used only in the experiment for generating the antiphase spectrum and is omitted for generating the in-phase spectrum. The low-power 90° pulses surrounding the final ^{1}H 180° pulse are part of the WATERGATE solvent-suppression scheme. The delay durations are $2\tau = 1/(2J_{IS})$ and $\Delta = 1/(2J_{IS})$. The phase cycle for the in-phase experiment is $\phi_1 = y, -y$; $\phi_2 = 2(x), 2(-x)$; and receiver $= x, 2(-x), x$. The phase cycle for the antiphase experiment is: $\phi_1 = y, -y$; $\phi_2 = 2(y), 2(-y)$; $\phi_3 = 4(x), 4(y), 4(-x), 4(-y)$; $\phi_4 = 8(x), 8(-x)$; and receiver $= x, 2(-x), x, -x, 2(x), -x$. Quadrature detection in the t_1 dimension is obtained by TPPI–States applied to ϕ_2 for the in-phase experiment or to ϕ_2 and ϕ_3 simultaneously for the antiphase experiment.

in which $J_{\mathrm{NH}}^{\mathrm{app}} = {}^{1}J_{\mathrm{NH}} + D_{\mathrm{NH}}$. The AP data set is scaled by an empirical factor $[\exp(-\overline{R}_{2S}\Delta)\,\sin(\pi J_{\mathrm{NH}}^{\mathrm{app}}\Delta)]^{-1}$ and the resulting data sets are added and subtracted to yield

$$\begin{aligned}\sigma_{\mathrm{add}} &= \{\cos(\Omega_N t_1)\,\cos(\pi J_{\mathrm{NH}}^{\mathrm{app}} t_1) + \sin(\Omega_N t_1)\,\sin(\pi J_{\mathrm{NH}}^{\mathrm{app}} t_1)\} I_x \\ &= \cos([\Omega_N - \pi J_{\mathrm{NH}}^{\mathrm{app}}] t_1) I_x \\ \sigma_{\mathrm{sub}} &= \{\cos(\Omega_N t_1)\,\cos(\pi J_{\mathrm{NH}}^{\mathrm{app}} t_1) - \sin(\Omega_N t_1)\,\sin(\pi J_{\mathrm{NH}}^{\mathrm{app}} t_1)\} I_x \\ &= \cos([\Omega_N + \pi J_{\mathrm{NH}}^{\mathrm{app}}] t_1) I_x.\end{aligned} \qquad [7.179]$$

These two density operators result in two spectra, one of which contains only the upfield doublet component and the other of which contains only the downfield doublet component.

For spectra recorded at high static magnetic field strengths, CSA/dipole relaxation interference causes the linewidth of the upfield doublet component to broaden relative to the downfield component. This effect, although barely evident in Fig. 7.54, is dramatically illustrated in Fig. 7.10 for spectra recorded at 800 MHz for the protein calbindin D_{28k} and, of course, is the basis for the TROSY technique. The broadening and loss of sensitivity of the upfield doublet component limits the precision with which the RDCs can be measured directly from the observed splitting. For ^{15}N-labeled or ^{13}C/^{15}N-labeled proteins, i.e., proteins that have not been deuterated at carbon sites, a simple approach to address this problem measures the frequency difference between the resonance position in a TROSY spectrum and the resonance position in a decoupled HSQC spectrum as $(^1J_{NH} + D_{NH})/2$ (*25*). The narrower linewidth of the resonance signal in the decoupled HSQC experiment, compared to the upfield component of the ^{1}H–^{15}N doublet, shown in Fig. 7.10, increases the precision of the measured RDCs, even though the apparent splitting is reduced by a factor of two.

For ^{2}H/^{15}N-labeled or ^{2}H/^{13}C/^{15}N-labeled proteins, i.e., proteins that have been deuterated at carbon sites, a superior approach incorporates the techniques of accordion spectroscopy and *J*-scaling into the TROSY experiment. A pulse sequence for one such method, called coupling-enhanced TROSY (CE-TROSY), is shown in Fig. 7.56. Two spectra are acquired, one with $\kappa = 0$, corresponding to the conventional TROSY spectrum, and another with κ set to a value between 0 and 1. The apparent splitting between resonance signals in the two spectra is given by $\kappa(^1J_{NH} + D_{NH})$. During the period κt_1, the resonance signal relaxes with the average rate constant $\overline{R}_{2S}$, because the ^{1}H 180° pulse interchanges the I^α and I^β spin states, rather than the relaxation rate constant for the desired TROSY component. Thus, overly large values of κ lead to decreased resolution and sensitivity for large proteins.

Eventually, of course, for larger proteins, resonance overlap in 2D spectra becomes too severe and 3D approaches are necessary to accurately measure RDCs in large partially aligned ^{2}H/^{13}C/^{15}N-labeled proteins. The HNCO experiment, discussed in Section 7.4.4.1, is the most sensitive and highly resolved 3D experiment for obtaining backbone resonance correlations. This experiment forms the basis for pulse sequences designed for measuring RDCs for nuclear spins in the polypeptide backbone. Pulse sequences incorporating the IPAP, TROSY/decoupled HSQC, and *J*-scaling approaches into the HNCO experiment,

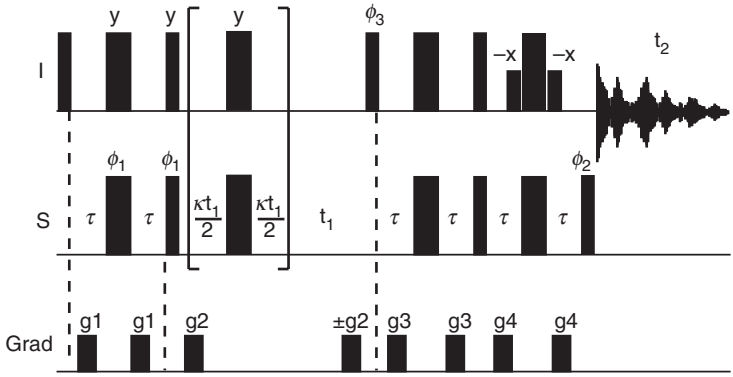

FIGURE 7.56 Pulse sequence for the CE-TROSY experiment incorporating *J*-scaling. Thin and thick rectangular bars represent 90° and 180° pulses, respectively. Pulses are applied with *x*-phase unless the phase is indicated above the bar. Short, wide rectangles are selective soft pulses applied at the frequency of the water resonance. Field gradient pulses are used for artifact and water suppression. For $\kappa = 0$, bracketed pulse sequence elements are omitted, the second gradient g_2 is negative, and the resulting pulse sequence is identical to the water flip-back TROSY experiment shown in Fig. 7.11b. Phase cycling is identical to that discussed in the caption to Fig. 7.11. When κ is nonzero, the bracketed pulse sequence elements are included, and the second gradient g_2 is positive. In order to select for the proper TROSY resonance, the phase cycles for pulse ϕ_1 are interchanged between the two data sets acquired for quadrature detection and Rance–Kay processing.

as discussed for 2D correlation spectroscopy, have been reported in the literature (*146*). For example, Yang and co-workers have introduced a suite of TROSY-HNCO triple-resonance pulse sequences that measure the one-bond $^1H^N$–^{15}N, ^{15}N–$^{13}C'$, and $^{13}C'$–$^{13}C^\alpha$, the two-bond $^1H^N$–$^{13}C'$, and the three-bond $^1H^N$–$^{13}C^\alpha$ RDCs (*154*), and new variants continue to be developed (*155*). The precision and accuracy of the IPAP, TROSY/decoupled HSQC, and TROSY *J*-scaling 2D and 3D methods have been evaluated (*156*).

References

1. S. W. Fesik, E. R. P. Zuiderweg, *Q. Rev. Biophys.* **23**, 97–131 (1990).
2. G. M. Clore, A. M. Gronenborn, *Prog. NMR Spectrosc.* **23**, 43–92 (1991).
3. A. Bax, S. Grzesiek, *Acc. Chem. Res.* **26**, 131–138 (1993).

4. L. P. McIntosh, F. W. Dahlquist, *Q. Rev. Biophys.* **23**, 1–38 (1990).
5. T. Yamazaki, W. Lee, C. H. Arrowsmith, D. R. Muhandiram, L. E. Kay, *J. Am. Chem. Soc.* **116**, 11655–11666 (1994).
6. D. M. LeMaster, *Q. Rev. Biophys.* **23**, 113–174 (1990).
7. M. Sattler, J. Schleucher, C. Griesinger, *Prog. NMR Spectrosc.* **34**, 93–158 (1999).
8. R. R. Ernst, G. Bodenhausen, A. Wokaun, "Principles of Nuclear Magnetic Resonance in One and Two Dimensions," pp. 1–610. Clarendon Press, Oxford, 1987.
9. Z. Serber, C. Richter, V. Dötsch, *ChemBioChem* **2**, 247–251 (2001).
10. A. Bax, M. Ikura, L. E. Kay, D. A. Torchia, R. Tschudin, *J. Magn. Reson.* **86**, 304–318 (1990).
11. G. Bodenhausen, D. J. Ruben, *Chem. Phys. Lett.* **69**, 185–189 (1980).
12. L. Müller, *J. Am. Chem. Soc.* **101**, 4481–4484 (1979).
13. T. J. Norwood, J. Boyd, J. E. Heritage, N. Soffe, I. D. Campbell, *J. Magn. Reson.* **87**, 488–501 (1990).
14. K. Pervushin, R. Reik, G. Wider, K. Wüthrich, *Proc. Natl. Acad. Sci. U.S.A.* **94**, 12366–12371 (1997).
15. A. Bax, R. Freeman, *J. Magn. Reson.* **44**, 542–561 (1981).
16. M. Rance, G. Wagner, O. W. Sørensen, K. Wüthrich, R. R. Ernst, *J. Magn. Reson.* **59**, 250–261 (1984).
17. A. Bax, A. F. Mehlkopf, J. Smidt, *J. Magn. Reson.* **35**, 373–377 (1979).
18. J. Santoro, G. C. King, *J. Magn. Reson.* **97**, 202–207 (1992).
19. G. W. Vuister, A. Bax, *J. Magn. Reson.* **98**, 428–435 (1992).
20. A. G. Palmer, J. Cavanagh, R. A. Byrd, M. Rance, *J. Magn. Reson.* **96**, 416–424 (1992).
21. A. Hammarström, G. Otting, *J. Magn. Reson., Ser. A* **109**, 246–249 (1994).
22. J. Cavanagh, J. Keeler, *J. Magn. Reson.* **77**, 356–362 (1988).
23. Ē. Kupče, H. Matsuo, G. Wagner, in "Biological Magnetic Resonance, 16: Modern Techniques in Protein NMR" (N. R. Krisha, L. Berliner, eds.), pp. 149–194. Kluwer Academic, New York, 1999.
24. D. P. Burum, R. R. Ernst, *J. Magn. Reson.* **39**, 163–168 (1980).
25. M. Ottiger, A. Bax, *J. Am. Chem. Soc.* **120**, 12334–12341 (1998).
26. T. Untidt, T. Schulte-Herbrüggen, B. Luy, S. J. Glaser, C. Griesinger, O. W. Sørensen, N. C. Nielsen, *Mol. Phys.* **95**, 787–796 (1998).
27. J. Cavanagh, A. G. Palmer, P. E. Wright, M. Rance, *J. Magn. Reson.* **91**, 429–436 (1991).
28. A. G. Palmer, J. Cavanagh, P. E. Wright, M. Rance, *J. Magn. Reson.* **93**, 151–170 (1991).
29. J. Cavanagh, M. Rance, *Annu. Rep. NMR Spectrosc.* **27**, 1–58 (1993).
30. J. Schleucher, M. Sattler, C. Griesinger, *Angew. Chem. Int. Ed. Engl.* **32**, 1489–1491 (1993).
31. M. Rance, *Bull. Magn. Reson.* **16**, 54–67 (1994).
32. M. Akke, P. A. Carr, A. G. Palmer, *J. Magn. Reson., Ser. B* **104**, 298–302 (1994).
33. D. W. Yang, L. E. Kay, *J. Biomol. NMR* **13**, 3–10 (1999).
34. T. Schulte-Herbrüggen, O. W. Sørensen, *J. Magn. Reson.* **144**, 123–128 (2000).
35. D. Nietlispach, *J. Biomol. NMR* **31**, 161–166 (2005).
36. R. H. Griffey, A. G. Redfield, *Q. Rev. Biophys.* **19**, 51–82 (1987).
37. K. Pervushin, R. Riek, G. Wider, K. Wüthrich, *J. Am. Chem. Soc.* **120**, 6394–6400 (1998).
38. E. Miclet, D. C. Williams, G. M. Clore, D. L. Bryce, J. Boisbouvier, A. Bax, *J. Am. Chem. Soc.* **126**, 10560–10570 (2004).
39. V. Tugarinov, R. Sprangers, L. E. Kay, *J. Am. Chem. Soc.* **126**, 4921–4925 (2004).
40. S. Grzesiek, A. Bax, *J. Am. Chem. Soc.* **115**, 12593–12594 (1993).
41. Y.-C. Li, G. T. Montelione, *J. Magn. Reson., Ser. B* **101**, 315–319 (1993).

42. J. Stonehouse, G. L. Shaw, J. Keeler, E. D. Laue, *J. Magn. Reson., Ser. A* **107**, 178–184 (1994).
43. B. A. Messerle, G. Wider, G. Otting, C. Weber, K. Wüthrich, *J. Magn. Reson.* **85**, 608–613 (1989).
44. G. W. Vuister, R. Boelens, R. Kaptein, R. E. Hurd, B. John, P. C. M. van Zijl, *J. Am. Chem. Soc.* **113**, 9688–9690 (1991).
45. L. E. Kay, P. Keifer, T. Saarinen, *J. Am. Chem. Soc.* **114**, 10663–10665 (1992).
46. G. Kontaxis, J. Stonehouse, E. D. Laue, J. Keeler, *J. Magn. Reson., Ser. A* **111**, 70–76 (1994).
47. C. Griesinger, O. W. Sørensen, R. R. Ernst, *J. Magn. Reson.* **84**, 14–63 (1989).
48. E. R. P. Zuiderweg, S. W. Fesik, *Biochemistry* **28**, 2387–2391 (1989).
49. D. Marion, P. C. Driscoll, L. E. Kay, P. T. Wingfield, A. Bax, A. M. Gronenborn, G. M. Clore, *Biochemistry* **28**, 6150–6156 (1989).
50. D. Marion, L. E. Kay, S. W. Sparks, D. A. Torchia, A. Bax, *J. Am. Chem. Soc.* **111**, 1515–1517 (1989).
51. S. Talluri, G. Wagner, *J. Magn. Reson., Ser. B* **112**, 200–205 (1996).
52. M. Ikura, L. E. Kay, R. Tschudin, A. Bax, *J. Magn. Reson.* **86**, 204–209 (1990).
53. G. M. Clore, A. Bax, A. M. Gronenborn, *J. Biomol. NMR* **1**, 13–22 (1991).
54. J. Cavanagh, M. Rance, *J. Magn. Reson.* **96**, 670–678 (1992).
55. S. W. Fesik, E. R. P. Zuiderweg, *J. Magn. Reson.* **78**, 588–593 (1988).
56. V. V. Krishnamurthy, *J. Magn. Reson., Ser. B* **106**, 170–177 (1995).
57. K. E. Kövér, V. J. Hruby, D. Uhrin, *J. Magn. Reson.* **129**, 125–129 (1997).
58. G. M. Clore, A. M. Gronenborn, *Annu. Rev. Biophys. Chem.* **20**, 29–63 (1991).
59. T. Frenkiel, C. Bauer, M. D. Carr, B. Birdsall, J. Feeney, *J. Magn. Reson.* **90**, 420–425 (1990).
60. M. Ikura, A. Bax, G. M. Clore, A. M. Gronenborn, *J. Am. Chem. Soc.* **112**, 9020–9022 (1990).
61. L. E. Kay, G. M. Clore, A. Bax, A. M. Gronenborn, *Science* **249**, 411–414 (1990).
62. D. R. Muhandiram, G. Y. Xu, L. E. Kay, *J. Biomol. NMR* **3**, 463–470 (1993).
63. G. M. Clore, L. E. Kay, A. Bax, A. M. Gronenborn, *Biochemistry* **30**, 12–18 (1991).
64. G. W. Vuister, G. M. Clore, A. M. Gronenborn, R. Powers, D. S. Garrett, R. Tschudin, A. Bax, *J. Magn. Reson., Ser. B* **101**, 210–213 (1993).
65. G. Zhu, A. Bax, *J. Magn. Reson.* **98**, 192–199 (1992).
66. L. E. Kay, M. Ikura, G. Zhu, A. Bax, *J. Magn. Reson.* **91**, 422–428 (1991).
67. L. E. Kay, M. Ikura, A. Bax, *J. Am. Chem. Soc.* **112**, 888–889 (1990).
68. A. Bax, G. M. Clore, P. C. Driscoll, A. M. Gronenborn, M. Ikura, L. E. Kay, *J. Magn. Reson.* **87**, 620–627 (1990).
69. M. Ikura, L. E. Kay, A. Bax, *J. Biomol. NMR* **1**, 299–304 (1991).
70. E. T. Olejniczak, R. X. Xu, S. W. Fesik, *J. Biomol. NMR* **2**, 655–659 (1992).
71. A. Bax, G. M. Clore, A. M. Gronenborn, *J. Magn. Reson.* **88**, 425–431 (1990).
72. L. E. Kay, M. Ikura, A. Bax, *J. Magn. Reson.* **91**, 84–92 (1991).
73. L. E. Kay, G.-Y. Xu, A. U. Singer, D. R. Muhandiram, J. D. Forman-Kay, *J. Magn. Reson., Ser. B* **101**, 333–337 (1993).
74. A. J. Shaka, C. J. Lee, A. Pines, *J. Magn. Reson.* **77**, 274–293 (1988).
75. M. Kadkhodaie, O. Rivas, M. Tan, A. Mohebbi, A. J. Shaka, *J. Magn. Reson.* **91**, 437–443 (1991).
76. A. Mohebbi, A. J. Shaka, *Chem. Phys. Lett.* **178**, 374–378 (1991).
77. S. P. Rucker, A. J. Shaka, *Mol. Phys.* **68**, 509–517 (1989).
78. M. Rance, *J. Magn. Reson.* **74**, 557–564 (1987).

79. G. M. Clore, A. Bax, P. C. Driscoll, P. T. Wingfield, A. M. Gronenborn, *Biochemistry* **29**, 8172–8184 (1990).
80. M. Ikura, L. E. Kay, A. Bax, *Biochemistry* **29**, 4659–4667 (1990).
81. L. E. Kay, M. Ikura, R. Tschudin, A. Bax, *J. Magn. Reson.* **89**, 496–514 (1990).
82. V. Tugarinov, R. Muhandiram, A. Ayed, L. E. Kay, *J. Am. Chem. Soc.* **124**, 10025–10035 (2002).
83. V. Tugarinov, L. E. Kay, *J. Am. Chem. Soc.* **125**, 13868–13878 (2003).
84. S. Grzesiek, A. Bax, *J. Magn. Reson.* **96**, 432–440 (1992).
85. F. Delaglio, D. A. Torchia, A. Bax, *J. Biomol. NMR* **1**, 439–446 (1991).
86. B. T. Farmer II, L. D. Venters, L. D. Spicer, M. G. Wittekind, L. Müller, *J. Biomol. NMR* **2**, 195–202 (1992).
87. M. Salzmann, G. Wider, K. Pervushin, K. Wüthrich, *J. Biomol. NMR* **15**, 181–184 (1999).
88. J. P. Loria, M. Rance, A. G. Palmer, *J. Magn. Reson.* **141**, 180–184 (1999).
89. A. Bax, M. Ikura, *J. Biomol. NMR* **1**, 99–104 (1991).
90. R. Powers, A. M. Gronenborn, G. M. Clore, A. Bax, *J. Magn. Reson.* **94**, 209–213 (1991).
91. D. R. Muhandiram, L. E. Kay, *J. Magn. Reson., Ser. B* **103**, 203–216 (1994).
92. R. T. Clubb, V. Thanabal, G. Wagner, *J. Magn. Reson.* **97**, 213–217 (1992).
93. R. Folmer, G. Otting, *J. Biomol. NMR* **16**, 229–233 (2000).
94. R. Bazzo, D. O. Cicero, G. Barbato, *J. Magn. Reson., Ser. B* **110**, 65–68 (1996).
95. F. Löhr, H. Rüterjans, *J. Biomol. NMR* **6**, 189–197 (1995).
96. S. Grzesiek, A. Bax, *J. Biomol. NMR* **3**, 185–204 (1993).
97. S. Grzesiek, A. Bax, *J. Am. Chem. Soc.* **114**, 6291–6293 (1992).
98. S. Grzesiek, A. Bax, *J. Magn. Reson.* **99**, 201–207 (1992).
99. A. C. Wang, P. J. Lodi, J. Qin, G. W. Vuister, A. M. Gronenborn, G. M. Clore, *J. Magn. Reson., Ser. B* **105**, 196–198 (1994).
100. G. T. Montelione, B. A. Lyons, S. D. Emerson, M. Tashiro, *J. Am. Chem. Soc.* **114**, 10974–10975 (1992).
101. S. Grzesiek, J. Anglister, A. Bax, *J. Magn. Reson., Ser. B* **101**, 114–119 (1993).
102. R. T. Clowes, W. Boucher, C. H. Hardman, P. J. Domaille, E. D. Laue, *J. Biomol. NMR* **3**, 349–354 (1993).
103. B. A. Lyons, G. T. Montelione, *J. Magn. Reson., Ser. B* **101**, 206–209 (1993).
104. T. M. Logan, E. T. Olejniczak, R. X. Xu, S. W. Fesik, *J. Biomol. NMR* **3**, 225–231 (1993).
105. M. Wittekind, L. Mueller, *J. Magn. Reson., Ser. B* **101**, 201–205 (1993).
106. B. A. Lyons, M. Tashiro, L. Cedergren, B. Nilsson, G. T. Montelione, *Biochemistry* **32**, 7839–7845 (1993).
107. E. W. Sayers, D. A. Torchia, *J. Magn. Reson.* **153**, 246–253 (2001).
108. N. Astrof, C. Bracken, J. Cavanagh, A. G. Palmer, *J. Biomol. NMR* **11**, 451–456 (1998).
109. L. E. Kay, A. Bax, *J. Magn. Reson.* **86**, 110–126 (1990).
110. M. Billeter, D. Neri, G. Otting, Y. Q. Qian, K. Wüthrich, *J. Biomol. NMR* **2**, 257–274 (1992).
111. R. Weisemann, H. Rüterjans, H. Schwalbe, J. Schleucher, W. Bermal, C. Greisinger, *J. Biomol. NMR* **4**, 231–240 (1994).
112. G. Montelione, G. Wagner, *J. Am. Chem. Soc.* **111**, 5474–5475 (1989).
113. G. Montelione, G. Wagner, *J. Magn. Reson.* **87**, 183–188 (1990).
114. P. Schmieder, V. Thanabal, L. P. McIntosh, F. W. Dahlquist, G. Wagner, *J. Am. Chem. Soc.* **113**, 6323–6324 (1991).
115. G. Wagner, P. Schmieder, V. Thanabal, *J. Magn. Reson.* **93**, 436–440 (1991).
116. O. W. Sørensen, *J. Magn. Reson.* **90**, 433–438 (1990).

117. J. C. Madsen, O. W. Sørensen, P. Sørensen, F. M. Poulsen, *J. Biomol. NMR* **3**, 239–244 (1993).
118. S. Seip, J. Balbach, H. Kessler, *Angew. Chem. Int. Ed. Engl.* **31**, 1609–1611 (1992).
119. S. Seip, J. Balbach, H. Kessler, *J. Magn. Reson., Ser. B* **104**, 172–179 (1994).
120. C. Griesinger, U. Eggenberger, *J. Magn. Reson.* **97**, 426–434 (1992).
121. G. T. Montelione, M. E. Winkler, P. Rauenbuehler, G. Wagner, *J. Magn. Reson.* **82**, 198–204 (1989).
122. Y. Karimi-Nejad, J. M. Schmidt, H. Rüterjans, H. Schwalbe, C. Griesinger, *Biochemistry* **33**, 5481–5492 (1994).
123. G. Wider, D. Neri, G. Otting, K. Wüthrich, *J. Magn. Reson.* **85**, 426–431 (1989).
124. M. Kurz, P. Schmieder, H. Kessler, *Angew. Chem. Int. Ed. Engl.* **30**, 1329–1331 (1991).
125. A. S. Edison, W. M. Westler, J. L. Markley, *J. Magn. Reson.* **92**, 434–438 (1991).
126. E. R. P. Zuiderweg, S. W. Fesik, *J. Magn. Reson.* **93**, 653–658 (1991).
127. R. X. Xu, E. T. Olejniczak, S. W. Fesik, *FEBS Lett.* **305**, 137–143 (1992).
128. U. Eggenberger, Y. Karimi-Nejad, H. Thüring, H. Rüterjans, C. Griesinger, *J. Biomol. NMR* **2**, 583–590 (1992).
129. S. D. Emerson, G. T. Montelione, *J. Am. Chem. Soc.* **114**, 354–356 (1992).
130. S. D. Emerson, G. T. Montelione, *J. Magn. Reson.* **99**, 413–420 (1992).
131. M. Sattler, H. Schwalbe, C. Griesinger, *J. Am. Chem. Soc.* **114**, 1126–1127 (1992).
132. M. D. Sørensen, S. M. Kristensen, J. J. Led, O. W. Sørensen, *J. Magn. Reson., Ser. A* **103**, 364–368 (1993).
133. G. W. Vuister, A. Bax, *J. Biomol. NMR* **2**, 401–405 (1992).
134. G. W. Vuister, A. Bax, *J. Am. Chem. Soc.* **115**, 7772–7777 (1993).
135. P. R. Blake, M. F. Summers, M. W. W. Adams, J.-B. Park, Z. H. Zhou, A. Bax, *J. Biomol. NMR* **2**, 527–533 (1992).
136. A. Bax, G. W. Vuister, S. Grzesiek, F. Delaglio, A. C. Wang, R. Tschudin, G. Zhu, *Meth. Enzymol.* **239**, 79–105 (1994).
137. S. Grzesiek, G. W. Vuister, A. Bax, *J. Biomol. NMR* **3**, 487–493 (1993).
138. G. W. Vuister, A. C. Wang, A. Bax, *J. Am. Chem. Soc.* **115**, 5334–5335 (1993).
139. G. W. Vuister, T. Yamazaki, D. A. Torchia, A. Bax, *J. Biomol. NMR* **3**, 297–306 (1993).
140. A. Bax, D. Max, D. Zax, *J. Am. Chem. Soc.* **114**, 6923–6925 (1992).
141. S. Grzesiek, M. Ikura, G. M. Clore, A. M. Gronenborn, A. Bax, *J. Magn. Reson.* **96**, 215–221 (1992).
142. S. J. Archer, M. Ikura, D. A. Torchia, A. Bax, *J. Magn. Reson.* **95**, 636–641 (1991).
143. C. Gayathri, A. A. Bothner-By, P. C. M. Van Zijl, C. Maclean, *Chem. Phys. Lett.* **87**, 192–196 (1982).
144. J. R. Tolman, J. M. Flanagan, M. A. Kennedy, J. H. Prestegard, *Proc. Natl. Acad. Sci. U.S.A.* **92**, 9279–9283 (1995).
145. N. Tjandra, S. Grzesiek, A. Bax, *J. Am. Chem. Soc.* **118**, 6264–6272 (1996).
146. N. Tjandra, A. Bax, *Science* **278**, 1111–1114 (1997).
147. J. H. Prestegard, C. M. Bougault, A. I. Kishore, *Chem. Rev.* **104**, 3519–3540 (2004).
148. M. Rückert, G. Otting, *J. Am. Chem. Soc.* **122**, 7793–7797 (2000).
149. M. R. Hansen, L. Mueller, A. Pardi, *Nat. Struct. Biol.* **5**, 1065–1074 (1998).
150. G. M. Clore, M. R. Starich, A. M. Gronenborn, *J. Am. Chem. Soc.* **120**, 10571–10572 (1998).
151. Y. Ishii, M. A. Markus, R. Tycko, *J. Biomol. NMR* **21**, 141–151 (2001).
152. H.-J. Sass, G. Musco, S. J. Stahl, P. T. Wingfield, S. Grzesiek, *J. Biomol. NMR* **18**, 303–309 (2000).
153. J. J. Chou, S. Gaemers, B. Howder, J. M. Louis, A. Bax, *J. Biomol. NMR* **21**, 377–382 (2001).

154. M. Ottiger, F. Delaglio, A. Bax, *J. Magn. Reson.* **131**, 373–378 (1998).
155. D. W. Yang, R. A. Venters, G. A. Mueller, W. Y. Choy, L. E. Kay, *J. Biomol. NMR* **14**, 333–343 (1999).
156. V. Vijayan, M. Zweckstetter, *J. Magn. Reson.* **174**, 245–253 (2005).
157. G. Kontaxis, G. M. Clore, A. Bax, *J. Magn. Reson.* **143**, 184–196 (2000).
158. A. S. Edison, F. Abildgaard, W. M. Westler, E. S. Mooberry, J. L. Markley, *Meth. Enzymol.* **239**, 3–79 (1994).